University of Glasgow | Experimental Particle Physics

Studies of Possible Improvements to the b-Jet Energy Resolution Applied to the Search for the Higgs Boson Produced in Association with a W Boson at the ATLAS Detector

Thomas Oliver Ravenscroft

School of Physics and Astronomy,
University of Glasgow

A thesis submitted to the University of Glasgow
for the degree of Doctor of Philosophy

July 2015

Abstract

This thesis presents a measurement of the cross-section for the production of a Higgs boson in association with a W boson. Where the Higgs boson decays to a pair of b-quarks and the W boson decays leptonically to a electron-neutrino pair or muon-neutrino pair. The measurements have been taken using 20 fb^{-1} of data collected at a centre-of-mass energy $\sqrt{s} = 8$ TeV from the ATLAS detector; one of the four main experiments at the Large Hadron Collider (LHC). An expected upper limit is calculated in the background-only hypothesis at 1.51 times the Standard Model expectation. The signal strength is measured at a Higgs boson mass $m_H = 125$ GeV to be $\mu = 3.22^{+0.71}_{-0.69}(\text{stat.})^{+1.03}_{-0.87}(\text{syst.})$

As part of the analysis performed, extensive studies have been carried out into the impact of the four jet calibrations used by the $WH \to l\nu b\bar{b}$ analysis for the Run I result. Jet calibrations are used to correct for detector effects and inefficiencies in the reconstruction of the jets. In addition to the studies on the current jet calibration methods, two additional jet calibrations are studied and their performance within the analysis are measured, with comparisons against the nominal expected upper limit. The first additional calibration replaces the current jet p_{T} calibration with one which uses different calibrations depending upon whether the jet contains a muon or not. By applying this calibration the expected upper limit improves to 1.50 times the Standard Model expectation.

The second calibration uses a regression to improve the b-jet resolution. Using well modelled variables, there is no change in the expected upper limit, however by considering all variables, the expected upper limit improves to 1.47 times the Standard Model expectation, giving a 2.5% improvement to the nominal analysis.

Declaration

I declare that the results here represent my own work unless references are made within the text to the work of others. This thesis is the result of research carried out as part of the Experimental Particle Physics group in the School of Physics & Astronomy within the University of Glasgow between October 2011 and April 2015. It has not been submitted as part of any other degree at the University of Glasgow or any other institution.

Thomas Oliver Ravenscroft

Acknowledgements

First and foremost I would like to thank the Science and Technology Facilities Council (STFC) for providing me with the funding to undertake the work for this Ph.D.

For giving me the opportunity to work as part of the experimental particle physics group at the University of Glasgow for my Ph.D, I would like to thank Tony Doyle.

I would like to thank my supervisors Dave Britton and Aidan Robson for their guidance for introducing me to working as part of the HSG5 group on ATLAS. I am thankful to Adrian Buzatu for his help, assistance and knowledge working towards further correcting the b-jets as part of the $WH \to l\nu b\bar{b}$ analysis.

I would like to thank Tom Doherty and Stan Thompson at Glasgow and Emil Obreskov at CERN for helping me achieve my ATLAS authorship for the work I did with the ATLAS software infrastructure team.

I would also like to thank the people in the UKLO at CERN for their assistance during my stay at CERN during my LTA. Thank you also, to all the friends I made during my LTA. you made the two years much more fun than they otherwise would have been.

For the never ending support and belief for what I could achieve I would like to thank my parents, Anne and Mark and my brothers Dave and Matt. Finally I would like to offer thanks to Becca for her support of the last two years and for putting up with me when I became stressed. I hope I was able to offer you the same courtesy.

Author's Contribution

Due to the nature of modern high energy physics experiments having collaborations from many people from different nationalities around the world, the results obtained in this thesis rely on work done by many other members of the ATLAS Collaboration. The Individual contributions made by the author are outlined below:

- **Part III:** The results obtained in this part were obtained by the author however, the ATLAS $VH(b\bar{b})$ group provided the methods for the background estimation, object and event selection, the derivation of the muon-in-jet calibration and the jet p_{T} calibration and the framework for deriving the final limit. In this part, the author made significant contributions in the following chapters:
  - **Chapter 6:** The author did extensive studies into the current jet calibration methods used in the $WH \to l\nu b\bar{b}$ analysis on ATLAS. Additional jet calibrations were also studied which have potential use in Run II analyses including; a re-derivation of the jet p_{T} calibration as well as using multivariate techniques in a regression analysis to improve the b-jet resolution.
  - **Chapter 9:** The methods and code to perform the statistical analysis and limit extraction were developed by other member of the ATLAS collaboration. The limit using the current jet calibrations was initially produced by other members of the $VH(b\bar{b})$ working group. The author produced inputs and extracted a limit to intially validate the current jet calibration methods and also to extract the limit for the additional jet calibrations.

Contents

List of Figures

List of Tables

Part I

Theory & Background

Chapter 1

Theory

The Standard Model of particle physics [1] is a gauge theory based upon quantum field theory. Formulated in the 1970s, it describes the interactions of fundamental matter and represents the current understanding of the Universe at an elementary particle level. The Large Hadron Collider (LHC) is being used amongst other physics goals, to test the Standard Model to an unprecedented level of accuracy using proton-proton collisions.

A brief overview of the Standard Model is given in Section 1.1, including an outline into the spontaneous breaking of electroweak symmetry which gives rise to the massive vector bosons and fermions observed in nature. For a detailed discussion into the workings of the Standard Model, see [2], and [3].

Proton-proton interactions are discussed in Section 1.2 and the Monte Carlo event generators used for the event simulation are described in Section 1.3.

1.1. The Standard Model

The Standard Model gives the best description of the physical universe; it describes the interactions between fermions which are the building blocks of matter. The interactions are mediated by the force carrying bosons. In the Standard Model, the fermions have a half-integer spin and the bosons, known as *gauge bosons* have spin-1.

To build the Standard Model, quantum field theory is used. There are three sectors which will be described in this section: quantum chromo-dynamics (QCD), electroweak theory, and the spontaneous electroweak symmetry breaking.

1.1.1. Fundamental Fermions

The fermions are split into two categories: *quarks* and *leptons*. There are six quarks split into three generations, each consisting of an up-type quark, with electrical charge $+2/3$ (named: 'up u', 'charm' c, and 'top' t) and a down-type quark with electrical charge $-1/3$ flavour (named: 'down' d, 'strange' s, and 'bottom' b). The arrangement of the quark flavours in their generations is shown below:

$$\begin{pmatrix} u \\ d \end{pmatrix} \begin{pmatrix} c \\ s \end{pmatrix} \begin{pmatrix} t \\ b \end{pmatrix}.$$

As with quarks, there are six leptons split into three generations. Each generation consists of an electronically charged lepton with charge -1 (named: 'electron' e^-, 'muon' μ^-, and 'tau' τ^-) and a neutrally charged neutrino. The arrangement of the lepton generations is shown below:

$$\begin{pmatrix} \nu_e \\ e^- \end{pmatrix} \begin{pmatrix} \nu_\mu \\ \mu^- \end{pmatrix} \begin{pmatrix} \nu_\tau \\ \tau^- \end{pmatrix}.$$

With each quark and lepton generation, the fermions increase in mass. The fundamental fermions have spin $1/2$, and each fermion has its own antiparticle counterpart; although there is an open question as to whether the neutrinos are their own antiparticle. The antiparticles have an identical mass to their counterparts but an opposite charge. The properties of the fundamental fermions are given in Table 1.1.

1.1.2. Fundamental Forces & Bosons

The interactions between the fermions are mediated by the force carrying bosons. There are four known fundamental forces: *strong*, *weak*, *electromagnetic*, and *gravitation*.

The strong nuclear force binds nuclei together, acting between quarks. It is the strongest of the four forces. Mediating between the strong interactions is the massless *gluon*, which carries a colour charge. The colour charge comes in three 'types': red, green, and blue. The gluons are able to interact with each other, which leads to the strength of the strong force *increasing* with distance. This property of self-interaction leads to *confinement*, where bare quarks are not observed in nature; only as colour neutral composite states. The theory describing the strong force is *quantum chromodynamics* (QCD).

The weak nuclear force is responsible for the decays of unstable particles; interacting between particles with weak isospin. The strength of the weak force is $\sim 10^5$ weaker than the strong force. The mediation of the weak force is performed by the $W^{\pm}$ and Z bosons. The $W^{\pm}$ have integer electric charge and the Z boson is electrically neutral. Both $W^{\pm}$ and Z bosons are massive leading to a short interaction distance of the weak force.

Interactions between electronically charged particles are mediated by the electromagnetic force. The electromagnetic force binds nuclei into atoms and binds atoms into more complex structures. The interactions are mediated by the photon which is a massless, electrically neutral particle. Unlike the gluon, there is no self-interaction between photons leading to an infinite range of the electromagnetic force. The theory which describes the electromagnetic force is *quantum electrodynamics* (QED) [4].

The gravitational force is the final of the four fundamental forces. It describes the attraction between massive bodies and is the weakest of all the forces; with a strength 10^{38} times weaker than the electromagnetic force. The weakness of gravity leads to a negligable effect on the interactions of microscopic particles. Since it is not yet formulated as a quantum field theory and not part of the Standard Model, it will not be described further.

A summary of the properties of the gauge bosons is shown in Table 1.1.

Particle	Spin	Charge	Mass [GeV]
Leptons			
Electron, e^-	$1/2$	-1	0.511×10^{-3}
Electron neutrino, ν_e	$1/2$	0	$< 2 \times 10^{-9}$
Muon, μ	$1/2$	-1	0.106
Muon neutrino, ν_μ	$1/2$	0	$< 2 \times 10^{-9}$
Tau, τ	$1/2$	-1	1.7768 ± 0.0001
Tau neutrino, ν_τ	$1/2$	0	$< 2 \times 10^{-9}$
Quarks			
Up, u	$1/2$	$+2/3$	$2.3^{+0.7}_{-0.5} \times 10^{-3}$
Down, d	$1/2$	$-1/3$	$4.8^{+0.5}_{-0.3} \times 10^{-3}$
Charm, c	$1/2$	$+2/3$	1.1275 ± 0.025
Strange, s	$1/2$	$-1/3$	$95 \pm 5 \times 10^{-3}$
Top. t	$1/2$	$+2/3$	173.2 ± 0.9
Bottom, b	$1/2$	$-1/3$	4.66 ± 0.03
Gauge Bosons			
Photon, γ	1	0	0
Gluon, g	1	0	0
$W^\pm$	1	± 1	80.385 ± 0.015
Z	1	0	91.1876 ± 0.0021
Higgs, H	0	0	125.7 ± 0.9

Table 1.1: A summary of the fundamental particles and their properties. Taken from [5].

1.1.3. Quantum Chromodynamics (QCD)

Quantum chromodynamics (QCD) [6] is a quantum field theory describing the strong interaction, using the $SU(3)$ gauge group. The colour charges are coupled between quarks and gluons. The theory is constructed by requiring invariance under local gauge transformations. There are eight associated generators of the $SU(3)$ group, representing the eight gluons. A ninth non-physical singlet is also present; acting equally on all quarks.

Self-interaction between gluons is brought about due to the non-abelian nature of the $SU(3)$ group. The self-interaction allows gluons to couple to other gluons in the QCD Lagrangian, since the gluons are the carriers of the colour charge. A peculiar property is brought about due to the self-interaction: as the distance between the quarks increases,

so does the strong force acting between them. This leads to enough energy present to create a new pair of quarks. As a result of this, quarks and gluons only ever exist in bound colourless states and never as bare colour charges.

During a high energy particle collision, or over short distances, the strong coupling between the quarks is weaker allowing them to behave more like free particles.

1.1.4. Electroweak Theory

The unification of the electromagnetic and weak forces was proposed in the min-1960s by Weinberg [7] and Salam [8], and would become known as the electroweak theory. It is thought of as one of the major triumphs of the twentieth century in physics. The proposal unified the two forces under the gauge group $SU(2)_L \times U(1)_Y$, where Y corresponds to the hypercharge field and L corresponds to the left-handed projected nature of the associated weak isospin field. The hypercharge and third component of weak isospin, I_3 are related to the electromagnetic charge, Q by the following relation:

$$Q = I_3 + Y. \tag{1.1}$$

A pillar of the theory is the requirement of local gauge invariance under local gauge transformations, leading to the emergence of vector gauge fields and associated vector gauge bosons. The associated gauge bosons are the massless singlet, B_μ and the massless triplet, $\mathbf{W}^i_\mu$ where i corresponds to the three isospin fields ($i = 1, 2, 3$).

The weak isospin fields act upon doublets shown in Equation 1.2:

$$\psi_L = \begin{pmatrix} u_i \\ d_i \end{pmatrix}, \begin{pmatrix} \nu_i \\ \ell_i \end{pmatrix}, \tag{1.2}$$

where u and d represent the up- and down-type quarks respectively for each generation, i. ν and ℓ represent the neutrino and associated lepton for each generation,. L indicates the left-handed projection of the doublet which is what is observed experiementally. This leads to the doublets being maximally parity violating. The right handed projections, ψ_R transform as singlet states, which are invariant under $SU(2)_L$.

Equations 1.3 and 1.4 show that the physical gauge bosons, γ, Z and $W^{\pm}$ result from mixing between gauge fields:

$$W_{\mu}^{\pm} = \frac{1}{\sqrt{2}}(W_{\mu}^{1} \mp W_{\mu}^{2}), \tag{1.3}$$

$$\begin{pmatrix} A_{\mu} \\ Z_{\mu}^{0} \end{pmatrix} = \begin{pmatrix} \cos\theta_W & \sin\theta_W \\ -\sin\theta_W & \cos\theta_W \end{pmatrix} \cdot \begin{pmatrix} B_{\mu} \\ W_{\mu}^{3} \end{pmatrix}, \tag{1.4}$$

where A_{μ} is the photon field, Z_{μ}^{0} is the Z field, θ_W is the weak mixing angle and $W_{\mu}^{\mp}$ correspond to the $W^{\mp}$ bosons. θ_W is related to the couplings of the weak neutral currents, g and charged currents, g' as:

$$\theta_W = \tan^{-1}\left(\frac{g'}{g}\right). \tag{1.5}$$

The weak neutral currents were discovered at the Gargamelle bubble chamber experiment at CERN in 1971 [9], and the $W^{\pm}$ and Z bosons were discovered by the UA1 and UA2 collaborations, also at CERN in 1983 [10–13].

1.1.5. Spontaneous Symmetry Breaking (SSB)

The unified theory of the electromagnetic, weak, and strong forces is defined by the local gauge group $SU(3)_C \times SU(2)_L \times U(1)_Y$ and its associated Lagrangian. For the conservation of local gauge symmetries in the gauge groups, the gauge bosons defined in Equations 1.3 and 1.4 must be massless along with the fermions. Experimental evidence has shown however, the $W^{\pm}$ and Z bosons as well as the fermions are all massive. To be able to assign masses to the fermions and the gauge bosons, the symmetry must be broken.

The mechanism for spontaneous symmetry breaking was first introduced by three groups working independantly: Higgs [14–16], Brout and Englert [17], and by Guralnik, Hagen, and Kibble [18]. The mechanism provides a solution for why the $W^{\pm}$ and Z bosons have mass. It is more commonly known as the Englert-Brout-Higgs mechanism or EBH mechanism.

To allow the electroweak Lagrangian to remain invariant while the vacuum state does not, which spontaneously breaks the electroweak symmetry; a complex scalar field

attaining a non-zero vacuum expectation value (VEV) defined as:

$$\phi = \begin{pmatrix} \phi^+ \\ \phi^0 \end{pmatrix}, \tag{1.6}$$

is introduced. The electroweak Lagrangian can be written in the following simple form:

$$\mathcal{L} = -\frac{1}{4}(\mathbf{F}_{\mu\nu} \cdot \mathbf{F}^{\mu\nu} + G_{\mu\nu}G^{\mu\nu}), \tag{1.7}$$

where $\mathbf{F}_{\mu\nu}$ and $G_{\mu\nu}$ are the respective weak isospin and field strength tensors which relate to the fields as follows:

$$\mathbf{F}_{\mu\nu} = \partial_\mu \mathbf{W}_\nu - \partial_\nu \mathbf{W}_\mu - g\mathbf{W}_\mu \times \mathbf{W}_\nu \tag{1.8}$$

$$G_{\mu\nu} = \partial_\mu B_\nu - \partial_\nu B_\mu, \tag{1.9}$$

where $\mathbf{W}_\mu = \{W^1_\mu, W^2_\mu, W^3_\mu\}$, B_μ is the singlet from the electromagnetic field, and g is the neutral current coupling strength. The introduction of the complex scalar field ϕ, yield an additional term of the form:

$$\mathcal{L}_\phi = (D_\mu\phi)^\dagger(D_\mu\phi) - V(\phi), \tag{1.10}$$

$$\text{with } D_\mu = \partial_\mu - \frac{1}{2}(igT_iW^i_\mu - ig'B_\mu), \tag{1.11}$$

where T_i are the $SU(2)$ group generators. The $V(\phi)$ term is the invariant and renormalisable scalar potential:

$$V(\phi) = \lambda(\phi^\dagger\phi) - \mu_{SM}\phi^\dagger\phi. \tag{1.12}$$

The values λ and μ_{SM} are constants which parameterise the self interaction and masses of the scalar field. When $V(\phi)$ is at a minimum, the expectation values ($\langle 0|\phi|0\rangle$) of the vacuum states are given by:

$$\langle 0|\phi|0\rangle = \frac{1}{\sqrt{2}} \begin{pmatrix} 0 \\ v \end{pmatrix}, \tag{1.13}$$

$$\text{where } v = \frac{\mu^2_{SM}}{\lambda}. \tag{1.14}$$

By considering small perturbations around the vacuum state, the masses of the physical particles are obtained. θ_i and H represent small variations in the four degrees of freedom of ϕ. By applying these small variations, then:

$$\phi = \exp\left[\frac{-i\theta_i T^i}{2v}\right]\frac{1}{\sqrt{2}}\begin{pmatrix} 0 \\ v+H \end{pmatrix}. \tag{1.15}$$

By using an appropriate gauge transformation, the phase fields θ_i can be set to zero, leaving only H. Inserting ϕ into the Lagrangian, H is identified as the scalar field with mass m_H:

$$m_H = \sqrt{2}\mu_{SM}. \tag{1.16}$$

The $W_\mu^\pm$ and Z_μ^0 fields acquire mass terms, m_W and m_Z which are related by:

$$m_W = m_Z \cos\theta_W = \frac{gv}{2}. \tag{1.17}$$

For the addition of fermion mass terms, Yukawa interactions between the fermions and the Higgs field are considered. The Yukawa interactions have coupling strength, g_f which is proportional to the mass of the fermion m_f such that the heavier fermions have a stronger coupling to the Higgs field. The coupling strength for a fermion is defined as:

$$g_f = im_f\frac{\sqrt{2}}{v}. \tag{1.18}$$

There is no prediction for the coupling strength given by the Standard Model, however it can be calculated using the observed masses of the fermions. The measured masses of the W and Z bosons can be used in conjuntion with the measured value of the fine structure constant for the determination of $\sin\theta_W$, v; μ_{SM} cannot be predicted however. Hence m_H is not directly predicted by the Standard Model, although indirect methods can be used to constrain the mass of the Higgs boson from theoretical considerations using precise electroweak data [19].

In July 2012, both ATLAS [20] and CMS [21] collaborations reported the discovery of a new boson whose properties were consistent with the Higgs boson.

1.2. Proton-Proton Interactions

A proton is a fermion consisting at the simplest level of three quarks; two up quarks and one down quark. Holding the quarks together inside the proton is the strong force, mediated by gluons. The three valence quarks exchange gluons which split further into additional quark pairs, known as *sea quarks*.

During a collision between two protons at a hadron collider, it is not the protons which interact, but the constituent quarks and gluons. The collisions between these quarks and gluons (partons) are classified into two categories: hard and soft; depending upon the momentum transferred in the collision. The hard scattering events produce two or more hard outgoing particles whereas the soft scattered elements of the collision are formed from the remains of either the original collision or secondary collisions between the partons. The soft scattered elements are collectively known as the *underlying event* (UE). An example of a collision between two protons is shown in Figure 1.1, highlighting the hard and soft scattering processes. Also shown is the emission of *final state radiation* (FSR) and *initial state radiation* (ISR) from incoming particles emitting QCD radiation in the form of gluons.

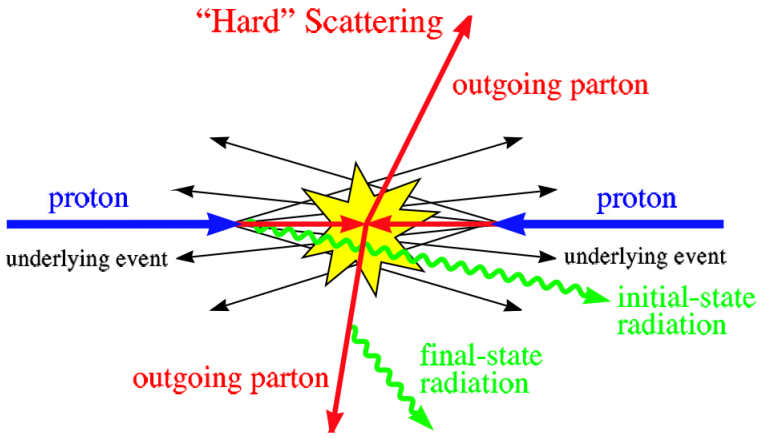

Figure 1.1: Illustration of the hard and soft scatterings along with the initial-state and final-state radiation as part of proton-proton collisions. Taken from [22]

The soft scatterings within a proton are not described using pertubative QCD, where the perturbative part refers to perturbation theory in mathematics whereby an approximate solution to a problem is found by starting from an exact solution of a related problem and a series of perturbations is added in series. Therefore the internal structure is described using experimental fits to data. The probability of finding a parton of flavour i, carrying a fraction of incoming proton momentum x_i is described using Parton Distribution

Functions (PDFs) of the form $f_i(x_i, Q^2)$, where Q^2 is the momentum transferred in the interaction. For the modelling of interactions within the proton, splitting functions and perturbative QCD are used as part of the DGLAP equations [23] to evolve the PDFs between different Q^2 values.

For the calculations of the cross-sections of interactions involving hadrons, the *factorisation theorem* plays an important role. The factorisation theorem allows the hard-scattering component of the interaction which is fully determined from perturbative QCD to be fully factorised from the soft-scattering component which is modelled using phenomenology and the parameters in such models are extracted from fits to data. For these reasons, the hard-scattering processes in proton-proton collisions are calculated from perturbative QCD, and the soft-scattering processes are described by PDFs.

For two protons with momenta P_1 and P_2 respectively, the cross-section for the scattering can be written as:

$$\begin{aligned}\sigma(P_1, P_2, Q^2) = \sum_{i,j} \int dx_1 dx_2 f_i(x_1, \mu_F) f_i(x_2, \mu_F) \\ \times \hat{\sigma}_{i,j\to X}\left(x_1 \cdot P_1, x_2 \cdot P_2, \alpha_s(\mu_R^2), \frac{Q^2}{\mu_F}, \frac{Q^2}{\mu_R}\right),\end{aligned} \tag{1.19}$$

where the sum of i and j is the sum over parton flavour, $\hat{\sigma}_{i,j\to X}$ is the partonic cross-section for partons i, j scattering to give X, and $f_i(x_1, \mu_F)$ are the PDFs. μ_F is the factorisation scale where the PDF is evaluated, setting the boundary for hard and soft processes, and μ_R is the renormalisation scale.

For calculations to all orders of perturbation theory, there is no dependence on the choice of scale for μ_F and μ_R. It is only possible for most processes however, to perform calculations for the first few terms in the expansion; leading to a dependence on scale. The dependence on scale does decrease with calculations to higher orders.

1.3. Monte Carlo Event Simulation

For a measurement in high energy physics, the simulation of events plays an important role. By simulating events, theoretical models may be tested against what is observed in nature. Simulation also allows for the calibration of the detector response and for estimating selection efficiencies in order to translate the observed events to a physical measurable quantity.

For the simulation; events are generated using Monte Carlo simulation. The process

for event simulation uses numerical integration for the calculation of matrix elements to generate events. The event generation can be broken down into four steps; calculation of the matrix element for simulating the hard scattering, adding ISR and FSR using a parton shower, hadronisation, and finally the embedding of the underlying event. Detailed information on Monte Carlo event simulation can be found in [24, 25].

The analysis presented uses several Monte Carlo generators for the simulation of signal and background processes. For each generator used, an outline of how it is used and its properties is given.

- PYTHIA [26] is a leading order (using simplest diagrams) generator used for almost all Standard Model processes. It is configured with the AU2 tune and uses the CTEQ6L1 PDFs [27] as part of this thesis. It is used for the generation of the signal as well as the diboson background processes.

- SHERPA [28] is another leading order generator used for the generation of $W/Z+$jets background processes. As part of the analysis shown in Part III, it is interfaced with CT10 PDFs [29] and uses massive b- and c-quarks. Filters are applied in order to separate the processes for events containing b, c, or light jets.

- POWHEG [30] is a framework for implementing next-to leading order (inclusion of single loop diagrams) calculations (NLO). It is interfacted with an event generator and matches the parton shower to the NLO matric element. For this thesis, POWHEG is interfaced with PYTHIA for the showering of the diboson, $t\bar{t}$, and single-top s-channel processes.

- ACERMC [31] is a leading order event generator dedicated to the simulation of Standard Model background processes. ACERMC performs the hard scattering process with the generation of the matrix element. Once this is completed, it is passed to a second generator for the showering and hadronisation. This thesis uses ACERMC interfaced with PYTHIA for the production of single-top t- and Wt-channels.

Chapter 2

Higgs Boson Production & Previous Results

The Standard Model has been tested to a high level of precision through experimental methods at particle colliders. Until its discovery by the ATLAS and CMS collaborations in 2012, the Higgs boson was one of the final pieces to be confirmed in the Standard Model. The Higgs boson offers an explanation as to why the particles in the Standard Model have mass and studying its properties is an important part in further testing the Standard Model and its theoretical predictions.

This chapter focusses on how the the Higgs boson is produced in a proton-proton collider in Section 2.1 and in Section 2.2, the decays it can follow. In Section 2.3 the results from searches for the Standard Model Higgs boson at previous colliders are discussed as well as the latest results from the LHC.

2.1. Higgs Boson Production at the LHC

There are several production mechanisms by which the Standard Model Higgs boson can be produced at the LHC. The diagrams for these processes are shown in Figure 2.1. Figure 2.2 shows the relationship between the mass of the Higgs boson and the theoretical cross-section, which is calculated via the method described in [32]. The values for the cross-section at $m_H = 125$ GeV for a centre of mass energy $\sqrt{s} = 8$ TeV, are shown in Table 2.1. The highest production rate at $m_H = 125$ GeV is gluon-fusion (ggF) [33], which occurs through quark loops. For the calcuation of the production cross-section, next-to next-to leading order (NNLO) QCD, NLO electroweak corrections and next-to

next-to leading logarithmic (NNLL) terms are used. The second most dominant process for Higgs production is vector boson fusion (VBF) [34]. Compared to the production cross-section of ggF it is an order of magnitude smaller. VBF cross-sections calculations use full NLO QCD and NLO electroweak corrections. Association production of a Higgs boson and a vector boson (VH) [35] has the next highest cross-section, with the Higgs production with association of a W-boson being slightly higher than that of the Z-boson. For the cross-section calculations for associated production with a vector boson, NLO electroweak and NNLO QCD corrections are used. The final production mechanism with the lowest production cross-section is the associated production of a Higgs boson with a top quark pair (ttH) [36]. For the calculation of the cross-section, only NLO QCD corrections are used. The uncertainties in Table 2.1 and Figure 2.2 are from PDF uncertainties and choices of factorisation and normalisation scales.

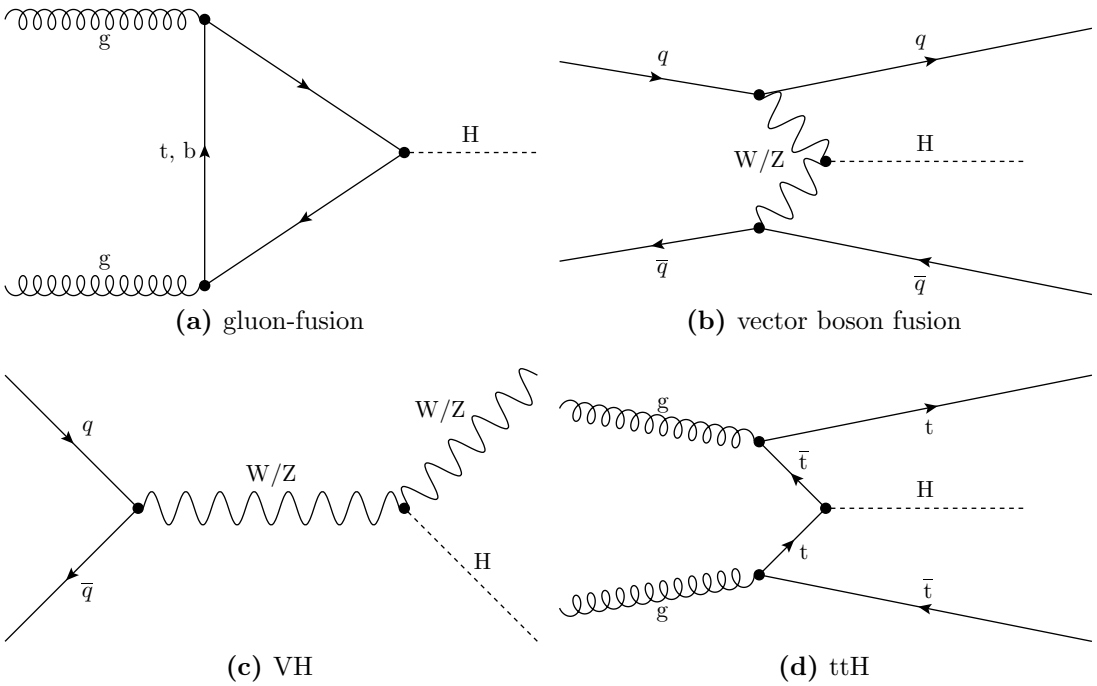

(a) gluon-fusion **(b)** vector boson fusion

(c) VH **(d)** ttH

Figure 2.1: Leading order feynman diagrams for the production mechanisms of the Higgs boson at the LHC; gluon-fusion (ggF), vector boson fusion (VBF), associated production of a Higgs boson with a vector boson (VH), and the associated production of a Higgs boson with top quarks (ttH)

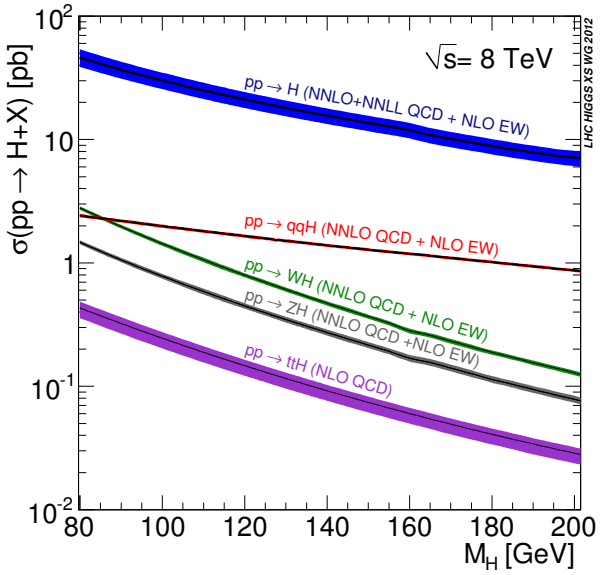

Figure 2.2: Cross-sections for the different Higgs boson production mechanisms at $\sqrt{s} = 8$ TeV as a function of Higgs boson masses m_H. Gluon-fusion dominates in at all masses, followed by vector boson fusion and the associated production mechanisms. The width of the lines represent the theoretical uncertainties on the cross-sections. Taken from [37].

Production Mechanism	Cross-section @ $m_H = 125$ GeV [pb]
ggF	$19.52^{+2.87}_{-2.87}$
VBF	$1.58^{+0.04}_{-0.05}$
WH	$0.70^{+0.03}_{-0.03}$
ZH	$0.39^{+0.02}_{-0.02}$
ttH	$0.13^{+0.02}_{-0.02}$

Table 2.1: The cross-sections for each of the Higgs boson production mechanisms at the LHC for a Higgs boson with a mass $m_H = 125$ GeV and at a centre-of-mass energy, $\sqrt{s} = 8$ TeV. Taken from [37].

2.2. Higgs Boson Decay Modes

There are a large number of potential channels via which the Higgs boson can decay within the Standard Model. Due to the strong dependence on coupling to mass, the Higgs boson decays favour heavy Vector bosons and fermions. Figure 2.3 shows the three main mechanisms via which the Higgs boson decays to two photons, vector bosons and fermions. The distribution of the branching fraction for the main decay channels as a function of Higgs boson mass, m_H is shown in Figure 2.4. Table 2.2 summarises the branching fraction for the most favourable decay modes at a Higgs boson mass, $m_H = 125$ GeV.

The most favourable decay mode at $m_H = 125$ GeV is the decay to a b-quark pair, followed by decays to W bosons. Another prominant decay is the Higgs boson decaying to gluon pairs. This process occurs via heavy quark loops, as seen for the ggF production.

The branching fraction of a decay mode at the LHC does not only depend on the mass of the final state. The final state signature and the cross-section of the background candidate events also are a factor. For this reason decays to a b- or c-quark and hadronic decays of W and Z bosons are less sensitive final states compared to decays to lepton final states.

The decay widths of the Higgs boson along with the branching fractions are computed using HDECAY [38], with the uncertainty calculations upon the branching fractions described in [37]. When available, the higher order QCD and electroweak corrections are applied.

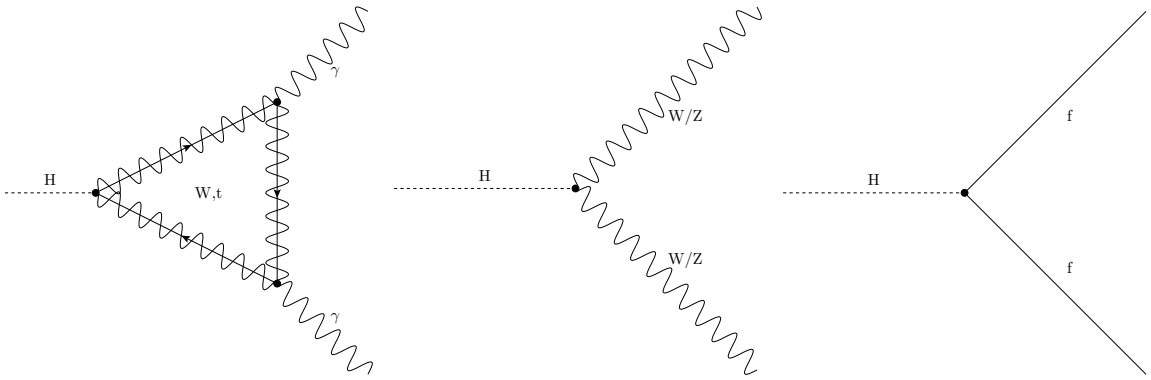

(a) Photons **(b)** Vector bosons **(c)** Fermions

Figure 2.3: The mechanisms via which the Higgs boson decays to photons (a), vector bosons (b), and fermions (c) within the Standard Model.

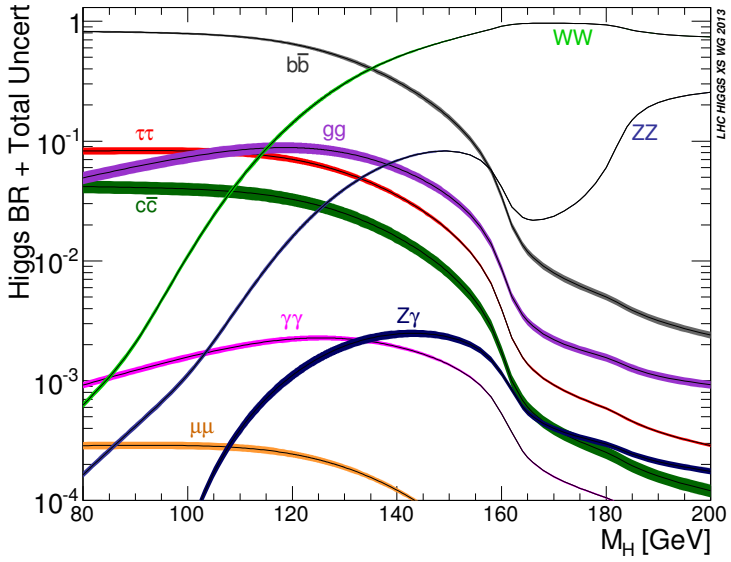

Figure 2.4: The branching rations of the Standard Model Higgs boson for a range of Higgs boson mass, m_H. At $m_H = 125$ GeV, the decays to a pair of b-quarks is most favourable followed by the decay to two W bosons. The uncertainties on the branching fraction and theoretical uncertainties are represented by the thickness of the lines. Taken from [37].

Decay Mode	Branching Fraction @ $m_H = 125$ GeV
$H \to b\bar{b}$	$5.77 \times 10^{-1}\ ^{+3.2\%}_{-3.3\%}$
$H \to WW$	$2.15 \times 10^{-1}\ ^{+4.3\%}_{-4.2\%}$
$H \to gg$	$8.57 \times 10^{-2}\ ^{+10.2\%}_{-10.0\%}$
$H \to c\bar{c}$	$2.91 \times 10^{-2}\ ^{+12.2\%}_{-12.2\%}$
$H \to \tau\tau$	$6.32 \times 10^{-2}\ ^{+5.7\%}_{-5.7\%}$
$H \to ZZ$	$2.64 \times 10^{-2}\ ^{+4.3\%}_{-4.2\%}$
$H \to \gamma\gamma$	$2.28 \times 10^{-3}\ ^{+5.0\%}_{-4.9\%}$
$H \to \mu\mu$	$2.20 \times 10^{-4}\ ^{+6.0\%}_{-5.9\%}$

Table 2.2: Table showing the branching fractions of the main Higgs boson decay channels for a Higgs boson mass of $m_H = 125$ GeV. The uncertainties are shown as percentages to emphsise the relative accuracy of each branching fraction calculation. Taken from [37].

2.3. Previous Searches & Results

This section will look at the results from previous searches for the Standard Model Higgs boson at the Large Electron Positron collider (LEP) [39–41], the Tevatron [42, 43], and will also discuss the discovery of the Higgs boson by the ATLAS and CMS collaborations which was made in July 2012. The final part of this section will discuss the latest combination between ATLAS and CMS for the Higgs boson Standard Model compatibility.

2.3.1. Large Electron Positron Collider (LEP)

LEP was an electron-positron collider at CERN, colliding the two at centre-of-mass energies between $\sqrt{s} =$ 90–209 GeV. The searches for the Standard Model Higgs boson performed at LEP were in the so-called 'Higgsstrahlung' production mechanism; where the Higgs boson is produced in association with a Z boson. The decay of the Higgs boson was predominantly to pairs of b-quarks. By a combination between the four LEP experiments (ALEPH, DELPHI, OPAL, and L3) an exclusion limit was placed on the mass of the Higgs boson of $m_H < 114.4$ GeV at a 95% confidence level [44].

2.3.2. The Tevatron

The Tevatron was a proton-antiproton collider based at the Fermilab Laboratory in Illinois. The beams of protons and antiprotons were collided at centre-of-mass energies $\sqrt{s} = 1.96$ TeV at two experiments, D0 and CDF. The Higgs boson searches at the Tevatron were performed in a wide array of channels with the most sensitive being decays to a pair of b-quarks and WW. A combination between the two experiments excluded the region 90–109 GeV and 149–182 GeV at a 95% CL, as well as observing a 3σ excess in the $b\bar{b}$ decay mode [45]. Figure 2.5 shows the results of this combination.

The direct searches at LEP and the Tevatron can be combined with precision electroweak measurements taken at LEP and the SLAC Large Detector to contrain the mass of the Higgs boson to 94^{+29}_{-24} GeV [19]; where the uncertainties are from experimental sources only.

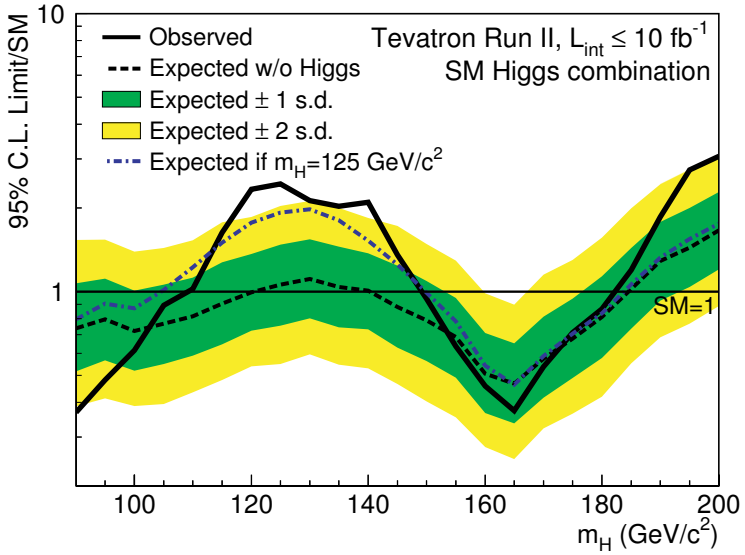

Figure 2.5: The observed and expected 95% CL production limits as a multiple of the Standard Model cross-section as a function of Higgs boson mass, combining the results from CDF and D0 in all decay modes. Taken From [45]

2.3.3. Large Hadron Collider (LHC)

On the 4$^{\text{th}}$ July 2012, the ATLAS and CMS collaborations announced the discovery of a new particle produced at the Large Hadron Collider (LHC) [20, 21]. Both experiments reported that the new particle was compatible with the Standard Model Higgs boson, with a mass of ~ 125 GeV. The results were taken from a combination of 5 fb^{-1} $\sqrt{s} = 7$ TeV and 5–6 fb^{-1} $\sqrt{s} = 8$ TeV data. The discovery was made predominantly in the ZZ and $\gamma\,\gamma$ decay channels with a combined excess observed in data yielding 5σ deviation from the background-only hypothesis.

By the end of Run I at the end of 2013, ~ 20 fb^{-1} of data had been collected at $\sqrt{s} =$ 8 TeV, allowing access to some of the less sensitive decay modes. A combination of CMS Higgs searched yields a best fit mass of $m_H = 125.02^{+0.26}_{-0.27}(\text{stat.})^{+0.14}_{-0.15}(\text{syst.})$ GeV and a signal strength relative to the Standard Model expectaion of $1.00 \pm 0.09(\text{stat.})^{+0.08}_{-0.17}(\text{theo.}) \pm 0.01(\text{syst.})$ This result is from a combination of $\gamma\gamma$, WW, ZZ, $b\bar{b}$, $\tau\tau$, and $\mu\mu$ decay modes as well as ttH production searches and searches for an invisible Higgs [46].

A combination of ATLAS Higgs boson searches in the $\gamma\gamma$, ZZ, WW, $Z\gamma$, $b\bar{b}$, $\tau\tau$ and $\mu\mu$ decay modes yielded a signal strength relative to the Standard Model expectation of $1.18^{+0.10}_{-0.10}(\text{stat.})^{+0.11}_{-0.10}(\text{syst.})^{+0.08}_{-0.07}(\text{theo.})$. All channels used for the combination were found to be compatible with the Standard Model Higgs boson with a mass, $m_H = 125.36$ GeV [47].

Given the Higgs boson decaying to a pair of b-quarks has the highest branching fraction and as yet there has been no discovery of the Higgs boson decaying to fermions; it is important to build on the work performed at LEP and the Tevatron in order to make the discovery. The most recent result for the search for the Higgs boson decaying to a pair of b-quarks, produced in association with a vector boson [48] has been performed using a multivariate technique. The analysis was split into three main channels based upon the lepton content of the vector boson decay; $Z \to \nu\nu$, $W \to \ell\nu$, and $Z \to \ell\ell$ for the 0-, 1-, and 2-lepton channels respectively. When these channels are combined, a 1.4σ excess is observed above the background only hypothesis. The ratio of measured signal yield to the Standard Model expectation is found to be $\mu = 0.52 \pm 0.32(\text{stat.}) \pm 0.24(\text{syst.})$ for a Higgs boson mass, $m_H = 125.36$ GeV. A cut-based cross-check of the 1-lepton analysis forms the basis of this thesis. A similar analysis was performed with the CMS experiment using a multivariate technique. The ratio of measured signal strength to that of the Standard Model was found to be $\mu = 1.0 \pm 0.5$.An excess of events was observed above the expected background with a local significance of 2.1σ [49].

Part II

Experimental Arrangement

Chapter 3

The LHC & The ATLAS Detector

3.1. The Large Hadron Collider (LHC)

The Large Hadron Collider (LHC), with a circumference of 26.7 km, is the largest particle accelerator at the European Organisation for Nuclear Research (CERN). The LHC and the main CERN site straddle the French-Swiss border on the outskirts of Geneva, close to the village of Meyrin. This section will first give an overview of the LHC itself in Section 3.1.1 before in Section 3.1.2 describing the details of the 2011 and 2012 data taking periods, which make up Run I of the LHC.

Extensive details of the workings of the LHC can be found in [50].

3.1.1. LHC Overview

The aim of the LHC is to gain a greater understanding of our Universe. For the majority of the data taking periods, beams of protons are collided at four points around the LHC: Compact Muon Solenoid (CMS); a general purpose detector placed at point 5, LHCb; whose focus is on B-physics, A Large Ion Colliding Experiment (ALICE); concentrates during the heavy-ion collisons at the LHC, studying the quark-gluon plasma. Finally, A Toroidal LHC Apparatus (ATLAS); a second general purpose detector placed at point 1, directly opposite CMS is in operation during both the proton-proton periods and the ion-ion periods. The LHC is the most energetic particle collider in the world with centre-of-mass energies in Run I of 7 TeV in 2011 and 8 TeV in 2012.

Before any of the collisons can take place there are a series of stages of acceleration which utilise elements of previous colliders in the complex [51]. The protons are initially

injected into the LINAC 2 and accelerated up to 50 MeV. The protons next flow into the Proton Synchrotron Booster (PSB) and are accelerated further up to $\sim$1.4 GeV. From here, the protons are passed into the Proton-Synchrotron (PS) to be accelerated to $\sim$25 GeV, then to the Super Proton Synchrotron (SPS) before entering the LHC ring at 450 GeV. Figure 3.1 shows a schematic diagram of the acceleration and collision of protons and heavy ions at CERN.

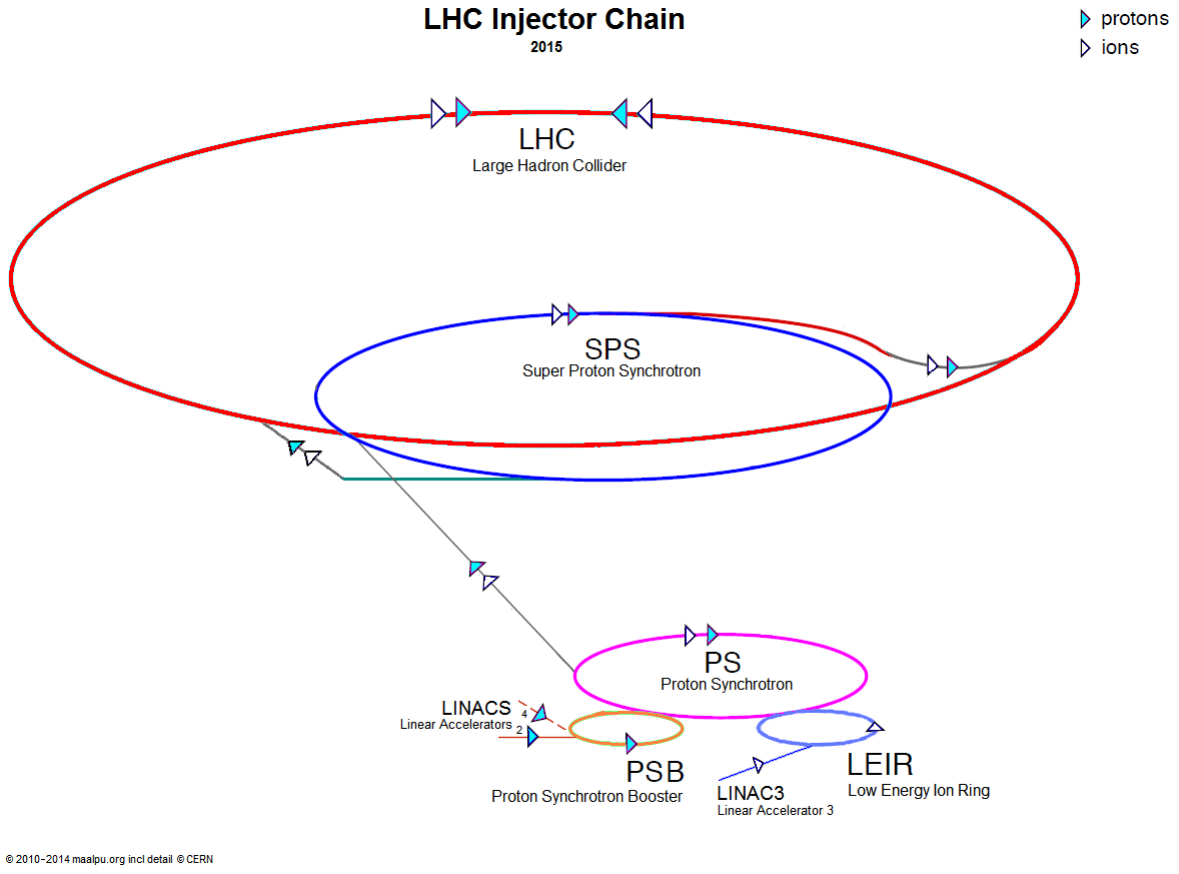

Figure 3.1: Schematic diagram of the accelerators which are located at CERN, which are used in the acceleration of protons and ions up to the desired energy for the physics runs. Taken from [52].

Once inside the LHC ring, the protons are accelerated to the desired energy using Radio Frequency (RF) cavities. The RF cavities are also used once the beams have reached the desired energy for the physics run, to keep the beams in bunches before they are collided. As a measure to keep the cost and space usage to a minimum, the two beam-pipes are housed in a single superconducting magnet. For bending the beams as well as keeping the orbit true, superconducting dipole magnets are used. For the focussing of the beams,

superconducting quadrupole magnets are used. For maintaining the superconducting properties of the magnets, such as the 8.33 T dipole strength, they must be cooled to 1.9 K. This is done using liquid helium.

For the analysis of physics processes, it is important to know information about the rate at which collisions will occur and the cross-section of the process. The rate at which collisions occur depends upon the instantaneous luminosity, $\mathcal{L}$ and the collision cross-section, σ. The rate is defined in Equation 3.1:

$$\frac{\mathrm{d}N}{\mathrm{d}t} = \mathcal{L} \cdot \sigma. \tag{3.1}$$

The total cross-section for proton-proton collisions is measured at the LHC by TOTEM, which is based in the same pit as CMS. For the 2012 run at 8 TeV, TOTEM measured the total cross-section for the LHC at 101.7 ± 2.9 mb[1] [53]. Using the LHC design luminosity of 1×10^{34} cm^{-2}s^{-1}, the rate at which collisions occur is approximately 100 MHz when averaged over time.

Many of the physics processes being measured at the LHC are rare and have small cross-sections. The rate at which these physics processes occur depends upon the cross-section for that process. The instantaneous luminosity is defined in Equation 3.2:

$$\mathcal{L} = \frac{N_b^2 n_b f_{\mathrm{rev}} F \gamma_r}{4\pi \epsilon_n \beta^*}, \tag{3.2}$$

where N_b is the number of particles in a bunch, n_b is the number of bunches per beam, f_{rev} is the revolution frequency, F is the geometric function to account for the crossing angle between the beams as they are not generally collided head on, γ_r is the relativistic Lorentz factor $(1 - \frac{v^2}{c^2})^{-\frac{1}{2}}$ and ϵ_n is a measure of how uniform the momentum of the particles in the beam is or, how small the beam can be squeezed. Finally, β^* is how small the beam is at the interaction point (IP).

Using Equation 3.2, it is possible to deduce ways of maximising the instantaneous luminosity including, increasing the number of particles per bunch, decreasing the bunch spacing and decreasing the size of the bunch at the IP by decresing ϵ_n and β^*.

The integrated luminosity (Equation 3.3) is a measure of how many collisions occur:

$$L = \int \mathcal{L} \cdot dt. \tag{3.3}$$

[1] 1 b $= 10^{-28}$ m^2

To calculate the number of events expected for a specific process with cross section σ_{p} in a data sample the cross section is multiplied by the integrated luminosity:

$$N_{\mathrm{events}} = L \cdot \sigma_{\mathrm{p}}. \tag{3.4}$$

3.1.2. LHC 2011 & 2012 Operation

The LHC began operation on the 10$^{\mathrm{th}}$ November 2009. The initial centre-of-mass energy for collisions was 900 GeV, by the end of 2009 the centre-of-mass energy had risen to 2.36 TeV making it the world's most energetic particle accelerator. In 2010 and 2011, the centre-of-mass energy was increased further to 7 TeV. The total integrated luminosity delivered to the ATLAS experiment in 2010 was 48.1 pb^{-1}. In 2011 this value increased to 5.43 fb^{-1}. For the 2012 data taking period, the centre-of-mass energy was increased to $\sqrt{s} = 8$ TeV, the number of particles per bunch was increased, and ϵ_n and β^* were decreased increasing the instantaneous luminosity. This led to an increase in the integrated luminosity delivered to ATLAS which was 22.8 fb^{-1}.

One of the largest complications in Run I has been pile-up[2]. There are two types of pile-up, in-time and out-of-time. In-time pile up refers to multiple interactions in the bunch crossing and out-of-time pile-up refers to the bunch spacing being shorter than the response time of the detector. The number of pile-up events per bunch crossing is given by equation 3.5:

$$N_{\mathrm{pu}} = \sigma_{\mathrm{MB}} \mathcal{L} \frac{\Delta_{\mathrm{tbc}}}{1 - f_{\mathrm{empty}}}, \tag{3.5}$$

where σ_{MB} and $\mathcal{L}$ are the cross section and instantaneous luminosity respectively, Δ_{tbc} is the time interval between two bunch crossings and f_{empty} is the fraction of empty bunches. In 2010, pileup was dominated by the in-time variety whereas as the energy increased and the decrease in the bunch spacing in 2011 and 2012 an increase in the out-of-time pile-up was observed. To correct for the out-of-time pile-up, an event-by-event correction [54] is applied using particles from the event of interest only. In the data taking periods between 2010 and 2012, an in-depth analysis of the detector performance was carried out. Figure 3.2 shows the instantaneous luminosity measured by ATLAS between 2010 and 2012 as well as the number events per bunch crossing, Figure 3.3 shows the progression of the integrated luminosity with time for 2011 and 2012. Table 3.1 shows a comparison

[2]Pile-up is defined as where a bunch crossing results in more than one collision

between operation parameters of the LHC in 2011 and 2012 with the nominal values of the LHC.

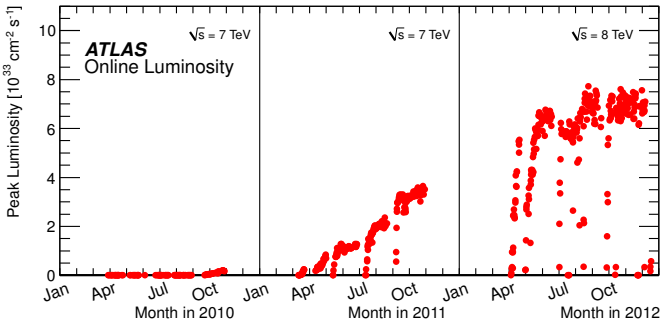

(a) Instantaneous luminosity per day 2010–2012

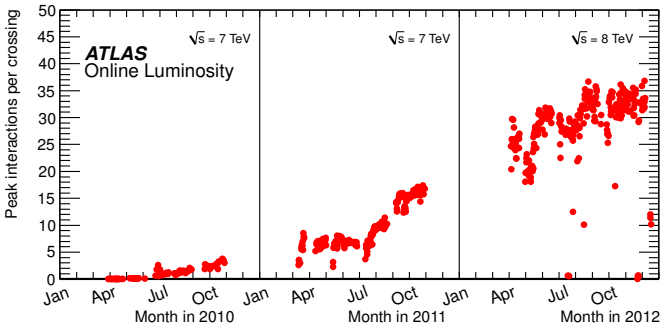

(b) Number of events per bunch crossing per day 2010–2012

Figure 3.2: The instantaneous luminosity and also the number of events per bunch crossing delivered to ATLAS during the Run I data taking period. Figure from [55].

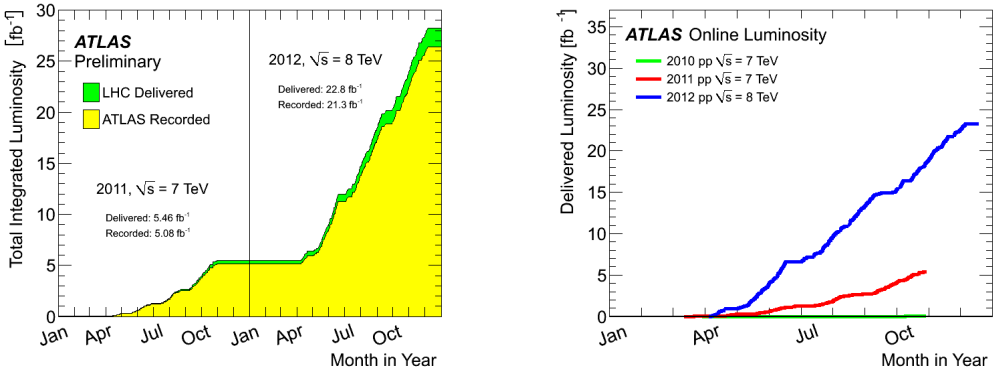

(a) Integrated luminosity per year 2011 and 2012 **(b)** Integrated luminosity over the course of a year, 2010, 2011 and 2012

Figure 3.3: The total delivered integrated luminosity per year (a) and for each year in Run I (b). Figures from [55].

Parameter	Nominal	2011 Data Run	2012 Data Run
Beam Energy	7 TeV	3.5 TeV	4 TeV
N_b	1.15×10^{11}	1.5×10^{11}	1.6×10^{11}
n_b	2808	1380	1380
Bunch Spacing (ns)	25	50	50
β^*	0.55	1.0	0.6
ϵ_n	3.75	1.9–2.3	1.7–3.0
Peak $\mathcal{L}$ ($\mathrm{cm}^{-2}\mathrm{s}^{-1}$)	1.0×10^{34}	3.6×10^{33}	7.7×10^{33}

Table 3.1: Table of the nominal [50] LHC run parameters compared with 2011 and 2012 [56].

3.2. A Toroidal LHC ApparatuS (ATLAS)

A Toroidal LHC AppuratuS (ATLAS) [57], is one of two (the other being CMS) general purpose particle-physics detectors based at the LHC. The ATLAS detector is located 100m below the surface, lying on top of the bedrock below Point 1 on the LHC ring. It is designed to study the physics which comes from the interactions of both proton-proton and ion-ion collisions. During a physics run, the environment in the detector becomes inhospitible from the rate of the collisions and the high radiation. The high energies allow the first study of physics at the TeV scale as well as precision measurements of the Standard Model. The design of ATLAS takes these into consideration along with possibilities of wider range of measurements including but not exclusively: precision measurements of flavour physics, QCD interactions, electroweak interactions, searching for and measuring the properties of the Higgs boson and also the potential to search for physics beyond the Standard Model as well as supersymmetry.

The conditions under which ATLAS operates combined with the vast array of measurements which are possible means that the detector was designed with the following criteria:

- Radiation-hard electronics and sensor elements combined with high detector granularity for high particle fluxes and overlapping events
- Full azimuthal coverage for missing transverse energy measurements and large pseudorapidity acceptance
- Vertex detectors are required close to the interaction region for the observation of secondary vertices for the reconstruction of τ-leptons and b-jets.

- Good charged-particle momentum resolution and reconstruction in the inner detector
- Exceptional electromagnetic (EM) calorimeter performance is required since the basis of many physics studies is formed by accurate electron and photon reconstruction. Good jet and missing transverse energy reconstruction in the full coverage hadronic calorimeter are also required.
- Good muon identification and momentum resolution over a wide momenta range and to determine the charge of high p_{T} muons
- Low transverse momenta objects need highly efficient triggering with good background rejection.

The main design performance goals are summarised in Table 3.2.

Detector Component	Resolution	η - Coverage	
		Measurement	Trigger
Tracking	$\sigma_{p_{\mathrm{T}}}/p_{\mathrm{T}} = 0.05\%\ p_T \oplus 1\%$	± 2.5	
EM Calorimetry	$\sigma_E\ /\ E = 10\%/\sqrt{E} \oplus 0.7\%$	± 3.2	± 2.5
Hadronic Calorimetry			
Barrel & End-Cap	$\sigma_E\ /\ E = 50\%/\sqrt{E} \oplus 3\%$	± 3.2	± 3.2
Forward	$\sigma_E\ /\ E = 100\%/\sqrt{E} \oplus 10\%$	$3.1 < \lvert\eta\rvert < 4.9$	$3.1 < \lvert\eta\rvert < 4.9$
Muon Spectrometer	$\sigma_{p_{\mathrm{T}}}/p_{\mathrm{T}} = 10\%$ at $p_{\mathrm{T}} = 1$ TeV	± 2.7	± 2.4

Table 3.2: Summary of the ATLAS detector performance goals. Units for E and p_{T} are in GeV. Taken from [57]

The components of the ATLAS detector are shown in Figure 3.4. ATLAS is the largest detector on the LHC ring at 44 m long and a 22 m diameter. There are four main detector subsystems: the inner detector which measures tracks, the EM calorimeter and the hadronic calorimeter which fully enclose the inner detector and finally the muon spectrometer. There are two magnetic subsystems: surrounding the inner detector is a 2 T solenoid used for momentum measurement and an air-core toroid magnetic system is incorperated into the muon spectrometer. The air-core toroid allows for maximum bending power whilst keeping material to a minimum, thus minimising scatter effects. There is also a three-tier trigger system, the first of which is hardware-based and the latter

two are software-based. The subsystems are described in more detail in the following subsections.

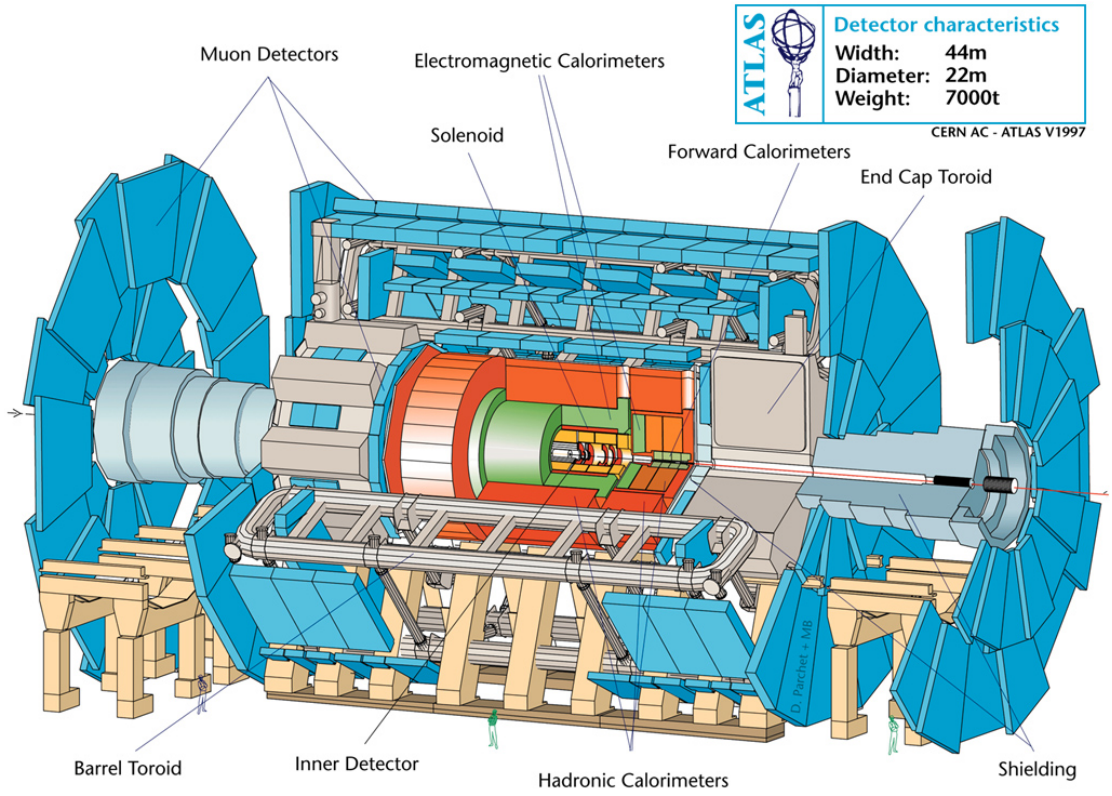

Figure 3.4: Diagram of the ATLAS detector showing the sub-detector systems. Taken from [58].

3.2.1. Co-ordinate Definitions

ATLAS uses a right handed co-ordinate system centred around the nominal interaction point. The x-axis points toward the centre of the LHC ring, the y-axis is positive upwards and the z-axis points along the beam pipe. Due to the cylindrical nature of the detector, polar co-ordinates (R, θ, ϕ) are defined: θ, the polar angle is measured upwards from the beam pipe, ϕ, the azimuthal angle is defined in the $x - y$ plane around the z-axis. To define the angular position of a massive object in the detector such as a jet relative to the beam axis, the *rapidity* is used. The rapidity is defined as:

$$y = \frac{1}{2} \ln \left[\frac{E + p_z}{E - p_z} \right], \tag{3.6}$$

where E is the energy and p_z is the momentum along the beam axis of the object. For particles which approach the speed of light in the region of $E >> M$, the pseudorapidity η, defined:

$$\eta = \ln \tan \left(\frac{\theta}{2} \right) \tag{3.7}$$

is an approximation to the rapidity, y. The distance between two objects in the $\eta - \phi$ plane can be defined as:

$$\Delta R = \sqrt{\Delta\eta^2 + \Delta\phi^2}, \tag{3.8}$$

where $\Delta\eta$ and $\Delta\phi$ are the respective differences in pseudorapidity and the azimuthal angle for the two objects. The transverse quantities of transverse energy, E_{T}, transverse momentum, p_{T} and transverse energy imbalance or 'missing transverse energy', $E_{\mathrm{T}}^{\mathrm{miss}}$ are defined in the $x - y$ plane.

3.2.2. Inner Detector

The inner detector (ID) was designed to provide both hermetic and robust pattern recognition, excellent momentum resolution, and both primary and secondary vertex measurements for charged tracks for particles with $p_{\mathrm{T}} > 0.5$ GeV within the pseudorapidity range of $|\eta| < 2.5$. There are three main components to the inner detector: the silicon pixel detector, a silicon microstrip detector (Semiconductor Tracker, SCT) and finally at larger radii, a transition radiation tracker (TRT). Surrounding all these elements is a 2 T superconducting solenoid magnet.

A diagram showing the components of the inner detector is shown in Figure 3.5. The sub-modules consist of two types of detectors, those which are concentric cylindrical layers form the 'barrel' whereas the disks which cover each end are referred to as 'end-caps'.

Pixel Detector

The pixel detector is the component closest to the beam pipe. In the pixel detector there are three layers in the barrel region and a total of six layers in the end cap region (three on each end). The layers are numbered 0 to 2 with the closest layer also called the b-layer due to its importance in identifying the secondary vertex of long lived particles associated with B-physics. The b-layer lies a distance of 50.5 mm away from the beam

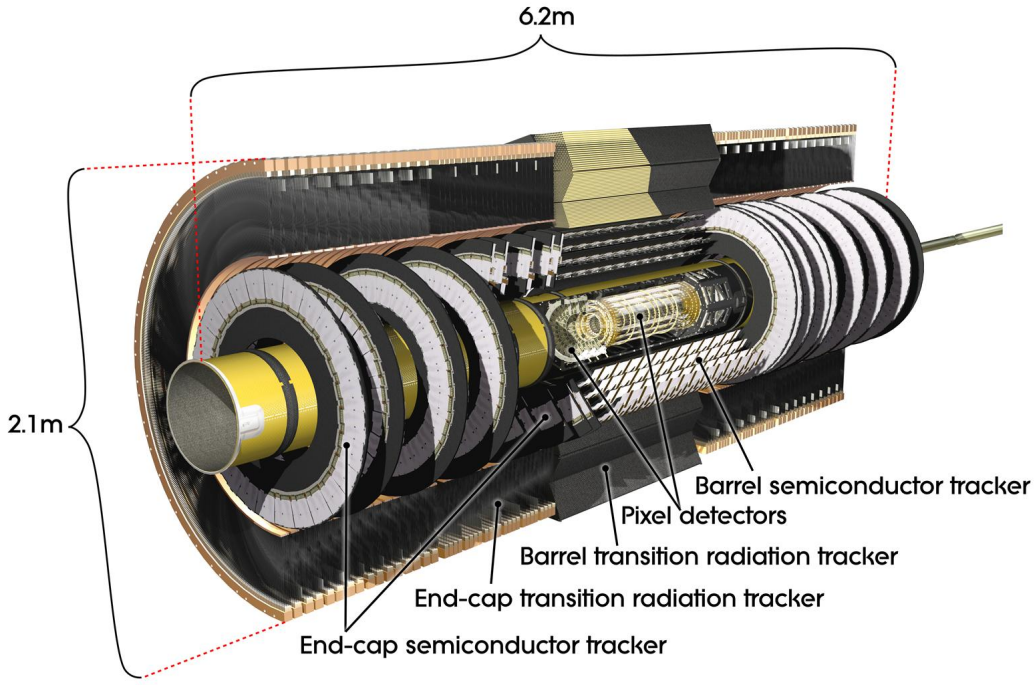

Figure 3.5: Diagram of the inner detector showing the sub-modules.

pipe. Due to the high radiation the pixel detector is receiving during physics runs, it will need to be replaced after three years of operation at nominal luminosity.

The layers of the pixel detector are formed of silicon modules consisting of 46,080 pixels. Each pixel sensor is identical and has dimensions 50×400 μm^2. In total there are approximately 80.4×10^6 readout channels. The spatial resolution of the pixel detector is 10 μm in the $R - \phi$ plane and 115 μm in the z direction in the barrel region and 10 μm in the $R - \phi$ plane, and 115 μm in the R plane in the end-cap region.

Semiconductor Tracker (SCT)

The SCT is a silicon microstrip detector. It consists of four layers in the barrel region and nine end-cap layers on each end. The barrel layers are placed at a distance of 29.9 mm from the beam pipe, surrounding the pixel detector. In total there are 4088 modules, the barrel contains 2112 and each end cap has 988.

SCT modules are made from two layers of single sided p-in-n silicon chips charged initially at 150 V. This voltage will rise to between 250 and 350 V as the detector ages with radiation exposure. Each SCT module contains 768 strips of 6.4 cm in length with a pitch of 80 μm. In the end-cap region, the average pitch is $\sim$80 μm. The strips in one

layer run parallel to the beam pipe along the barrel and along the R axis in the end-cap. The other layer is placed at a stereo angle of 40 mrad to form a two sided module. In total there are 6.3×10^6 readout channels.

The signal from the SCT is read out in a binary form, there is a large charge collection threshold of 1 fC to maximise the signal efficiency whilst also minimising noise. To form a space-point, there needs to be a hit on either side of the module. The stereo angle gives the ability to determine the position along the strip where the hit occured. This gives resolution in the z and R directions in the barrel and end-cap respectively. The spatial resolution of the SCT is 17 μm in $R-\phi$ and 580 μm in $z(R)$ in the barrel (end caps).

Transition Radiation Tracker (TRT)

The transition radiation tracker (TRT) is a straw drift tube tracker which uses transition radiation in particle identification. The modules in the tracker consist of 4 mm diameter straw tubes which have been filled with a gas mixture (70% Xe, 27% CO_2 and 3% O_2). A tungsten wire runs the length of each tube to collect the charge. In the barrel region of the detector, the straws run parallel to the beam pipe, they lie 73 straws deep and each straw is 144 cm long. In the end-cap region the straws are 37 cm long and run radially out from the beam pipe. In total there are 351,000 readout channels. The resolution of the TRT is 130 μm in the $R-\phi$ region only, with no resolution in the z direction. Despite the low resolution because of the large number of measurements made (up to 36 hits per track) the TRT contributes significantly to the momentum resolution.

The straws themselves are interwoven with polypropelene fibres in the barrel and polypropelene foils in the end-cap. When a charged particle crosses the boundary between a straw and fibre, a photon is emitted which is absorbed by the gas mixture, producing a signal much larger than minimum-ionising particles. The TRT can perform particle identification by using the dependence on particle type in the energy of the transition radiation. For an 20 GeV electron, the transition radiation is approximately 200 keV whereas for a 20 GeV pion, the transition radiation is 1 keV. By counting the number of hits above a higher energy threshold, this difference in energy can be exploited.

3.2.3. Calorimetry

The ATLAS calorimeters lie outside the inner detector and the magnetic field of the inner detector. There are two distinct calorimeters in ATLAS, the electromagnetic

calorimeter and the hadronic calorimeter. Upon entering the calorimeters, the particle produces a 'shower' of secondary particles. The particle shower in the electromagnetic calorimeter contains electrons, photons and positrons. They are normally fully contained inside the electromagnetic calorimeter allowing them to be fully reconstructed. The hadronic calorimeter showers contain more particle types including neutrons. Neutrinos and muons are not detected and will spill out of the calorimeter. The energy from the hadronic showers is not fully reconstructed meaning a calibration of the energy response is required. Having good containment inside the calorimeters is not only important for energy reconstruction but also for good missing transverse energy ($E_{\mathrm{T}}^{\mathrm{miss}}$) measurement and to prevent punch-through into the muon spectrometers.

The calorimeters cover the range $|\eta| < 4.9$. Over this large range, different materials are used. Figure 3.6 shows the different components in place in the different pseudorapidity regions. Surrounding the inner detector, the calorimeter has a high granularity to allow for precision measurements of electrons and photons. Other parts of the calorimeter have larger granularity since they are designed to reconstruct jets and measure the $E_{\mathrm{T}}^{\mathrm{miss}}$.

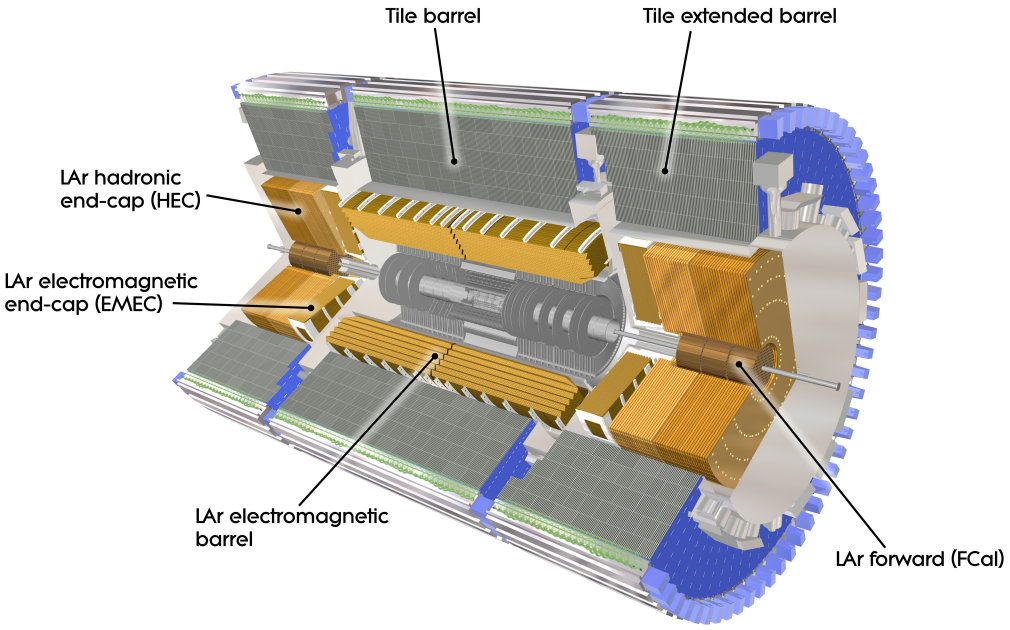

Figure 3.6: Figure showing different materials used at different regions of pseudorapidity in the ATLAS Calorimeters, taken from [59].

The total thickness of the detector is another important factor in preventing punch-through to the muon system. The total thickness of the electromagnetic calorimeter

is greater than 22 X_0 (radiation lengths) in the barrel and greater than 24 X_0 in the end-cap regions. The total thickness of the hadronic calorimeters is approximately 11 nuclear interaction lengths (λ). This is sufficient to accurately measure the energy of the jets and to reduce the punch-through into the muon spectrometer.

Electromagnetic Calorimeter

The electromagnetic (EM) calorimeter uses liquid argon (LAr) as the active detector medium. LAr was chosen due to its linear behaviour, stability of the response in time and its radiation hardness. The absorber is made from lead. The charged particles inside the EM shower ionise the LAr and the electrons drift to the copper electrodes in the prescense of an electric field.

The EM calorimeter is divided into two half barrels which extend up to $|\eta| < 1.475$ and between them is a 4 mm gap at $z = 0$. On either end there are two coaxial wheels which make up the end-cap region, they are named the EMEC. The first wheel covers the area $1.375 < |\eta| < 2.5$ and the second $2.5 < |\eta| < 3.2$. Due to additional material being required to cool the components of the detector, there is a 'crack' region between $1.375 < |\eta| < 1.52$; in this region the energy resolution is significantly degraded.

The barrel region of the calorimeter has an accordian-like structure of lead absorbers and copper electrodes, and liquid argon fills the 2.11 mm gap between the absorbers. This shape allows for several active layers in depth. The geometry allows for full coverage in ϕ and also avoids cracks. Figure 3.7 shows the varying of the folding angles of the accordian structure with radial distance, which keeps the gap between the LAr and the accordian wave constant. Another feature highlighted in Figure 3.7 is the different granularity in the layers making up the calorimeter. The first layer has the highest granularity: each cell in the layer has $\Delta\eta \times \Delta\phi = 0.0031 \times 0.098$. This fine granularity allows the shower shape to be measured which is an important input to the particle identification. The second layer collects the most energy from the EM shower; the dimensions of the cells in this layer are $\Delta\eta \times \Delta\phi = 0.025 \times 0.0245$. The third layer collects the tail end of the energy and has the lowest segmentaion with cell dimensions of $\Delta\eta \times \Delta\phi = 0.05 \times 0.0245$.

The inner wheel of the EMEC is also segmented into three layers with the same granularity as the barrel, and in the outer wheel the granularity is larger and varies as a function of pseudorapidity. A LAr presampler exists for the region $|\eta| < 1.8$ and it is used to correct for energy lost by decays of particles traversing the material before the calorimeters. It also aids in the discrimination between $\pi^0 \to \gamma\gamma$ decays and incident photons.

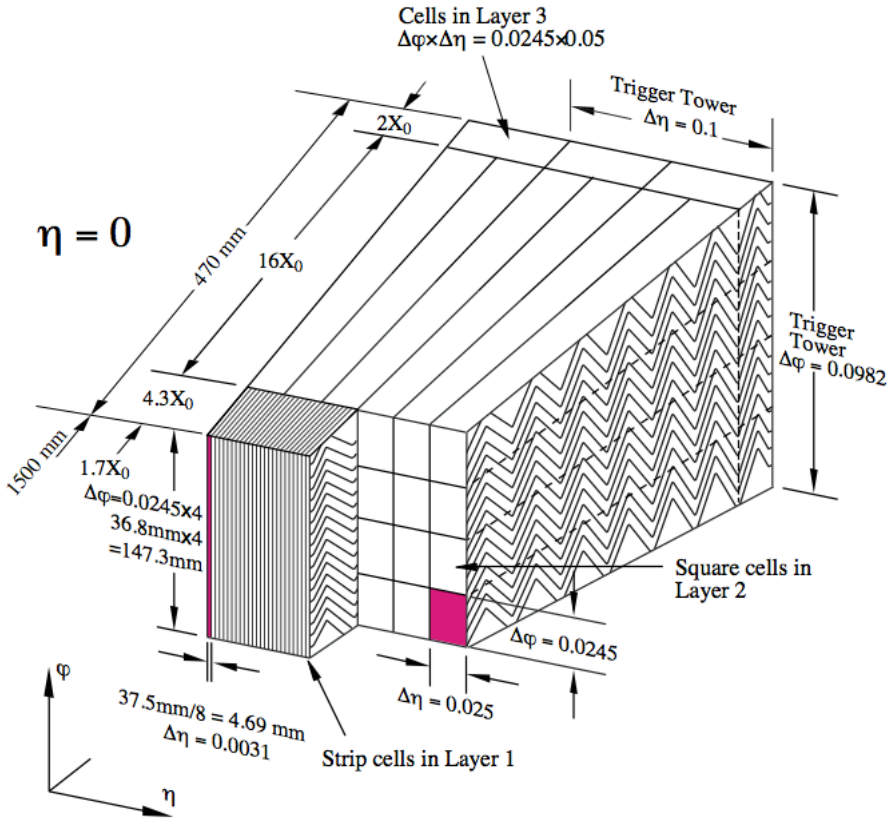

Figure 3.7: Barrel Module of the electromagnetic calorimeter showing the granularity in η and ϕ of the accordian geometry. Taken from [57]

Hadronic Calorimeter

There are three main parts which make up the ATLAS hadronic calorimeter: the tile calorimeter, the hadronic calorimeter end-cap (HEC), and the forward calorimeter (FCAL). The tile calorimeter is constructed using a steel absorber and plastic scintillator for the active medium. The HEC and the FCAL use liquid argon.

The tile calorimeter is made up of a barrel and two extended calorimeters. The central barrel is 5.8m long and covers a pseudorapidity range of $|\eta| < 1.0$, and the extended barrel covers a pseudorapidity of $0.8 < |\eta| < 1.7$. Both the barrel and the extended barrels are segmented azimuthally into 64 modules over 3 layers. The size of these layers is 1.5 (1.5), 4.1 (2.6) and 1.8 (3.3) interaction lengths (λ) for the barrel (extended barrel) regions. The signal from the tile calorimeter is read out using wavelength shifter fibres attached to each end of the scintillator which feed into photomultipliers. The fibres are grouped into cells with $\Delta\phi \times \Delta\eta = 0.1 \times 0.1$ granularity in the first two layers and a granularity of $\Delta\phi \times \Delta\eta = 0.1 \times 0.2$ in the final layer.

The HEC consists of two wheels (HEC1 and HEC2) in each end cap which are located directly behind the EMEC. They share the same cryostat as the EMEC also. The HEC covers $1.5 < |\eta| < 3.2$ overlapping with the tile calorimeter on one side and the FCAL on the other, to avoid cracks in the transition regions. In each wheel there are 32 wedges and the wheel is split into two layers in depth. The wedges in HEC1 (HEC2) are constructed from 24 (16) copper plates which are 25 mm (50 mm) thick, with a 12.5 mm (25 mm) front plate. The gap between each of the copper plates is 8.5 mm and is where the liquid argon is contained. Inside the liquid argon gaps are split further by three electrodes into four drift spaces 1.8 mm thick to avoid the build up of ions from the higher fluxes and energies in the forward region of the detector.

The final calorimeter is the forward calorimeter, The FCAL is 10 λ deep and split into three layers and covers $3.1 < |\eta| < 4.9$ overlapping with the HEC. The first FCAL1 is made from copper and is designed for electromagnetic measurements, the second and third layers FCAL2 and FCAL 3 and constructed from tungsten as the passive material. FCAL2 and FCAL3 mostly perform hadronic measurements, tungsten was chosen for its high density which will contain the showers inside the calorimeter and prevent the spread to the muon spectrometer. Further minimisation of energy losses from the FCAL through cracks between the calorimeters are done by placing the FCAL close to the other end-cap systems which provides a hermetic design.

3.2.4. Muon Spectrometers

The final layer of the ATLAS detector is the muon spectrometer, which sits outside the calorimeters. The muon spectrometer has two main purposes: to precisely measure the momentum of the muons which pass through it, and to trigger on events which contain muons. A diagram showing the main components of the muon spectrometer can be found in Figure 3.8.

To measure the momentum of the muons, the muon spectrometer lies inside a large superconducting air core toroid magnet system which provides a magnetic field orthogonal to the direction of the muon momentum measurements which will bend the muons in the $R - z$ plane. In total there are three air core toroids which generate the magnetic field, a barrel and two end caps. The strength in the toroid magnets is approximately 0.5 T and 1 T in the barrel and end-caps respectively. The bending power of the magnets is characterised by the magnetic field integral and measures differently for different regions of pseudorapidity. In the barrel region, the toroid provides 1.5–5.5 Tm

of bending power in the range $0 < |\eta| < 1.4$; in the end-cap the bending power is measured to be in the range 1–1.75 Tm in the range $1.6 < |\eta| < 2.7$. In the overlap region ($1.4 < |\eta| < 1.6$) between the barrel and end-cap, the bending power is much lower.

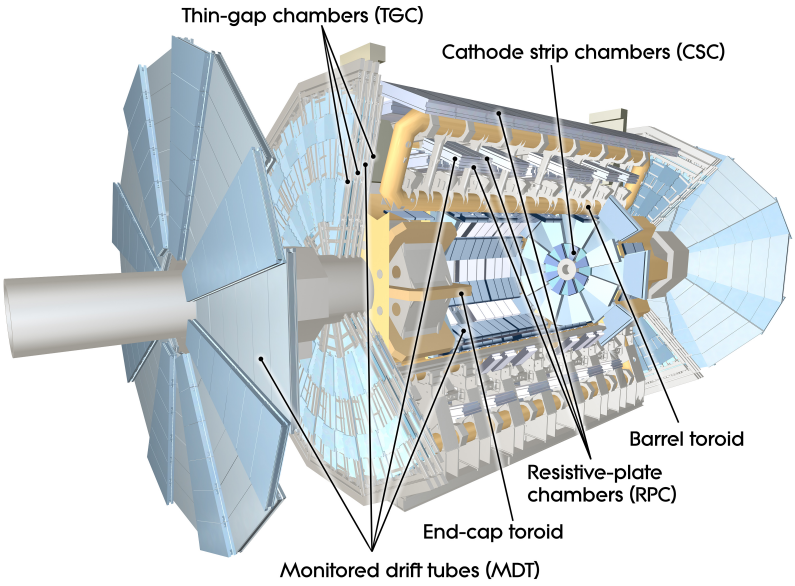

Figure 3.8: Schematic diagram showing the various components of the muon spectrometer in the ATLAS detector. Taken from [60].

There are four types of muon chamber in the muon spectrometer: two which measure the muon momentum, and two which provide the triggering. The precision muon momentum measurements are provided by the Monitored Drift Tubes (MDTs) and the Cathode Strip Chambers (CSCs). The MDTs cover the pseudorapidity for $|\eta| < 2.7$, they are filled with an argon, carbon dioxide mixture with a tungsten-rhenium cathode to read out the electrons from the collisions. For the inner layers ($2.0 < |\eta| < 2.7$) CSCs work alongside the MDTs due to the higher rates and backgrounds in this region. The CSCs are multiwire proportional chambers which give a higher granularity compared to the MDTs allowing them to better cope with the higher fluxes. The triggering is performed by the Resistive Plate Chambers (RPCs) in the region $|\eta| < 1.05$ and the Thin Gap Chambers (TGCs) cover $1.05 < |\eta| < 2.4$. The TGCs also provide measurements for $|\eta| < 2.7$ in the $x - y(\phi)$ plane.

3.2.5. ATLAS Trigger System

Due to the high event rate, ATLAS uses a three level trigger to reduce the initial collision rate of approximately 100 MHz to a rate of between 20 and 1000 Hz which will used for offline reconstruction, storage and analysis.

The first level is the L1 trigger which uses custom electronics inside the muon spectrometer and the calorimeters to identify hard scattering processes such as high p_{T} muons, electrons, photons, jets and τ-leptons which decay hadronically. The L1 trigger also selects events with a large missing transverse energy or a large total transverse energy. The maximum latency of the L1 trigger is only 2.5 μs, in which time it must reduce the event rate down to 60 kHz. To do this in the short time period, only low granularity signals from the muon chambers and the calorimeters are used. Regions of Interest (RoIs) are defined by the L1 trigger in η and ϕ which surround the area of the detector which caused the trigger to fire; these are then passed to the higher trigger levels for further study.

The last two trigger layers, the L2 and the event filter (EF) use software algorithms. Collectively they are known as the High Level Trigger (HLT). The L2 and the EF use more detector information to refine the decision made by the previous level. This is done alongside tightening the selection requirements to further reduce the rate. The L2 takes 100 ms and reduces the rate to 3.5 kHz. The EF which has full access to the event readout in the RoIs uses offline object reconstruction algorithms to reduce the rate to approximately 200 Hz and takes up to 1 s for a decision.

3.2.6. ATLAS Detector Simulation

The simulation of the ATLAS detector is an important step in the generation of simulated Monte Carlo events. The simulation of the detector is done using GEANT4 software [61] as part of the simulation framework [62]. The input to GEANT4 is the output from the Monte Carlo event generation as described in Section 1.3 in the standard HepMC format, with all prompt decays being taken care of by the generator. The simulator then propagates these particles through the ATLAS detector. GEANT4 simulates the interaction of the particles with the detector material.

Within the detector simulation, GEANT4 can specify a wide range of particle interactions, including electromagnetic, hadronic and optical at various energy ranges. The output from GEANT4 simulation is digitised such that it is the same format which is read

out from the detector allowing the same software which performs data reconstruction to be used.

3.2.7. Luminosity Measurement

A precise measurement of the luminosity collected by ATLAS is important for the measurement of cross-sections in standard model analyses as it forms a dominant systematic uncertainty. The luminosity measurement plays a direct role in determining the sensitivities of new physics. The luminosity of the LHC can be expressed as:

$$\mathcal{L} = \frac{\mu_{\text{inel}} n_b f_r}{\sigma_{\text{inel}}}, \tag{3.9}$$

where μ_{inel} is the average number of inelastic collisions per bunch crossing, n_b is the number of branches colliding, f_r is the machine revolution frequency and σ_{inel} is the pp inelastic cross-section. The total luminosity measured by ATLAS can be monitored by measuring the observed interaction rate per cross-section, μ_{vis}. This quantity can be used to rewrite Equation 3.9 as:

$$\mathcal{L} = \frac{\mu_{\text{vis}} n_b f_r}{\sigma_{\text{vis}}}. \tag{3.10}$$

The observed cross-section (σ_{vis}) is calculated by $\sigma_{\text{vis}} = \epsilon\sigma_{\text{inel}}$, where ϵ is the efficiency of a particular detector or algorithm used to measure μ_{vis}. To calculate the visible cross-section, the luminosity scale for a particular detector or algorithm must be calibrated.

ATLAS has two detectors which are used for the measurement of μ_{vis}: LUCID [63] and BCM [64]. LUCID is Cherenkov detector designed for measuring luminosity. It comprises 16 polished aluminium tubes filled with C_4F_{10} gas. The tubes surround the beam pipe each side of the interaction point at a distance of 17 m. They cover a pseudorapidity range of $5.6 < |\eta| < 6.0$. An incoming flux of particles enters the tubes at an angle, creating Cherenkov photons which reflect off the walls of the tubes into photomultiplier tubes (PMTs) at the rear of the tubes. When the PMT records a 'hit' above a certain threshold, it co-ordinates with the LHC clock to record the event rate separately for each bunch crossing.

BCM (Beam Conditions Monitor) is made up of four diamond sensors which are chosen for their radiation hardness and fast readout, on each side of the interaction point around the beam pipe in a cross pattern. The BCM is also used to monitor

background levels and it can issue a beam-abort request if beam losses look like they will damage the ATLAS detector components. Having a fast readout, the BCM can provide a bunch-by-bunch signal which is used to measure μ_{vis}. Since LUCID and BCM have different efficiencies, their measure values of μ_{vis} will differ, so they require separate calibrations.

The calibration of σ_{vis} is done using *van der Meer* (vdM) scans to determine the absolute luminosity from the machine properties. During theses scans the size and shape of the interaction region is measured by reconstructing the relative interaction rates as a function of transverse beam separation [65]. The delivered luminosity can be written as:

$$\mathcal{L} = \frac{n_b f_r n_1 n_2}{2\pi \Sigma_x \Sigma_y}, \tag{3.11}$$

where n_1 and n_2 are the number of protons per bunch in the two beams and Σ_x and Σ_y are the horizontal and vertical widths of the colliding beams. In a vdM scan, the beams are separated by a known distance which allows the measurement of the Σ_x and Σ_y. Combining these with an external measurement of the bunch charge product $(n_1 \cdot n_2)$ which is done using two DC current transformers which have a high accuracy but they are unable to resolve individual bunch charges, and two fast beam current transformers (FBCT) which have a lower accuracy but can resolve the bunches [66], a direct luminosity measurement for when the beams are unseparated is made. Comparing this peak luminosity to the peak interaction rate which is measured by LUCID or BCM, and using Equations 3.10 and 3.11 σ_{obs} can be measured. This allows the absolute normalisation of the luminosity to be enabled.

This measured value for the luminosity is cross-checked using independent measurements made using the ATLAS calorimeters. The current collected in the PMT from the tile calorimeter and the total ionisation current in the liquid argon in the FCAL are related to the mean number of interacting particles in the calorimeter, and so are sensitive to the luminosity.

Chapter 4

Object Reconstruction

In this chapter, the algorithms which reconstruct physics objects from the detector after the online trigger selection are described. First, the tracks in the inner detector and muon spectrometer are reconstructed. These are then combined with energy deposits in the calorimeters to assemble the basic objects used in offline analysis such as: electrons, muons, jets, photons and τ-leptons. The missing transverse energy is also measured.

The different particles will interact differently with each of the sub-detectors inside the ATLAS detector. Figure 4.1 shows that neutral particles such as the photon and the neutron do not deposit any tracks in the inner detector and deposit all their energy in the EM calorimeter and hadronic calorimeter respectively. The charged particles such as the electrons and charged hadrons will leave curved tracks in the inner detector. The electron will deposit all energy in the EM calorimeter whereas the charged hadron will leave small amounts of energy in the EM calorimeter with the majority of the energy being deposited in the hadronic calorimeter. Muons will leave curved tracks in the inner detector, deposit small amounts of energy in the EM and hadronic calorimeters and leave a track in the Muon Spectrometer. The neutrinos will not leave any tracks or deposit any energy in any part of the detector systems.

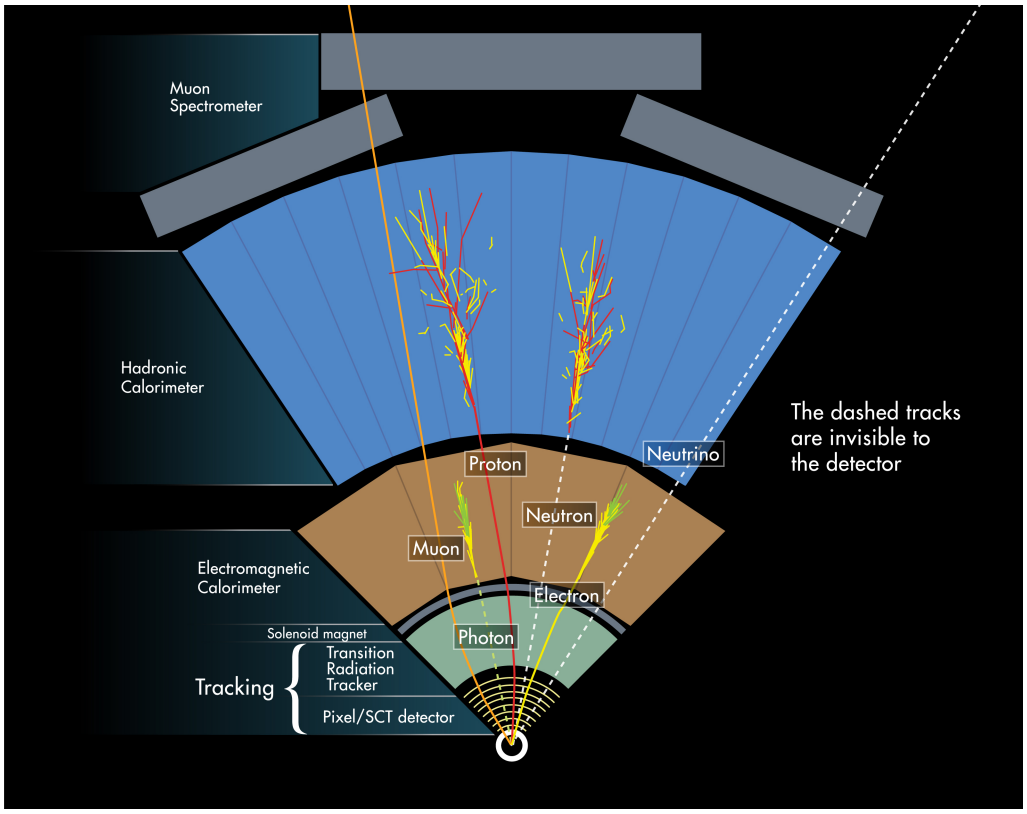

Figure 4.1: Schematic diagram showing how different types of particle interact with the ATLAS detector. Taken from [67]

4.1. Data Acquisiton

The measurements made in Part III utilise the full dataset collected by ATLAS during the 2012 physics run of proton-proton collisions. During the 2012 physics run, the dataset is split into *periods* which are further broken down into *runs*. A run usually corresponds to one fill of the LHC, and a period is made up of runs in which the environments of the trigger, detector and accelerators have similar conditions. A run is further broken down into *luminosity blocks* which correspond to approximately two minutes of run time. During a run, there may be problems with some of the components in the detector which will inhibit the reconstruction of the objects during offline analysis. One such example happened during the 2011 data taking period where there was a problem with the EM calorimeters front end board caused by high voltage. To get around this problem, the luminosity blocks which are affected are listed in a Good Run List. After using the Good Run List to remove the luminosity blocks the integrated luminosity for the 2012 data taking period is 20 fb^{-1} with an uncertainty of 2.8%.

4.2. Charged Particle Track Reconstruction

As charged particles travel through the Inner Detector (ID) they travel along curved trajectories due to the influence of the magnetic field which surrounds the ID (see Section 3.2.2 for more details on the ID). As they traverse along their path, the particles interact with the silicon which is registered as hits in the detector components. These are used by the tracking algorithms to reconstruct the particle track, which can be used to identify which particle was responsible for leaving them. Inside the ID, there are hundreds of hits due to the high levels of pile-up and the high collision energies. To properly reconstruct the tracks, the tracking algorithm must be able to associate each hit in the detector with a track as well as reconstructing the track parameters. As well as pile-up causing a high density of hits, the particles will also be interacting with 'dead material[1]' in the detector which will cause multiple scatterings, ionisation energy loss, and for electrons, bremsstrahlung which causes further energy loss. For the track reconstruction, ATLAS uses The New ATLAS Track Reconstruction (NEWT) [68] which includes two principal tracking algorithms, described in Sections 4.2.1 and 4.2.2.

4.2.1. Inside-Out Tracking

The primary tracking strategy in the ID is inside-out tracking which begins closest to the beam pipe and moves out to the other ID components. Inside-out tracking uses a series of modules (algorithms) to reconstruct the tracks using both a global pattern recognition and local pattern recognition from the output of the global pattern search.

The first step is to build a three-dimensional *space-point*. The space-point can be created directly from the hits in the silicon detector. For hits in the SCT, the algorithm makes use of the nature of the module; each module is made from two silicon layers placed back-to-back separated by a stereo angle which is used to determine the three-dimensional space-point. Because hits are required on both sides of the module, the SCT has built-in noise suppression.

Track seeds are then formed from these reconstructed space-points by applying a search for more space-points in the direction of the track which has been determined from the three layers of the pixel detector and the initial layer of the SCT.

With the track seeds built, the track building can begin. A Kalman fitter-smoother tool [69] follows the track trajectory, adding successive hits to the fit. The Kalman fitter

[1]Dead material indludes material not used in reconstruction, such as cables and detector monitoring equipment

can predict the track measurement in the next layer as it continuously updates the track information and covariances in the current layer. Energy loss via bremsstrahlung is not well modelled by the Kalman fitter due to its non-Gaussian nature, however, multiple scattering and ionisation energy loss are well modelled. Only 10% of the track seeds will go on to form track candidates.

The next module is used for solving ambiguities. Many of the tracks will share hits and will be from fake tracks which are from reconstructed hits which do not originate from a single source. The classification of tracks is done using a track scoring strategy. This will penalise those tracks which are fake and will reward the tracks with many hits with the overall aim to provide the track with a score. A quality cut is applied and those tracks with a score high enough to pass the cut move onto the next and final stage; those which fail the cut are discarded. For tracks which share a hit, the score is assigned to the track with the higher score and the total track score being re-evaluated for both tracks.

The final stage extends the silicon tracks into the TRT. These tracks are refitted once again, using all the information in all three sub-detectors. The tracks which after the TRT refitting have a higher track score than before TRT refitting are kept, and the rest are neglected.

4.2.2. Outside-In Tracking

In certain instances the inside-out strategy for track reconstruction will fail to find a track seed due to decays from secondary vertices inside the inner detector or photon conversions may leave insufficient hits to pass the track scoring in the inside-out method. Electrons may impart their energy before reaching the TRT leaving no tracks and failing the track scoring in the inside-out method.

The outside-in method has a two step procedure for track reconstruction. Starting from the TRT segments which are not associated with tracks reconstructed using the inside-out method and moving in through the SCT and the pixel detector. A hit pattern is found using a Hough transform [70] in the TRT segments by resolving missing hit information along the drift tube. This pattern is then fed into the same Kalman fitter technique used in the inside-out strategy, making use of the drift time information. The Kalman fitter allows the track to be extended into the SCT and pixel detectors onto tracks which are not already associated to hits.

4.3. Primary Vertex

4.3.1. Primary Vertex Reconstruction

In order to locate where a particle in a collision originated, and to be able to reconstruct the parameters of the object including the longitudinal and transverse impact parameters which are used for distinguishing leptons from conversions or secondary decays inside jets, the primary interaction vertex (PV) of the collision must be located with a high efficiency. Once the track reconstruction algorithms described in Section 4.2 have completed, the vertexing algorithms start on their task. On ATLAS the vertex reconstruction is split into two groups: finding and fitting. The vertex candidates are found by following the reconstructed tracks to a point where they intersect, the fitting reconstructs the vertex positions and the covariance matrix and estimate the quality of the vertex by fitting the locations of the incident tracks. Challenges facing the vertex reconstruction algorithms include distinguishing the primary and secondary vertices as well as the consideration of the optimal separation of tracks positioned between different vertices.

To reconstruct the primary vertex (PV), ATLAS uses two similar methods, *finding-after-fitting* and *finding-through-fitting*. Finding-after-fitting starts by placing a pre-selection on the tracks in the bunch crossing region; the tracks are then ordered according to their z-impact parameter and track clusters are searched for using a sliding window approach [71], where each track cluster is an independent PV candidate. Using a vertex fitter, the PV candidates are cleaned of outliers and a χ^2 is calculated between the vertex candidate and the track is calculated. The vertex is refitted in a process which is repeated until no incomplete tracks remain.

Finding-through-fitting is a similar procedure but it deals with outliers in a cleaner manner. Like the fitting-after-finding procedure, a pre-selection on the tracks is used to form vertex seeds. Using an *Adaptive Multi Vertex Fitter* [72], the vertex is reconstructed using a Kalman fitter to minimise the sum of the squared distances of all the tracks from the vertex position. After the initial fit, the outliers are used to create a new seed and each seed has a weight assigned to have less of a pull on the vertex position. This fitting process is repeated until the χ^2 probability of the outlier fits is greater than 1.

4.3.2. Primary Vertex Modelling

The modelling of the track and vertex reconstruction is important as mis-modelling can lead to larger uncertainties on physics measurements. Figures 4.2 and 4.3 show the reconstruction of tracks and vertices on ATLAS from hits in the inner detector.

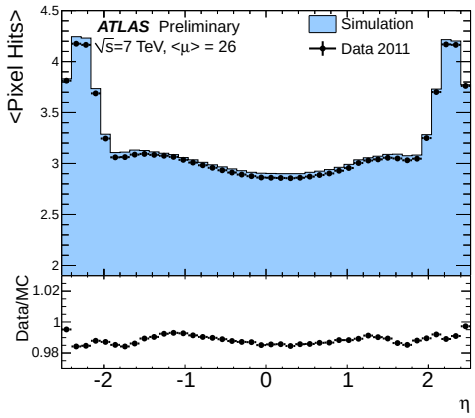

(a) Pixel Hits

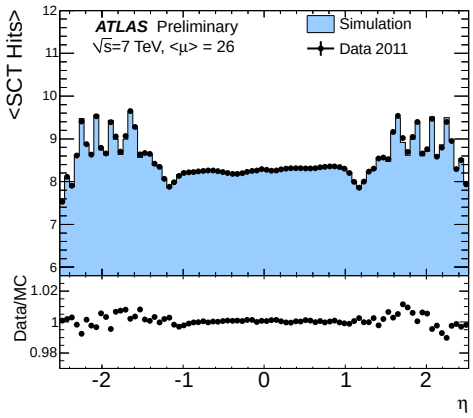

(b) SCT Hits

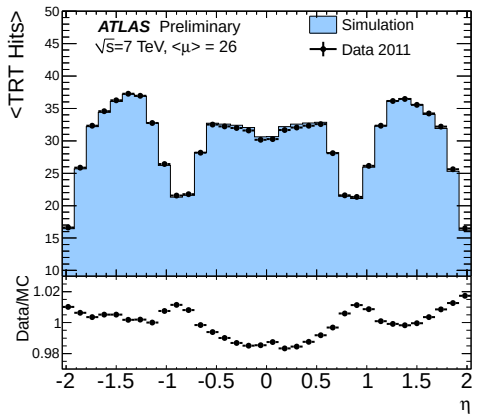

(c) TRT Hits

Figure 4.2: The number of pixel, SCT and TRT hits as a function of η from the 2011 initial (A1) dataset and corresponding simulation sample. Taken from [73].

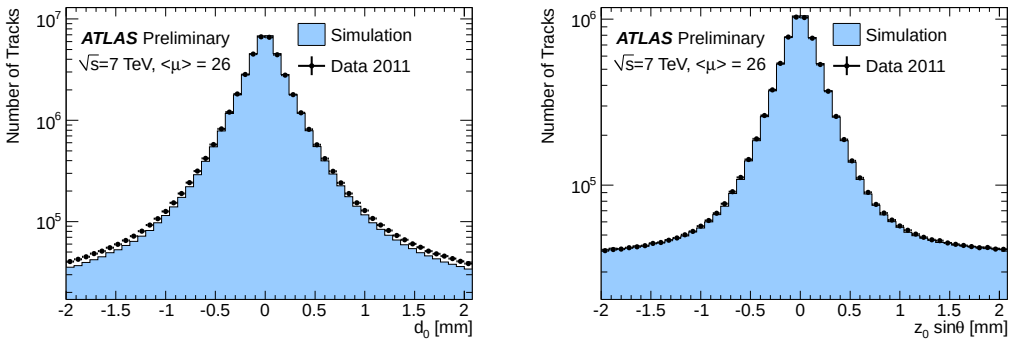

(a) Transverse Impact Parameter **(b)** Longitudinal Impact Parameter

Figure 4.3: The impact parameter distributions with respect to the primary vertex tracks from the 2011 A1 dataset and the corresponding simulation sample. Taken from [73].

Figure 4.2 shows mis-modelling between the data and the simulation of the order of 2% when comparing pixel, SCT and TRT hits. When looking at the impact parameter distributions in Figure 4.3 the data and simulation agreement is to within 5%; most of this mis-modelling is in the tails of the distributions and arises due to uncertainties on the contributions from secondary vertices, cluster merging or limitations of modelling the detector material. The high pile-up environment inside ATLAS increases the number of fake tracks and vertices due to the probability of more interactions between objects in the detector. The PV reconstruction efficiency has been shown to affected by the high pile-up in [73].

4.4. Electrons

4.4.1. Electron Trigger

In Section 3.2.5, the ATLAS three level trigger system is described. Events containing electrons are initially triggered on at L1 using reduced granularity trigger towers ($\Delta\eta \times \Delta\phi = 0.1 \times 0.1$) to identify the positions of Regions of Interest (RoI) as well as to compute the $E_{\mathrm{T}}^{\mathrm{miss}}$ of electromagnetic (EM)-clusters with a 1 GeV precision. A sliding window algorithm is used to identify local maxima for the formation of EM-clusters based on a 4×4 block of trigger towers. The trigger is fired if the central 2×2 core region contains one pair of neighbouring towers with a combined energy above a certain threshold. At L2, the RoIs identified at L1 are further analysed, and electron algorithms

are used to build cell clusters within $\Delta\eta \times \Delta\phi = 0.4 \times 0.4$ in the second layer of the EM-calorimeter to identify the largest energy deposit closest to the L1 position. This pre-seed is then centered on a 3×7 ($\Delta\eta \times \Delta\phi = 0.075 \times 0.175$) grid in the barrel ($|\eta| < 1.4$) and a 5×5 ($\Delta\eta \times \Delta\phi = 0.125 \times 0.125$) grid in the end-cap ($1.4 < |\eta| < 2.47$) region in order to accumulate energy. In the EF, offline algorithms for identification and reconstruction which are described in Section 4.4.3 and 4.4.2 respectively. Slightly looser cuts are applied in order to remain fully efficient offline [74].

The bandwidth allocated to the electron triggers is 30% of the total EF output. To meet the demands of the increasing instantaneous luminosity during the 2011 and 2012 data taking periods, the trigger thresholds were tightened to keep the bandwidth at an acceptable level. At the start of 2011, the energy threshold in place on the EF trigger was 20 GeV, and this rose to 22 GeV once the instantaneous luminosity increased above 2×10^{33} cm^{2}s^{-1}. Once the luminosity increased to 3×10^{33} cm^{2}s^{-1}, the identification requirements at L2 and EF were tightened, varying L1 thresholds with η were introduced to account for varying material before the calorimeter, and the L1 thresholds were brought to be closer to the EF threshold. To reduce the L1 rate, a hadronic leakage cut was applied. During 2012, the EF threshold was increased further to 24 GeV.

4.4.2. Electron Reconstruction

In the central region of the detector ($|\eta| < 2.5$), electrons are reconstructed by matching the reconstructed tracks in the inner detector to clusters of energy deposited in the EM-calorimeter [75, 76]. This is the standard procedure for reconstructing electrons and is described in more detail below. The forward regions ($2.5 < |\eta| < 4.9$) has no inner detector tracking available, therefore electrons are reconstructed from the calorimeter clusters alone; this procedure is also described below.

Central Region Electron Reconstruction

Electron reconstruction in the central region begins with the creation of a preliminary set of seed clusters which are formed from calorimeter cells measuring 0.025×0.025 in the ϕ, η plane, located in the second layer of the EM-calorimeter. The cells are formed using a sliding window algorithm where a window of 3×5 towers moves over the cells locating energy deposits greater then 2.5 GeV. The reconstructed tracks are then extrapolated from their last measurement point to the middle layer in the EM-calorimeter. The tracks

are required to match within $\Delta\eta < 0.05$ of the cluster position. Due to the bending caused by the solenoid magnet, the tracks have different constraints in ϕ. If the cluster falls on the side of the track in the direction the track bends, the cluster must be within $\Delta\phi < 0.1$. If the cluster falls on the opposite side, then the requirement is $\Delta\phi < 0.05$. This asymmetry in ϕ requirement is to account for the large amount of energy lost by the electron from bremsstrahlung due to the large amount of material in the inner detector which increases the bending, especially at high η. To be reconstructed, the seed cluster must have at least one matching track. The seed clusters with no tracks are considered as photon candidates. If the candidate has several tracks matching, silicon hits are preferred as they are less likely to come from a photon conversion. In the case of TRT-only tracks, only matching in ϕ is required due to the limited η resolution in the TRT.

Using a sliding window measuring $\Delta\eta \times \Delta\phi = 0.075 \times 0.175$ (0.125×0.125) in the barrel (end-cap) which corresponds to 3×7 (5×5) towers, local maxima are searched for. To construct the energy of the cluster four components are considered, the energy deposited in the material before the EM-calorimeter, the energy measured in the cluster, the estimated energy deposited outside the detected area (lateral leakage) and finally, energy deposited beyond the EM-calorimeter (longitudinal leakage). These four terms together determine the measured energy of the cluster in the presampler (where available) and in all the layers of the calorimeter using detailed simulation in both the active and dead regions of the detector. $Z \to e^+e^-$ and $J/\psi \to e^+e^-$ measurements give further calibrations to the electron candidate energy. The η and ϕ of the electron candidate are determined from silicon hits if they exist, otherwise cluster η-pointing is used. The energy of the electron candidate is taken from the cluster energy.

Forward Region Electron Reconstruction

Although not used in the analysis described in Part III, the forward electron reconstruction is included for completeness. Since the inner detector does not cover the region $|\eta| > 2.5$, electrons cannot be reconstructed with the same technique as central electrons. Unlike central electrons, forward electrons are reconstructed solely from soley energy deposits in the EM-calorimeter. *Topological Clusters* [71] are used for the reconstruction. The topological clusters are formed by grouping neighbouring cells which contain energy above a certain threshold together into clusters. For this reason, the topological clusters have varying sizes. Cells with a signal to noise ratio above a high threshold t_{seed} are used as cluster seeds. Neighbouring cells with a low threshold t_{cell} of signal to noise are added to the cluster. If the neighbouring cells pass an intermediate signal to noise threshold

they are labelled as secondary seeds $t_{\text{secondary}}$. For electrons, the threshold for t_{seed} is set equal to $t_{\text{neighbour}}$. The lower threshold at the perimeter ensures the tails of the showers are not discarded. The high threshold for seeds suppresses noise from electronics and pile up.

An electron candidate is created if the cluster has passed a transverse energy selection of E_{T} GeV. The direction of the candidate is defined by the barycentre of the cells belonging to the cluster in the EM-calorimeter. The energy component is calculated from the energy of the cells in the cluster which are corrected for energy loss before the calorimeter and lateral and longitudinal leakages.

Electron Reconstruction Efficiency

Electron reconstruction efficiencies on ATLAS are performed using the tag and probe techique described in [76] using $Z \rightarrow e^+e^-$ which offer a clean environment for study, $W \rightarrow e\nu$ to further increase statistics, and $J/\psi \rightarrow e^+e^-$ decays which extend the measurements into low E_{T} regions. Figure 4.4 shows the efficiecy in 2011 drops by 4% between the central and forward η regions. In the 2012 run, the overall efficiencies have increased by 2% and the efficiencies are comparable between central and forward regions. Good agreement between data and simulation is observed in the distributions of η and E_{T}. At low E_{T}, the efficiency improves by 6% between 2011 and 2012. The effciencies obtained in simulation are corrected to data using a function derived from the scale-factors [77].

The charge misidentification of electrons is also identified using a tag and probe method. The misidentification occurs primarily from interactions which take place in the inner detector. The rate of misidentification is found to be $\sim$0.5% (8%) in the barrel (edge of the tracker). Rates observed in simulation are well modelled to those observed in data [76]

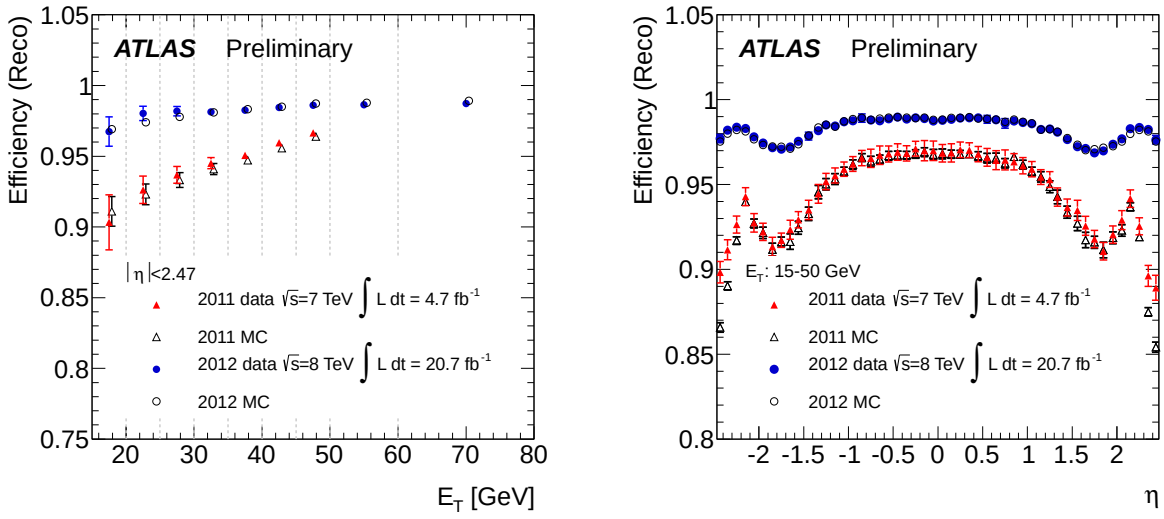

(a) E_{T} **(b)** η

Figure 4.4: Electron reconstruction efficiencies for 2011 and 2012 as a function of cluster η and cluster E_{T}. The comparison between data (solid) and Monte Carlo simulation (open). Taken from [78].

4.4.3. Electron Identification

Electron identification using reconstructed electrons described in Section 4.4.2 can be done using either a cut-based approach which applies sequential cuts on selected variables to identify electrons or a multivariate likelihood approach which allows for a more powerful approach to signal and background separation.

Cut-Based Electron Identification

Selections are made based upon electromagnetic shower shape, the quality of the tracks, track-calorimeter matching and particle identification information from the TRT amongst others. Figure 4.5 shows a comparison of shower shapes between isolated electrons and major backgrounds for the ratio of transverse energy in the first hadronic calorimeter layer compared to the transverse energy in the EM-calorimeter (R_{had1}) and the ratio of energy in the EM-calorimeter compared to the track momentum $\left(\frac{E}{p}\right)$ There are three electron types denoted `Loose++`, `Medium++` and `Tight++`, each of which has a tighter background selection at a cost of lower signal efficiency. A fourth electron type was added during for the 2012 data taking period denoted `multilepton`, this was optimised for the low energy electrons in $H \to ZZ^* \to 4l$. `Multilepton` has a similar efficiency to

`Loose++` selection but an improved background rejection. The decay $H \to ZZ^* \to 4l$ is not described in this thesis so the `Multilepton` selection will not be described further. The `Loose++` and `Medium++` electrons have the cut based variables used as an input into a multivariate analysis program (TMVA [79]) for cut optimisation. The optimisation is done in 10 bins of cluster η and 11 bins of cluster E_{T} from 5 GeV to $>$ 80 GeV. The details of the selections made for each of the electron types is described below [78].

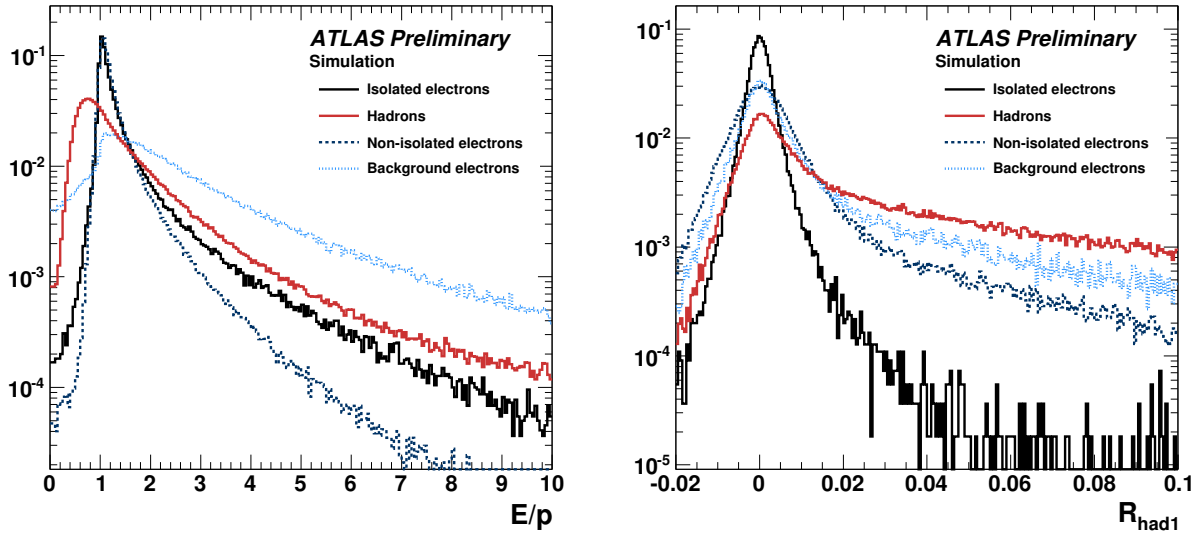

(a) $\frac{E}{p}$ **(b)** R_{had1}

Figure 4.5: Comparing shower shapes of variables used for electron identification selection in isolated electrons and major backgrounds in electron reconstruction. Taken from [75].

- **`Loose++`:** For the selection of `Loose++` electrons, the shower shape variables are cut on to distinguish between electromagnetic showers which originate from electrons or photons and hadronic showers from particles in jets. A hadronic calorimeter leakage cut is applied to compensate for the crack between the barrel and extended barrel in the hadronic calorimeter. Other shower shape cuts are placed on the width of the shower at different layers inside the EM-calorimeter and the energy ratio difference between the largest energy deposit in the first layer of the EM-calorimeter to the total energy. Selections are made on the number of silicon hits; at least seven hits are required with at least one being in the pixel detector. This cut is performed to reject electron decays from pions and ensures good track quality. Finally the

separation of tracks to the cluster is required to be $|\eta| < 0.015$ to ensure the track and cluster are from the same physical particle.

- **`Medium++`:** To be considered a `Medium++` electron, the selections made for `Loose++` electrons are applied and further cuts are made in addition. The shower shape cuts are tightened to reject more backgrounds such as neutral pions. A cut on the impact parameter[2] of $|d_0| < 5$mm is applied. Electrons are required to have a hit in the b-layer in the inner detector to reject photon conversions. Charged hadrons are rejected by applying TRT selections. The track-cluster matching criteria is tightened to $|\eta| < 0.005$. Further cuts are applied on the fraction of shower energy deposited in the third layer of the EM-calorimeter to compensate for loosening the requirements in the first layer.

- **`Tight++`:** The selection for `Medium++` electrons must be passed with additional selections to be considered a `Tight++` electron. The shower shape variable selection is tightened to be equal or tighter than for `Medium++` electrons. An additional ϕ-cut is added for the cluster-track matching requirement, $\Delta\phi < 0.02$, further cuts are applied to the ratio of cluster energy to track momentum. The impact parameter selection made for `Medium++` electrons is tightened to $|d_0| < 1$mm. `Tight++` candidates which are matched to reconstructed photon conversions are rejected.

Likelihood Electron Identification

Multivariate techniques are powerful since they allow for the combined evaluation of several properties when making selection decisions. The likelihood (LH) method was chosen for electron identification to make use of the signal and background probability density functions (PDFs) of the discriminating variables. An overall probability is calculated for the electron object to be signal or background from the PDFs. The probabilities are combined into a discriminant $d_{\mathcal{L}}$, on which a cut is applied:

$$d_{\mathcal{L}} = \frac{\mathcal{L}_S}{\mathcal{L}_S + \mathcal{L}_B}, \mathcal{L}_S(\vec{x}) = \prod_{i=0}^{n} P_{s,i}(x_i), \tag{4.1}$$

where $\vec{x}$ is the vector of variable values, and $P_{s,i}(x_i)$ is the value of the signal PDF of the i^{th} variable evaluated at x_i. In the same way, $P_{b,i}(x_i)$ refers to the background PDF.

[2]Impact parameter is defined as the distance between the track and the primary vertex

Variables measuring the effects of bremsstrahlung are included in conjunction with those with significant discriminating power. Simple cuts are applied on the quality of the tracks to make sure a high quality 4-vector measurement is obtained.

There are three operating points of the electron LH selections, LOOSE, MEDIUM and VERY TIGHT. These are equivalent to the `MultiLepton`, `Medium++` and `Tight++` selections in the cut-based in terms of efficiencies but have better background rejection. The LOOSE LH uses variables which are most useful in discriminating against light flavour jets and a b-layer cut is applied to reject photon conversions. For MEDIUM and VERY TIGHT regimes, additional d_0 variables and conversion bitwise operators are used to reject heavy flavour jets and conversions. To a good approximation, the VERY TIGHT sample is a subset of the LOOSE LH objects. The LH for each operating point is constructed from 9×6 sets of PDFs divided into nine $|\eta|$ bins and six E_{T}bins which are chosen to balance the data statistics with $|\eta|$ and E_{T} shape variations [78].

Electron Identification Efficiencies

The identification efficiency for electrons is measured using a tag and probe method similar to that used in measuring the electron reconstruction efficiency. Figure 4.6 shows the identification efficiency as a function of the number of primary vertices for the 2011 and 2012 datasets. In 2012, the efficiency improved by $\sim 5\%$ with respect to 2011. The overall trend is as the number of vertices increases, the efficiency decreases. An event with 18 reconstructed vertices has a 3% lower efficiency compared to an event with only one reconstructed primary vertex in 2012. The agreement between data and simulated Monte Carlo events is shown in Figure 4.7 as a function of E_{T}. The `Loose++` electrons have good agreement between data and Monte Carlo simulation. The reason for this poor modelleling in the `Medium++` and `Tight++` is due to the mis-modelling of the shower-shape variables used in the cut-based selection. Scale factors are derived from a function of η and E_{T} and are applied to the Monte Carlo simulated events to match the data.

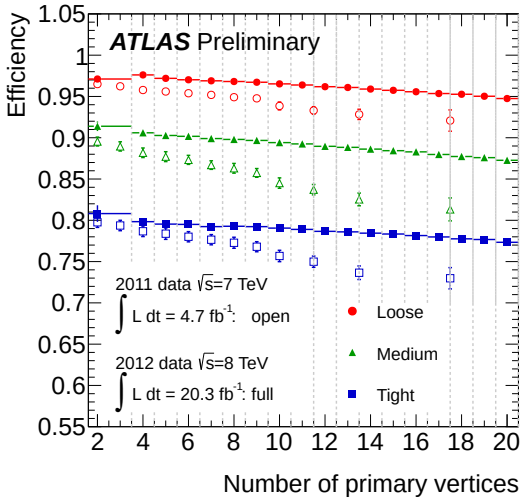

Figure 4.6: Electron identification efficiencies as a function of number of primary vertices for the 2011 (open) and 2012 (closed) datasets. Taken from [78].

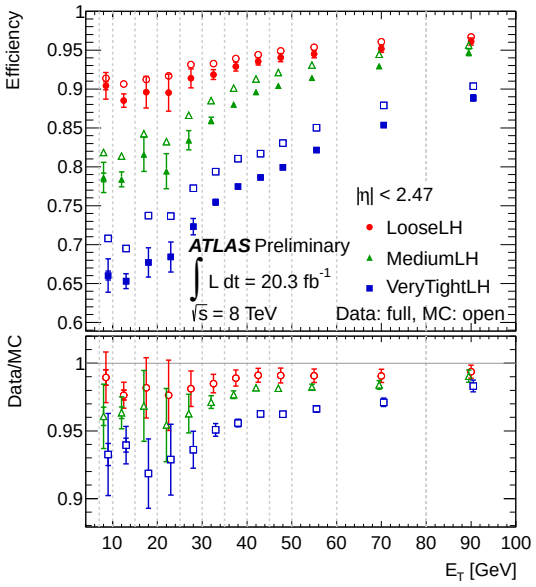

Figure 4.7: The efficiency of each of the electron identification levels as a function of E_T. Highlighting the comparison between data (full) and Monte Carlo simulations (open). The `Loose++` selection has the best agreement between data and Monte Carlo. Taken from [78].

4.5. Muons

4.5.1. Muon Trigger

As described in Section 3.2.5, ATLAS operates a three level trigger system. In the Muon Spectrometer, the L1 trigger utilises the RPC modules in the barrel ($|\eta| < 1.05$) and TGC modules in the end-cap ($|\eta| < 2.4$). More information on the Muon Spectrometer can be found in Section 3.2.4. The RPC and TGC modules provide rough measurements of η, p_{T} and ϕ of the muon candidate as well as identifying to a high accuracy the bunch crossings containing a muon candidate. Figure 4.8 shows the arrangement of the trigger chambers in the Muon Spectrometer on ATLAS; there are three layers in the barrel and three layers in each end-cap. The trigger has a coverage of $\sim$80% in the barrel and $\sim$99% in the end-caps. The reduction in the barrel is due to the incomplete coverage of all three layers of the Muon Spectrometer and the crack between the two halves of the Muon Spectrometer at $\eta = 0$. The L1 trigger identifies 'Regions of Interest' (RoIs) using the three layers of the RPC in the barrel ($|\eta| < 1.05$) region and three layers of TGC in the end-cap ($1.05 < |\eta| < 2.4$) to give the position information to be used by the HLT. The coincidences in η and ϕ are generated seperately. To form the trigger result, the coincidences require hits in the muon *roads* which represent an envelope containing trajectories from the interaction point above a chosen p_{T} threshold. In 2011, the p_{T} threshold in L1 for a primary single muon was 15 GeV. This rose to 20 GeV in 2012.

For the muon HLT, similar algorithms are used as for the online muon reconstruction which is described in Section 4.5.2. At L2, the trigger RoI defined in L1 is refined using precision hit data collected in the MDT and CSC modules. To build a result, the L2 trigger uses three sequential algorithms. The first uses information only from L1 trigger hits in the Muon Spectrometer to build a trajectory for the candidate muon. It opens up a narrow road around the L1 trigger chamber hits to construct Muon Spectrometer tracks by measuring the MDT drift times and positions. A rough p_{T} measurement is obtained using a lookup table. The next algorithm combines the tracks built in the Muon Spectrometer with tracks in the Inner Detector to form refined muon candidate. The p_{T} of the muon candidate is calculated using a combined fit which uses the tracks in the Muon Spectrometer and accounts for the energy deposited in the EM- and hadronic calorimeter [80].

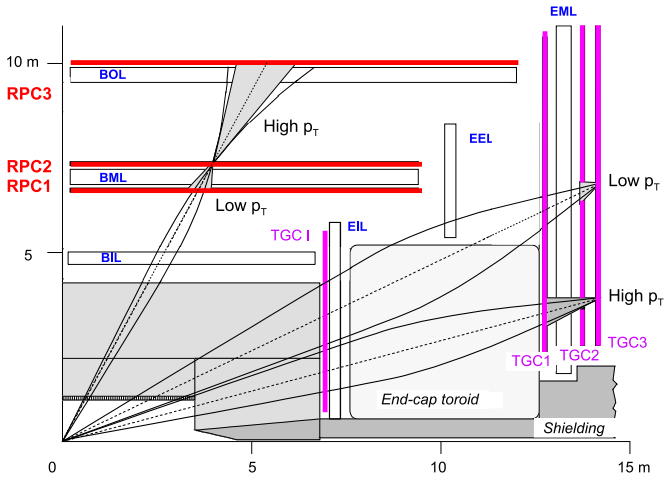

Figure 4.8: Cross section view of the L1 muon trigger chambers. Figure from [80].

The EF trigger uses the full offline algorithms on the RoIs identified in the L1 and L2 triggers. There are two main strategies for muon candidate reconstruction; *inside-out* and *outside-in*. In outside-in, the tracks in the Muon Spectrometer are extrapolated back to the interaction point to form a muon candidate. The inside-out strategy starts from tracks reconstructed in the inner detector and extrapolates those out to the Muon Spectrometer. During the 2011 data taking period, ATLAS ran both strategies in parallel for online muon reconstruction. This was to reduce the risk of losing events. During 2012, to reduce the processing time only the outside-in was used initially. Only events which failed were then passed through inside-out [81]. In 2011 the single muon trigger threshold was 18 GeV, this rose to 24 GeV in 2012 due to the increased luminosity resulting in an increased trigger rate.

4.5.2. Muon Reconstruction & Identification

There are several 'types' of muon which are reconstructed on ATLAS which use different criteria depending upon the information available in the different sub-detectors [82]. The different types of muon are:

- **Stand-Alone Muon:** The trajectory of the muon is reconstructed only in the Muon Spectrometer. The track is extrapolated back to the point closest to the beamline to determine the track parameters at the Interaction Point with the energy loss estimated in the calorimeters. The Stand-Alone muons allow the acceptance to be extended between $2.5 < |\eta| < 2.7$ where there is no coverage from the Inner Detector.

- **Combined Muon:** For the Combined Muon, the track reconstruction is performed separately in the Inner Detector and the Muon Spectrometer, by combining these two reconstructed tracks a Combined Muon is formed. These are the main type of muon used in analyses.

- **Segment Tagged Muon:** Once a track in the Inner Detector is extrapolated back to the Muon Spectrometer and it contains at least one track in the MDT and CSC chambers it can be classed as a Segment Tagged Muon. By allowing only one track to be reconstructed, Segment Tagged muons allow the acceptance to be increased for low p_{T} muons or if they fall into regions with only one layer of muon detectors.

- **Calorimeter Tagged Muon:** The track in the Inner Detector has to be associated with an energy deposit in the calorimeter which is compatible with a minimum ionising particle. Calorimeter Tagged muons are optimised for the region $|\eta| < 0.1$ and for $25 < p_{\mathrm{T}} < 100$ GeV muons. These muons have the lowest purity but they cover regions which are uninstrumented in the Muon Spectrometer.

To reconstruct muons, ATLAS implements two chains which run in parallel, `STACO` [83] and `MuID` [84]. Both chains provide similar performance when reconstructing all four muon categories. Each uses a different approach when combining the Inner Detector and Muon Spectrometer tracks; the `MuID` performs a global refit of hits in the Muon Spectrometer and Inner Detector, whereas `STACO` weights the relative contributions according to the covariance matrix to combine the Inner Detector and Muon Spectrometer tracks statistically.

Muon Reconstruction & Identification Efficiencies

Since there are two sub-detectors (Inner Detector and Muon Spectrometer) involved in the muon reconstruction for $|\eta| < 2.5$, this enables a precise determination of the reconstruction efficiency in this region. For $|\eta| < 2.5$ a tag and probe method uses $Z \to \mu^+\mu^-$ and $J/\psi \to \mu^+\mu^-$ events, similar to the calculation of the electron efficiencies described in Section 4.4.2. Figure 4.9 shows the muon reconstruction as a function of η for $Z \to \mu^+\mu^-$ events with $p_{\mathrm{T}} > 10$ GeV. The different types of muon are also highlighted. At $|\eta| < 0.1$, the efficiency decreases due to the crack in this region. Using Calorimeter Tagged muons recovers the efficiency which was lost. The overall efficency remains constant at 99% when combining all types of muon. The efficiencies calculated in data are compared to those calculated in simulated Monte Carlo events in Figure 4.10. Good agreement is observed in both distributions of η and p_{T}. As with electrons, scale factors are applied to the Monte Carlo to reproduce the observed efficiencies in data.

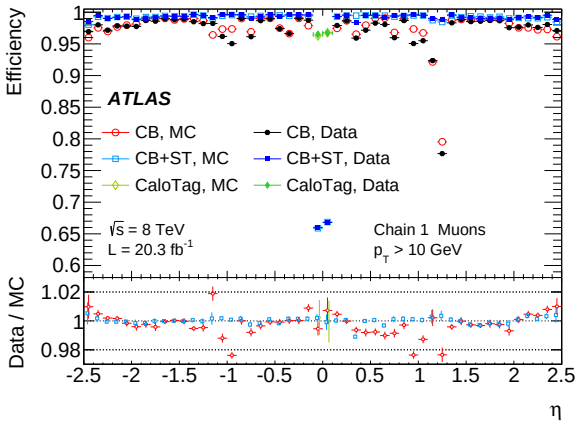

Figure 4.9: Muon reconstruction efficiency as a function of η measured with $Z \to \mu^+\mu^-$ events for muons with $p_{\mathrm{T}} > 10$ GeV. Calorimeter Tagged muons recover the efficiency in the region $|\eta| < 0.1$. Taken From [82].

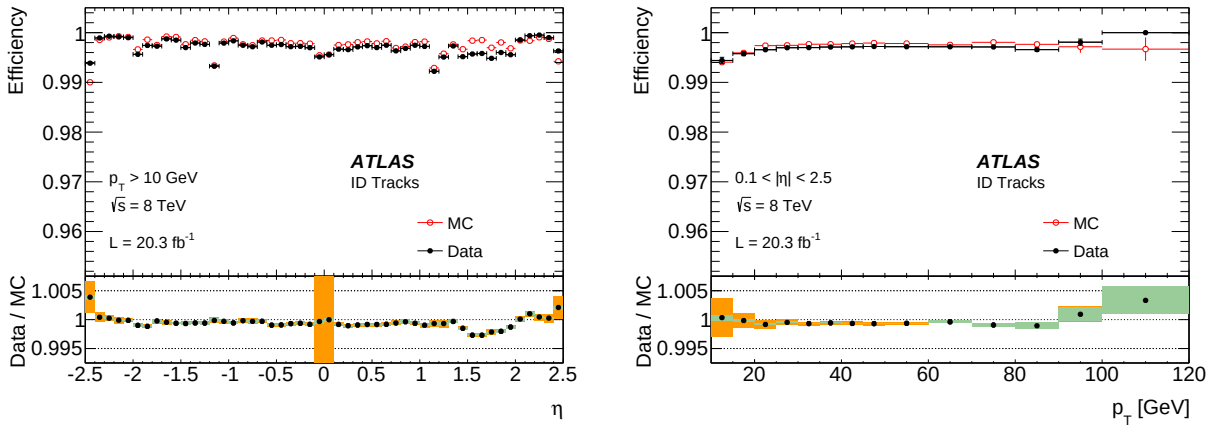

(a) η **(b)** p_{T}

Figure 4.10: The muon reconstruction efficiency as a function of η(a) and p_{T} (b) measured in $Z \to \mu^+\mu^-$ events for muons with $p_{\mathrm{T}} > 10$ GeV. Good agreement between data and Monte Carlo simultion is observed. Orange shading in the bottoms panel indicates statistical and systematic uncertainties whereas the green band indicates statistical uncertainty alone. Taken from [82].

In the region $2.5 < |\eta| < 2.7$, Stand-Alone muons provide the largest efficiency since Combined muons require hits in the Inner Detector. To exploit the full acceptance of the Muon Spectrometer, muons need to be reconstructed in this region. To calculate the efficiency in this forward region, $Z \to \mu^+\mu^-$ events are compared to Standard Model calculations. The scale factors for the efficiency are calculated from the ratio of the ratio of $Z \to \mu^+\mu^-$ in data and Monte Carlo for $2.5 < |\eta| < 2.7$ and the ratio of $Z \to \mu^+\mu^-$ events in data and Monte Carlo in the region $2.2 < |\eta| < 2.5$. In each of the ratios, only one of the reconstructed muons is requred to be in the forward region, the other is a central muon ($|\eta| < 2.2$). The central muon is requred to be a Combined muon whereas the forward muon can be either Combined or Stand-Alone. The scale factors are applied to the Monte Carlo to reproduce the data.

4.6. Jets

During pp collisions, short-lived partons are produced in an event. These partons hadronise before they reach the detector and produce a collimated shower of particles which are collectively known as a jet. There are two ways which a jet can be reconstructed on ATLAS, the first uses the information in the tracks in the Inner Detector (*Track Jets*), the second uses the energy deposited in the calorimeter (*Caloimeter Jets*). The measurements made in this thesis have been taken using calorimeter jets, so the main focus on this section will be their reconstruction in Section 4.6.1. b-tagging forms a major part of the analysis described in Part III and will be described in Section 4.6.3, and a discussion of calibration using the Jet-Energy Scale and Global-Sequential calibrations follows in Section 4.6.4.

4.6.1. Jet Reconstruction

During jet reconstruction for calorimeter jets, the calorimeter cells are first combined into clusters before passing to a jet reconstruction algorithm. ATLAS uses two types of clustering algoritms, *topological* clustering and *calorimeter tower* clustering [85].

- **Topological Clusters:** The topological clustering algorithm starts from a *seed* cell where the signal to noise ratio (SNR) is greater than 4. Noise is defined as the estimated energy in the cell divided by the root-mean squared of the energy distribution measured in events triggered at random bunch crossings. Neighbouring cells are added iteratively to the cluster if they have an SNR greater than two. Finally, all neighbouring calorimeter cells are added to the topological cluster. A splitting step is included to separate showers from close-by particles. If the energy of a neighbouring cell exceeds 500 MeV, a new seed is formed. The energy of the cluster is defined to be the sum of the energy in the cells contributing to the cluster. The cell direction is determined from the weighted averages of pseudorapidity and azimuthal angle of the constituent cells. Noise fluctuations in the detector mean clusters can obtain negative energy. These negative energy clusters are unphysical so are rejected.

- **Calorimeter Tower Clusters:** The calorimeter towers are constructed in a static grid of calorimeter cells of size $\Delta\eta \times \Delta\phi = 0.1 \times 0.1$. If the cells are larger than these dimensions or have special geometry as in the Forward Calorimeters, a

weight is applied which defines the fraction of the cells' energy attributed to the tower. The noise suppressed towers use the topological cluster algorithm so only calorimeter cells that are included in the topological clusters are used.

Once the clusters have been formed, jet algorithms are applied to relate them to the underlying QCD interactions. The algorithms must adhere to criteria to make sure the reconstructed jet is an accurate description of the interaction. There should be no resulting effect on the jet reconstruction if the particle splits into two collinear particles (The algorithm must be *collinear safe*). Soft particles which are present between jet components should not have an effect the jet reconstruction (should be *infrared safe*). The detector resolution and sources of noise should impose little or no effect, and the jet reconstruction should be invariant under Lorentz boosts in the z direction. Finally, the algorithm should be efficient enough to work within the time constraints of an analysis framework.

For ATLAS measurements, the anti-k_{T} algorithm [86] is used for jet reconstruction. The anti-k_{T} algorithm is a sequential combination algorithm whereby a distance $d_{i,j} = \min(p_{\mathrm{T},i}^{2p}, p_{\mathrm{T},j}^{2p})\frac{\Delta R_{i,j}^2}{R^2}$ is calculated for all pair of objects and the distance between the beam and the object $d_{i,B} = p_{\mathrm{T},i}^{2p}$ is calculated for all objects, where $p_{\mathrm{T},i}$ is the transverse momentum for object i and similarly for j. The $\Delta R_{i,j}$ is the distance between objects i and j in the η and ϕ plane. R controls the size of the jet and is analagous to the jet cone size in a cone based algorithm. The measurements in this thesis require $R = 0.4$. If the minimum of all $d_{i,j}$ and $d_{i,B}$ is $d_{i,j}$ the objects will be merged; if $d_{i,B}$ is the minimum, the object will be considered a jet and the object removed from the object list. This process is repeated until no objects remain. The anti-k_{T} algorithm is both collinear and infrared safe as the soft radiation is clustered into hard objects, resulting in a regular conical jet, which are experimentally desired as they give a well defined jet area which can be used in pile-up suppression. The conservation of energy and momentum is maintained by summing the four-momenta of the constituent objects inside the jet cone, allowing for a meaningful jet mass definition.

4.6.2. Jet Selection

The selection of real jets produced from hard-scattering events and the rejection of background fake-jets is important for physics analyses. The main sources of background in jet selection include where a proton in an event collides with residual gas in the beam (Beam-gas event), the interactions in tertiary collimators far away from ATLAS (Beam-

Halo event), Cosmic-ray muons overlapping in-time with events and general detector noise. There are four sets of criteria for selecting jets based upon the event topology and jet kinematics, the four levels are: LOOSER, LOOSE, MEDIUM and TIGHT. LOOSER jets provide the highest signal efficiency with a 50% fake-jet rejection factor. The TIGHT selection has the highest background rejection rate but at a cost of signal efficiency. The two intermediate levels apply tighter selections on top of the LOOSER selection, increasing the background rejection factor. Jet selection discriminating variables correspond to several pieces of experimental information including jet p_{T}, the fraction of energy in the EM-calorimeter or Hadronic calorimeter and the overall quality of the reconstructed jet calculated as a weighted sum over the energy squared, averaged over the quality of the calorimeter cells; among others [87].

Jet Selection Efficiency

The efficiency of the jet selection is measured using a tag and probe method on events with two jets at high p_{T}; the reference jet (tag) is required to pass a tightened selection and be back to back with the other jet (probe). Figure 4.11 shows the results of the tag and probe as a function of jet p_{T} in bins of η for jets reconstructed using the anti-k_{T} algorithms with $R = 0.4$. The measured efficiency for LOOSER is above 99.8%, this falls to 97% for LOOSE jets. For MEDIUM and TIGHT jets, the efficiency falls further due to selections made on the jet charge fraction. These cuts only affect the MEDIUM and TIGHT jets at lower p_{T}. At $p_{\mathrm{T}} > 50$ GeV, the efficiency is 99% whereas for jets with $p_{\mathrm{T}} = 25$ GeV, the efficiency is 96% for MEDIUM jets and 85% for TIGHT jets. Good agreement is observed between data and simulated Monte Carlo in the LOOSER and LOOSE selections. Differences are observed for the MEDIUM and TIGHT jets but these do not exceed 0.2% and 1% respectively, for jets with $p_{\mathrm{T}} > 40$ GeV. At lower p_{T}, larger differences are observed, these do not exceed 1%(2%) for MEDIUM(TIGHT) jets [87].

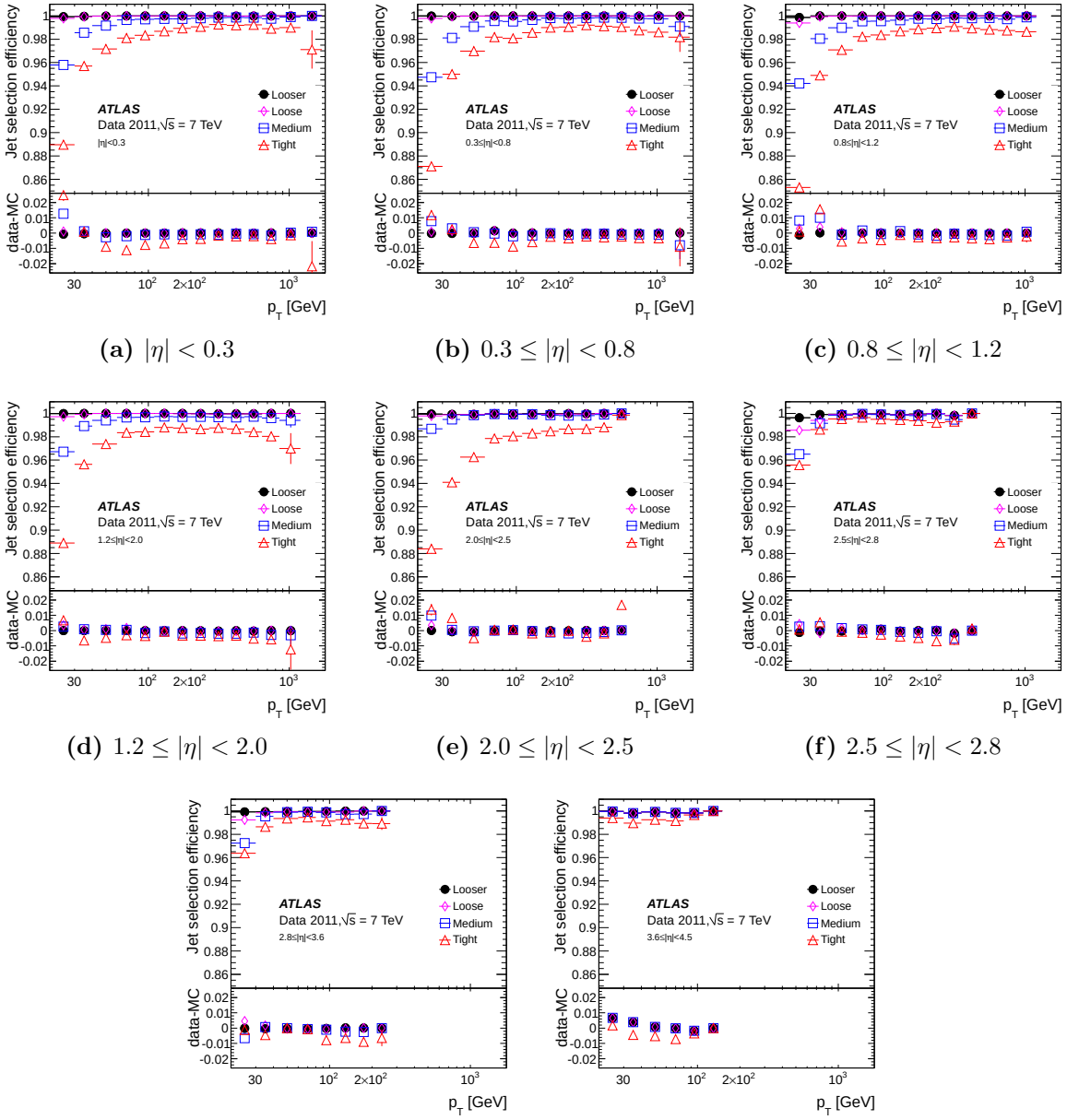

(a) $|\eta| < 0.3$ **(b)** $0.3 \leq |\eta| < 0.8$ **(c)** $0.8 \leq |\eta| < 1.2$

(d) $1.2 \leq |\eta| < 2.0$ **(e)** $2.0 \leq |\eta| < 2.5$ **(f)** $2.5 \leq |\eta| < 2.8$

(g) $2.8 \leq |\eta| < 3.6$ **(h)** $3.6 \leq |\eta| < 4.5$

Figure 4.11: Jet selection efficiency as a function of jet p_{T} for anti-k_{T}, $R = 0.4$ jets binned in η. Showing the selection efficiencies for the four sets of jet selection criteria. The data, Monte Carlo comparison is also made. Taken from [87].

4.6.3. *b*-jet Identification

The ability to distinguish the flavour of a jet, separating b from c or other light jets (u, d, s, g) is crucial for many analyses performed on ATLAS. b-quarks which produce b-hadrons have a unique signature which allows them to be discriminated from other jet flavours. The decay time for a B-hadron is relatively long ($\sim 1 \times 10^{-12}$ s) compared to other quark flavours. This longevity allows the b-hadron to travel up to ~ 3 mm inside the detector before decaying. The identification of b-jets forms an integral part of the measurements presented in Part III. The algorithms used in the b-jet identification (b-tagging) exploit the decay length by requiring a certain number of tracks to be reconstructed at the secondary vertex and information beyond the secondary vertex.

b-tagging Algorithms

There are a number of different b-tagging algorithms used on ATLAS for analysis. The algorithms fall into three categories based upon features of a b-hadron decay. The first type uses the impact parameter. In the $r\phi$ projection this is the transverse impact parameter whereas in the z direction it is known as the longitudinal impact parameter. Decays from b- or c-hadrons tend to have a positive impact parameter since the track extrapolation will cross the jet direction in front of the primary vertex. The IP3D algorithm uses a likelihood technique where impact parameter variables are compared to smoothed and normalised distributions of b- and light-jets.

The next type of algorithm uses secondary vertex information as a disciminant for b-jets and light-jets; all the two-track pairs which form a good vertex are selected. Tracks which are too close to the primary vertex and those not associated with a jet are rejected along with those found to be compatible with material interactions. A single vertex is built by combining the remaining tracks, this is then passed to an algorithm which iteratively removes tracks until a good χ^2 is achieved. The SV1 algorithm takes advantage of three properties associated with a secondary vertex in order to discriminate b-jets from light-jets; the invariant mass of the tracks, the ratio of the sum of energies in the vertex against the energies in the jet and the total number of two-track vertices. These properties are used as input into a likelihood ratio along with the ΔR between the jet axis and the line joining the primary vertex to the secondary vertex.

The final type of b-tagging algorithm uses the decay chain reconstruction as an input to the JetFitter algorithm. JetFitter exploits the topology of weak b- and c-hadron decays inside a jet. A Kalman fitter is used to find a common line between the primary vertex

and b- and c-hadron, the positions of the vertices are identified along the line giving a time of flight of the b-hadron. A likelihood technique using the SV1 variables along with the flight time information is used to find the likelihood of jet being a b-jet [88].

Due to the likelihood techniques used in the IP3D, SV1 and the Kalman fitter used in JetFitter, the techniques can be combined to form the MV1 algorithm [88–90]. The MV1 algorithm uses an artificial neural network trained on b-jets as signal and light-jets as background to compute a tag weight. During the 2012 data taking period, the MV1 algorithm was improved in order to achieve higher c-jet rejection by training on a mixture of c- and light-jets. The higher c-jet rejection came at the cost of lower light-jet rejection at higher tagging weights. One of the major benefits from using the MV1c algorithm for reconstructing b-jets is the ability to apply both upper and lower cuts on the tagging weight. This technique is referred to as *continuous* b-tagging; it allows for the analyses to be split into regions of high sensitivity through the use of multiple tagging weight selections (working points). The analysis presented in this thesis employs three such working points at 50%, 70% and 80% for TIGHT, MEDIUM and LOOSE categories respectively.

b-tagging Uncertainty Measurements

The performance of a b-tagging algorithm is categorised by the efficiency of the tagger, defined as the fraction of correctly tagged b-jets as a function of falsely tagged b-jets. The efficiency of b-tagging in the MV1c algorithm is measured using dileptonic top-pair events as input into a combinatorial likelihood method. To pass selection, both W-bosons from the decay of the top-quark must decay leptonically. The tagging weight and the p_{T} of each of the top-quark decays is passed to a likelihood function to calculate the efficiency. The resultant scale factors are calculated as the ratio of the efficiency measured in data against that measured in simulated Monte Carlo events. Figure 4.12 shows the measured efficiencies for both data and Monte Carlo simulation as a function of jet p_{T} along with the scale factors applied to the Monte Carlo for a working point of 70% [89].

The c- and light-jet calibration is done calculated using mass difference measurements for D^{*+} mesons in jets satisfying and not satisfying the b-tagging requirements and a simultaneous fit being performed on this distribution. The parameters of the fit which describe the shapes of the signal and background shapes are required to be equal for both distributions. The efficiency is introduced as an extra parameter to account for the difference in D^{*+} yields in tagged and un-tagged jets. Figure 4.13 shows the measured

efficiencies in data and Monte Carlo simulation and their scale factors as a function of p_{T} for a working point of 70%, There is no observed dependence on jet p_{T} [90].

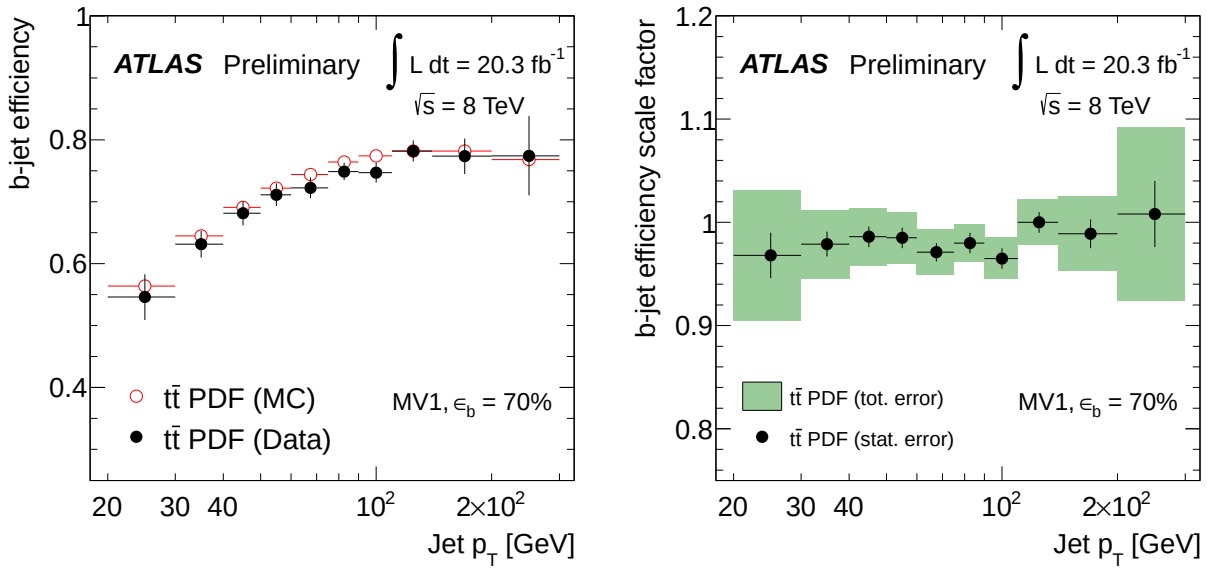

(a) b-jet Efficiency **(b)** b-jet Efficiency Scale Factor

Figure 4.12: The efficiencies and scale factors calculated from semi-leptonically decaying $t\bar{t}$ events. Taken from [89].

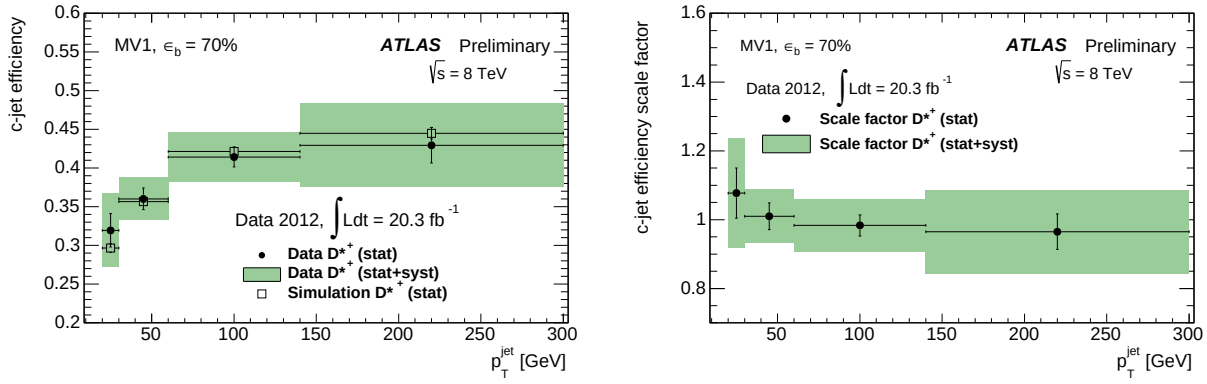

(a) c-Jet Efficiency **(b)** c-jet Efficiency Scale Factor

Figure 4.13: The measured efficiencies and scale factors for c-jets, calculated using decays from D^{*+} mesons. Taken from [90].

4.6.4. Jet Calibrations

Once reconstructed using the calorimeter energy deposited in the EM-calorimeter, the jets are calibrated to the EM-scale. Due to the non-compensating nature of the ATLAS detector, where the response for leptons and photons is better than for hadrons, this leads to the p_{T} of the reconstructed hadrons is measured to be 15–55% lower than the true value. Fluctuations of the hadronic shower in the electromagnetic content as well as energy losses due to dead material lead to a degraded measurements of the resolution and the jet energy compared to particles interacting solely with the EM-calorimeter [91]. There are two calibrations used on jets in the analysis presented in Part III to correct for the mis-measurement of hadronic jets. Jet-Energy Scale (JES) and Global Sequential Calibration (GSC). These are described below.

Jet Energy Scale (JES)

The first calibration for jets is aimed at correcting the response[3] of the jet to unity by applying a correction as a function of jet p_{T} and η. The JES calibration consists of three steps; an initial pile-up correction, a vertex correction and a correction to correct the jet energy and pseudorapidity. The pile-up correction is used so that the derived energy calibration does not depend on the number of primary vertices; the average additional energy from the additional proton-proton interactions is subtracted from energy measured in the calorimeters.

The second stage corrects the direction of the jet. Calorimeter jets are reconstructed using the centre of the ATLAS detector as a reference for the jet direction calibration. The direction correction re-calculates the jet four-momentum back to the primary vertex using the vector from the primary vertex to the centre of the topological cluster. This correction improves the angular resolution whilst leaving the jet energy unaffected.

The final part of the JES calibration restores the jet energy of the reconstructed jet to the energy of the Monte Carlo truth[4] jet and also the pseudorapidity of the jet. The choice of Monte Carlo truth jet used for the JES studies exlcudes all muons and neutrinos and those performed in Chapter 6 excludes muons or neutrinos from W or Z bosons coming from the hard interaction to avoid double counting. The energy calibration starts by identifying isolated calorimeter jets by matching a truth jet within $\Delta R = 0.3$. An

[3] Response is defined as: $\mathcal{R} = \frac{E^{jet}_{reco}}{E^{jet}_{truth}}$ for each jet.

[4] the truth particles in Monte Carlo simulation are those which have not been passed through the detector simulation

isolated jet is defined as a jet with no other jets with $p_{\mathrm{T}} > 7$ GeV within $\Delta R = 2.5R$ where R is the jet distance parameter. The calibration is parameterised as a function of uncalibrated jet energy and uncorrected pseudorapidity. The energy of each pair of reconstructed and truth jets is measured in bins of truth jet energy ($E^{\mathrm{jet}}_{\mathrm{truth}}$) and measured pseudorapidity in the detector (η_{det}). The average jet response for each ($E^{\mathrm{jet}}_{i\mathrm{truth}}$,$\eta_{\mathrm{det}}$)-bin is defined as the peak position of a Gaussian fit to the response distribution. The calibration ($\mathcal{F}_{\mathrm{calib}}$) is obtained for the jet response in each ($E^{\mathrm{jet}}_{\mathrm{truth}}$,$\eta_{\mathrm{det}}$)-bin j using:

$$\mathcal{F}_{\mathrm{calib}}(E^{\mathrm{jet}}_{\mathrm{EM}}) = \sum_{i=0}^{N_{\mathrm{max}}} \alpha_i (\ln E^{\mathrm{jet}}_{\mathrm{EM}}), \tag{4.2}$$

where α_i are free parameters and N_{max} is chosen between 1 and 6 depending on the goodness of fit. The jet energy scale is defined as $1/\mathcal{F}_{\mathrm{calib}}$:

$$E^{\mathrm{jet}}_{\mathrm{EM+JES}} = \frac{E^{\mathrm{jet}}_{\mathrm{EM}}}{\mathcal{F}_{\mathrm{calib}}|\eta_{\mathrm{det}}}. \tag{4.3}$$

At low energies, the correction factor is 2.1; this decreases to 1.2 at high jet energies in the most forward region. The pseudorapidity is calibrated in ($E^{\mathrm{jet}}_{\mathrm{truth}}$,$\eta_{\mathrm{det}}$)-bins as the average distance between truth and reconstructed η ($\Delta\eta = \Delta\eta_{\mathrm{truth}} - \Delta\eta_{\mathrm{reco}}$). The correction factor is small ($\Delta\eta = 0.01$) in most regions of the calorimeter but does rise in transition regions [87].

Once the jets have been calibrated, in-situ techniques are used to correct the data to Monte Carlo sumulation using the p_{T} balance of a jet against a well measured object. There are three methods used; the first uses events containing a Z boson or a photon and a recoiling jet. The momentum of the jet is compared to the well measured photon or Z boson. The second method measures the p_{T} of a photon and a recoiling hadron in the same manner. The final method is used for correcting high p_{T} jets by measuring the momentum imbalance to a low p_{T} jet which has been calibrated using a photon or Z boson as described above [92].

Figure 4.14 shows the impact of the JES calibration for b-jets reconstructed for use in the analysis presented in Part III, in terms of the reconstructed jet energy and the response for all reconstructed jets, comparisons are made to the EM-scale and to truth jets. The shape and the mean of the reconstructed energy matches well to the truth jet values after the JES calibration, the same is also true for the response.

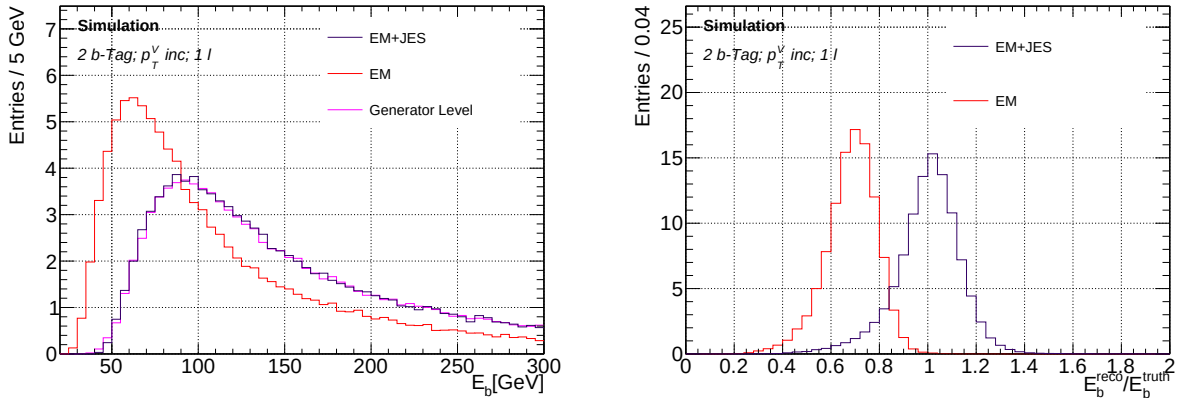

(a) Jet Energy **(b)** Jet Response

Figure 4.14: The impact of the JES calibration in terms of jet energy and response for b-jets reconstructed for the $WH \to l\nu b\bar{b}$ analysis. The JES corrects the response of the reconstructed jet to that of the truth jet.

Global Sequential Calibration (GSC)

Global Sequential (GS) Calibration uses a series of multiplicative corrections to the jet energy measurements. The GS corrections are based upon global jet observables, such as longitudinal structure of the energy deposits within the calorimeters, tracking information, and information relating to the muon chambers behind a jet. Tracking information is used to reduce the difference in calorimeter response observed in light quarks and gluon-initiated jets. Calorimeter and muon chamber information is used to improve the resolution of the jet energy in low and high energy jets respectively. The GS calibrations can be applied at any stage during the calibration process. The effect on the jets is to improve the resolution whilst maintaining the scale.

The jets used for the calibration are required to be isolated such that no other calorimeter jets are withing $\Delta R = 2.5R$ where R is the jet algorithm distance parameter, only one truth jet with $p_{\mathrm{T}} > 7$ GeV is allowed within $\Delta R = 1.5R$. The average jet response for the calorimeter jets used in GSC is defined as $\mathcal{R} = \left\langle \frac{p_{\mathrm{T}}^{\mathrm{jet}}}{p_{\mathrm{T}}^{\mathrm{truth}}} \right\rangle$, where $p_{\mathrm{T}}^{\mathrm{jet}}$ and $p_{\mathrm{T}}^{\mathrm{truth}}$ are the calorimeter jet and truth jet (within $\Delta R = 0.3$) respectively. A Gaussian fit is applied to the average response distribution over a 1.6σ range, and the jet energy resolution $\left(\frac{\sigma}{p_{\mathrm{T}}}\right)$ is used to determine the jet energy fluctuations. The correction applied to the jet energy is derived by inverting the average response, and the average response is then scaled back to match the initial value so that the average energy does not vary. This requirement ensures the resolution improves whilst maintaining the scale. The

corrections are applied in bins of $|\eta|$ and are only applied to jets with $p_{\mathrm{T}} > 15$ GeV.

After applying the GSC to EM+JES jets, the relative improvement in resolution is 35%(20%) in barrel (end-cap) regions. For jets with $p_{\mathrm{T}} > 30$ GeV, there is no observed change in average response, however for $p_{\mathrm{T}} < 30$ GeV jets a 1–1.5% change is observed [93].

Figure 4.15 compares the EM+JES calibration to the EM+JES+GS calibration as well as to the truth jet, as a function of jet p_{T} for jets reconstructed for $WH \to l\nu b\bar{b}$ analysis. The improved resolution is observed with minimal change in the jet response.

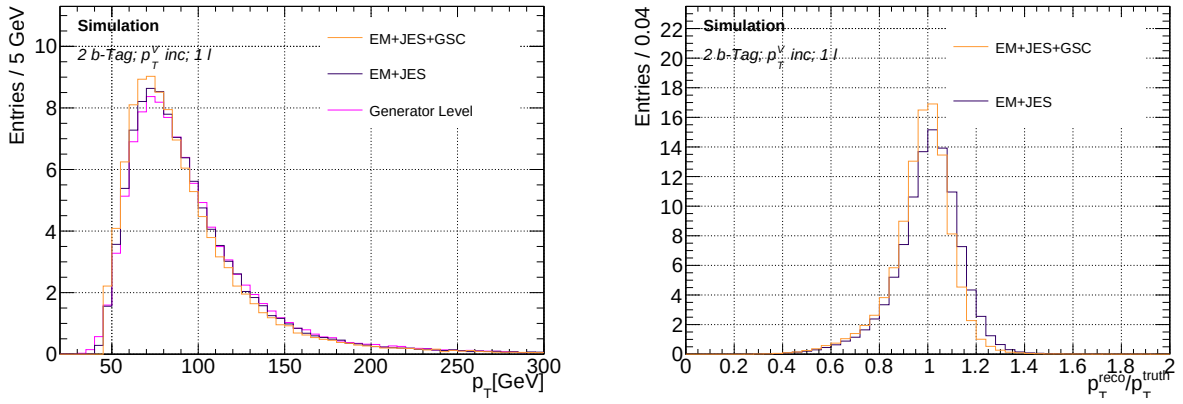

(a) Jet p_{T} **(b)** Jet Response

Figure 4.15: The impact of the GS calibration in addition to the JES calibration in terms of jet $p_{\mathrm{T}}$and response. The resolution of the GSC improves with respect to the JES calibration, whilst maintaining the scale.

4.7. Missing Transverse Energy ($E_{\mathrm{T}}^{\mathrm{miss}}$)

The missing transverse energy $E_{\mathrm{T}}^{\mathrm{miss}}$ in an event is defined as the momentum imbalance in the plane transverse to the beam, assuming conservation of momentum. This imbalance may signal the presence of particles which are unseen by the detector such as neutrinos or more exotic supersymmetric particles [94, 95]. The measurements made in this thesis rely on an accurate reconstruction of the missing energy to accurately reconstruct the four-momenta of the components of $WH \to l\nu b\bar{b}$. The $E_{\mathrm{T}}^{\mathrm{miss}}$ reconstruction relies on the contributions from energy deposits in the calorimeters and tracks in the muon spectrometers, where the calorimeter objects are associated with high p_{T} parent objects which are added in a specific order; electrons, photons, hadronically decaying τ-leptons, jets and muons. Calorimeter cells which are not associated with a topological cluster

are added to a soft term. The x and y components which make up the $E_{\mathrm{T}}^{\mathrm{miss}}$ vector are defined as:

$$E_{\mathrm{T}}^{\mathrm{miss}} = \sqrt{(E_{\mathrm{x}}^{\mathrm{miss}})^2 + (E_{\mathrm{y}}^{\mathrm{miss}})^2}, \tag{4.4}$$

where each component in Equation 4.4 can be deconstructed into calorimeter and muon components as follows:

$$E_{\mathrm{x(y)}}^{\mathrm{miss}} = E_{\mathrm{x(y)}}^{\mathrm{miss},e} + E_{\mathrm{x(y)}}^{\mathrm{miss},\gamma} + E_{\mathrm{x(y)}}^{\mathrm{miss},\tau} + E_{\mathrm{x(y)}}^{\mathrm{miss,jets}} \tag{4.5}$$

$$+E_{\mathrm{x(y)}}^{\mathrm{miss,SoftTerm}} + E_{\mathrm{x(y)}}^{\mathrm{miss},\mu}. \tag{4.6}$$

Each component of Equation 4.6 is the negative sum of the calibrated object, projected onto the x and y directions. The $E_{x(y)}^{miss,SoftTerm}$ is constructed from clusters which are not associated with topological clusters and the clusters with $p_T < 20$ GeV.

The SoftTerm in the event can be affected by pile-up, since $E_{\mathrm{x(y)}}^{\mathrm{miss,SoftTerm}}$ can have a large impact on the momentum balance in the event. To suppress the impact of pile-up, tracks can be used since they can be associated with a primary vertex. The SoftTerm is scaled by the soft term vertex fraction (STVF):

$$\mathrm{STVF} = \left(\frac{\sum_{\mathrm{tracks_{ST},PV}} p_{\mathrm{T}}}{\sum_{\mathrm{tracks_{ST}}} p_{\mathrm{T}}} \right), \tag{4.7}$$

where the sums are taken over the tracks unmatched to physics objects and PV denotes the tracks associated with the primary vertex [95]. Figure 4.16 shows the performance of the $E_{\mathrm{T}}^{\mathrm{miss}}$ reconstruction with and without the pile-up suppressions. In the $E_{\mathrm{T}}^{\mathrm{miss}} > 75$ GeV region, the agreement between data and Monte Carlo simulation is much improved by scaling the SoftTerm.

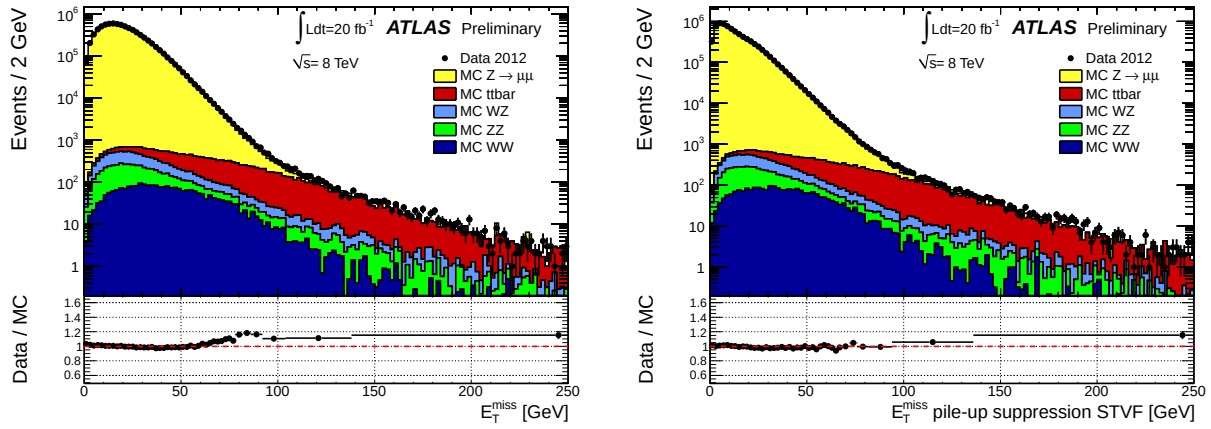

(a) No pile-up Suppression **(b)** STVF Suppression

Figure 4.16: Reconstruction of $E_{\mathrm{T}}^{\mathrm{miss}}$ with and without pile-up suppression. Taken from [95]

.

Part III

$WH \rightarrow l\nu b\bar{b}$ Analysis

Chapter 5

Object & Event Selection

For a physics analysis, the selection starts with setting requirements for basic physics objects (electrons, muons, jets and missing transverse energy) in an event. Details concerning the reconstruction of objects used as part of the $WH \to l\nu b\bar{b}$ analysis are shown in Chapter 4. Once the objects have been selected, they are passed through an event selection which has the overall aim of maintaining a high signal acceptance of a leptonically decaying vector boson (either electron or muon) and a Higgs boson decaying to a pair of b-jets; whilst rejecting potential background events.

Details of the selection of objects required for the $WH \to l\nu b\bar{b}$ analysis are given in Section 5.1, before the details of the event selection are given in Section 5.2.

5.1. Object Selection

This section discusses the selection of physics objects as part of the $WH \to l\nu b\bar{b}$ analysis at $\sqrt{s} = 8$ TeV. The events are selected primarily using single-lepton triggers. In the muon sub-channel, $E_{\mathrm{T}}^{\mathrm{miss}}$ triggers are also used to compensate for the limited number of muon trigger chambers. An initial preselection is performed requiring the charged particles reconstructed to have $p_{\mathrm{T}} > 400$ MeV. The primary vertex is selected from all the reconstructed vertices that have at least three tracks, as the one that has the largest sum of associated track squared transverse momenta.

5.1.1. Muons

Muons are categorised into four types, according to the way they are reconstructed. The four categories; calorimeter tagged (CT), stand-alone (SA), combined (CB) and segment tagged (ST), are all used as part of the $WH \to l\nu b\bar{b}$ analysis. The reconstruction of muon candidates is performed using the Muonboy algorithm [84], with the quality of the candidate being described as loose, medium or tight (see Section 4.5).

To be selected, CB and ST muons must pass the muon combined performance (MCP) groups inner detector criteria. The impact parameter, d_0 and z_0 relative to the primary vertex are required to satisfy: $|d_0| < 0.1$ mm and $z_0 < 10$ mm. CB and ST muons are required to have $p_{\mathrm{T}} > 7$ GeV within $|\eta| < 2.7$ and fall under the tight quality selection as defined in Section 4.5. The ratio of the sum of the p_{T} of the tracks to the total p_{T} within a cone of $\Delta R < 0.2$ around the muon direction must be less than 0.1.

The SA muons requirements are: $p_{\mathrm{T}} > 7$ GeV within $2.5 < |\eta| < 2.7$ with a tight quality selection. The calorimeter tagged muons must satisfy the same MCP, d_0, z_0 and isolation requirements as combined and stand-alone muons. Due to where the calorimeter tagged muons have their highest reconstruction efficiency in the ATLAS detector, they must have $p_{\mathrm{T}} > 20$ GeV within $|\eta| < 0.1$ with a quality selection of a calorimeter muon tag greater than 10 or a calorimeter likelihood value greater than 0.9.

Details of a muon candidate selection are summarised for each category in Table 5.1.

Criteria	Selection
Identification	Combined (CB) Tight Muons
	Segment-tagged (ST) Tight Muons
	Calorimeter Tagged (CT) Tight Muons
	Standalone (SA) Tight Muons
Kinematic Cuts	CB+ST: $p_{\mathrm{T}} > 7$ GeV, $\lvert\eta\rvert < 2.7$
	SA: $p_{\mathrm{T}} > 7$ GeV, $2.5 < \lvert\eta\rvert < 2.7$
	CT: $p_{\mathrm{T}} > 20$ GeV, $\lvert\eta\rvert < 0.1$
Inner Detector	$N^{\mathrm{hits}}_{\mathrm{pixel}} + N^{\mathrm{dead}}_{\mathrm{pixel}} > 0$
	$N^{\mathrm{hits}}_{\mathrm{SCT}} + N^{\mathrm{dead}}_{\mathrm{SCT}} > 4$
	$N^{\mathrm{holes}}_{\mathrm{pixel}} + N^{\mathrm{holes}}_{\mathrm{SCT}} < 3$
	$0.1 < \lvert\eta\rvert < 1.9$: $N^{\mathrm{tot}}_{\mathrm{TRT}} > 5$; $N^{\mathrm{Outliers}}_{\mathrm{TRT}} < 0.9 \times N^{\mathrm{tot}}_{\mathrm{TRT}}$
	where $N^{\mathrm{tot}}_{\mathrm{TRT}} = N^{\mathrm{hits}}_{\mathrm{TRT}} + N^{\mathrm{Outliers}}_{\mathrm{TRT}}$
Impact Parameter	$\lvert d_0\rvert < 1$ mm
	$\lvert z_0\rvert < 10$ mm
Track Isolation	$\sum_{\mathrm{tracks}} p_{\mathrm{T}}(\Delta R < 0.2)/p^{\mu}_{\mathrm{T}} < 0.1$
Overlap Removal	Reject CT muon if within $\Delta R < 0.2$ of ST or CB muon

Table 5.1: Table showing a summary of the selection of muons used as part of the $WH \to l\nu b\bar{b}$ analysis. $N^{\mathrm{hits}}(N^{\mathrm{holes}})$ represents the number of hits (missing hits) in an area of the inner detector. N^{dead} refers to the number of dead sensors the muon has crossed in a sub-detector.

5.1.2. Electrons

Electrons are reconstructed in the central region ($\lvert\eta\rvert < 2.5$) of the ATLAS detector by matching reconstructed tracks to energy deposits in the EM-calorimeter. The calorimeter deposits are reconstructed using a sliding window algorithm described in Section 4.4.2.

For the $WH \to l\nu b\bar{b}$ analysis, a likelihood method is used for the identification of electrons, calculating the probability of an object being an electron. There are three categories of electron available: Loose, Medium, and VeryTight, in order of increasing probability. For the $WH \to l\nu b\bar{b}$ analysis, reconstructed electrons must pass the VeryTight likelihood selection outlined in [78], including $E_{\mathrm{T}} > 25$ GeV and be within the central region of the detector, $\lvert\eta\rvert < 2.5$ inclusive of the crack region at $1.37 < \lvert\eta\rvert < 1.52$. The tracks in the inner detector are isolated by requiring the ratio of the sum of the p_{T} of the tracks within a cone of $\Delta R < 0.2$ over the electron p_{T} to be less

than 0.04. Calorimeter energy deposits have a similar isolation requirement; the ratio of the sum of the E_{T} in a cone of $\Delta R < 0.3$ over the electron E_{T} must be less than 0.4. If a jet is reconstructed within $\Delta R < 0.4$ of an electron, the jet is removed and if an electron is reconstructed within $\Delta R < 0.2$ of a muon, the electron is removed, unless the muon is a CT muon. In this case the muon is rejected. A summary of the electron selection for the $WH \to l\nu b\bar{b}$ analysis is given in Table 5.2.

Criteria	Selection
Identification	VeryTightLH
Kinematic Cuts	$E_{\mathrm{T}} > 25$ GeV, $\lvert\eta\rvert < 2.5$
Track Isolation	$\sum_{\mathrm{tracks}} p_{\mathrm{T}}(\Delta R < 0.2)/p_{\mathrm{T}}^{e} < 0.04$
Calorimeter Isolation	$\sum_{\mathrm{cluster}} E_{\mathrm{T}}(\Delta R < 0.3)/E_{\mathrm{T}}^{e} < 0.04$
μ-e Isolation	CB, ST & SA: reject electron if within $\Delta R < 0.2$ of muon CT: reject muon if within $\Delta R < 0.2$ of electron
Jet - e Isolation	Reject electron if within $\Delta R < 0.4$ of jet

Table 5.2: Table showing a summary of the selection requirements for electrons as part of the $WH \to l\nu b\bar{b}$ analysis.

5.1.3. Jets & Missing Transverse Energy

Jets are reconstructed from topological clusters in the calorimeter using the anti-k_T algorithm with a radius parameter of 0.4. Once a collection of jets is established, the jet energy scale (JES) and global sequential calibrations are applied. A description of the reconstruction and calibration of jets is given in Section 4.6, with a detailed study into the effects of the calibration in Section 6.1.

There are two categories of jets, used in the $WH \to l\nu b\bar{b}$ analysis: signal and forward. Signal jets are used for the construction of a Higgs boson candidate, whereas forward jets are used for the suppression of $t\bar{t}$ background. To be considered a signal jet, the candidate must lie within $|\eta| < 2.5$ and have $p_{\mathrm{T}} > 20$ GeV. Forward jet candidates must lie in the region $2.5 < |\eta| < 4.5$ and have $p_{\mathrm{T}} > 30$ GeV. For the suppression of jets originating from pile-up interactions, the scalar sum of the p_{T} of the tracks associated with the jet, originating from the primary vertex must be above 50% of the total jet p_{T}. This is achieved by placing a cut on the jet vertex fraction (JVF) to be less than 0.5. The JVF is the fraction of track momentum associated with the jet. The cut on JVF is

only applied to jets with $p_{\mathrm{T}} < 50$ GeV and $|\eta| < 2.4$. If a jet has no associated tracks, it is retained.

To avoid double-counting; if a jet and a muon are separated by $\Delta R < 0.4$, the jet is discarded if there are less than three associated tracks as this jet is likely to be the product of a showering muon inside the calorimeter. If the jet has more than 3 tracks, the muon is discarded. A summary of the selection criteria for signal and forward jets is shown in Table 5.3.

Criteria	Selection
Identification	Anti-k_t, $R = 0.4$ Topological jets
Kinematic Cuts	**Signal:** $p_{\mathrm{T}} > 45$ GeV, $\|\eta\| < 2.5$ (leading) $p_{\mathrm{T}} > 20$ GeV, $\|\eta\| < 2.5$ (sub-leading) **Forward:** $p_{\mathrm{T}} > 30$ GeV. $2.5 < \|\eta\| < 4.5$
jet - e Isolation	Reject electron if within $\Delta R < 0.4$ of jet
jet - μ Isolation	Reject muon if $n_{\mathrm{tracks}} > 3$ and within $\Delta R < 0.4$ Reject jet if $n_{\mathrm{tracks}} < 3$ and within $\Delta R < 0.4$
b-tagging	**Loose:** 80% Efficiency **Medium:** 70% Efficiency **Tight:** 50% Efficiency

Table 5.3: Table showing a summary of the selection requirements for jets as part of the $WH \to l\nu b\bar{b}$ analysis.

b-Jets

The long lifetime of a b-hadron is exploited using the MV1c algorithm as discussed in Section 4.6.3. For the $WH \to l\nu b\bar{b}$ analysis, three such working points are used, *loose* (L) has an 80% b-jet efficiency, *medium* (M) has a 70% b-jet efficiency and *tight* (T) has a 50% efficiency.

Missing Transverse Energy

Missing transverse energy, $E_{\mathrm{T}}^{\mathrm{miss}}$ is measured as the negative vector sum of the transverse momentum associated with energy clusters in the calorimeter within $|\eta| < 4.9$, following the prescription in Section 4.7. The $E_{\mathrm{T}}^{\mathrm{miss}}$ reconstruction forms a vital part of the reconstruction of the W-boson however, there are no selection requirements placed on the $E_{\mathrm{T}}^{\mathrm{miss}}$ at object level.

5.2. Event Selection

A summary of the event selection is given in Table 5.4. For the $WH \to l\nu b\bar{b}$ analysis, events are required to contain one tight lepton, either electron or muon, with no additional loose leptons. The selected lepton is required to match the lepton trigger from which the object was selected.

The events are categorised by the number of jets in the event; there must be exactly two or three jets to qualify for the 2- and 3-jet categories respectively. The selected jets are then passed to the MV1c algorithm. There must be no more than two jets passing the loose requirements for b-tagging. In 3-jet events, if the lowest p_{T} jet is b-tagged it is discarded. The leading b-tagged jet must have $p_{\mathrm{T}} > 45$ GeV.

To be considered a tight tagged event, both selected jets must pass the tight requirements; those not classified as tight but satisfying the medium tagging requirements form the medium category. If both tagged jets do not meet the medium requirements but do meet the loose requirements, they form the loose category. If only one jet satisfies the loose requirement it forms the 1 b-tag category. In both 2- and 3-jet categories, the Higgs boson candidate is formed by the 2 b-tagged jets in all the 2 b-tag categories. For the 1 b-tag category, the b-tagged jet along with the highest p_{T} jet form the dijet pair.

Further categories are defined according to the transverse momentum of the W-boson, p_{T}^{V}. The $WH \to l\nu b\bar{b}$ analysis uses five p_{T}^{V} categories: $p_{\mathrm{T}}^{V} < 90$ GeV, $90 < p_{\mathrm{T}}^{V} < 120$ GeV, $120 < p_{\mathrm{T}}^{V} < 160$ GeV, $160 < p_{\mathrm{T}}^{V} < 200$ GeV, and $p_{\mathrm{T}}^{V} > 200$ GeV. Each of the p_{T}^{V} categories place different requirements on the angular separation of the dijet pair ΔR. The differing requirements between the categories reduce the W/Z + jets backgrounds. The maximum values reduces the $t\bar{t}$ production and the minimum value is removed in the highest p_{T}^{V} category to maximise the signal efficiency in the region with the lowest background contribution.

A requirement on the transverse mass of the W-boson m_{T}^{W} is imposed to reduce

the $t\bar{t}$ background contribution. Where m_{T}^{W} is defined as the transverse mass and is calculated from the transverse momentum, p_{T}^{ℓ} and azimuthal angle, ϕ^{ℓ} of the charged lepton and from the missing transverse momentum magnitude, $E_{\mathrm{T}}^{\mathrm{miss}}$ and its azimuthal angle, ϕ^{miss}: $m_{\mathrm{T}}^{W} = \sqrt{2p_{\mathrm{T}}^{\ell}E_{\mathrm{T}}^{\mathrm{miss}}(1-\cos(\phi^{\ell}-\phi^{\mathrm{miss}}))}$. For the reduction of the multijet background, requirements are imposed on the scalar sum of the $E_{\mathrm{T}}^{\mathrm{miss}}$ and transverse momentum of the two leading jets, H_{T}.

Variable	Selection				
p_{T}^{V}[GeV]	0–90	90–120	120–160	160–200	> 200
$\Delta R(\mathrm{jet}_1, \mathrm{jet}_2)$	0.7–3.4	0.7–3.0	0.7–2.3	0.7–1.8	< 1.4
m_{T}^{W}[GeV]	< 120				
H_{T}[GeV]	> 180		-		
$E_{\mathrm{T}}^{\mathrm{miss}}$[GeV]	-		> 20		> 50

Table 5.4: Table summarising the event selection for the $WH \to l\nu b\bar{b}$ analysis. Events are split into categories of p_{T}^{V} with different selections for events in the different p_{T}^{V} categories

Following the event selection, further energy corrections are applied to the b-jets. The first calibration applies a correction to jets based upon whether or not the b-jet contains a muon. The second calibration applies a p_{T}-dependent correction determined from a comparison to generator level p_{T} distributions. Further details regarding both these calibrations as well as studies into their impact on the $WH \to l\nu b\bar{b}$ analysis can be found in Section 6.1.

Figure 5.1 shows the distributions following the event selection in the 2-jet loose category, inclusive in p_{T}^{V} for the $E_{\mathrm{T}}^{\mathrm{miss}}$, m_{T}^{W}, dijet p_{T}, ΔR, and p_{T}^{V}. The background estimation methods are described in Chapter 7.

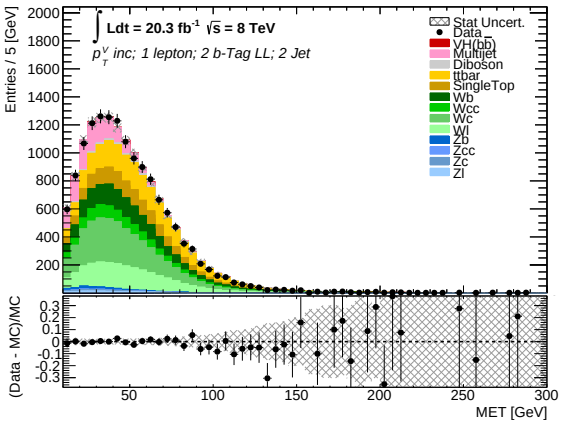

(a) $E_{\mathrm{T}}^{\mathrm{miss}}$

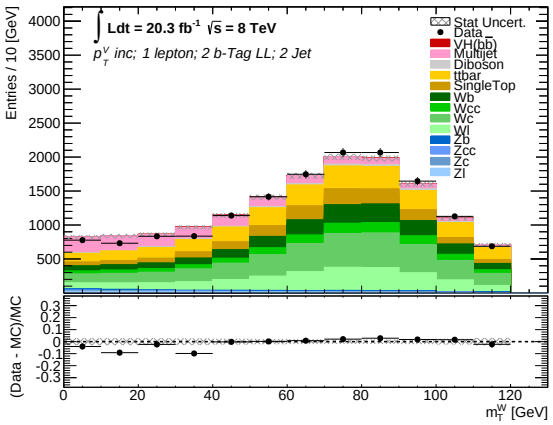

(b) m_{T}^{W}

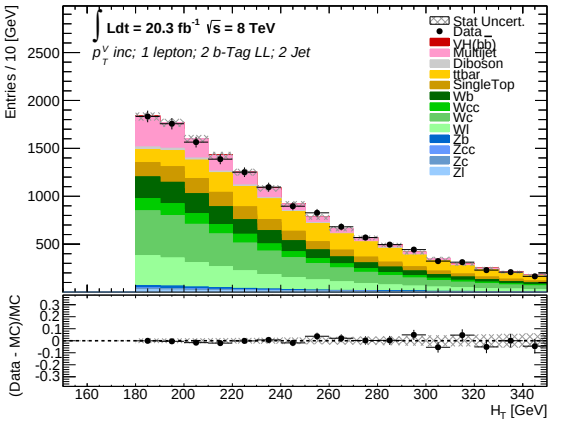

(c) H_{T}

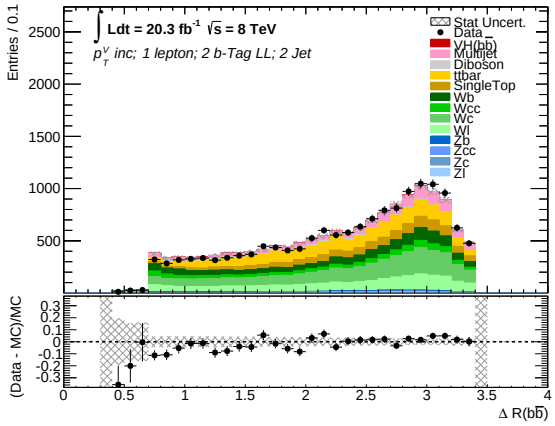

(d) ΔR

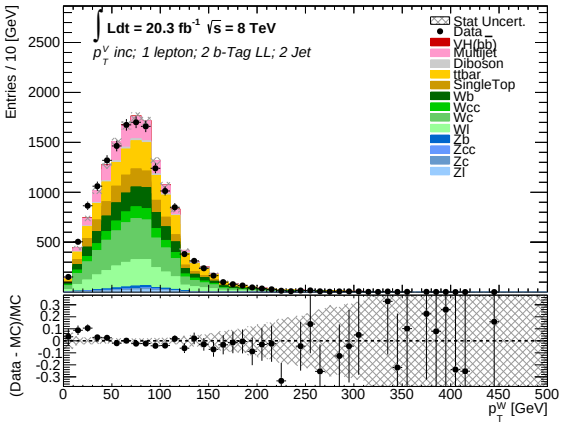

(e) p_{T}^{V}

Figure 5.1: Distributions for variables used in the event selection for the $WH \to l\nu b\bar{b}$ analysis. Distributions are for the 2-jet loose category, inclusive of p_{T}^{V}. The shaded grey band indicates the statistical uncertainties.

5.2.1. Signal Characterisation

The signal samples for the $WH \to l\nu b\bar{b}$ analysis where $\ell = e, \mu$ or τ are modelled using Monte Carlo simulation produced using the PYTHIA8 generator, configured with the AU2 tune and CTEQ6L1 PDF [27], interfaced to PHOTOS [96] for QED final state radiation and TAUOLA [97] for τ-decay simulation. The samples are generated for the Higgs boson mass range between $m_H = 110$ GeV and $m_H = 140$ GeV at 5 GeV intervals.

The main signal process arises from the production of $q\bar{q} \to (W \to \ell\nu)(H \to b\bar{b})$, however additional small amount of signal arise from the processes $q\bar{q} \to (Z \to \ell\ell)(H \to b\bar{b})$ and $gg \to (Z \to \ell\ell)(H \to b\bar{b})$. Table 5.5 summarises the contributions to the signal acceptance as well as the cross-section times branching fraction ($\sigma \times$ BR) which are taken from [98].

Process	$\sigma \times$ BR [fb]	Acceptance [%]
$q\bar{q} \to (W \to \ell\nu)(H \to b\bar{b})$	131.7	3.7
$q\bar{q} \to (Z \to \ell\ell)(H \to b\bar{b})$	14.9	1.1
$gg \to (Z \to \ell\ell)(H \to b\bar{b})$	1.3	0.7

Table 5.5: Summary of the cross-section times branching fraction and signal acceptance percentages after the event selection is applied to the contributing signal processes.

Chapter 6

Jet Calibration Studies

The most powerful discriminant in the $WH \to l\nu b\bar{b}$ system against background events which come from non-resonant decays is the dijet mass. Jets however are not the most precise objects available; it is therefore imperative to maximise the dijet mass resolution defined as the ratio of the width of the dijet mass distribution and the mean of the dijet mass distribution. This is done using a series of jet calibrations which are described in this chapter.

Section 4.6.4 describes in detail the jet energy scale (JES) and global sequential calibration (GSC) jet calibrations which are applied to all jets on ATLAS. For the $WH \to l\nu b\bar{b}$ analysis described in this thesis there are two additional jet calibrations which are only applied to b-jets. The first calibration corrects for jets which contain a muon inside and the second performs a calibration based upon the inverse of the response (defined as the ratio of reconstructed value and the generator value) of the jet p_{T}. These jet calibrations are examined and evaluated in Section 6.1. Section 6.2 describes an alternative to the jet p_{T} calibration and in Section 6.3 an additional jet calibration using a regression training is presented. All measurements use events passing a 2 jet, 2 b-tag, p_{T}^{V} inclusive and lepton inclusive event selection.

When evaluating the performance of jet calibrations, the values for the mean and width are taken after a fit to a function. There are a number of options available for the fitting function including a Gaussian, Novosibirsk and Bukin function [99]. The disadvantage of using a Gaussian is that the shapes of dijet mass distributions have long tails which are not well modelled in a Gaussian fit. The Novosibirsk function does not follow the peak of the dijet mass distribution. For these reasons all measurements of the mean and width of the dijet mass are taken after the application of a Bukin fit, with each fit being performed within ± 2 standard deviations of the mean. There are six parameters which are input into the Bukin function, which control the overall

normalisation, the position of the peak, the width which is taken as the full-width at half-maximum divided by 2.35, the asymmetry of the peak, and the size of the upper and lower tails.

6.1. Current b-Jet Calibration Methods

As described in Section 4.6.4 there are two jet calibration methods which are applied to all jets inclusive of flavour; JES and GSC. When applied in the $WH \to l\nu b\bar{b}$ analysis, the JES calibration has the effect of increasing the mean of the dijet mass at the expense of the dijet width. The addition of the GSC has the effect of improving the width of the dijet mass reconstruction, whilst the mean remains constant. Figure 6.1 shows the impact of applying the JES and GSC to the dijet mass distribution and also for the dijet response; defined as the ratio of the reconstructed value to the generator level value. The generator level jets are reconstructed using the anti-k_T algorithm with a radius of $R = 0.4$. To eliminate double counting of particle content within the jet and those arriving from the hard interaction, muons and neutrinos from W or Z decays are excluded from generator level reconstruction. Table 6.1 summarises the effects of applying the two initial jet calibrations, in terms of mean, width, resolution of the dijet pair and also the dijet response. A 7% improvement in the dijet width is observed with the GSC with an overall improvement in the resolution of 5%. In an ideal scenario, the reconstructed dijet pair mass shape would match with that of the generator dijet pair. With the addition of the GSC to improve the jet resolution there is a 1.5% decrease in the response.

Calibration	Mean [GeV]	Width [GeV]	Resolution	Response
EM	76.4 ± 1.4	13.3 ± 0.1	0.174 ± 0.013	0.65 ± 0.01
EM+JES	118.3 ± 1.8	15.2 ± 1.3	0.132 ± 0.011	1.00 ± 0.01
EM+JES+GSC	116.6 ± 1.7	14.1 ± 1.2	0.121 ± 0.011	0.99 ± 0.01

Table 6.1: The effect of applying the jet energy scale and global sequential calibrations to the electromagnetic (EM) jet as part of the $WH \to l\nu b\bar{b}$ analysis in terms of mean, width and resolution of the dijet pair.

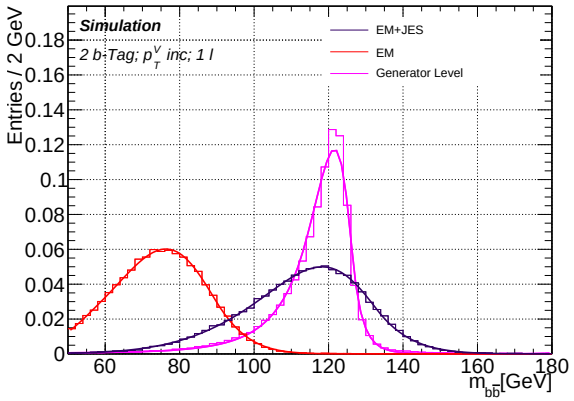

(a) JES Calibration dijet mass

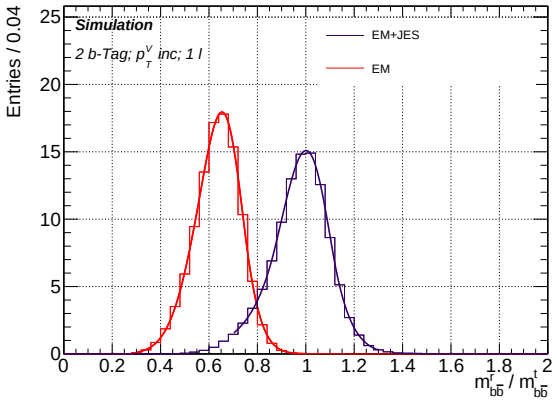

(b) JES dijet response

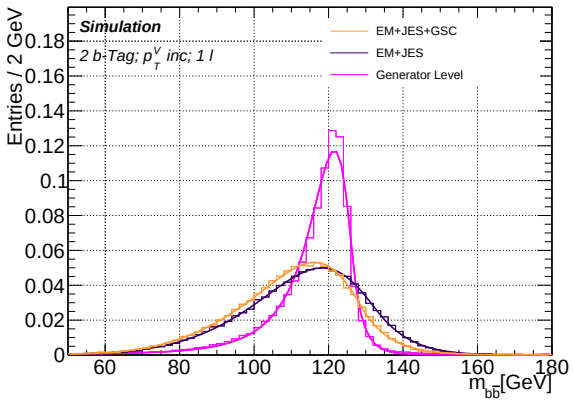

(c) GSC dijet mass

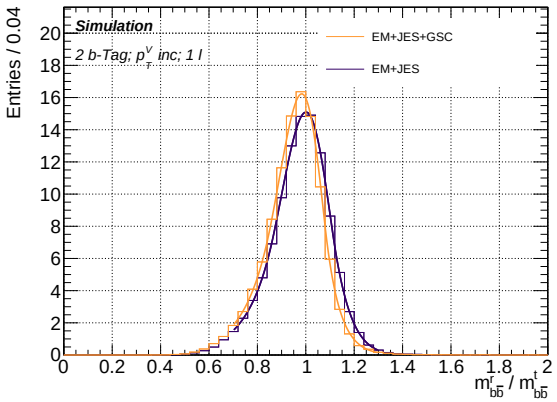

(d) GSC dijet response

Figure 6.1: Shape comparisons between the application of no calibration and the jet-energy scale calibration for the dijet mass (a) and the dijet response (b) as well as comparisons between jet-energy scale and the application of the global-sequential calibration to for the dijet mass (c) and the dijet response (d).

6.1.1. Muon-in-Jet Calibration

The first of the analysis specific calibrations applied solely to b-jets is the 'muon-in-jet' (denoted 'Mu') correction. Muons are minimum ionising particles meaning that their interaction with the ATLAS calorimeters is minimal. To take this into account the 4-vector of the jet needs to be calibrated for their presence. The muon 4-vector is added to the 4-vector of the jet after energy deposited in the calorimeter by the muon has been removed. To meet the requirements for a muon, the candidates must pass the criteria outlined in Table 6.2.

Criteria	Value
Type	Tight `MuID` & MCP hits requirements
p_{T} [GeV]	> 4
$\Delta R(\mu, \mathrm{jet})$	< 0.4

Table 6.2: The requirements for the muon candiates in order to be used in the muon-in-jet calibration.

The effect of applying this calibration after the application of GSC is shown in Figure 6.2 for the dijet mass distribution as well as the dijet response. The distributions are for all jets. Table 6.3 shows numerically the improvements gained with the muon-in-jet calibration compared to GSC. The width and resolution both improve by 11%, while the changes in mean mass and the dijet response are negligable.

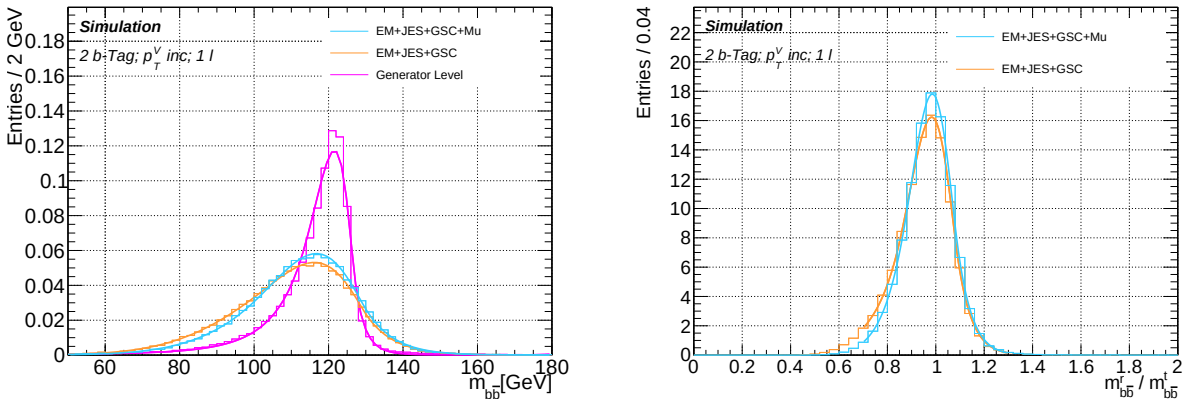

(a) dijet $m_{b\bar{b}}$ **(b)** dijet response

Figure 6.2: Shape comparisons between the GSC and muon-in-jet calibrations to the generator level for the dijet mass distributions and the response.

Calibration	Mean [GeV]	Width [GeV]	Resolution	Response
EM+JES+GSC	116.6 ± 1.7	14.1 ± 1.2	0.121 ± 0.011	0.99 ± 0.01
EM+JES+GSC+Mu	116.9 ± 1.6	12.7 ± 1.2	0.108 ± 0.010	0.99 ± 0.01

Table 6.3: The effect of applying a calibration to correct for cases of a muon within a jet. An 11% improvement in the width and resolution is observed compared to the GSC.

6.1.2. Jet p_{T} Calibration

After the muon-in-jet calibration, the jet energies have different scales (mean of the distribution) for different jet p_{T} ranges. This is due to mis-modelling of the jet energy in the calorimeter which is most prominant at low energies, where the calorimeters are least efficient. The final calibration (denoted $p_{\mathrm{T}}^{\mathrm{Reco}}$) corrects the reconstructed jet scale to unity using the generator information through the factor q, defined:

$$q = \frac{p_{\mathrm{T}}^{\mathrm{r}}}{p_{\mathrm{T}}^{\mathrm{t}}}, \tag{6.1}$$

where $p_{\mathrm{T}}^{\mathrm{r}}$ is the reconstructed jet p_{T} after the muon-in-jet calibration, and $p_{\mathrm{T}}^{\mathrm{t}}$ is the generator level p_{T}. The correction factor (q) applied to each jet p_{T} bin is shown in Figure 6.3 which has been extracted using a $ZH \rightarrow llb\bar{b}$ sample at $m_H = 125$ GeV. For low p_{T} jets ($20 < p_{\mathrm{T}} < 30$ GeV) a 18% correction is required whereas for high p_{T} jets ($p_{\mathrm{T}} > 100$ GeV) only a 2-3% correction is required. The correction factor is applied by scaling both the jet energy and p_{T} terms of the 4-vector, this in effect scales the jet mass.

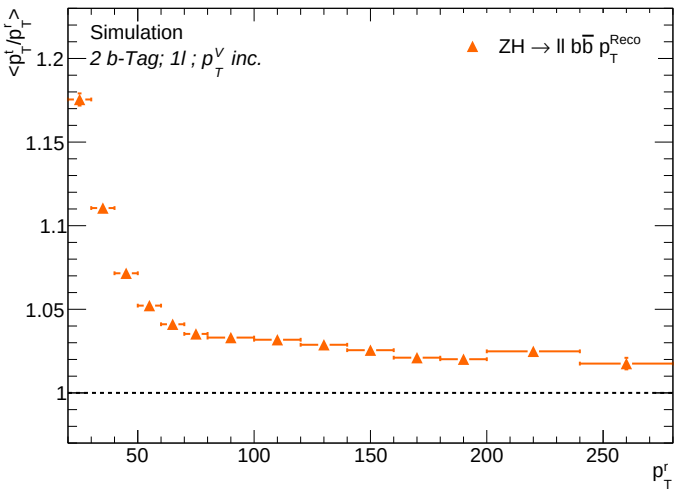

Figure 6.3: The correction factor applied to each jet p_{T} bin derived using a $ZH \rightarrow llb\bar{b}$ sample at $m_H = 125$ GeV as part of the jet p_{T} calibration.

The effect of having the $p_{\mathrm{T}}^{\mathrm{Reco}}$ calibration in addition to the previous jet calibrations is shown in Figure 6.4 for the dijet mass distribution and for the dijet response, comparing the $p_{\mathrm{T}}^{\mathrm{Reco}}$ (pT) calibration to the previous muon-in-jet correction and also to the generator level. Numerical comparisons of the improvements gained against the muon-in-jet

correction are shown in Table 6.4. The mean of the dijet mass distribution increases from 116.9 GeV to 122.9 GeV, and the width narrows by $\sim$2.5%. These changes have the overall effect of improving the resolution by 8%. The application of the $p_{\mathrm{T}}^{\mathrm{Reco}}$ calibration over-corrects the dijet response by 3%. An over correction is observed with respect to the generator level due to all jets being treated with the same regardless of particle content within the jet cone.

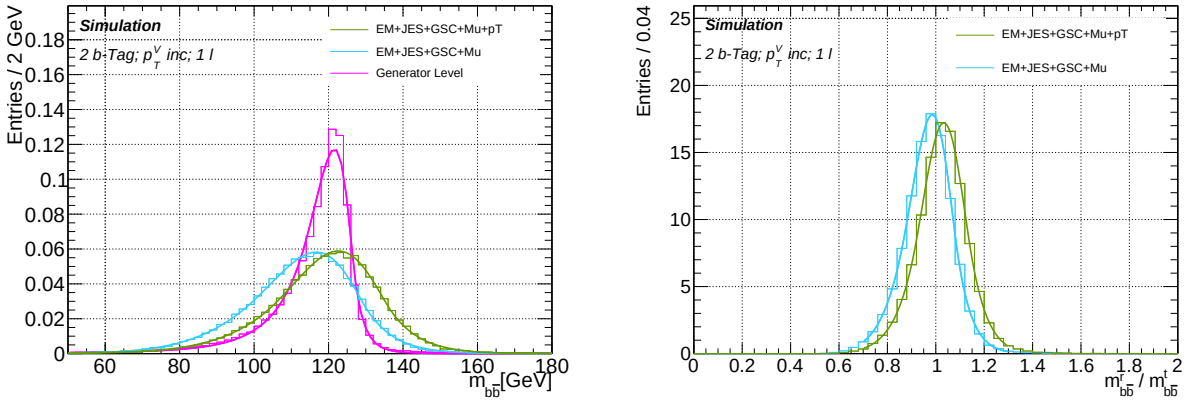

(a) dijet $m_{b\bar{b}}$ **(b)** dijet response

Figure 6.4: Shape comparisons after the muon-in-jet calibration and jet p_{T} calibration compared to the generator level for the dijet mass distribution and the dijet response. The mean of the dijet mass has been increased and the width has narrowed after the applicaltion of the jet p_{T} calibration.

Calibration	Mean [GeV]	Width [GeV]	Resolution	Response
EM+JES+GSC+Mu	116.9 $\pm$ 1.6	12.7 $\pm$ 1.2	0.108 $\pm$ 0.010	0.99 $\pm$ 0.01
EM+JES+GSC+Mu+pT	122.9 $\pm$ 1.7	12.4 $\pm$ 1.2	0.101 $\pm$ 0.010	1.03 $\pm$ 0.01

Table 6.4: Numerical comparison between jets after the muon-in-jet calibration and the jet p_{T} calibration. An 8% improvement is gained with the jet p_{T} calibration in addition to the improvements gained after using the muon-in-jet calibration.

6.1.3. Current Jet Calibrations Summary

There are currently four jet calibrations used as part of the $WH \to l\nu b\bar{b}$ analysis on ATLAS; two (JES and GSC) which are applied to all jets inclusive of flavour and a further two which are specific to the $WH \to l\nu b\bar{b}$ analysis (muon-in-jet and $p_{\mathrm{T}}^{\mathrm{Reco}}$) to

further calibrate jets which contain a muon and finally calibrate the overall p_{T} scale.

Figure 6.5 summarises the effect of these calibrations on the dijet mass in the 1D plane (a), dijet response (c), a 2D representation of how the mean (response) and width (width) evolve with each additional jet calibration in (c)((d)). A numerical summary of the impact of each jet calibration is shown in Table 6.5 along with the generator level, included for comparison.

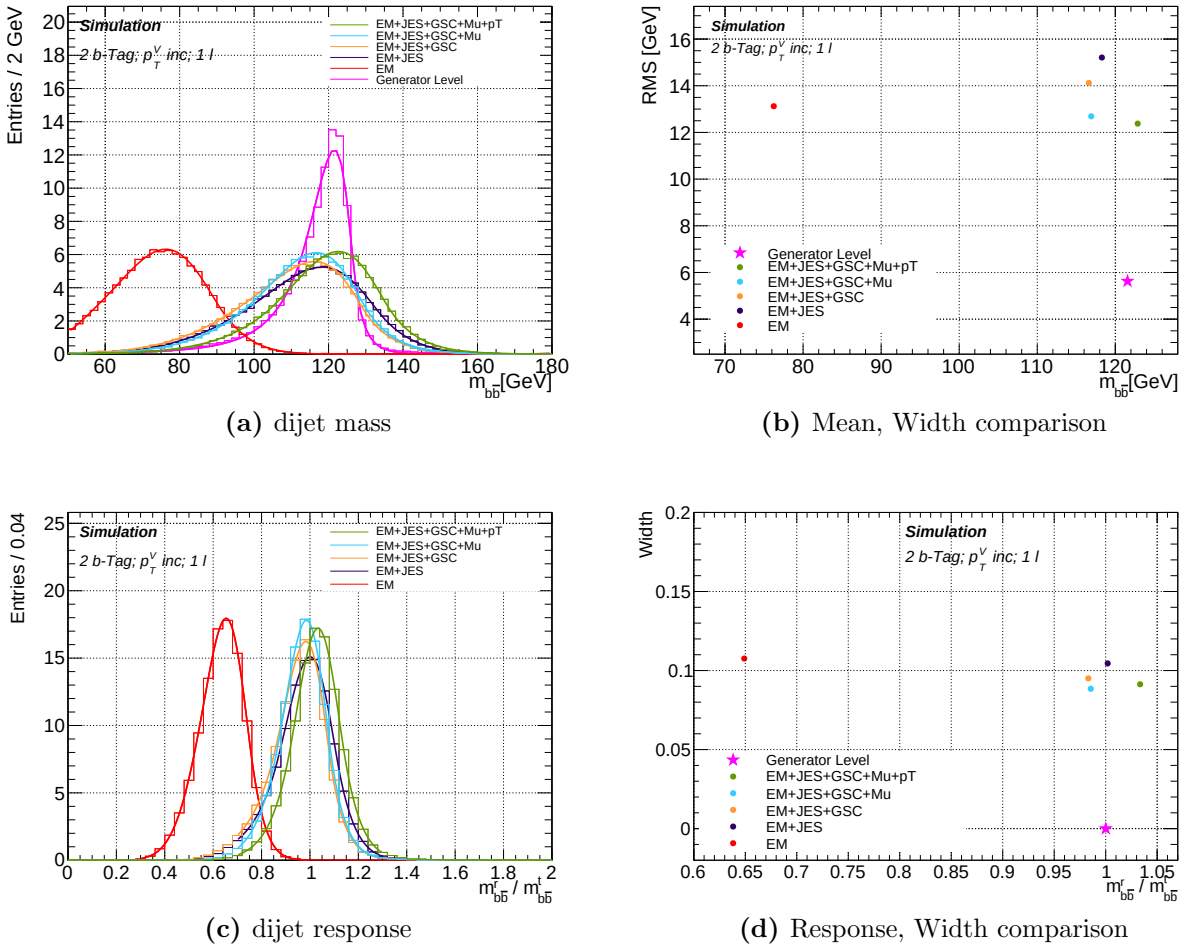

(a) dijet mass

(b) Mean, Width comparison

(c) dijet response

(d) Response, Width comparison

Figure 6.5: Summary of the jet calibrations currently used as part of the $WH \to l\nu b\bar{b}$ analysis on ATLAS. 1D plots for the dijet mass (a) and dijet response (c) and a 2D representation of the changes in mean and width for the dijet mass (b) and the response (d).

With the addition of each of the jet calibrations, it is shown that each of the corrections improve the mass or resolution or both. With an EM+JES dijet pair, there is a 2.5 GeV underestimation in the mean of the dijet mass. This increases to a 3 GeV over-

Correction	Mean [GeV]	RMS [GeV]	Resolution	Response
EM	76.4 ± 1.4	13.3 ± 0.1	0.174 ± 0.013	0.65 ± 0.01
EM+JES	118.3 ± 1.8	15.2 ± 1.3	0.132 ± 0.011	1.00 ± 0.01
EM+JES+GSC	116.6 ± 1.7	14.1 ± 1.2	0.121 ± 0.011	0.99 ± 0.01
EM+JES+GSC+Mu	116.9 ± 1.6	12.7 ± 1.2	0.108 ± 0.010	0.99 ± 0.01
EM+JES+GSC+Mu+pT	122.9 ± 1.7	12.4 ± 1.2	0.100 ± 0.010	1.03 ± 0.01
Generator Level	121.7 ± 1.3	5.0 ± 0.952	0.043 ± 0.008	1.00 ± 0.00

Table 6.5: Numerical summary of the changes to the mean, width, resolution and response after each of the jet calibrations are applied. The generator level is also included for comparison.

estimation with the $p_{\mathrm{T}}^{\mathrm{Reco}}$ calibration. Between the EM+JES and the $p_{\mathrm{T}}^{\mathrm{Reco}}$ jets there is an 18% improvement in the width of the dijet pair and a 22% improvement in the resolution. There is however a degradation between the response of an EM+JES dijet pair and a dijet pair after the $p_{\mathrm{T}}^{\mathrm{Reco}}$ calibration, by 3%.

A useful statistical tool which allows the measurement of the impact of each jet calibration as part of the $WH \rightarrow l\nu b\bar{b}$ analysis is the bin-by-bin sensitivity which can be caluclated using Equation 6.2 as the signal, s divided by the square root of the background, b summed in quadrature for each histogram bin.:

$$\text{sensitivity} = \sqrt{\sum_{\text{bins}} \left(\frac{\mathrm{s}}{\sqrt{\mathrm{b}}} \right)^2} \tag{6.2}$$

The bin-by-bin sensitivity for the current jet calibrations are summarised in Table 6.6, using 50 bins in the range $0 < m_{b\bar{b}} < 500$ GeV. For each additional jet calibration, a non-negligible improvement is found with a 6% improvement between EM+JES and the final $p_{\mathrm{T}}^{\mathrm{Reco}}$ calibrations. This is due to the greater signal and background separation acheived from the improvements made to the jet resolution.

Calibration	Sensitivity
EM	0.917
EM+JES	0.974
EM+JES+GSC	0.985
EM+JES+GSC+Mu	1.035
EM+JES+GSC+Mu+pT	1.039

Table 6.6: The bin-by-bin sensitivity values after each jet calibration when applied to the $WH \to l\nu b\bar{b}$ analysis, using 50 bins in the range $0 < m_{b\bar{b}} < 500$ GeV.

6.2. Re-derived Jet p_{T} Calibration

6.2.1. Jet p_{T} Calibration Derived with a $WH \to l\nu b\bar{b}$ Sample

For the published $WH \to l\nu b\bar{b}$ analysis [48] that is the basis for this thesis, the correction factors used as part of the $p_{\mathrm{T}}^{\mathrm{Reco}}$ calibration were derived using a $ZH \to llb\bar{b}$ sample and then were applied for use as part of the $WH \to l\nu b\bar{b}$ analysis. A potential improvement can be gained by instead, deriving the correction factors using a $WH \to l\nu b\bar{b}$ sample at $m_H = 125$ GeV and applying these to the jets as part of the $p_{\mathrm{T}}^{\mathrm{Reco}}$ calibration, since this gives a more accurate representation of the jets in the $WH \to l\nu b\bar{b}$ analysis. The correction factors derived using the $WH \to l\nu b\bar{b}$ sample are shown in Figure 6.6, where they are compared to those derived from the $ZH \to llb\bar{b}$ sample.

For high p_{T} jets ($p_{\mathrm{T}} > 100$ GeV) the correction factors derived using the $WH \to l\nu b\bar{b}$ sample are much the same as those derived using the $ZH \to llb\bar{b}$ sample where they require a $\sim$3% correction. For low p_{T} jets ($20 < p_{\mathrm{T}} < 30$ GeV) the correction factor has decreased to $\sim$13%. The effects of the newly derived $p_{\mathrm{T}}^{\mathrm{Reco}}$ using a $WH \to l\nu b\bar{b}$ sample (denoted pT2) are summarised in Figure 6.7 with comparisons made to the $ZH \to llb\bar{b}$ derived sample and also to the generator level. Numerical comparisons are shown in Table 6.7 for the mean mass of the dijet distribution, the width, resolution and also the response. The changes between the mass and the width are negligible but lead to a 1% decrease in the resolution. A 1% improvement in the response is observed. The minimal changes observed can be explained due to minimal difference between events used for deriving the correction factors.

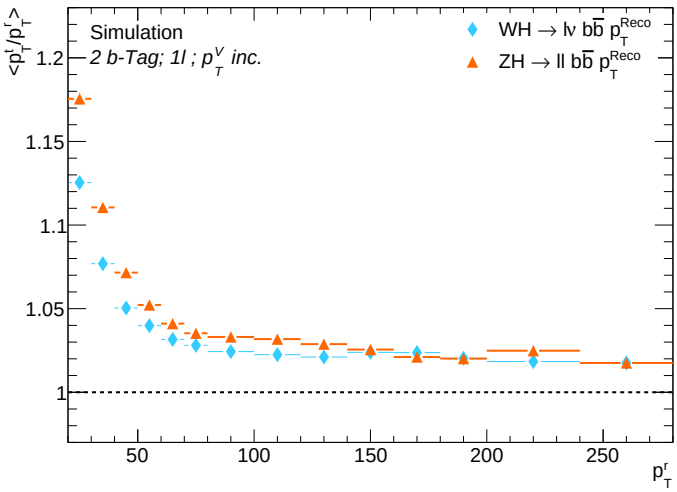

Figure 6.6: A comparison between the correction factors derived using a $ZH \to llb\bar{b}$ sample and corrections factors derived using a $WH \to l\nu b\bar{b}$ sample as part of the $p_{\mathrm{T}}^{\mathrm{Reco}}$ jet calibration.

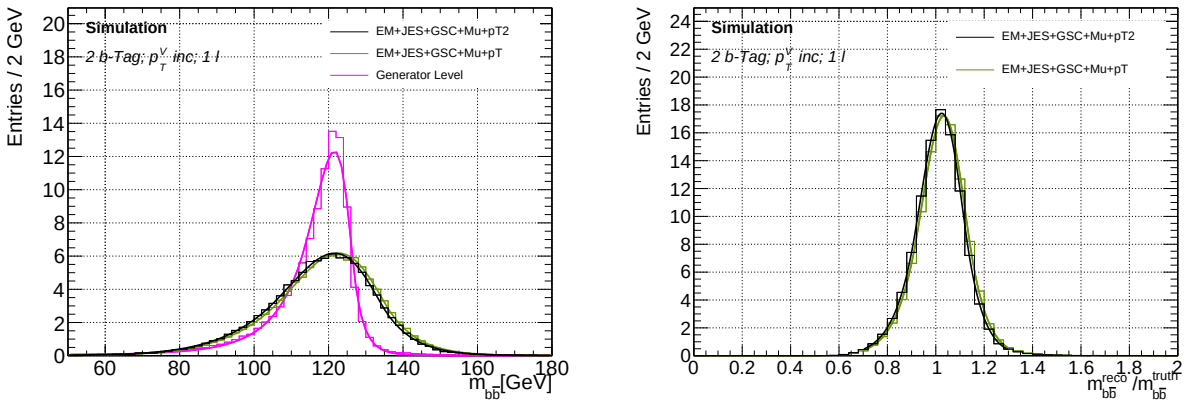

(a) dijet $m_{b\bar{b}}$ **(b)** dijet response

Figure 6.7: Shape comparisons between $p_{\mathrm{T}}^{\mathrm{Reco}}$ calibration derived using a $WH \to l\nu b\bar{b}$ sample (pT2) and a $ZH \to llb\bar{b}$ sample (PT) and the generator level, for the dijet mass distribution and the dijet response.

6.2.2. Muon Dependent Jet p_{T} Calibration

Within the b-jet cone, the b-quark decays to a c-quark and a W-boson. The c-quark subsequently decays to a d-quark and a second W-boson. The W-bosons can decay leptonically to a charged lepton and neutrino, or hadronically to two quarks. Due to lepton universality, there is no preference to the flavour of the leptons. Studies have

Correction	Mean [GeV]	RMS [GeV]	Resolution	Response
EM+JES+GSC+Mu+Pt	122.9 ± 1.7	12.4 ± 1.17	0.101 ± 0.010	1.03 ± 0.01
EM+JES+GSC+Mu+Pt2	121.9 ± 1.7	12.4 ± 1.17	0.102 ± 0.010	1.02 ± 0.01
Generator Level	121.7 ± 1.3	5.0 ± 0.95	0.043 ± 0.008	1.00 ± 0.00

Table 6.7: Comparisons between the mean, width, resolution and response between correction factors derived using a $WH \to l\nu b\bar{b}$ sample (pT2) and a $ZH \to llb\bar{b}$ sample (pT) as part of the $p_{\mathrm{T}}^{\mathrm{Reco}}$ calibration.

shown that there is a 32% chance that a W-boson will decay via a lepton-neutrino pair, which means, in $\sim$10.7% of cases the charged lepton is a muon. Another possibility of W-boson decay is via a τ-lepton and neutrino. The τ-lepton decays to a muon or electron and two neutrinos in 17.8% of cases. Overall, in $\sim$12% ($\sim$12%) of b-jets a muon (electron) and neutrino is present [5].

By first understanding the differences in event reconstruction for events with a muon within the b-jet and those events without a muon within the b-jet, a jet p_{T} calibration can be derived, depending whether or not a muon exists within the b-jet cone. An illustration of the effect of the current jet calibrations to the dijet mass and the dijet response on b-jets with zero, one or two muons inside is shown in Figure 6.8 where the area of each of the samples has been normalised to unity for a shape comparison. The values for the dijet mean, width, resolution and the dijet response are compared in Table 6.8 Both the distributions and the values are given after the $p_{\mathrm{T}}^{\mathrm{Reco}}$ calibration derived using $ZH \to llb\bar{b}$ events.

Number of Muons	Mean [GeV]	Width [GeV]	Resolution	Response
Zero	123.6 ± 1.8	12.1 ± 1.26	0.098 ± 0.010	1.04 ± 0.01
One	119.1 ± 3.4	13.0 ± 2.43	0.110 ± 0.018	1.01 ± 0.03
Two	116.9 ± 14	13.7 ± 9.84	0.117 ± 0.085	0.98 ± 0.10
Inclusive	122.9 ± 1.7	12.4 ± 1.17	0.101 ± 0.010	1.03 ± 0.01

Table 6.8: Comparisons between jets with zero, one or two muons to the number of muons in jet inclusive category of the dijet mean, width, resolution and the dijet response. The values are after the jet p_{T} calibration derived using $ZH \to llb\bar{b}$ events.

As the number of muons within the jet cone increases, the reconstructed mass decreases and the width and the resolution both increase. The response also decreases with the number of muons inside the jet, due to the presence of neutrinos. For jets with two

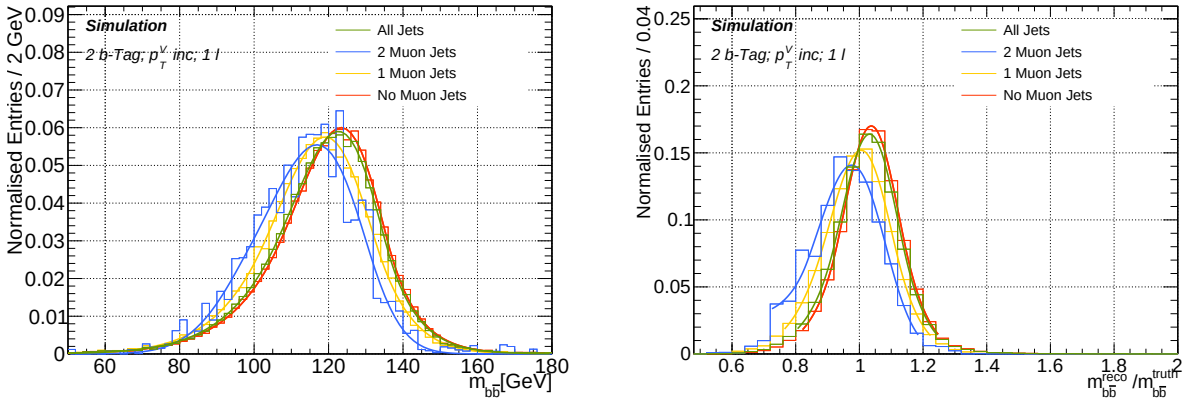

(a) dijet $m_{b\bar{b}}$ **(b)** dijet response

Figure 6.8: Comparisons between jets with zero, one or two muons against inclusive of number of muons in jet for the dijet mass and dijet response distributions for jets after the current jet p_{T} calibration. The area of each of the distributions is normalised to unity.

muons inside, the statistics are low, leading to the large uncertainties as only $\sim 1\%$ of jets contain 2 muons. The inclusive sample lies in between jets with zero muons and jets with one muon, which is expected from the statistical composition of each of the samples.

If a new $p_{\mathrm{T}}^{\mathrm{Reco}}$ calibration was derived so that different correction factors are applied depending whether the jet contains a muon or not, it would lead to a more accurate calibration of the jets. Figure 6.9 shows a comparison of the correction factors required to calibrate the jets based upon whether the jets contain a muon or not. For jets with a muon inside, they require a larger correction factor than those with no muon; for jets with low p_{T} ($20 < p_{\mathrm{T}} < 30$ GeV) the difference is $\sim 1\%$, whereas for high p_{T} jets ($p_{\mathrm{T}} > 100$ GeV), the difference in correction factors for jets with a muon compared to jets without increases to $\sim 5\%$.

By replacing the $p_{\mathrm{T}}^{\mathrm{Reco}}$ calibration currently used as part of the $WH \to l\nu b\bar{b}$ analysis with one derived separately for jets with muons and jets without muons, a more accurate jet reconstruction is obtained. The effect of applying the muon-in-jet dependent $p_{\mathrm{T}}^{\mathrm{Reco}}$ calibration ($p_{\mathrm{T}}^{\mu,\mathrm{Reco}}$) for each of the muon-in-jet categories is shown in Figure 6.10 for the dijet mass and the dijet response, All distributions are normalised with an area of unity. A numerical comparison between the muon-in-jet categories and inclusive of all jets is made in Table 6.9.

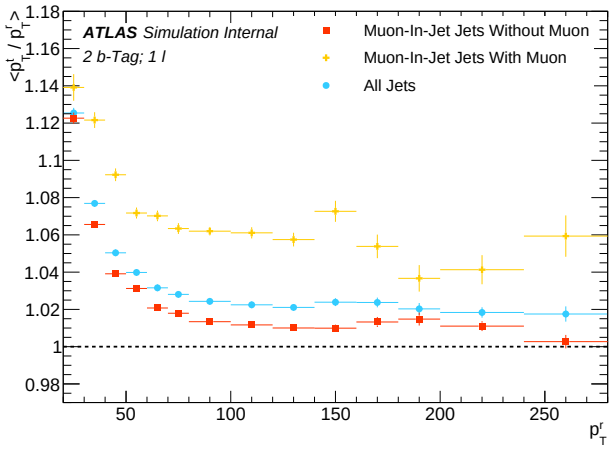

Figure 6.9: Comparison of the correction factors required for each jet p_{T} bin for jets with muons, jets without muons and all jets.

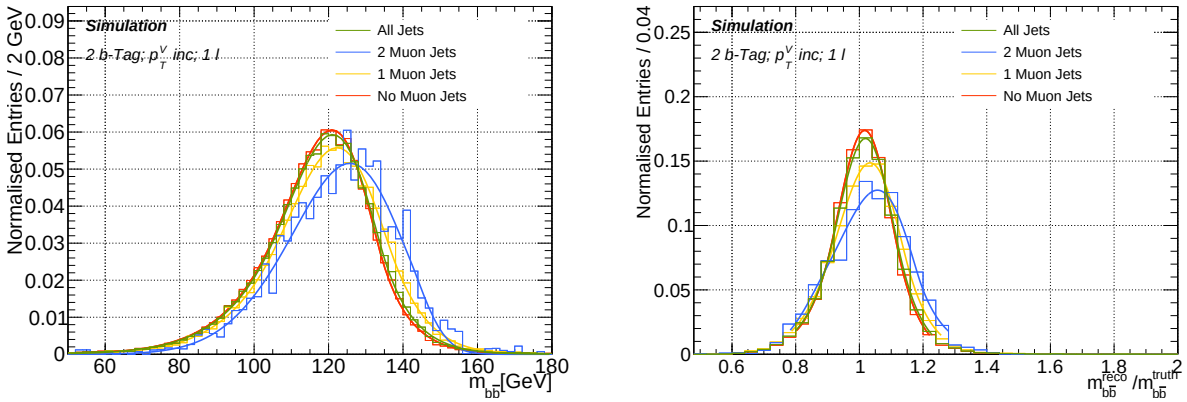

(a) dijet $m_{b\bar{b}}$ **(b)** dijet response

Figure 6.10: Comparisons of the shapes of the dijet mass and dijet response distributions for jets with zero, one or two muons compared to the inclusive jet sample after a number of muons-in-jet dependent jet p_{T} calibration.

The effect of the $p_{\mathrm{T}}^{\mu,\mathrm{Reco}}$ calibration is: for jets with no muon, the nominal calibration was too high and for jets with at least one muon, the correction factors were too low. This is illustrated in Figure 6.9. The one and two muons-in-jet categories were merged for the application of the scale factors due to the low number of events containing 2 muons. Inclusive of number of muons-in-jet, the mass reconstruction is better modelled, and slight improvements in the width and resolution are also observed. There is also a 1% improvement in the dijet response. These improvements lead to a conclusion that using a $p_{\mathrm{T}}^{\mu,\mathrm{Reco}}$ calibration leads to an improved jet reconstruction.

Number of Muons	Mean [GeV]	Width [GeV]	Resolution	Response
Zero	121.2 ± 1.8	12.0 ± 1.24	0.099 ± 0.010	1.02 ± 0.01
One	122.4 ± 3.5	13.3 ± 2.50	0.109 ± 0.018	1.03 ± 0.03
Two	125.8 ± 14.7	14.9 ± 10.4	0.119 ± 0.084	1.06 ± 0.11
Inclusive	121.3 ± 1.6	12.3 ± 1.16	0.101 ± 0.010	1.02 ± 0.01
Generator Level	121.7 ± 1.3	5.0 ± 0.95	0.043 ± 0.008	1.00 ± 0.00

Table 6.9: Replacing the current jet p_{T} calibration with one using different correction factors based upon whether the jet contains a muon or not. Comparing the mean, width, resolution and dijet response for jets with zero, one or two muons.

Figure 6.11 shows a comparison between the $p_{\mathrm{T}}^{\mu,\mathrm{Reco}}$ calibration and the nominal $p_{\mathrm{T}}^{\mathrm{Reco}}$ used as part of the $WH \to l\nu b\bar{b}$ analysis for the dijet mass and dijet response distributions. From the shapes, the peak of the $p_{\mathrm{T}}^{\mu,\mathrm{Reco}}$is higher due to the 0.5% improvement in the width. Both calibrations use the same number of events. A visual representation of the effect of the muon-in-jet dependent $p_{\mathrm{T}}^{\mathrm{Reco}}$ in terms of mean mass and width of the dijet mass distribution and the response and width of the response is shown in Figure 6.12, a slight improvement is observed.

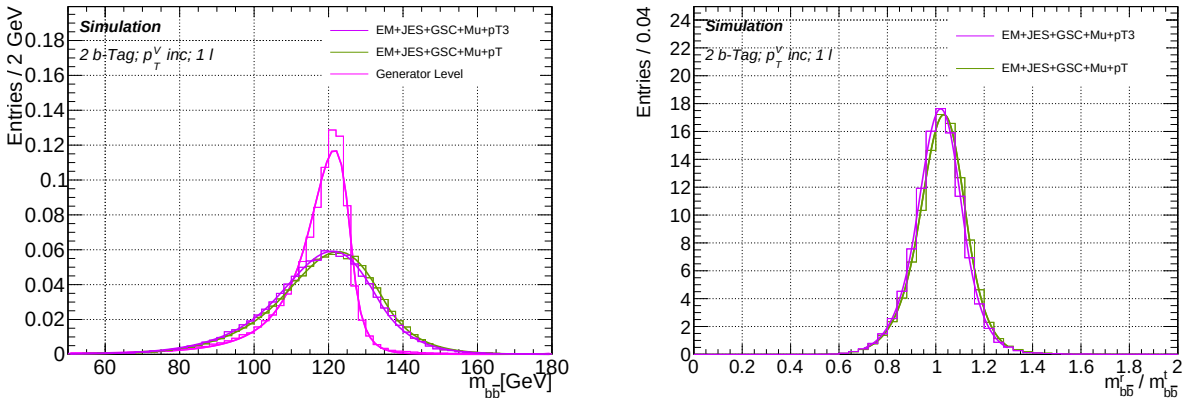

(a) dijet $m_{b\bar{b}}$ **(b)** dijet response

Figure 6.11: Shape comparison between a $p_{\mathrm{T}}^{\mu,\mathrm{Reco}}$ calibration, the jet p_{T} calibration used as part of the $WH \to l\nu b\bar{b}$ analysis and the generator value for the dijet mass analysis and the dijet response.

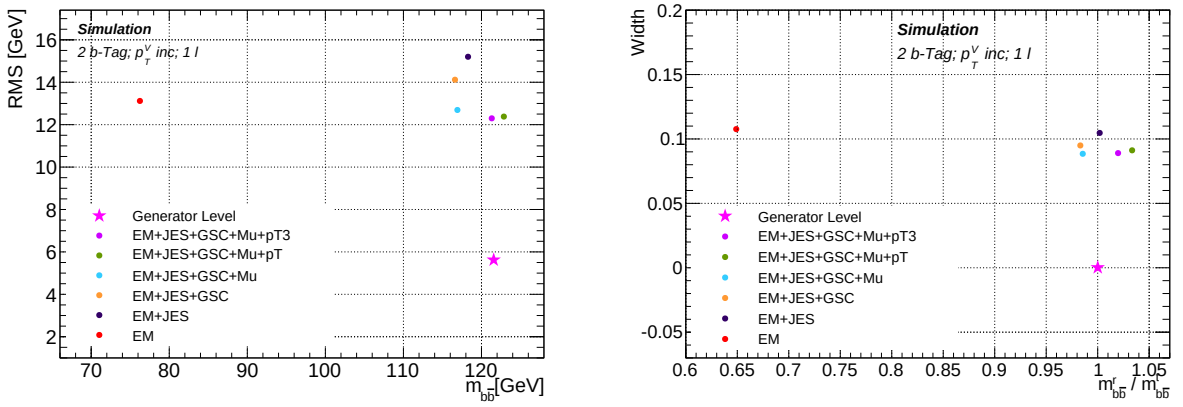

(a) dijet $m_{b\bar{b}}$ **(b)** dijet response

Figure 6.12: Replacing the jet p_{T} calibration with one using different correction factors depending if a muon lies within the jet, showing the effect on the mean and width of the dijet mass distribution and the response and width in the dijet response distribution.

6.2.3. Jet p_{T} Calibration Re-derivation Summary

A re-derivation of the jet p_{T} calibration was carried out using a $WH \to l\nu b\bar{b}$ sample with $m_H = 125$ GeV instead of using a $ZH \to llb\bar{b}$ sample which had been used as part of the current jet calibrations. This achieved a dijet mass reconstruction which matched closer to the generator level than the nominal $p_{\mathrm{T}}^{\mathrm{Reco}}$ calibration did. There was no change in the width or resolution and a 1% improvement was obtained in the dijet response. It was observed that depending upon the number of muons within the jet cone, the mass, width, resolution and response had different values due to the presence of a neutrino when a muon is inside the jet. By having different correction factors for jets with a muon inside compared to jets with no muon present, instead of treating all jets the same, gave a 0.5% improvement to the width and a 1.5% improvement to the response on using the $p_{\mathrm{T}}^{\mathrm{Reco}}$ derived using a $ZH \to llb\bar{b}$ sample. The results comparing the initial $ZH \to llb\bar{b}$ derived calibration to the $WH \to l\nu b\bar{b}$ derived calibration and the $p_{\mathrm{T}}^{\mu,\mathrm{Reco}}$ calibration are shown in Table 6.10.

Calibration	Mean	Width	Resolution	Response
EM+JES+GSC+Mu+Pt	122.9 ± 1.7	12.4 ± 1.17	0.101 ± 0.010	1.03 ± 0.01
EM+JES+GSC+Mu+Pt2	121.9 ± 1.7	12.4 ± 1.17	0.102 ± 0.010	1.03 ± 0.01
EM+JES+GSC+Mu+Pt3	121.3 ± 1.6	12.3 ± 1.17	0.101 ± 0.010	1.02 ± 0.01
Generator Level	121.7 ± 1.3	5.02 ± 0.95	0.043 ± 0.008	1.00 ± 0.00

Table 6.10: Summary of rederiving the jet p_{T} calibration using a $WH \to l\nu b\bar{b}$ sample and also using different correction factors based upon whether or not the jet contains a muon or not. Comparisons are made to the current jet p_{T} calibration and also to the generator level.

As a measure of the updated jet calibrations performance as part of the $WH \to l\nu b\bar{b}$ analysis, the sensitivities have been calculated for both of the re-derivations. The results are shown in Table 6.11 where comparisons are made to the current $p_{\mathrm{T}}^{\mathrm{Reco}}$ calibration. Between the current $p_{\mathrm{T}}^{\mathrm{Reco}}$ and the $p_{\mathrm{T}}^{\mathrm{Reco}}$ derived using a $WH \to l\nu b\bar{b}$ sample, there is negligible change to the sensitivity, however, when treating jets with muons inside differently to those jets with no muon inside a slight improvement is obtained in the 2 jet, 2 b-tag, p_{T}^{V} inclusive, lepton inclusive region. For this reason, the muon-in-jet dependent $p_{\mathrm{T}}^{\mathrm{Reco}}$ calibration will be used a starting point for applying a calibration using a regression technique, described in section 6.3

Calibration	Sensitivity
EM+JES+GSC+Mu+pT	1.039
EM+JES+GSC+Mu+pT2	1.039
EM+JES+GSC+Mu+pT3	1.042

Table 6.11: Compaing the bin-by-bin sensitivity for the re-derivations of the jet p_{T} calibrations for the 2 Jet, 2 b-tag, p_{T}^{V} inclusive, lepton inclusive category. Using 50 bins in the range $0 < m_{b\bar{b}} < 500$ GeV.

6.3. Regression Training Calibration

Applying a muon-in-jet dependent $p_{\mathrm{T}}^{\mathrm{Reco}}$ instead of the nominal $p_{\mathrm{T}}^{\mathrm{Reco}}$; the dijet mass reconstruction is improved to match much closer to the generator level distribution. The generator level however, has a much narrower dijet width and improved resolution. The reconstruction of the major backgrounds to the $WH \to l\nu b\bar{b}$ search align much closer to the background generator level distribution than the signal reconstruction does. Figure 6.13 shows a comparison between a $WH \to l\nu b\bar{b}$ signal sample at $m_{\mathrm{H}} = 125$ GeV reconstructed after $p_{\mathrm{T}}^{\mu,\mathrm{Reco}}$ and generator level in (a) and a comparison between the reconstructed and generator level for a $t\bar{t}$ sample, one of the major backgrounds to the $WH \to l\nu b\bar{b}$ analysis is shown in (b).

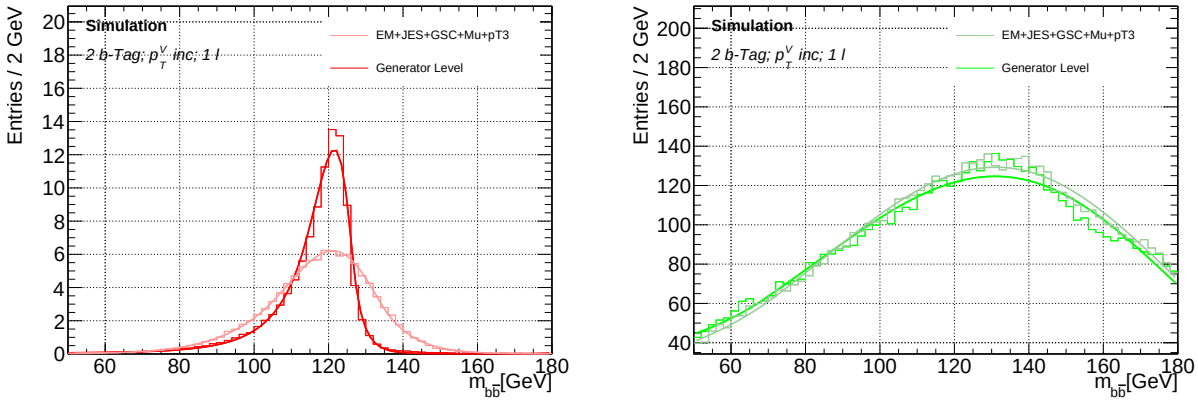

(a) $WH \to l\nu b\bar{b}$ **(b)** $t\bar{t}$

Figure 6.13: Comparison between generator level and reconstructed events for $WH \to l\nu b\bar{b}$ and $t\bar{t}$ processes. For the $t\bar{t}$ process, the generator level and reconstructed match closer than for the $WH \to l\nu b\bar{b}$ sample.

6.3.1. Training the Regression

The current jet calibrations used identify causes for the poor jet reconstruction, then derive and apply a calibration technique to correct for the feature. A second technique has been utilised by both CMS and CDF to improve the b-jet resolution as part of the $WH \to l\nu b\bar{b}$ analysis. CMS and CDF use multivariate regression techniques. For the Run I result, CMS applied a boosted decision tree (BDT) on top of an equivalent JES calibration which saw a 22% narrowing of the dijet width [49]. CDF used an artificial neural network (ANN), using TMultilayerPerceptron [100] for their regression technique [101],

applying it again in addition to the equivalent JES calibration.

In an attempt to further improve the jet resolution and the $WH \rightarrow l\nu b\bar{b}$ analysis sensitivity, a regression technique similar to that used by CDF, using TMultiLayerPerceptron will be used on events after the $p_{\mathrm{T}}^{\mu,\mathrm{Reco}}$ calibration, to correct the reconstructed jet p_{T} to that of the generator level.

A Neural Network (NN) is adopted as it allows a linear combination of Sigmoid functions which can approximate any function according to Equation 6.3:

$$g(\vec{x}_i) = \sum_{i}^{Inputs} \alpha_i \cdot f(x_i), \tag{6.3}$$

where $g(\vec{x}_i)$ is the output function, $f(x_i)$ is the activation function which describes the output function and α_i is the parameter which the NN training is attempting to calculate for each input variable, i. Other important features which are fed into a NN training are the learning method, hidden layers and a list of variables which are input to the training. For every input variable in the trainings used there was one hidden layer. The hidden layers are used to add complexity to the training to aid the solving of the problem at hand. The learning method describes the algorithm used by the neural network in order to in the case of the regression, find the parameter α_i. In all the regressions used as part of this thesis, the BFGS learning method was used [102]. This method is useful for solving unconstrained non-linear optimisations and seeks a stationary point of a function.

The NN trainings will be on a per-jet basis, so that the input variables used will be per-jet rather than per-event. The types of variables available to be used as input to the trainings include jet kinematics, calorimeter and track variables, and also variables associated with the secondary vertex. Jet kinematic variables include the jet energy and p_{T} of the jet. The calorimeter and track variables include: the electromagnetic-fraction (EMF), the jet-vertex fraction (JVF), fraction energy from the jets in the final layer of the EM-calorimeter (FracEM3) or in the hadronic calorimeter (FracTile0), the number of tracks associated with the jet (NTrk), the width of the tracks (TrkWidth), the total p_{T} within the tracks (SumPtTrk) and the width of the jet (Width). Secondary vertex variables are synonymous with a b-jet, and the variables available include: the secondary vertex mass (SvpM), number of tracks (SvpNTrk), the distance between the primary and secondary vertex along the x- and y-directions (SvpX, SvpY) and the errors associated with the distance measurements (SvpErrX, SvpErrY). The secondary vertex distance measurements can be combined in order to calculate the distance and the error on the overall separation between primary and secondary vertex (SVpLxy, SvpErrLxy). Other potential input variables are whether or not the jet contains a muon, and whether or

not the jet contains a secondary vertex. To be used as input to the NN training, these variables need to be well modelled in simulated Monte Carlo as this is what is used to perform the training. The modelling of the potential input variables for the 2 jet, 2 b-Tag, p_{T}^{V} inclusive and lepton inclusive category are shown in Figure 6.14 for the kinematic variables, the track and calorimeter variables are shown in Figure 6.15 and the secondary vertex variable modelling is shown in Figures 6.16 and 6.17. Separate trainings were performed for the 3 jet, 2 b-tag, p_{T}^{V} inclusive, lepton inclusive category and information about these trainings can be found in Appendix A.1.

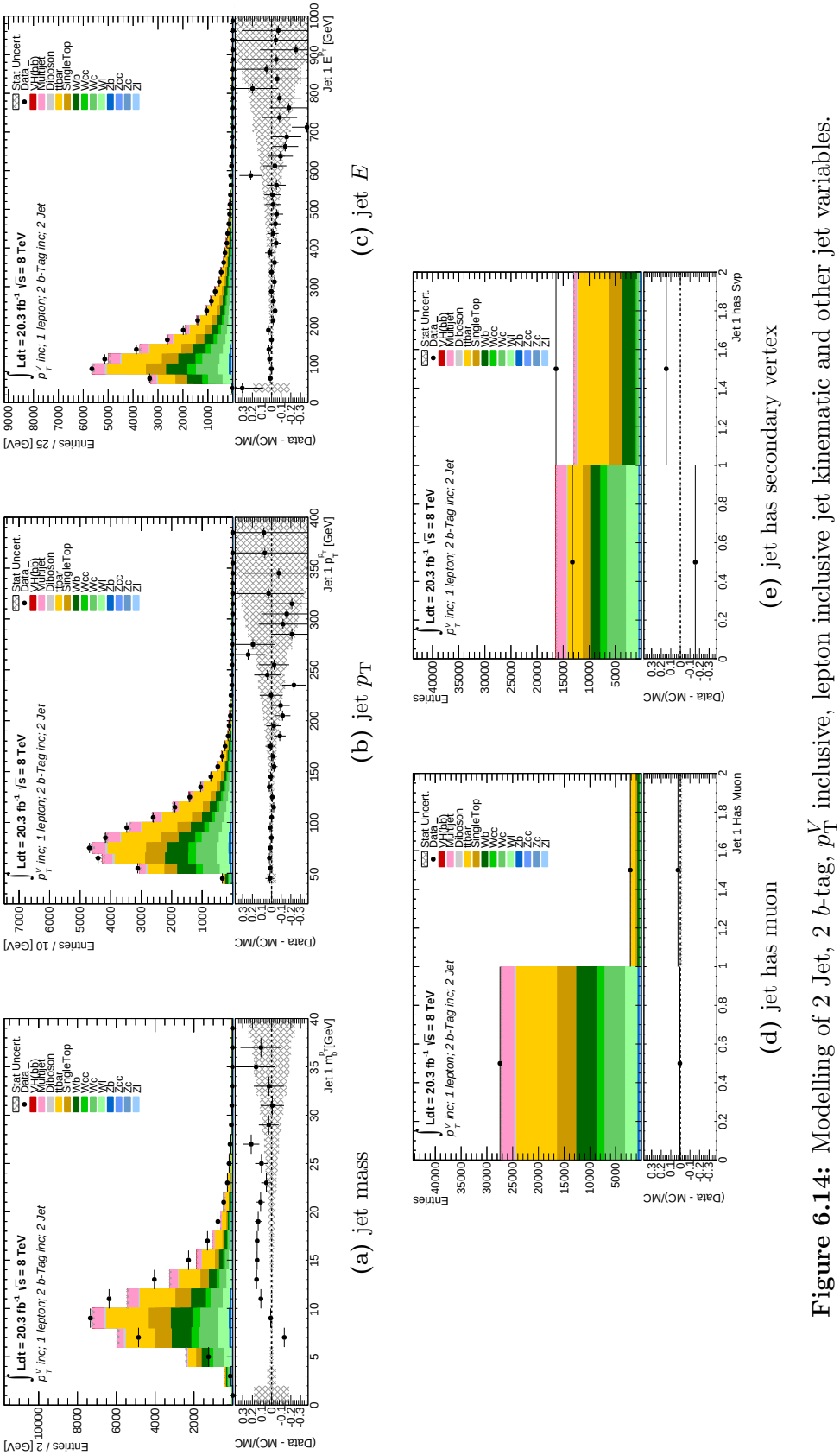

(a) jet mass

(b) jet p_{T}

(c) jet E

(d) jet has muon

(e) jet has secondary vertex

Figure 6.14: Modelling of 2 Jet, 2 b-tag, p_{T}^{V} inclusive, lepton inclusive jet kinematic and other jet variables.

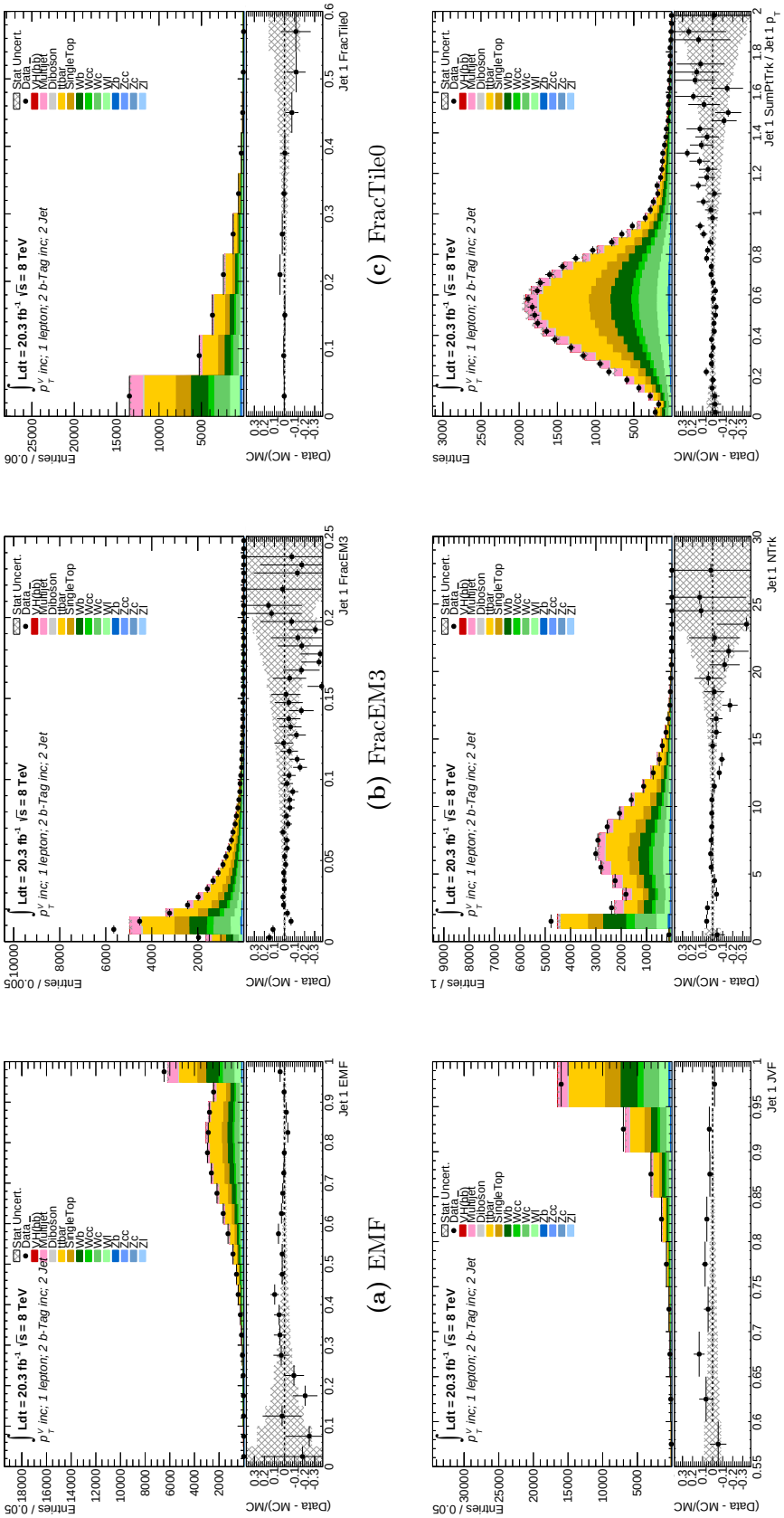

Figure 6.15: Modelling of 2 jet, 2 b-tag, p_{T}^{V} inclusive, lepton inclusive jet track and calorimeter variables.

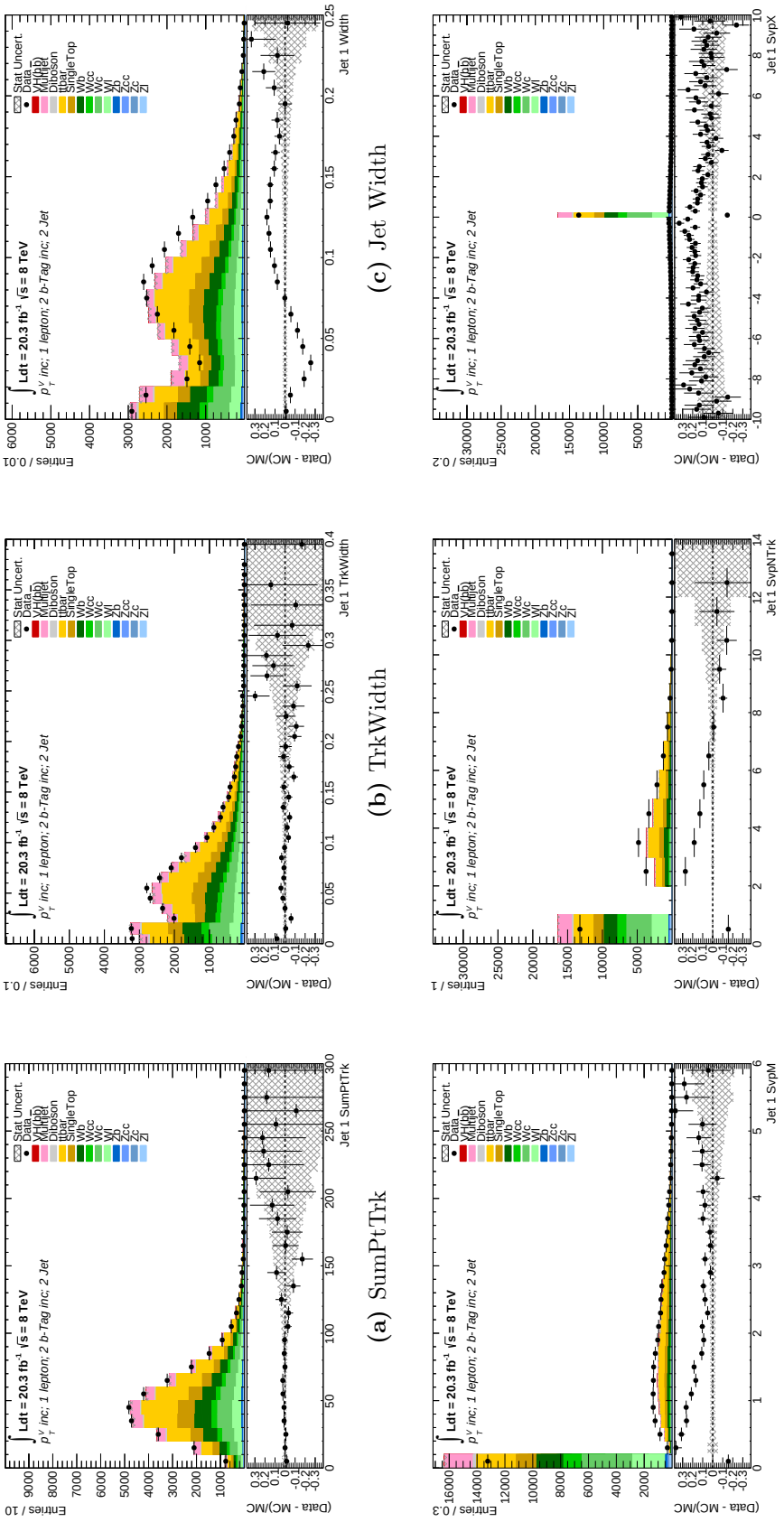

Figure 6.16: Modelling of 2 jet, 2 b-tag, p_{T}^{V} inclusive, lepton inclusive jet track, calorimeter variables, and a selection of secondary vertec variables.

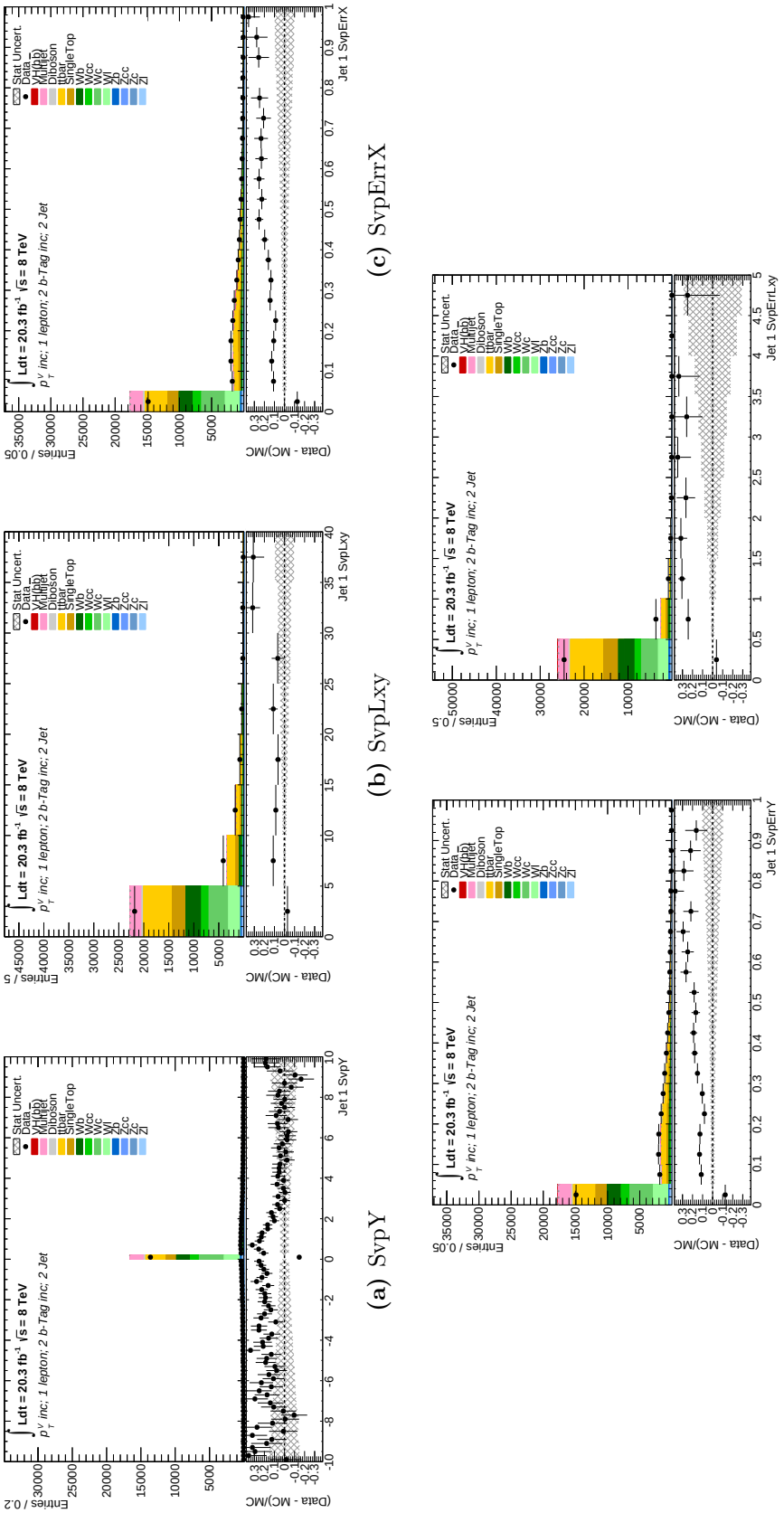

(a) SvpY (b) SvpLxy (c) SvpErrX

(d) SvpErrY (e) SvpErrLxy

Figure 6.17: Modelling of 2 jet, 2 b-tag, p_{T}^{V} inclusive, lepton inclusive variables associated with a secondary vertex.

After studying the modelling of the potential NN input variables, the variables which are well modelled and will be used for the NN training are the following: jet p_{T} and E, hasMuon, EMF, FracTile0, FracEM3, NTrk, SumPtTrk / p_{T}, SumPtTrk and TrkWidth. The secondary vertex variables available are poorly modelled in simulated Monte Carlo, as is the hasSV variable. The reconstruction of a secondary vertex is important for the NN to learn the signature of a b-jet. For this reason, SvpLxy has been included in the trainings due to it having the best modelling from the list of secondary vertex variables.

The next step is to perform the NN training and apply it as a jet calibration in addition to the previous calibrations, on top of the $p_{\mathrm{T}}^{\mu,\mathrm{Reco}}$ calibration. The training of the NN is performed over half the events, with the other half being used as a test sample. The reduction on the NN error takes place over many cycles or 'epochs' over the events. As the number of epochs rises, the NN error falls as a reciprocal function. If too many epochs are used, this leads to over-training causing the NN error to sharply increase. To optimise the NN training, three trainings are performed. After each training, the impact of the input variables is analysed and the variable with the weakest impact is removed before the NN is re-trained. This method is used so that the strongest performing variables can have a larger impact on the training with the removal of nuisance variables.

The information which is used as input to the initial NN training is shown in Table 6.12. Between trainings, only the list of input variables will change. The overtraining test and the impact of variables is shown in Figure 6.18 (a) and (b) respectively. There is no evidence of overtraining and the NN error has reached the minimum value. For the second training, the hasMuon variable is removed as it has the weakest impact on the initial NN training. All other elements remain constant. Figure 6.19 shows the results of the overtraining test in (a) and the impact of each of the variables in (b); there is no evidence of over-training in the second neural network and the NN error reaches a minimum. For the final training, the jet energy variable was removed as it had the least impact on the training of the second NN. The reults of the third NN training are in Figure 6.20; (a) shows the error reaches a minimum and no over-training and (b) shows the impact of each of the variables on the training.

Input Parameter	Value
Acivation Function	Sigmoid
Learning Method	BFGS
Epochs	100
Input Variables	E, p_{T}, EMF, FracTile0, FracEM3, NTrk, SumPtTrk / p_{T}, SumPtTrk, TrkWidth, SvpLxy, hasMuon
Output Variable	jet p_{T}

Table 6.12: The input parameters used in the initial neural network training. After each training, one input variable will be removed before being re-trained.

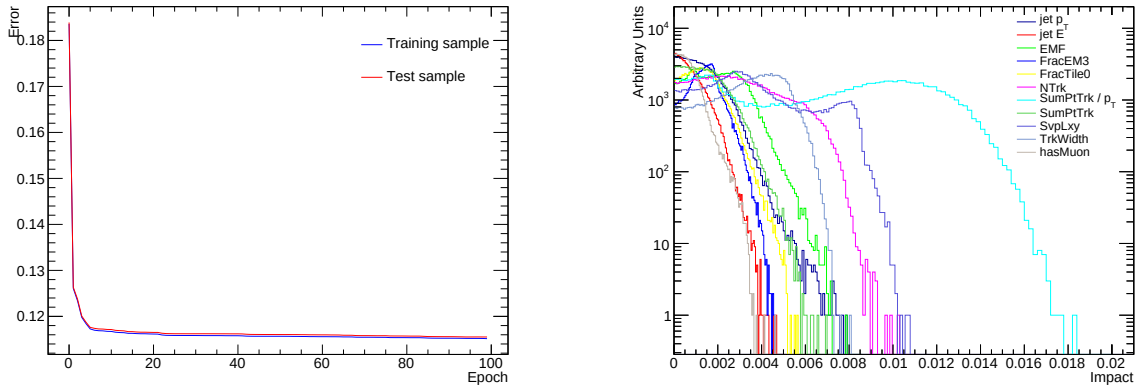

(a) Over-training test

(b) Variable Impact

Figure 6.18: The NN error as a function of epoch number to test for over training (a) and the impact each of the input variables has on the training of the initial neural network.

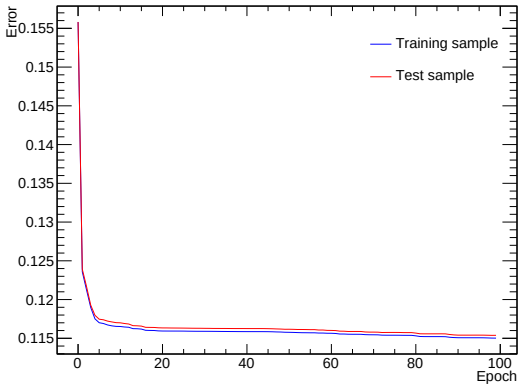

(a) Over-training test

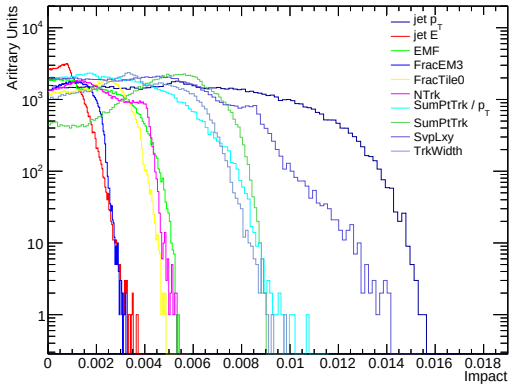

(b) Variable Impact

Figure 6.19: The NN error as a function of epoch number to test for over training (a) and the impact each of the input variables has on the training of the second neural network.

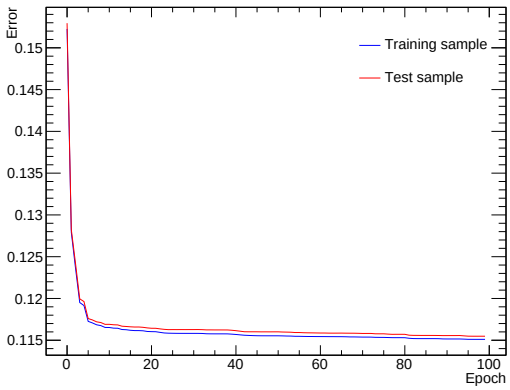

(a) Over-training test

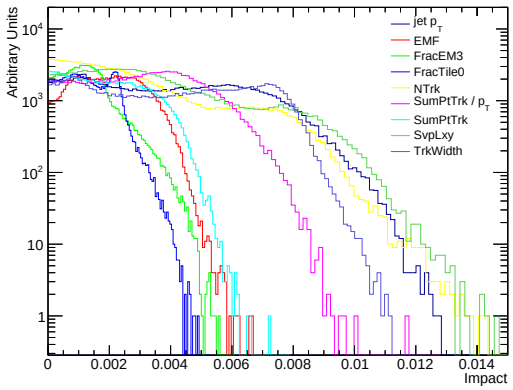

(b) Variable Impact

Figure 6.20: The NN error as a function of epoch number to test for over training (a) and the impact each of the input variables has on the training of the final neural network.

In order to study the effects of the neural networks, each of the trainings are added on top of the $p_{\mathrm{T}}^{\mu,\mathrm{Reco}}$ calibration. For calculating the changes in sensitivity, the neural networks were applied to both the signal and the background processes. The sensitivities for each of the neural networks (NNJ1–3) are shown in Table 6.13 split into bins of p_{T}^{V} as for a limit calculation, this is the procedure followed. For the sensitivity calculation, the values for the neural networks are compared to those found for the $p_{\mathrm{T}}^{\mu,\mathrm{Reco}}$ calibration, using 50 bins in the range $0 < m_{b\bar{b}} < 500$ GeV. The nominal jet calibrations have been

abbreviated to 'CC' in Table 6.13.

Calibration	p_{T}^{V} Bin [GeV]				
	$p_{\mathrm{T}}^{V} < 90$	$90 < p_{\mathrm{T}}^{V} < 120$	$120 < p_{\mathrm{T}}^{V} < 160$	$160 < p_{\mathrm{T}}^{V} < 200$	$p_{\mathrm{T}}^{V} > 200$
CC+pT3	0.668	0.448	0.467	0.466	0.733
CC+pT3+NNJ1	0.670	0.448	0.469	0.469	0.739
CC+pT3+NNJ2	0.671	0.449	0.470	0.468	0.735
CC+pT3+NNJ3	0.671	0.450	0.469	0.466	0.732

Table 6.13: Comparing the sensitivities separated into p_{T}^{V} bins for the jets after the $p_{\mathrm{T}}^{\mu,\mathrm{Reco}}$ calibration and between the neural network calibrations.

For all the regressions there is a slight improvement in all p_{T}^{V} bins compared with the $p_{\mathrm{T}}^{\mu,\mathrm{Reco}}$. At low p_{T}^{V}, there is $< 1\%$ difference between each of the regressions. In the high p_{T}^{V} bins however, where the $WH \to l\nu b\bar{b}$ analysis is more sensitive, the NNJ1 regression provides the highest sensitivity. For this reason, NNJ1 will be studied further.

Table 6.14 shows a comparison between the $p_{\mathrm{T}}^{\mu,\mathrm{Reco}}$ calibration, the NNJ1 and the generator level for the dijet mass reconstruction, width, resolution and the dijet response. The mass reconstruction has decreased slightly; moving further away from the generator level. For the dijet width, resolution and response there is negligable difference between the $p_{\mathrm{T}}^{\mu,\mathrm{Reco}}$ and the NNJ1 calibrations. Figure 6.21 shows visually the changes in shape between the $p_{\mathrm{T}}^{\mu,\mathrm{Reco}}$ and NNJ1 with a reference to the generator level for the dijet mass and the dijet response. There is no observed difference between the two calibrations. This observation is reinforced by Figure 6.22, which shows a two-dimensional respresentation of the changes in mean mass and width (a) and the response and width (b). The $p_{\mathrm{T}}^{\mu,\mathrm{Reco}}$ calibration and NNJ1 markers overlap significantly.

Calibration	Mean [GeV]	Width [GeV]	Resolution	Response
CC+Pt3	121.3 ± 1.6	12.3 ± 1.17	0.101 ± 0.010	1.02 ± 0.01
CC+Pt3+NNJ1	121.2 ± 1.7	12.4 ± 1.17	0.102 ± 0.010	1.02 ± 0.01
Generator Level	121.7 ± 1.3	5.02 ± 0.95	0.041 ± 0.008	1.00 ± 0.00

Table 6.14: Comparisons between the $p_{\mathrm{T}}^{\mu,\mathrm{Reco}}$, the regression and the generator level; comparing the dijet mass, width resolution and the response.

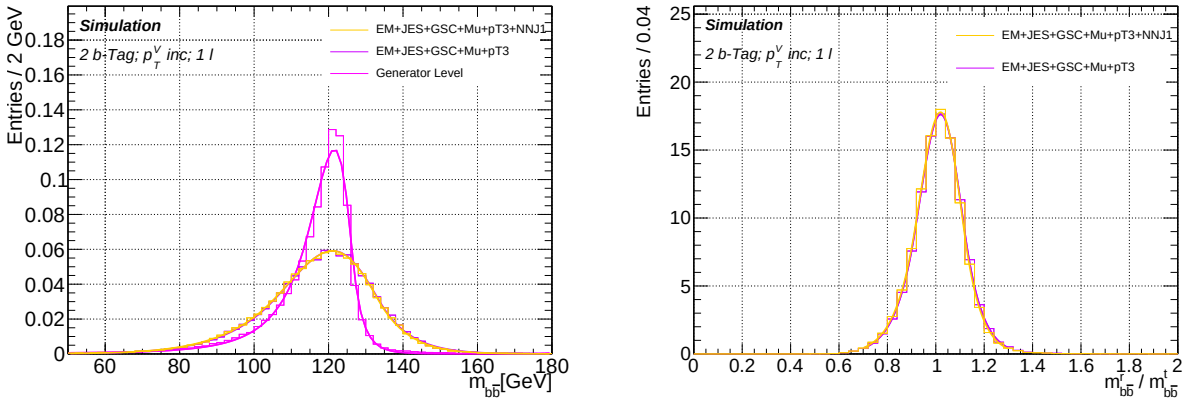

(a) dijet mass **(b)** dijet response

Figure 6.21: Shape comparison between the muon-in-jet $p_{\mathrm{T}}^{\mathrm{Reco}}$, regression and the generator level for the dijet mass and dijet response distributions.

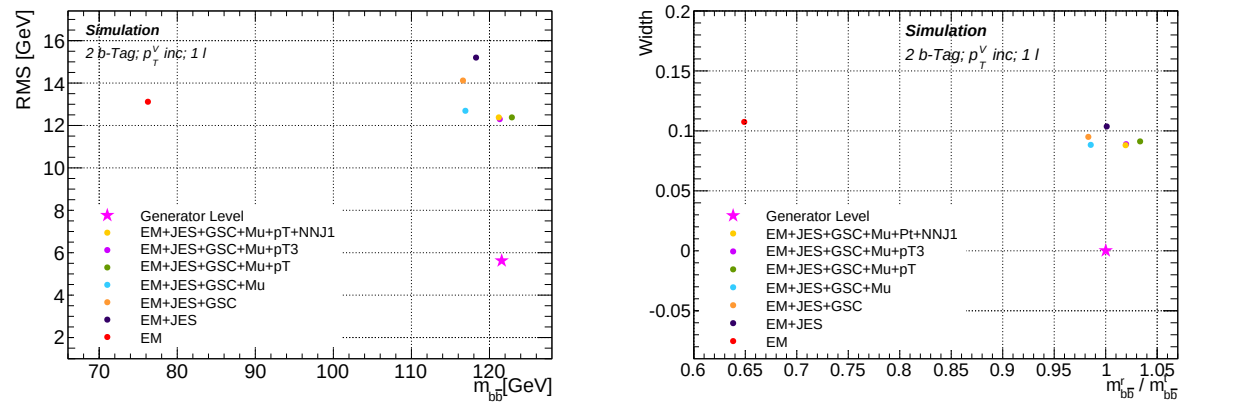

(a) dijet mass, mean and width comparison **(b)** dijet response, response and width comparison

Figure 6.22: Two-dimensional representation of the effect the regression has on the mean and width and response and width with the previous jet calibrations.

In an attempt to measure the possible improvements are to be gained using a regression, a final neural network has been trained using identical learning method, number of epochs, activation function and output variable. The list of input variables has been updated to include a wider array of secondary vertex variables which are synomynous with a reconstructed b-jet. Using these variables will improve the learning and give an improved result in Section 9.4.2, however the majority of variables associated with the secondary vertex are poorly modelled meaning the neural network is no longer vaild to be used as part of the analysis but it can illustrate the potential improvement to the analysis were the modelling improved. The updated list of variables are as follows: jet p_{T}, jet E, EMF,

JVF, FracEM3, FracTile0, SumPtTrk / jet p_{T}, SumPtTrk, SvpLxy, SvpErrLxy, SvpM, SvpNTrk, TrkWidth, Width and hasMuon.

6.3.2. Regression Jet Calibration Summary

Three per-jet regressions have been trained to be applied as a jet calibration as part of the $WH \to l\nu b\bar{b}$ analysis in addition to the $p_{\mathrm{T}}^{\mu,\mathrm{Reco}}$ calibration. Each regression has been trained with the same input configuration with only the weakest variable being removed in each consecutive training. The initial training has been put forward due to its improved sensitivity in the high p_{T}^{V} region compared to the latter two. With respect to the nominal $p_{\mathrm{T}}^{\mathrm{Reco}}$ calibration, the regression observes improved mass reconstruction and a 1.5% improvement in the dijet response. Negligible changes are observed in the dijet width and resolution. Table 6.15 summarises the effect on the dijet mass, width resolution and response with applying both the $p_{\mathrm{T}}^{\mu,\mathrm{Reco}}$ and the regression instead of the nominal $p_{\mathrm{T}}^{\mathrm{Reco}}$ calibration.

Calibration	Mean [GeV]	Width [GeV]	Resolution	Response
EM+JES+GSC+Mu+Pt	122.9 ± 1.7	12.4 ± 1.17	0.101 ± 0.010	1.03 ± 0.01
CC+Pt3+NNJ1	121.2 ± 1.7	12.4 ± 1.17	0.102 ± 0.010	1.02 ± 0.01
Generator Level	121.7 ± 1.3	5.02 ± 0.95	0.041 ± 0.008	1.00 ± 0.00

Table 6.15: Comparing the use of a $p_{\mathrm{T}}^{\mu,\mathrm{Reco}}$ and a regression to the generator level and the nominal $p_{\mathrm{T}}^{\mathrm{Reco}}$ calibration for the dijet mass, width, resolution and dijet response.

Figure 6.23 shows visually the improvements and compares the shape of the $p_{\mathrm{T}}^{\mu,\mathrm{Reco}}$ and regression to the nominal $p_{\mathrm{T}}^{\mathrm{Reco}}$ calibration. The taller peak with the regression indicates an improvement in the width since both calibrations are applied to the same number of events.

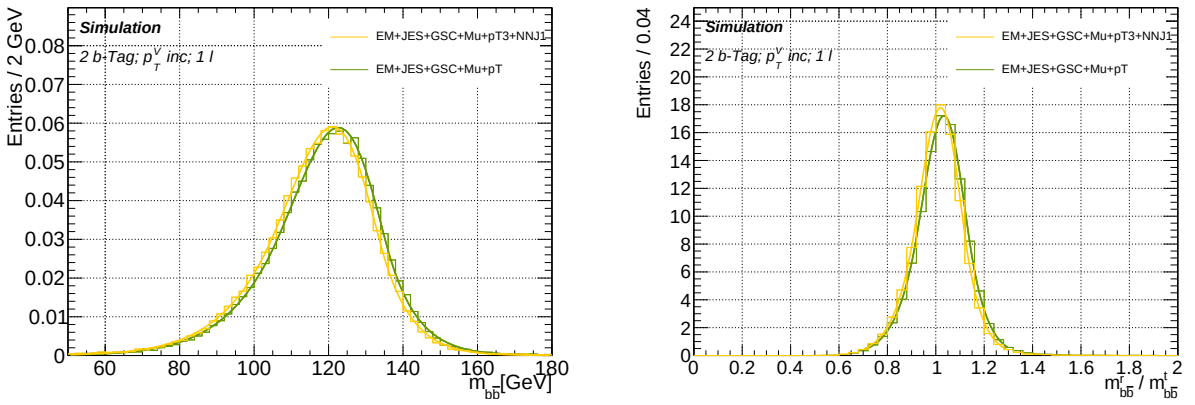

(a) dijet mass **(b)** dijet response

Figure 6.23: Shape comparison between the nominal $p_{\mathrm{T}}^{\mathrm{Reco}}$ and using a $p_{\mathrm{T}}^{\mu,\mathrm{Reco}}$ calibration with an additional regression for the dijet mass and the dijet response

Chapter 7

Background Estimation

The estimation of the background contributions forms a crucial part of the analysis for modelling the data. The main method used as part of the $WH \to l\nu b\bar{b}$ analysis for estimating background contributions is to get the shape from Monte Carlo simulation and estimate the normalisations in control regions. This method is used for the estimation of the $W/Z + l$ backgrounds. For $W/Z + c\,l$ and $W/Z +$ hf ('hf' is the summation of bl, bc cc and bb backgrounds), $t\bar{t}$, single-top and diboson (WW, WZ and ZZ) backgrounds, Monte Carlo simulation is used for the shape estimation, however there is no good control region available so other methods are used for the nomalisation estimation.

The final background, QCD multijet, is estimated in a data driven method; first defining a multijet enriched region before deriving a multijet distribution and normalising this to data. The estimation of the QCD multijet is described in Section 7.1, before the Monte Carlo simulated backgrounds are described in Section 7.2.

7.1. Data Driven Background Estimation

7.1.1. QCD Multijet Estimation

The QCD multijet background arises from jets faking charged leptons and from real missing transverse energy $E_{\mathrm{T}}^{\mathrm{miss}}$ in the event. A data driven method is used as for a Monte Carlo generated sample to be produced, a unrealistic amount of computing resources would be required.

In the $WH \to l\nu b\bar{b}$ analysis, the method for extracting the QCD multijet background

is divided into the following three stages, which will be described in futher detail before the results of the distribution normalisation are shown:

- QCD multijet region event selection
- The promotion of 1 b-tag events to the 2 b-tag category (spoofing)
- The QCD multijet normalisation

Multijet Template Creation

To select events with an enriched QCD multijet content, the lepton selection in the signal region is modified to be orthogonal to the signal region and is summarised in Table 7.1. Medium leptons are required with electrons meeting the `Medium++` requirements. The track isolation, iso_{track} is modified to: $0.05(0.07) < iso_{\text{track}} < 0.12(0.5)$ for electrons(muons). The calorimeter isolation (iso_{calo}) is also modified to $iso_{\text{calo}} < 0.07$. The data and simulated Monte Carlo from the electroweak backgrounds are passed through the modified event selection with a QCD multijet distribution being constructed by subtracting the modified Monte Carlo simulation selection from the modified data event selection.

Property	Selection	
	Electron	Muon
Quality	`Medium++`	Medium
iso_{track}	$0.05 < iso_{\text{track}} < 0.12$	$0.07 < iso_{\text{track}} < 0.5$
iso_{calo}	$iso_{\text{calo}} < 0.07$	

Table 7.1: Summary of the modified lepton selection in the creation of a QCD multijet enriched region.

1 b-tag Event Promotion

The distributions produced have a large number of events in the 1 b-tag and looser 2 b-tag categories, however in the 2 b-tag, high p_{T}^{V} bin, the number of events is low. The kinematics of the 1 b-tag events have been shown to match well with the kinematics of the 2 b-tag events in all 2 b-tag regions in the muon sub-channel and the 2L b-tag

region in the electron sub-channel [48]. The tight tagged electron events have considerable differences in kinematics to the 1 b-tag region. The difference between electron and muon events arises due to muon multijet events predominantly coming from heavy-flavour jet decays, whereas electron events consist of a mixture of heavy-flavour jet decays, light jets, or photons faking electrons.

Since the kinematics match closely in the mentioned regions, a procedure has been developed to assign an MV1c value to the un-tagged jet in the 1 b-tag region. The procedure is implemented separately for electron and muon sub-channels. Once the procedure has been implemented, the electron events are kinematically re-weighted to match with the original 2 b-tag distribution. Finally, a smoothing function is applied five times to eliminate any statistical fluctuations which arise from the re-weighting. The final 2 b-tag distribution consists of $\sim$10% original 2 b-tag events which are not discarded.

Multijet Background Normalisation

The QCD multijet distributions for all regions have been created but then still need to be normalised. The normalisation is performed using TMinuit [103] as a fit to data using the $E_{\mathrm{T}}^{\mathrm{miss}}$ distribution. The electroweak and multijet backgrounds are permitted to float separately leading to separate normalisation scale factors for electroweak backgrounds and multijet background. The normalisation is performed separately for electron and muon sub-channels, 2- and 3-jet events and 1 and 2 b-tag events. The 2 b-tag region is fitted inclusively of b-tagging efficiency due to the small contribution in the tight category. To help the minimisation obtain the scale factors, the global fit is performed to obtain ratios of post-fit yield to prefit yield for the electroweak backgrounds. These are then assigned to the electroweak backgrounds during the minimisation as part of the multijet background estimation.

Table 7.2 shows the normalisation scale factors obtained from the function-minimisation for the electroweak backgrounds and multijet backgrounds for 2- and 3-jet events in the 1 and 2 b-tagging categories, separately for electron and muon events. The results of the function-minimisation are shown in the $E_{\mathrm{T}}^{\mathrm{miss}}$distribution for electron and muon 2-jet events for 1 and 2 b-tag events in Figure 7.1, and the 3-jet results in Figure 7.2.

Category		Scale Factors			
		Electron		Muon	
		Electroweak	Multijet	Electroweak	Multijet
1 b-tag	2-jet	1.05	0.959	0.935	1.12
	3-jet	0.932	1.03	0.856	1.32
2 b-tag	2-jet	1.05	0.0800	0.958	0.118
	3-jet	1.01	0.0623	0.884	0.121

Table 7.2: Table of normalisation scale factors to be applied to the electroweak backgrounds and multijet backgrounds in the electron and muon sub-channels for 2 and 3-jet events in the 1 and 2 b-tag categories. The scale factors are derived using the $E_{\mathrm{T}}^{\mathrm{miss}}$ distribution.

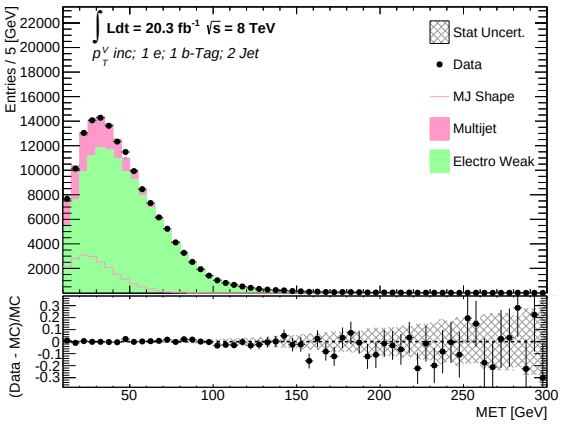

(a) 1 b-tag, electron

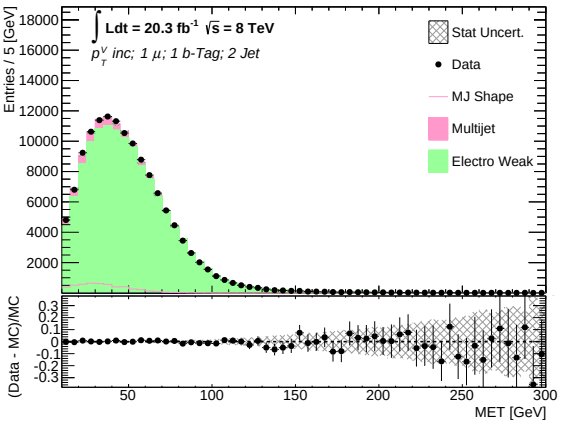

(b) 1 b-tag, muon

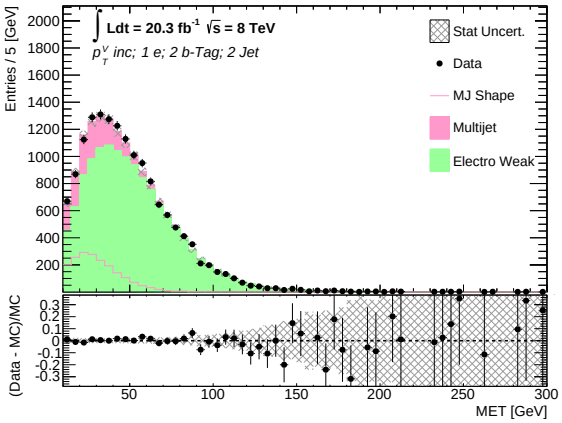

(c) 2 b-tag, electron

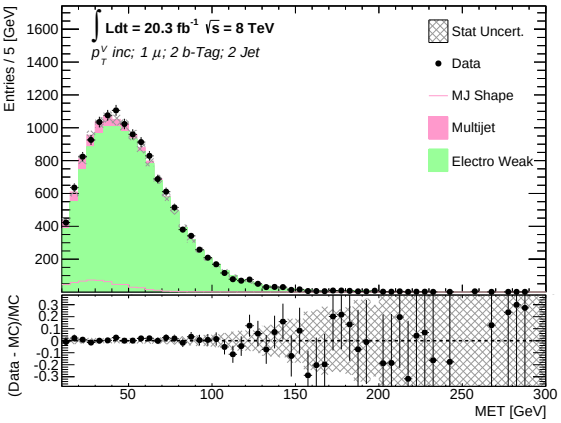

(d) 2 b-tag, muon

Figure 7.1: $E_{\mathrm{T}}^{\mathrm{miss}}$ distributions after the application of the electroweak and multijet scale factors derived using a fit to data. The distributions are for 2-jet events in the electron and muon sub-channels in the 1 and 2 b-tagging regions.

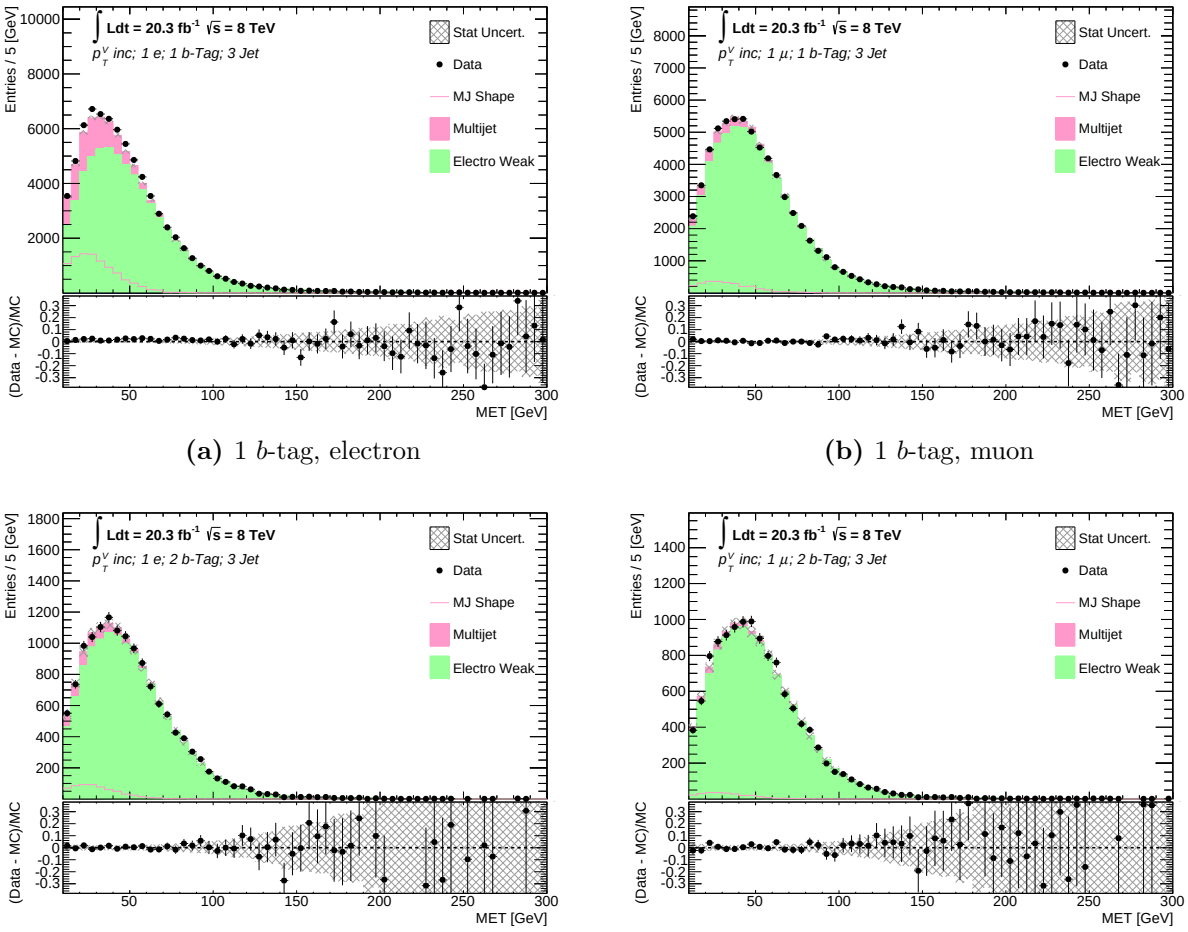

(a) 1 b-tag, electron

(b) 1 b-tag, muon

(c) 2 b-tag, electron

(d) 2 b-tag, muon

Figure 7.2: $E_{\mathrm{T}}^{\mathrm{miss}}$ distributions after the application of the electroweak and multijet scale factors derived using a fit to data. The distributions are for 3-jet events in the electron and muon sub-channels in the 1 and 2 b-tagging regions.

7.2. Monte Carlo Simulation Background Estimation

For the estimation of the $W/Z+$jets, top, and diboson backgrounds several Monte Carlo generators are utiilised for the modelling of the shape for each process. For each process, a description of the method used to estimate the shape as well as information pertaining to the Monte Carlo generator used will be given in this section. The normalisations of the backgrounds is performed using control regions; the $W/Z+$jets background normalisation is constrained using the 1 b-tag control region. The other backgrounds do not have a pure control region from which the normalisations can be derived. For these processes,

the normalisations are initially constrained using comparisons between the nominal Monte Carlo generator and other generators, before being allowed to float within these constraints during the global fit. Further detailed information regarding the systematic uncertainties associated with the background estimation along with information about the global fit are given in Chapter 9.

7.2.1. W/Z + jets Estimation

For the generation of W/Z + jets, the SHERPA generator is used with massive b and c quarks and also interfaced with CT10 PDFs. In order to increase the number of events in the W/Z + hf processes without increasing the amount of resources used, filters were developed to select events containing b, c or light hadrons. The events were also filtered further to select events with a high transverse momentum by splitting the samples into the following p_{T} regions: $p_{\mathrm{T}} < 40$ GeV, $40 < p_{\mathrm{T}} < 70$ GeV, $70 < p_{\mathrm{T}} < 140$ GeV, $140 < p_{\mathrm{T}} < 280$ GeV, $280 < p_{\mathrm{T}} < 500$ GeV and $p_{\mathrm{T}} > 500$ GeV. Table 7.3 summarises the Monte Carlo generators used for the production of W/Z + jets processes.

Process	Generator	$\sigma \times$ BR
$W \to \ell\nu$	SHERPA 1.4.1	12.07 nb
$Z/\gamma^* \to \ell\ell$ ($m_{\ell\ell} > 40$ GeV)	SHERPA 1.4.1	1.24 nb
$Z/\gamma^* \to \nu\nu$ ($m_{\nu\nu} > 5$ GeV)	SHERPA 1.4.1	6.71 nb

Table 7.3: Table summarising the generator used for the production of the W/Z + jets processes along with the cross-section times branching ratio ($\sigma \times$ BR) to normalise the processes at $\sqrt{s} = 8$ TeV.

W + jets

The modelling of $W + \ell$ and $W + c\,l$ have been studied using control regions of 0 and 1 b-tag events, whereas Monte Carlo studies have been performed for the study of the W + hf background.

The 0 b-tag region predominantly consisits of $W + l$ events whereas the 1 b-tag region consists of a mixture of mainly $W + l$ and $W + c\,l$. A mis-modelling of events in the regions for both electron and muon sub-channels in the p_{T}^{V} and $\Delta\phi(\mathrm{jet}_1, \mathrm{jet}_2)$ distributions is observed. This mis-modelling cannot be explained by poor modelling of the multijet

background due to its low contribution in the muon sub-channel. To overcome this mis-modelling, a data driven correction is applied in the form of a continuous function, fit to the ratio of the data to the backgrounds. A migration of events between high and low p_{T}^{V} is required which led to separate corrections for events with $p_{\mathrm{T}}^{V} < 120$ GeV and those with $p_{\mathrm{T}}^{V} > 120$ GeV.

Due to its signal like appearence and lacking of a good control region, $W + \mathrm{hf}$ is a difficult background to estimate. To overcome the lack of a control region, generator studies are performed in order to probe variations in the kinematic distributions which is done at generator level and also probe the variations in flavour composition at reconstructed level. There are two methods used to make these comparisons; the first method compares the nominal SHERPA sample with the b-filter applied to a SHERPA generated sample of $W + bb$ where no b's are included from the parton shower. The second method compares the SHERPA sample to aMC@NLO+HERWIG++ sample and POWHEG+PYTHIA8 sample, in order to test the sensitivity differences in the matrix element, higher order effects and parton showering.

Z + jets

A similar disagreement is observed in $Z + \mathrm{jets}$ as was observed in the $\Delta\phi(\mathrm{jet}_1, \mathrm{jet}_2)$ distribution for $W + \mathrm{jets}$ in the 0 and 1 b-tag regions. To correct for this mis-modelling a correction is applied only in the $Z + l$ background separately for $p_{\mathrm{T}}^{V} < 120$ GeV and $p_{\mathrm{T}}^{V} > 120$ GeV events. $Z + \mathrm{hf}$ is excluded from the correction as the mis-modelling is not observed in the 2 b-tag regions which has a higher proportion of $Z + \mathrm{hf}$ events. The correction is applied in the form $a(1 + bx)$ to the ratio of data minus non-Z background against $Z + \mathrm{jets}$. With this correction applied, good agreement is observed for less than 2% change in the normalisation.

A missmodelling of p_{T}^{V} is also observed which increases with the requirement for b-tags. A correction of the form $a + b\log(p_{\mathrm{T}}^{V})$ is applied to the ratio of the data minus non-Z background over $Z + \mathrm{jets}$ background. The correction is applied to $Z + b/c$ events only.

7.2.2. Top Estimation

The top backgrounds consist of the $t\bar{t}$ pair production and single-top production. For the single-top backgrounds, these are split into three channels; s-, t- and Wt-channel. The

$t\bar{t}$ pair production events are produced using POWHEG interfaced with PYTHIA. A filter is also applied to specify that at least one W from the top decays into a charged lepton. The parton showering and hadronisation is generated using the *Perugia2011C* tune, which uses a CTEQL1 PDF. For the generation of single-top events, the t- and Wt-channel use POWHEG+PYTHIA and the s-channel is simulated with ACERMC+PYTHIA. All the single-top channels use CTEQL1 PDF with *Perugia2011C* tune. A summary of the generators used along with the cross-section times branching ratio ($\sigma \times \text{BR}$) for each of the top background processes is given in Table 7.4.

Process	Generator	$\sigma \times$ BR
$t\bar{t}$	POWHEG+PYTHIA8	252.89 pb
s-channel	POWHEG+PYTHIA8	5.61 pb
t-channel	ACERMC+PYTHIA8	87.76 pb
Wt-channel	ACERMC+PYTHIA8	22.37 pb

Table 7.4: Table summarising the generators used for the production of the $t\bar{t}$ and single-top processes. The cross-section times branching ratio ($\sigma \times \text{BR}$) is also shown, used to normalise the process for $\sqrt{s} = 8$ TeV.

A disagreement is observed between generators in the $\Delta\phi(\text{jet}_1, \text{jet}_2)$ distribution in both the $t\bar{t}$ processes. A calibration has been added to reweight the average p_{T} of the top Monte Carlo to that observed in data. For the single-top processes, modelling studies are performed within other groups in ATLAS.

7.2.3. Diboson Estimation

The diboson background includes the production processes originating from a final state containing WW, WZ or ZZ. The largest contributions to the $WH \to l\nu b\bar{b}$ analysis are the $W \to \ell\nu$ and $Z \to bb$ with smalller contributions from the other processes where a jet or lepton has been mis-tagged.

All three diboson final state processes are produced using POWHEG interfaced with PYTHIA8. For the production of WZ and ZZ final states, only events with $m_{\ell\ell} > 20$ GeV with one of the vector bosons decaying hadronically are considered. A summary of the generators used for the diboson production is shown in Table 7.5 along with the cross-section times branching fraction ($\sigma \times \text{BR}$) which is used for the normalisation of the backgrounds to $\sqrt{s} = 8$ TeV.

Process	Generator	$\sigma \times$ BR
WW	PowHeg+Pythia8	52.44 pb
WZ	PowHeg+Pythia8	9.24 pb
ZZ	PowHeg+Pythia8	3.17 pb

Table 7.5: Table summarising the generators used for the production of the diboson (WW, WZ and ZZ) backgrounds. The WZ and ZZ processes require $m_{\ell\ell} > 20$ GeV and at least one vector boson to decay hadronically. The cross-section times branching fraction ($\sigma \times$ BR) is also shown and as it is used for the normalisation of each process to $\sqrt{s} = 8$ TeV.

Chapter 8

Prefit Distributions & Yield Tables

Once the background estimations have been performed, distributions in each signal or control region of the variable used as input to the global fit (described in detail in Chapter 9) are produced, to check the initial modelling of variables and that the background estimations are reasonable.

A total of four regions are used as input to the global fit: the 1 b-tag control region used for constraining the $W+l$ and $Z+l$ normalisation scale factors, and the three 2 b-tag signal regions split based upon the b-tagging efficiency.

This chapter goes through each of the four regions in the 2-jet category only; for completeness, Appendix A.2 provides the analogous details for the 3-jet distributions. For each region, the distributions are split by the transverse momentum of the vector boson (p_{T}^{V}) in order to increase the analysis sensitivity. In the 1 b-tag region there are two p_{T}^{V} bins; $p_{\mathrm{T}}^{V} < 120$ GeV and $p_{\mathrm{T}}^{V} > 120$ GeV. For each of the three 2 b-tag regions, there are five p_{T}^{V} bins: $p_{\mathrm{T}}^{V} < 90$ GeV, $90 < p_{\mathrm{T}}^{V} < 120$ GeV, $120 < p_{\mathrm{T}}^{V} < 160$ GeV, $160 < p_{\mathrm{T}}^{V} < 200$ GeV, and $p_{\mathrm{T}}^{V} > 200$ GeV.

8.1. 2 jet, 1 b-Tag Control Region

As part of the global fit, the 1 b-tag control region is used to contrain the normalisations of the $V+l$ backgrounds, where V is either a W or Z boson. The distribution which is used as input to the fit is the b-tagging value, MV1c. The distributions before the global fit are shown for both p_{T}^{V} bins in Figure 8.1 and Table 8.1 shows the yield tables for each p_{T}^{V} bin.

There is slight mis-modelling between data and the total signal and background, this

is most prominant in the low p_{T}^{V} bin. Since the uncertainties placed upon the processes in the yield table are taken from statistical sources only, once the global fit is performed, systematic uncertainties will improve the agreement. The uncertainties displayed in the distributions are from the statistical and systematic uncertainties. More than 50% of the total contribution to the overall backgrounds is from $W + l$ and $W + cl$ process, with other large contributions from the $W + \mathrm{hf}$ and top ($t\bar{t}$ and single-top) backgrounds, which contribute $\sim 20\%$ to the total in both p_{T}^{V} bins.

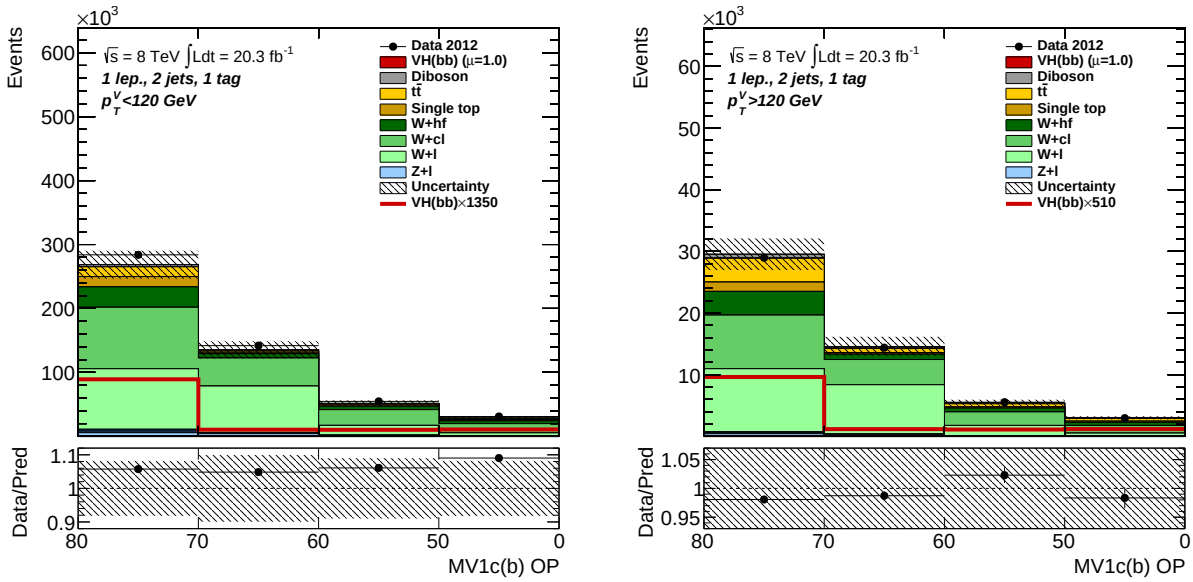

(a) $p_{\mathrm{T}}^{V} < 120$ GeV **(b)** $p_{\mathrm{T}}^{V} > 120$ GeV

Figure 8.1: MV1c distributions in the 1 b-tag control region before the global fit for 2-jet events. The distributions are shown for the two p_{T}^{V} regions used as input to the global fit; (a) $p_{\mathrm{T}}^{V} < 120$ GeV and (b) $p_{\mathrm{T}}^{V} > 120$ GeV.

Sample	1-tag	
	$p_{\mathrm{T}}^{V} < 120$ GeV	$p_{\mathrm{T}}^{V} > 120$ GeV
VH	89.3 ± 9.5	25.7 ± 5.1
VV	6037.6 ± 77.7	1185.3 ± 34.4
$t\bar{t}$	21040.2 ± 145.1	5433.5 ± 73.7
s-top	22263.0 ± 149.2	2162.3 ± 46.5
W+l	187062.9 ± 432.5	20239.8 ± 142.3
W+cl	179038.4 ± 423.1	16218.3 ± 127.4
W+hf	48305.0 ± 219.8	5860.6 ± 76.6
Z+l	11235.3 ± 106.0	845.6 ± 29.1
Z+cl	4397.8 ± 66.3	277.3 ± 16.7
Z+hf	4217.7 ± 64.9	259.5 ± 16.1
Total	483687.2 ± 695.5	52507.9 ± 229.1
Data	511393	51826

Table 8.1: Table of prefit yields for 1-lepton 2-jet 1-tag events. The uncertainties are from statistical sources only.

8.2. 2 jet, 2 LL b-Tag Signal Region

The first signal region uses a b-tagging efficiency of 80% and is denoted 'loose' (L). The dijet mass distribution is used as input to the global fit for each of the five p_{T}^{V} bins. The prefit distributions are shown in Figure 8.2 for each p_{T}^{V} bin and the corresponding yield tables are shown in Table 8.2.

Accross all p_{T}^{V} bins, excellent agreement is observed within the uncertainties between the data and the total signal and background. For low p_{T}^{V} bins, the QCD multijet is a large background ($\sim 10\%$) decreasing to an insignificant amount at higher p_{T}^{V}. The main contribution at low p_{T}^{V} are the $W+l$, $W+cl$, $W+\mathrm{hf}$, $t\bar{t}$ and single-top processes. These backgrounds contribute similar proportions of the total backgrounds at high p_{T}^{V}, however, the total yield is lower. The $Z+\mathrm{jets}$ backgrpunds contribute negligible amounts in all p_{T}^{V} bins and diboson (VV) makes a 1–5% contribution depending upon p_{T}^{V}.

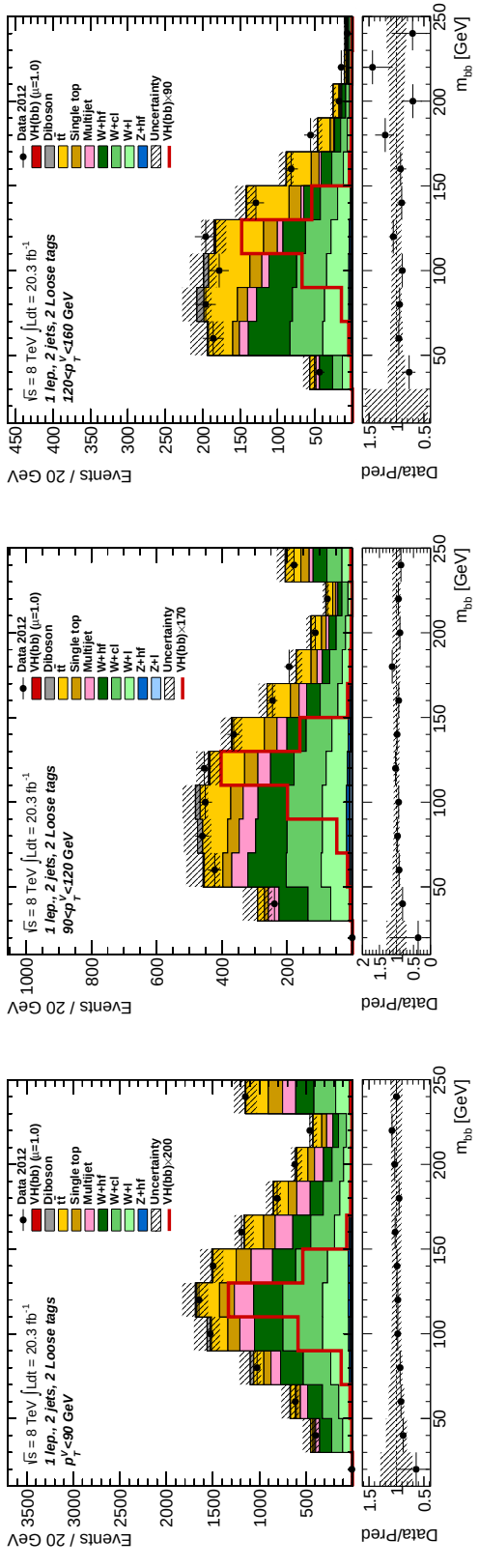

(a) $p_{\mathrm{T}}^{V} < 90$ GeV

(b) $90 < p_{\mathrm{T}}^{V} < 120$ GeV

(c) $120 < p_{\mathrm{T}}^{V} < 160$ GeV

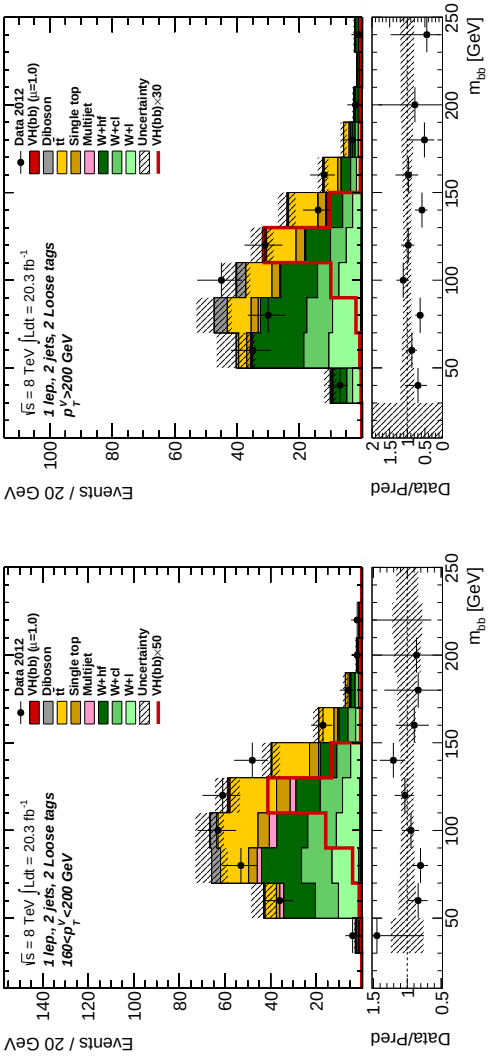

(d) $160 < p_{\mathrm{T}}^{V} < 200$ GeV

(e) $p_{\mathrm{T}}^{V} > 200$ GeV

Figure 8.2: Dijet mass distributions in the 2 L b-tag signal region before the global fit for 2-jet events. The distributions are shown for all five p_{T}^{V} regions used as input to the global fit; $p_{\mathrm{T}}^{V} < 90$ GeV, $90 < p_{\mathrm{T}}^{V} < 120$ GeV, $120 < p_{\mathrm{T}}^{V} < 160$ GeV, $160 < p_{\mathrm{T}}^{V} < 200$ GeV and $p_{\mathrm{T}}^{V} > 200$ GeV.

Sample	2L-tag				
	$p_{\mathrm{T}}^{V} < 90$ GeV	$90 < p_{\mathrm{T}}^{V} < 120$ GeV	$120 < p_{\mathrm{T}}^{V} < 160$ GeV	$160 < p_{\mathrm{T}}^{V} < 200$ GeV	$p_{\mathrm{T}}^{V} > 200$ GeV
VH	13.6 ± 3.7	5.1 ± 2.3	3.3 ± 1.8	1.5 ± 1.2	1.8 ± 1.4
VV	129.1 ± 11.4	43.0 ± 6.6	21.3 ± 4.6	8.1 ± 2.9	8.9 ± 3.0
$t\bar{t}$	1680.9 ± 41.0	667.7 ± 25.8	320.1 ± 17.9	81.2 ± 9.0	44.5 ± 6.7
s-top	1084.9 ± 32.9	286.3 ± 16.9	93.6 ± 9.7	22.3 ± 4.7	13.7 ± 3.7
W+l	1743.7 ± 41.8	513.6 ± 22.7	173.8 ± 13.2	48.3 ± 6.9	40.1 ± 6.3
W+cl	2662.7 ± 51.6	759.0 ± 27.6	232.0 ± 15.2	58.5 ± 7.6	37.5 ± 6.1
W+hf	2085.9 ± 45.7	663.5 ± 25.8	242.3 ± 15.6	70.9 ± 8.4	68.1 ± 8.3
Z+l	104.9 ± 10.2	40.9 ± 6.4	9.0 ± 3.0	1.4 ± 1.2	0.6 ± 0.8
Z+cl	67.4 ± 8.2	24.9 ± 5.0	5.4 ± 2.3	0.9 ± 0.9	0.3 ± 0.6
Z+hf	148.6 ± 12.2	53.4 ± 7.3	11.7 ± 3.4	2.4 ± 1.5	0.8 ± 0.9
MJ_e	957.4 ± 30.9	248.9 ± 15.8	46.2 ± 6.8	10.0 ± 3.2	1.8 ± 1.3
MJ_μ	505.1 ± 22.5	63.0 ± 7.9	8.8 ± 3.0	1.6 ± 1.3	0.5 ± 0.7
Total	11184.1 ± 105.8	3369.2 ± 58.0	1167.4 ± 34.2	307.1 ± 17.5	218.6 ± 14.8
Data	10946	3200	1107	292	180

Table 8.2: Table of prefit yields for 1-lepton 2 and 3-jet 2L-tag events The uncertainties are from statistical sources only.

8.3. 2 jet, 2 MM b-Tag Signal Region

The second signal region uses a b-tagging efficiency of 70%, denoted 'medium' (M). As with the other signal regions, the dijet mass distribution is used as input into the global fit for each p_{T}^{V} bin. The prefit distibutions for each p_{T}^{V} bin in the 2M-tagged category are shown in Figure 8.3. The tables of yield are shown in Table 8.3.

Good agreement is observed in all p_{T}^{V} bins between the data and total signal and backgrounds. The contribution made by QCD multijet is lower compared to the 2L category: less than 10% at low p_{T}^{V}, decreasing sharply to an insignificant amount at higher p_{T}^{V}. The signal fails to make a significant contribution, even in the most sensitive high p_{T}^{V} bin. The largest background contributions, as with the 2L category are from $W+\mathrm{hf}$ and $t\bar{t}$ processes, contributing to 70% across all p_{T}^{V} bins. The other $W+\mathrm{jets}$ processes along with s-top and diboson make up the remaining backgrounds.

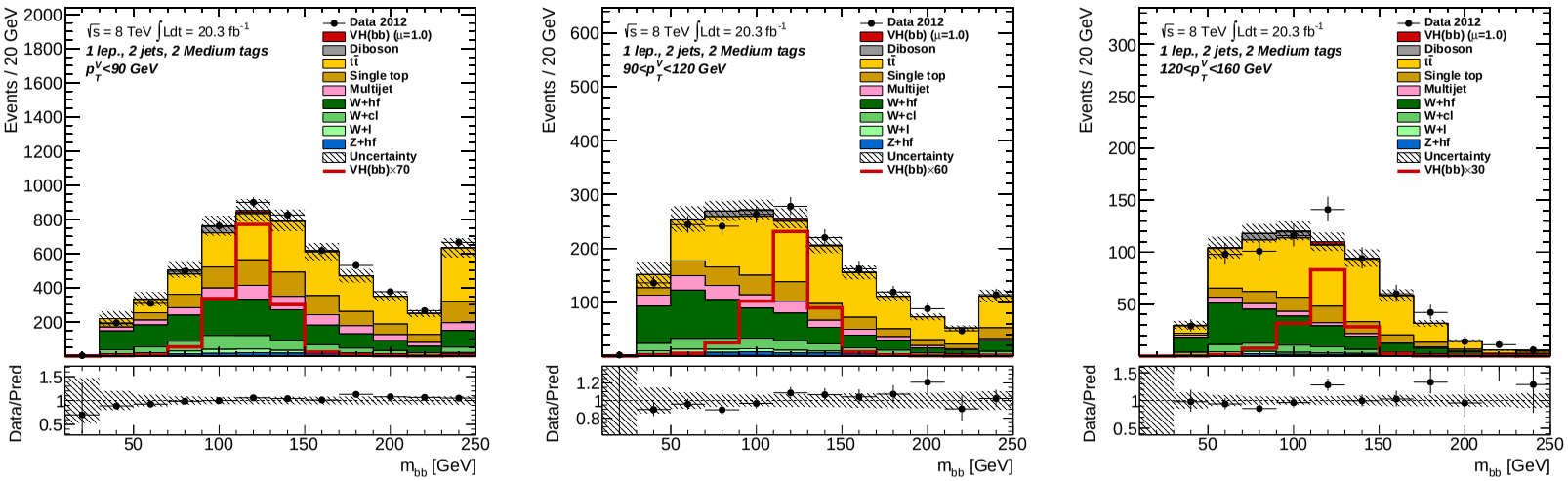

(a) $p_{\mathrm{T}}^{V} < 90$ GeV **(b)** $90 < p_{\mathrm{T}}^{V} < 120$ GeV **(c)** $120 < p_{\mathrm{T}}^{V} < 160$ GeV

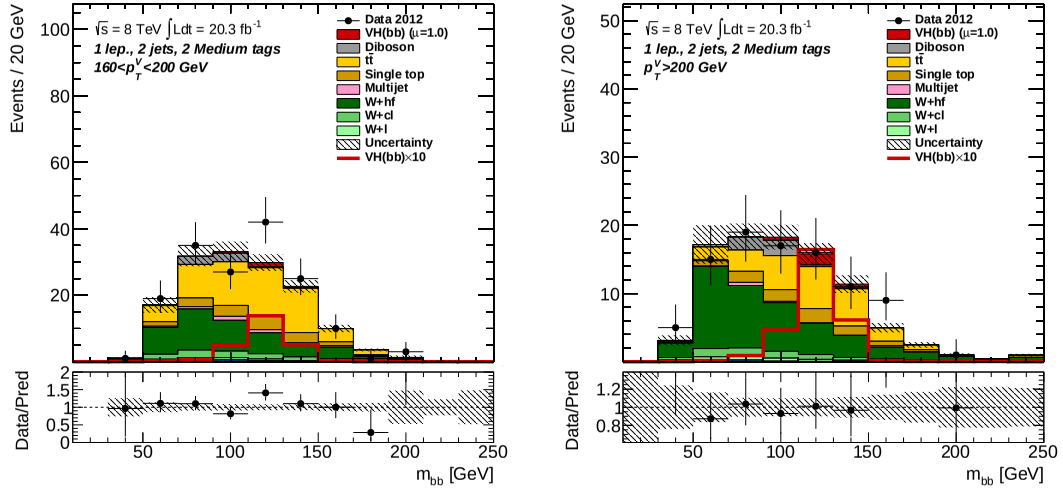

(d) $160 < p_{\mathrm{T}}^{V} < 200$ GeV **(e)** $p_{\mathrm{T}}^{V} > 200$ GeV

Figure 8.3: Dijet mass distributions in the 2 M b-tag signal region before the global fit for 2-jet events. The distributions are shown for all five p_{T}^{V} regions used as input to the global fit; $p_{\mathrm{T}}^{V} < 90$ GeV, $90 < p_{\mathrm{T}}^{V} < 120$ GeV, $120 < p_{\mathrm{T}}^{V} < 160$ GeV, $160 < p_{\mathrm{T}}^{V} < 200$ GeV and $p_{\mathrm{T}}^{V} > 200$ GeV.

Sample	2M-tag				
	$p_{\mathrm{T}}^{V} < 90$ GeV	$90 < p_{\mathrm{T}}^{V} < 120$ GeV	$120 < p_{\mathrm{T}}^{V} < 160$ GeV	$160 < p_{\mathrm{T}}^{V} < 200$ GeV	$p_{\mathrm{T}}^{V} > 200$ GeV
VH	21.5 ± 4.6	7.8 ± 2.8	5.2 ± 2.3	2.5 ± 1.6	2.9 ± 1.7
VV	81.0 ± 9.0	27.3 ± 5.2	14.1 ± 3.8	5.6 ± 2.4	4.9 ± 2.2
$t\bar{t}$	2053.7 ± 45.3	795.2 ± 28.2	340.6 ± 18.5	61.9 ± 7.9	24.7 ± 5.0
s-top	983.7 ± 31.4	255.3 ± 16.0	78.7 ± 8.9	16.1 ± 4.0	9.3 ± 3.1
W+l	129.7 ± 11.4	37.9 ± 6.2	11.4 ± 3.4	3.1 ± 1.8	2.5 ± 1.6
W+cl	473.2 ± 21.8	132.3 ± 11.5	38.5 ± 6.2	9.3 ± 3.1	5.4 ± 2.3
W+hf	1393.1 ± 37.3	448.6 ± 21.2	168.1 ± 13.0	46.0 ± 6.8	42.7 ± 6.5
Z+l	7.4 ± 2.7	3.0 ± 1.7	0.6 ± 0.8	0.1 ± 0.3	0.0 ± 0.2
Z+cl	12.8 ± 3.6	4.8 ± 2.2	1.0 ± 1.0	0.2 ± 0.4	0.1 ± 0.2
Z+hf	107.3 ± 10.4	40.7 ± 6.4	8.8 ± 3.0	1.4 ± 1.2	0.5 ± 0.7
MJ_e	384.2 ± 19.6	147.2 ± 12.1	23.2 ± 4.8	4.5 ± 2.1	0.9 ± 1.0
MJ_μ	142.4 ± 11.9	13.3 ± 3.7	2.2 ± 1.5	0.2 ± 0.4	–
Total	5790.1 ± 76.1	1913.4 ± 43.7	692.3 ± 26.3	150.8 ± 12.3	94.0 ± 9.7
Data	5951	1914	712	163	93

Table 8.3: Table of prefit yields for 2-jet 2M-tag events. The uncertainties are from statistical sources only

8.4. 2 jet, 2 TT b-Tag Signal Region

The final signal region denoted 'tight' (T) uses a 50% b-tagging efficiency. The dijet mass distribution for each of the five p_{T}^{V} bins is input to the global fit. Prefit distributions for each of the p_{T}^{V} bins of the dijet mass are shown in Figure 8.4 with the tables of yield shown in Table 8.4.

Excellent agreement is observed between data and the total signal and backgrounds in all p_{T}^{V} bins, especially in the highest p_{T}^{V} bin. The $t\bar{t}$ process contributes to 50% of the total background at low p_{T}^{V} bin, this contribution decreases as the p_{T}^{V} increases. As p_{T}^{V} increases the W + hf process increases to 50% from 20% in the lowest p_{T}^{V} bin. The signal starts to make a significant contribution for tight tagged b-jets. At low p_{T}^{V}, there is a 5% contribution, increasing to 6% at higher p_{T}^{V}.

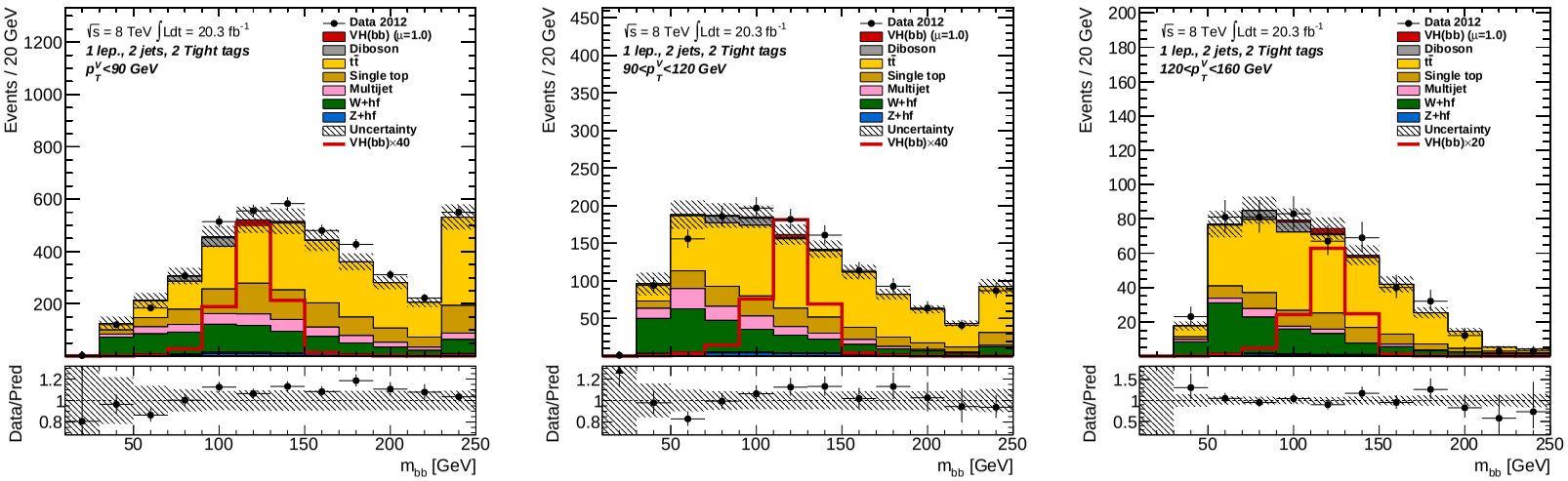

(a) $p_{\mathrm{T}}^{V} < 90$ GeV (b) $90 < p_{\mathrm{T}}^{V} < 120$ GeV (c) $120 < p_{\mathrm{T}}^{V} < 160$ GeV

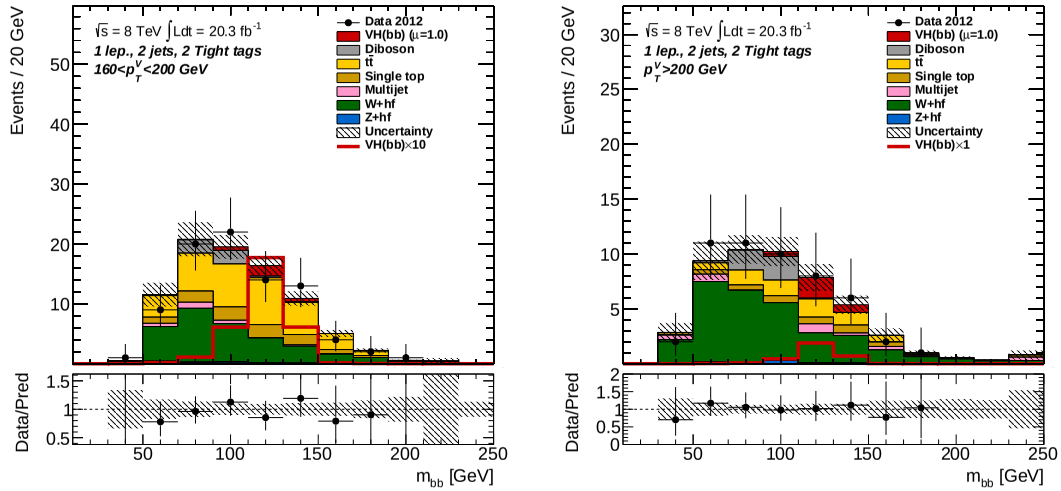

(d) $160 < p_{\mathrm{T}}^{V} < 200$ GeV (e) $p_{\mathrm{T}}^{V} > 200$ GeV

Figure 8.4: Dijet mass distributions in the 2 L b-tag signal region before the global fit for 2-jet events. The distributions are shown for all five p_{T}^{V} regions used as input to the global fit; $p_{\mathrm{T}}^{V} < 90$ GeV, $90 < p_{\mathrm{T}}^{V} < 120$ GeV, $120 < p_{\mathrm{T}}^{V} < 160$ GeV, $160 < p_{\mathrm{T}}^{V} < 200$ GeV and $p_{\mathrm{T}}^{V} > 200$ GeV.

Sample	2T-tag				
	$p_{\mathrm{T}}^{V} < 90$ GeV	$90 < p_{\mathrm{T}}^{V} < 120$ GeV	$120 < p_{\mathrm{T}}^{V} < 160$ GeV	$160 < p_{\mathrm{T}}^{V} < 200$ GeV	$p_{\mathrm{T}}^{V} > 200$ GeV
VH	23.9 ± 4.9	8.8 ± 3.0	5.9 ± 2.4	3.1 ± 1.8	3.1 ± 1.8
VV	64.0 ± 8.0	22.2 ± 4.7	12.3 ± 3.5	5.0 ± 2.2	4.3 ± 2.1
$t\bar{t}$	1930.7 ± 43.9	722.7 ± 26.9	278.9 ± 16.7	34.0 ± 5.8	7.1 ± 2.7
s-top	795.5 ± 28.2	194.1 ± 13.9	58.5 ± 7.6	10.2 ± 3.2	3.8 ± 2.0
W+l	4.2 ± 2.0	1.0 ± 1.0	0.3 ± 0.5	0.1 ± 0.2	0.0 ± 0.2
W+cl	24.6 ± 5.0	7.4 ± 2.7	2.4 ± 1.6	0.4 ± 0.6	0.3 ± 0.5
W+hf	730.0 ± 27.0	258.2 ± 16.1	103.4 ± 10.2	31.4 ± 5.6	29.3 ± 5.4
Z+l	0.1 ± 0.3	0.1 ± 0.3	0.0 ± 0.1	0.0 ± 0.0	0.0 ± 0.0
Z+cl	0.5 ± 0.7	0.1 ± 0.3	0.0 ± 0.2	0.0 ± 0.0	0.0 ± 0.0
Z+hf	69.6 ± 8.3	28.0 ± 5.3	5.6 ± 2.4	1.1 ± 1.1	0.6 ± 0.8
MJ_e	230.0 ± 15.2	103.0 ± 10.1	15.0 ± 3.9	2.6 ± 1.6	2.8 ± 1.7
MJ_μ	87.6 ± 9.4	7.9 ± 2.8	0.6 ± 0.8	–	–
Total	3960.7 ± 62.9	1353.4 ± 36.8	483.1 ± 22.0	87.9 ± 9.4	51.3 ± 7.2
Data	4255	1376	494	86	51

Table 8.4: Table of prefit yields for 2-jet 2T-tag events. The uncertainties are from statistical sources only

Chapter 9

Limit Setting Procedure & Results

The final link in the analysis chain is the calculation of the profile likelihood, which is used to test the expectations from simulation against the data.

A description of the systematic uncertainties and their sources is given in Section 9.1.2. The use of the systematic uncertainties along with an outline of the method used to build the likelihood profile is given in Section 9.2. Once the likelihood profile is complete, normalisation scale factors from the statistical and systematic uncertainties are applied to the input distributions. These, along with the yield tables, are shown in Section 9.3. Finally, the limit results obtained from a maximum-likelihood fit are examined in Section 9.4, initially for the nominal analysis, using the current jet calibration methods, and then applying the alternate jet calibration methods described in Chapter 6.

9.1. Systematic Uncertainties

9.1.1. Systematic Uncertainties Introduction

To build a model of information going into the maximum-likelihood (global) fit, nuisance parameters (NPs) are assigned to the systematic uncertainties. There are two types of NP: floating normalisations, which are constrained using log-normal probability density functions (PDF) to prevent the normalisations becoming negative during the fit; and a prior constrained NP, where the variation is constrained within a reasonable range.

The $WH \rightarrow l\nu b\bar{b}$ analysis has a total of 192 NPs which include 80 coming from experimental uncertainties. The large number of NPs is because they are decorrelated across the backgrounds and regions of phase space. The global fit uses templates which

are derived from predicted yields for signal and background events. The systematic uncertainties are varied with respect to the nominal up-and-down by one standard-deviation ($\pm 1\sigma$). Those NPs which are found to have a negligible effect on the final result are 'pruned' region-by-region. For shape uncertainties, the pruning occurs for variations across all bins that are below 0.5%. Further pruning is done in regions with less than 2% signal contribution and where the variations affect the background by less than 0.5%. These pruning steps reduce the overall number of systematic variations by a factor of two from the near twenty-thousand systematic-variation template pairs for all regions and NPs.

The behaviour of the global fit is evaluated using checks on how much the NP is pulled away from the nominal value. Additional checks on how much the uncertainty is reduced with respect to the nominal uncertainty and which correlations develop between systematic uncertainties which were initially uncorrelated are also performed. The impact of each systematic uncertainty is measured by performing the fit a second time, fixing the uncertainty to the initial fitted value. All other uncertainties are permitted to vary to maintain the correlations. The magnitude of the shift with respect to the fitted value is a measure of the systematic impact.

9.1.2. Systematic Sources & Estimation

The following tables show the systematics, the number of associated NPs and the value for the systematics affecting the modelling of the signal, QCD multijet and simulated backgrounds. 'S' represents a shape only uncertainty and 'float' represents a floating normalisation. The experimental systematic sources are also described.

Signal Systematic Uncertainties

Table 9.1 lists the systematics associated with the signal modelling. There are separate uncertainties for $q\bar{q} \to WH$, $q\bar{q} \to ZH$ and $gg \to ZH$. The ZH processes are included as part of the signal as they make a non-negligible contribution to the $WH \to l\nu b\bar{b}$ analysis. $gg \to ZH$ uncertainties are larger due to only being calculated to leading order. The cross-section uncertainties are taken from the LHC cross-sections working group [32] for both the scale and the PDF uncertainties. An uncertainty on the branching ratio of 3.3% is applied for $m_H = 125$ GeV with decays to final states other than $b\bar{b}$ contributing less than 1%. Signal samples are used for the derivation of acceptance uncertainties according

to the recipe given in [104]. p_{T}^{V} shape uncertainties are applied following the procedure given in [105], which typically results in a 2% uncertainty applied to the p_{T} distributions, rising to 2.5% in the highest p_{T}^{V} bin.

Systematic	Value	NPs
Cross-section (scale)	1%	2
Cross-section (PDF)	2.4% ($q\bar{q}$) 17% (gg)	2
Branching Ratio	3.3%	1
2-jet Acceptance (scale)	1.5%–3.3%	2
3-jet Acceptance (scale)	3.3%–4.2%	2
p_{T}^{V} shape (scale)	S	2
Acceptance (PDF)	2%–5%	2
p_{T}^{V} shape (NLO EW correction)	S	1
Acceptance (parton shower)	7%–13%	1

Table 9.1: Summary of the signal specific systematic uncertainties displaying the uncertainty and the associated number of nuisance parameters. 'S' represents a shape only uncertainty.

QCD Multijet Systematic Uncertainties

Table 9.2 summarises the list of systematics associated with the QCD multijet background. The normalisation uncertainties arise from the statistical uncertainties of the multijet fit and the subtraction of the non-multijet background subtraction done to create the multijet template. The smaller size of the muon sub-channel gives uncertainties three times larger than the 11%, 14% and 22% obtained for the respective LL, MM and TT normalisation uncertainties in the electron sub-channel. Multijet shape uncertaintie are assessed by comparing the multijet enriched selection region to the nominal region.

Experimental Systematic Uncertainties

The experimental systematic uncertainties considered include the trigger selection, object reconstruction and identification, as well as object calibration and resolution. There is a 2.8% uncertainty placed upon the integrated luminosity derived using the method in [106].

Systematic	Value	NPs
Normalisation (muon)	12%–60%	6
Normalisation (electron)	3%–22%	6
Track Isolation	S	10
Spoof re-weighting	S	2

Table 9.2: Summary of the systematic uncertainties associated with the QCD multijet background. Displaying the number of nuisance parameters and the variation associated with each systematic.

A 4% uncertainty is placed upon the average number of interactions. The uncertainties placed upon electrons and muons from trigger isolation and identification efficiencies is less than 1%. For events with $E_{\mathrm{T}}^{\mathrm{miss}} = 100$ GeV, a 4.5% correction to the trigger measurement is applied; this value falls to 1% for $E_{\mathrm{T}}^{\mathrm{miss}} > 120$ GeV. Jet energy scale (JES) uncertainties arise from a range of sources including pile-up, flavour composition and in-situ calibration. For central jets, the uncertainties range from 3%–1% for jets with $p_{\mathrm{T}} = 20$ GeV and 1 TeV respectively. The jet energy resolution (JER) uncertainty applied ranges from 10%–20% for $p_{\mathrm{T}} = 20$ GeV jets, depending upon the η, falling to 5% for jets with $p_{\mathrm{T}} > 200$ GeV. An 8% uncertainty is applied to the $E_{\mathrm{T}}^{\mathrm{miss}}$ calibration and a 2.5% uncertainty is applied to the calorimeter energy clusters not from a reconstructed object. For the majority of the p_{T} range a 2–3% uncertainty is applied to the jets as a simulation-to-data scale factor to account for the b-tagging uncertainty measurements which vary as a function of p_{T}. For $p_{\mathrm{T}} = 20$ GeV the uncertainty rises to 5% and for $p_{\mathrm{T}} > 200$ GeV, this value rises further to 8%.

Simulated Background Systematic Uncertainties

Table 9.3 lists the systematics associated with the simulated background processes: $W+$jets, $Z+$jets, $t\bar{t}$, single-top, and diboson. The $V+$hf processes (V represents either a W or a Z boson) has contributions from Vbb, Vcc and Vbl. The 1 b-tag category allows for normalisation scale factors for $V+l$ events to be derived. For $V+$hf and $V+c\,l$ processes, no control region exists resulting in the normalisations being allowed to float freely in the global fit. Constraints are placed upon $W+bb$ events by making comparisons at generator level between other Monte Carlo generators.

The $t\bar{t}$ uncertainties arise from comparisons between different Monte Carlo generators to the nominal generator used. A reweighting of the reconstructed $t\bar{t}$ p_{T} distribution

is done to make sure the distribution is in agreement with the generator level. Half of this calibration is assigned as a systematic uncertainty. For the single-top production channels (s-, t- and Wt-channel) it is difficult to obtain a control region for any of the three production mechanisms. The $WH \to l\nu b\bar{b}$ analysis relies on in this case, simulated Monte Carlo comparisons taken from recipes derived by the ATLAS single-top group.

The diboson (WW, ZZ and WZ) production channels also have the issue of obtaining a control region. As with single-top, simulated Monte Carlo comparisons are made alongside theoretical calculations for modelling the systematics.

Systematic	Value	NPs
$Z+$jets		
Zl Normalisation, 3/2-jet ratio	5%	1,1
Zcl Normalisation	Float	1
Zcl 3/2-jet ratio	26%	1
$Z+$hf Normalisation	Float	1
$Z+$hf 3/2-jet ratio	20%	1
$Z+$hf / Zbb ratio	12%	4
$\Delta\phi(\text{jet}_1,\text{jet}_2), p_{\text{T}}^V, m_{b\bar{b}}$	S	4,2,2
$W+$jets		
Wl Normalisation, 3/2-jet ratio	10%	1,1
Wcl Normalisation	Float	1
Wcl, $W+$hf 3/2-jet ratio	10%	1
$W+$hf Normalisation	Float	1
Wbl / Wbb ratio	35%	3
Wbc / Wbb, Wcc / Wbb ratio	12%	1,1
$\Delta\phi(\text{jet}_1,\text{jet}_2), p_{\text{T}}^V, m_{b\bar{b}}$	S	6,6,2
$t\bar{t}$		
$t\bar{t}$ Normalisation	Float	3
$t\bar{t}$ 3/2-jet ratio	20%	2
High / Low-p_{T}^V ratio	7.5%	1
Top-quark p_{T}, $m_{b\bar{b}}$, $E_{\text{T}}^{\text{miss}}$	S	1,1,1
Single top		
Cross-section	4% (s-, t-channel, 7% (Wt))	3
Acceptance (generator)	3%–53%	3
$m_{b\bar{b}}$, $p_{\text{T}}^{b_1}$	S	1,1
Diboson		
Cross-section & Acceptance (scale)	3%–29%	1,1
Cross-section & Acceptance (PDF)	2%–4%	1,1
$m_{b\bar{b}}$	S	2

Table 9.3: Summary of the systematic uncertainties pertaining to Monte-Carlo simulated background processes, displaying the number of nuisance parameters and the variation associated with each systematic. 'S' represents a shape only uncertainty.

9.2. Limit Setting Procedure

The statistical analysis of the data uses a binned likelihood function which can be expressed as Equation 9.1; as a product of Poisson probability terms:

$$\text{Pois}(n|\mu\text{S}+\text{B})\left[\prod_{\text{bins}}^{N}\frac{\mu\nu_b^{\text{sig}}+\nu_b^{\text{bkg}}}{\mu S+B}\right] \tag{9.1}$$

μ is the signal strength which is normalised to the Standard Model Higgs boson production cross-section value so that any deviation from this value is a deviation from the Standard Model. μ is multiplied by the expected signal yield (ν_b^{sig}) for each bin b. ν_b^{bkg} represents the expected background value for each bin. The number of observed events in each bin is described by n_b. The expected signal and background events have a dependence upon the systematic uncertainties which are described by a set of nuisance parameters (θ)(NPs). When the NPs shift from their nominal value of zero, a penalty term (Pois(m|B_{CR})), where m and B_{CR} are the measured and expected number of events used to determine the nominal value. The likelihood can be expressed as a function in terms of μ and θ as shown in Equation 9.2.

$$\mathcal{L}(\mu,\theta)=\text{Pois}(n|\mu\text{S}+\text{B})\left[\prod_{\text{bins}}^{N}\frac{\mu\nu_b^{\text{sig}}+\nu_b^{\text{bkg}}}{\mu S+B}\right]\text{Pois}(m|B_{\text{CR}}) \tag{9.2}$$

For the $WH\rightarrow l\nu b\bar{b}$ analysis, the likelihood is maximised leading to a maximum log-likelihood value (Equation 9.3) which is used in conjunction with the test statistic q_μ is constructed from the profile likelihood:

$$q_\mu=2\ln\frac{\mathcal{L}(\mu,\hat{\hat{\theta}}_\mu)}{\mathcal{L}(\hat{\mu},\hat{\theta})}, \tag{9.3}$$

where $\hat{\mu}$ and $\hat{\theta}$ are the parameters to maximise the likelihood within $0\leq\hat{\mu}\leq\mu$. $\hat{\hat{\theta}}_\mu$ are the NPs which maximise the likelihood for a given μ [107]. An upper-limit is placed upon the signal strength against the Standard Model with a 95% confidence level (CL). Using a CL_s method alongside the test statistic measuring the compatibility to the background-only and the signal-plus-background models, an exclusion limit is derived [108].

To control the flavour fractions of the W/Z + jets background in the 1 b-tag region, the MV1c distribution is used in this region to build the likelihood function. The 2 b-tag category is sub-divided into three categories (LL, MM and TT) based upon the b-tagging

efficiency. See Section 5.2 for event selection details. To build the likelihood function in each of the 2 b-tag categories, the dijet invariant mass distribution of the two signal jets is used. Table 9.4 summarises which distributions are used to build the likelihood profile in each category. To constrain the top ($t\bar{t}$ and single-top) backgrounds, the 3-jet category is used due to its top-enriched nature. The inclusion of the 1 b-tag category is due to the constraints it allows on the W/Z + jets normalisation.

Category		Distribution
1 b-Tag	2-jet	MV1c
	3-jet	MV1c
2 b-tag (LL)		$m_{b\bar{b}}$
2 b-tag (MM)	2-jet	$m_{b\bar{b}}$
2 b-tag (TT)		$m_{b\bar{b}}$
2 b-tag (LL)		$m_{b\bar{b}}$
2 b-tag (MM)	3-jet	$m_{b\bar{b}}$
2 b-tag (TT)		$m_{b\bar{b}}$

Table 9.4: The distributions used to build the likelihood function for each of the categories used as part of the $WH \to l\nu b\bar{b}$ analysis.

Each of the tagging categories is further sub-divided into bins of the p_{T} of the vector boson, p_{T}^{V}. The 2 b-tag categories are split into five bins (0–90 GeV, 90–120 GeV, 120–160 GeV, 160–200 GeV and $>$ 200 GeV). The expected sensitivity of the $WH \to l\nu b\bar{b}$ analysis improves by using two p_{T}^{W} bins in the 1 b-tag category compared with not using the 1 b-tag category at all. Using five bins in the 1 b-tag category would require careful modelling of the systematics but would also allow access to jet p_{T} distributions which are parameterised as a function of the flavour-tagging scale factors. As a compromise, two p_{T}^{V} bins are used ($p_{\mathrm{T}}^{V} < 120$ GeV and $p_{\mathrm{T}}^{V} > 120$ GeV).

For the limit extraction and global fit, the input distributions are parsed through a transformation designed to optimise the binning of the distributions. The transformation used is described by equation 9.4

$$Z = \frac{z_{\mathrm{s}} n_{\mathrm{s}}}{N_{\mathrm{s}}} + \frac{z_{\mathrm{b}} n_{\mathrm{b}}}{N_{\mathrm{b}}}, \tag{9.4}$$

where Z is the value being calculated for the bin widths, and N_{s} and N_{b} are the total respective signal and background events in the distribution. n_{s} and n_{b} are the number of

signal and background events in the bin and z_{s} and z_{b} are parameters which are used to tune the algorithm, which in the case of the $WH \to l\nu b\bar{b}$ analysis are calculated to be optimised at $z_{\mathrm{s}} = 6(4)$ and $z_{\mathrm{b}} = 2(2)$ for the 2-(3-)jet category. The calculation is achieved by starting in the last bin, and then the range is increased by adding a bin, one-by-one from right to left. At each step, Z is calculated until $Z > 1$. At this stage, the bins which formed part of the calculation are rebinned into a single bin. The process is repeated from the last untransformed bin. Using this transformation results in a 2% increase in the analysis sensitivity compared to using the untransformed distribution. A visual example of the transform is given in Figure 9.1 for the 3-jet, $p_{\mathrm{T}}^{V} < 90$ GeV, 2 loose-tagged b-jets region before going into the global fit

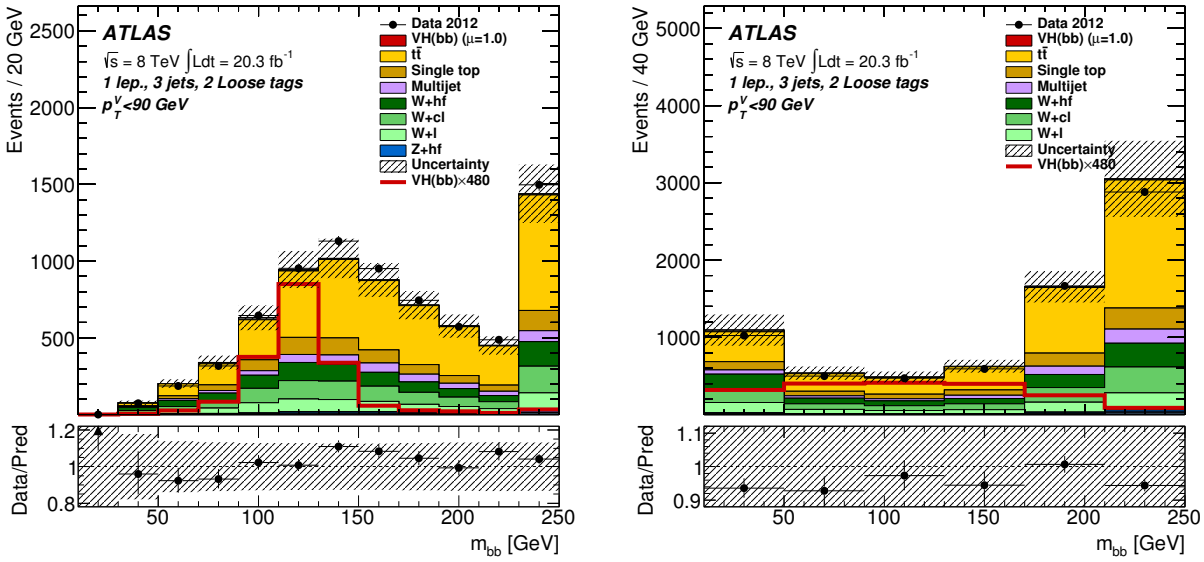

(a) un-transformed $m_{b\bar{b}}$ **(b)** transformed $m_{b\bar{b}}$

Figure 9.1: The effect of applying the bin-optimisation transformation used to increase the analysis sensitivity. The distributions are for the 3-jet, 2 loose-tagged b-jets with $p_{\mathrm{T}}^{V} < 90$ GeV. With the transformation, the sensitivity increases by 2% compared to no transformation.

In the global fit, the data have power to constrain the normalisations of the major background NPs which have been left free to float in the globl fit. In the case of the $WH \to l\nu b\bar{b}$ analysis this includes $t\bar{t}$, Wbb and Wcl. The resulting normalisations are shown in Table 9.5.

Process	Scale Factor
$t\bar{t}$	0.99 ± 0.07
Wbb	0.78 ± 0.13
Wcl	1.32 ± 0.11

Table 9.5: Normalisation scale factors applied to the $t\bar{t}$, Wbb and Wcl backgrounds, obtained from the global fit to data. The errors contain statistical and systematic uncertainties.

9.3. Post Fit Distributions & Yield Tables

The following subsections show the distributions and yield tables for the distributions which were input into the global fit for the signal and control regions. The distributions and yield tables are shown for the 2-jet category (3-jet post-fit distributions and yield tables are shown in Appendix A.3). Each signal or control region is split into the p_{T}^{V} categories used as part of the global fit. The distributions shown have been transformed using the procedure outlined in Section 9.2.

9.3.1. 2 jet, 1 b-Tag Control Region

The MV1c distribution is input into the global fit as it allows access to the flavour fractions which make up W/Z + jets processes. The events are split into two p_{T}^{V} categories; $p_{\mathrm{T}}^{V} < 120$ GeV and $p_{\mathrm{T}}^{V} > 120$ GeV. Figure 9.2 shows the MV1c distributions in the 1 b-tag control region for each p_{T}^{V} bin after applying the statisitical and systematic normalisations obtained during the global fit. The event yields are shown in Table 9.6 for the inclusive MV1c range for 2-jet events.

Both of the distributions and the yield tables show excellent agreement between the data and the total signal and background. The largest contributions to the background in both p_{T}^{V} bins come from $W+$jets which contribute to $> 80\%$ of the total background. The top backgrounds along with the $Z+$jets backgrounds make up most of the remaining 20%. In this category there are negligible contributions from the QCD multijet and small contributions from diboson processes.

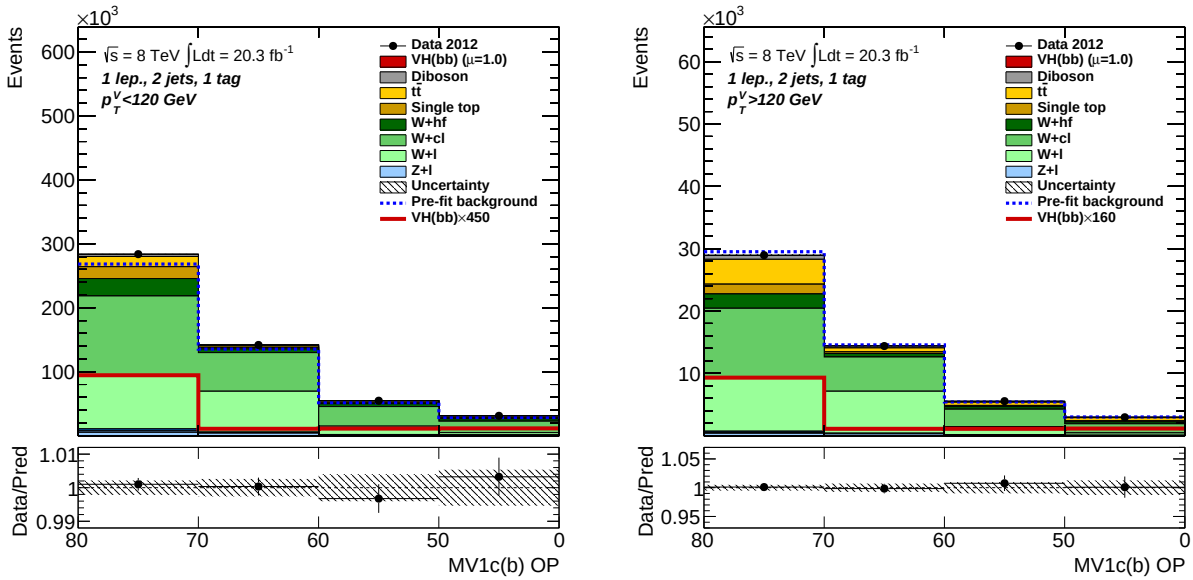

(a) $p_{\mathrm{T}}^{V} < 120$ GeV **(b)** $p_{\mathrm{T}}^{V} > 120$ GeV

Figure 9.2: MV1c distributions in the 1 b-tag control region after the application after the global fit for 2-jet events. The distributions shown are for the two p_{T}^{V} regions used as input to the fit; (a) $p_{\mathrm{T}}^{V} < 120$ GeV (b) $p_{\mathrm{T}}^{V} > 120$ GeV.

Sample	1-tag	
	$p_{\mathrm{T}}^{V} < 120$ GeV	$p_{\mathrm{T}}^{V} > 120$ GeV
VH	283.7 ± 100.1	79.0 ± 28.2
VV	6042.5 ± 163.6	1148.2 ± 131.5
$t\bar{t}$	22186.3 ± 1322.7	5601.9 ± 356.3
s-top	25520.5 ± 4393.0	2228.8 ± 167.8
W+l	162916.0 ± 13860.0	17022.6 ± 1423.0
W+cl	234586.6 ± 15510.4	20888.1 ± 1530.6
W+hf	40921.4 ± 6089.8	3570.7 ± 658.4
Z+l	10248.5 ± 1001.2	749.6 ± 94.4
Z+cl	4401.3 ± 119.2	277.5 ± 7.5
Z+hf	4221.1 ± 114.3	259.7 ± 7.0
Total	511327.8 ± 799.7	51826.2 ± 226.2
Data	511393	51826
$\frac{\text{Sim}-\text{Data}}{\sigma}$	-0.06	0.0

Table 9.6: Table of post-fit yields for 2-jet 1 b-tag events. The uncertainties are the full post-fit errors including all nuisance parameters with priors, floating normalizations, and the correlations deduced from the data. The difference in the data and the postfit simulation is compared to σ which is obtained from the sum in simulation as the sum in quadrature of the postfit and Poissonian error.

9.3.2. 2 jet, 2 LL b-Tag Signal Region

To increase the $WH \to l\nu b\bar{b}$ analysis sensitivity, semi-continuous b-tagging is implemented. There are three tagging categories within the 2 b-tagging region. The 'loose' category uses an 80% tagging efficiency. As with the other 2 b-tagging categories, for the loose region, the dijet mass distribution is input into the global fit. The post-fit distributions are shown in Figure 9.3 for the five p_{T}^{V} bins in the 2-jet category. Table 9.7 shows the event yields for each of the p_{T}^{V} bins in the 2-jet catefory.

The agreement between data and the total signal and background varies with each p_{T}^{V} bin. In all bins, the agreement is within the uncertainties. The largest contributions are the W+jets and top backgrounds, contributing more than 75% of the total background in all p_{T}^{V} bins. The other large background contribution is from the QCD multijet which has $\sim$10% at low p_{T}^{V}. There is an insignificant signal contribution in the lowest p_{T}^{V} bins.

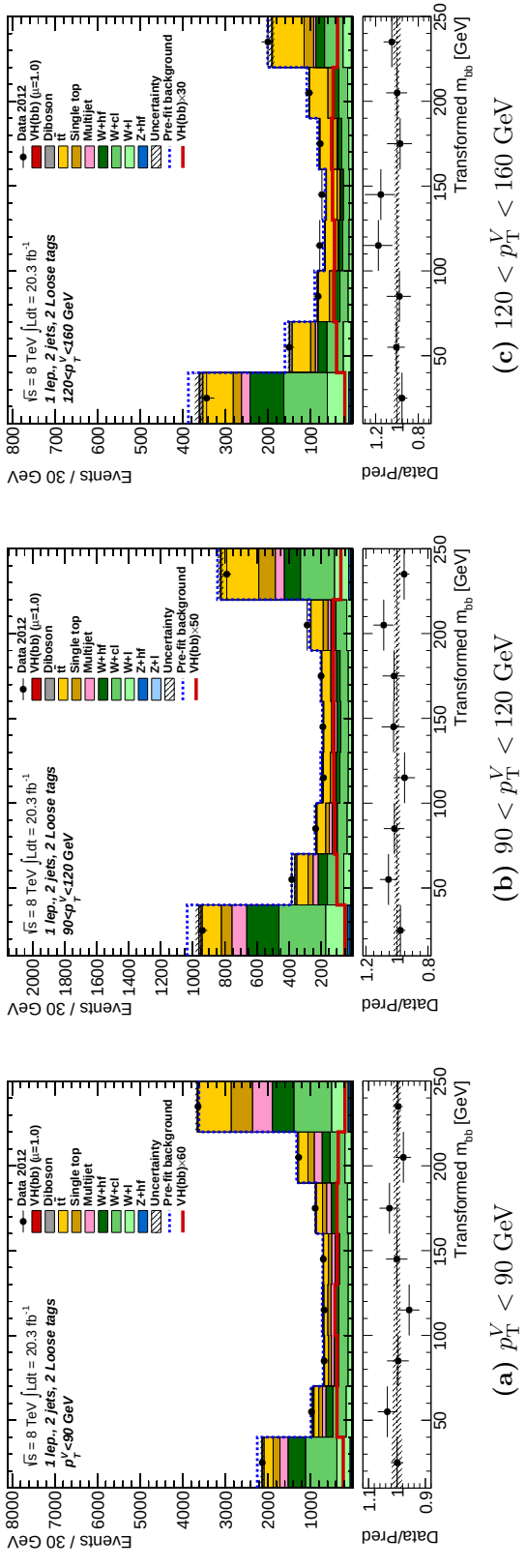

(b) $90 < p_{\mathrm{T}}^{V} < 120$ GeV

(c) $120 < p_{\mathrm{T}}^{V} < 160$ GeV

(a) $p_{\mathrm{T}}^{V} < 90$ GeV

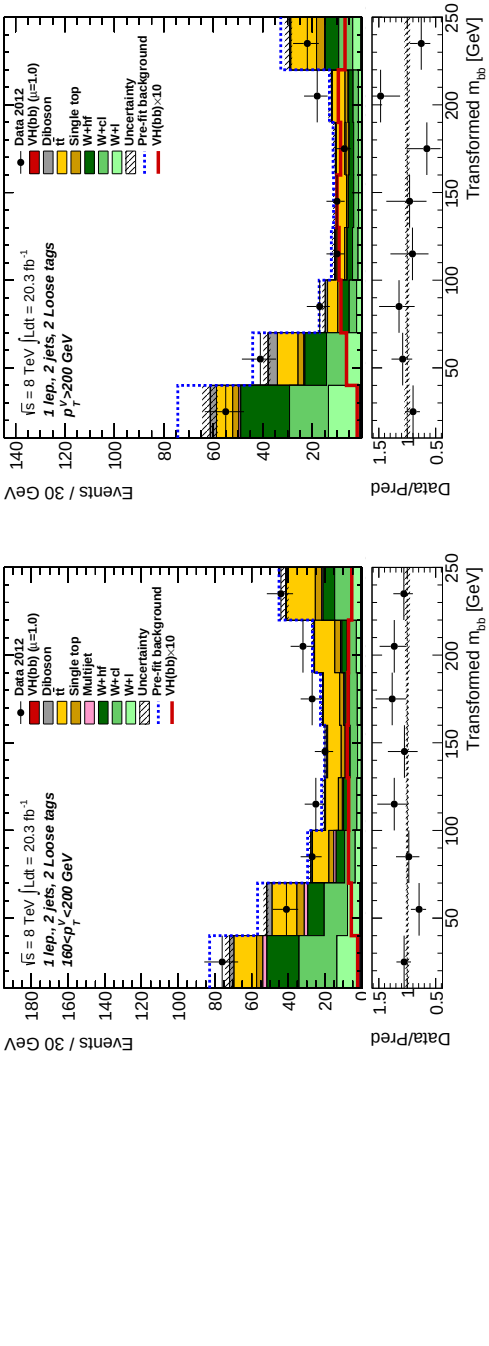

(e) $p_{\mathrm{T}}^{V} > 200$ GeV

(d) $160 < p_{\mathrm{T}}^{V} < 200$ GeV

Figure 9.3: Dijet mass distributions in the 2 loose b-tag region after the application of the global fit for 2-jet events. The distributions shown are for the five p_{T}^{V} bins used for the global fit; (a) $p_{\mathrm{T}}^{V} < 90$ GeV, (b) $90 < p_{\mathrm{T}}^{V} < 120$ GeV, (c) $120 < p_{\mathrm{T}}^{V} < 160$ GeV, (d) $160 < p_{\mathrm{T}}^{V} < 200$ GeV and (e) $p_{\mathrm{T}}^{V} > 200$ GeV.

Sample	2L-tag				
	$p_{\mathrm{T}}^{V} < 90$ GeV	$90 < p_{\mathrm{T}}^{V} < 120$ GeV	$120 < p_{\mathrm{T}}^{V} < 160$ GeV	$160 < p_{\mathrm{T}}^{V} < 200$ GeV	$p_{\mathrm{T}}^{V} > 200$ GeV
VH	44.5 ± 15.4	16.5 ± 5.7	10.9 ± 3.7	5.0 ± 1.7	6.0 ± 2.1
VV	129.2 ± 3.5	43.0 ± 1.2	21.3 ± 0.6	7.6 ± 1.3	8.2 ± 2.1
$t\bar{t}$	1804.1 ± 106.8	714.0 ± 43.5	338.7 ± 20.6	84.7 ± 5.4	45.7 ± 4.5
s-top	1215.9 ± 184.9	315.1 ± 45.3	96.1 ± 7.8	23.0 ± 1.7	13.8 ± 1.1
W+l	1345.4 ± 167.8	387.0 ± 47.9	129.4 ± 16.0	35.3 ± 4.5	28.8 ± 3.8
W+cl	3174.5 ± 193.1	887.2 ± 57.3	270.0 ± 18.2	66.3 ± 4.5	41.0 ± 3.2
W+hf	1711.6 ± 247.6	490.2 ± 74.8	169.0 ± 24.9	47.8 ± 7.0	44.9 ± 6.9
Z+l	105.0 ± 2.8	33.8 ± 4.2	9.0 ± 0.2	1.4 ± 0.0	0.6 ± 0.0
Z+cl	67.5 ± 1.8	24.9 ± 0.7	5.4 ± 0.1	0.9 ± 0.0	0.3 ± 0.0
Z+hf	148.7 ± 4.0	53.4 ± 1.4	11.7 ± 0.3	2.4 ± 0.1	0.8 ± 0.1
MJ_e	881.9 ± 89.2	215.0 ± 28.1	34.5 ± 10.8	7.2 ± 3.2	1.3 ± 0.6
MJ_μ	372.7 ± 94.3	46.6 ± 12.0	8.8 ± 0.0	1.6 ± 1.2	0.5
Total	11001.0 ± 93.0	3226.8 ± 40.1	1104.8 ± 17.1	283.3 ± 4.9	191.8 ± 6.1
Data	10946	3200	1107	292	180
$\frac{\mathrm{Sim-Data}}{\sigma}$	0.39	0.38	-0.06	-0.5	0.78

Table 9.7: Table of post fit yields for 2-jet 2L-tag events. The uncertainties are the full postfit errors including all nusicance parameters with priors, floating normalizations, and the correlations deduced from the data. The difference in the data and the postfit simulation is compared to σ which is obtained from the sum in simulation as the sum in quadrature of the postfit and Poissonian error.

9.3.3. 2 jet, 2 MM b-Tag Signal Region

The second b-tagging category is the 'medium' (M) tagged region, which uses a 70% tagging efficiency. The dijet mass distributions are input into the global fit and are shown in Figure 9.4 after the with the normalisation applied for the five p_{T}^{V} bins and for 2-jet events. The event yields for each p_{T}^{V} bin in the 2-jet, medium tagged category are shown in Table 9.8.

In all p_{T}^{V} bins, there is good agreement between data and total background and signal. Comparing to the loose region, there is a larger contribution to the total background from $W+\mathrm{hf}$ processes. The top ($t\bar{t}$ and single-top) backgrounds contribute $\sim$60% of the total backgrounds at low p_{T}^{V}. In the highest p_{T}^{V} bin, the signal has a 10% contribution compared to $\sim$1% at low p_{T}^{V}. As for the loose category, the QCD multijet has a large contribution at low p_{T}^{V}(10%). As the p_{T}^{V} increases, the QCD multijet background contribution becomes negligible.

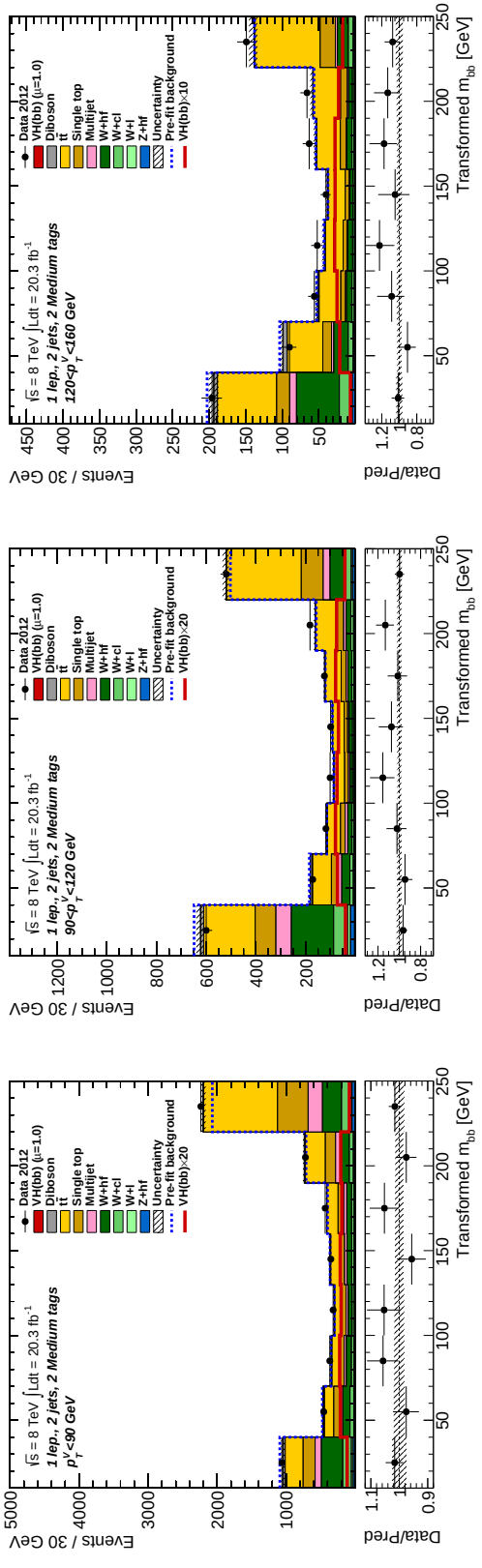

(b) $90 < p_{\mathrm{T}}^{V} < 120$ GeV

(c) $120 < p_{\mathrm{T}}^{V} < 160$ GeV

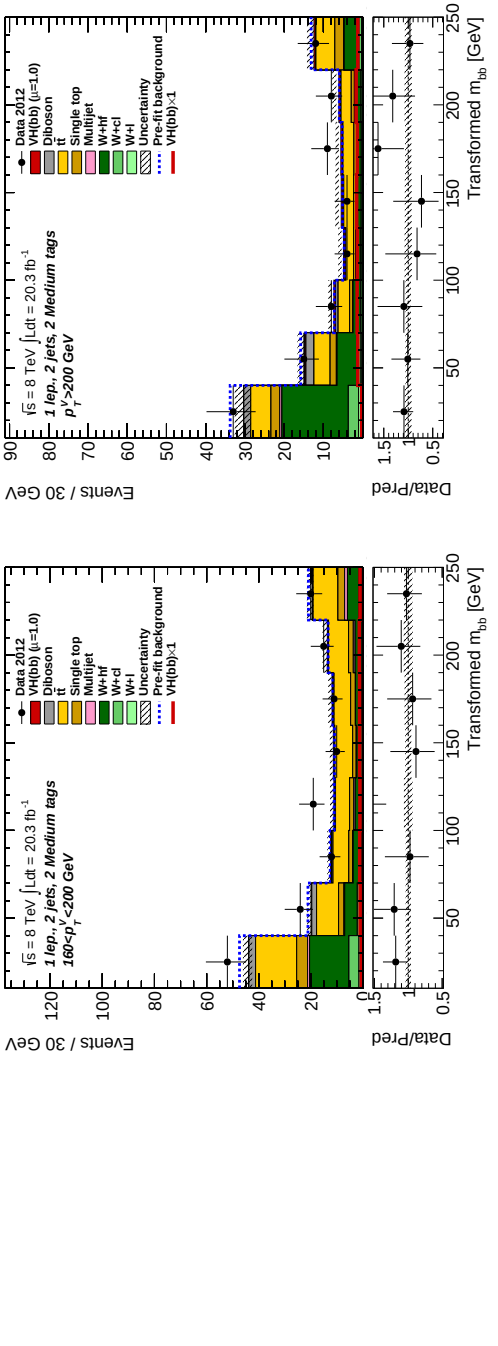

(d) $160 < p_{\mathrm{T}}^{V} < 200$ GeV

(e) $p_{\mathrm{T}}^{V} > 200$ GeV

Figure 9.4: Dijet mass distributions in the 2 medium b-tag region after the application of the global fit for 2-jet events. The distributions shown are for the five p_{T}^{V} bins used for the global fit; (a) $p_{\mathrm{T}}^{V} < 90$ GeV, (b) $90 < p_{\mathrm{T}}^{V} < 120$ GeV, (c) $120 < p_{\mathrm{T}}^{V} < 160$ GeV, (d) $160 < p_{\mathrm{T}}^{V} < 200$ GeV and (e) $p_{\mathrm{T}}^{V} > 200$ GeV.

Sample	2M-tag				
	$p_{\mathrm{T}}^{V} < 90$ GeV	$90 < p_{\mathrm{T}}^{V} < 120$ GeV	$120 < p_{\mathrm{T}}^{V} < 160$ GeV	$160 < p_{\mathrm{T}}^{V} < 200$ GeV	$p_{\mathrm{T}}^{V} > 200$ GeV
VH	73.3 ± 25.0	26.3 ± 9.0	17.6 ± 6.0	8.5 ± 2.9	10.1 ± 3.4
VV	83.0 ± 5.1	28.2 ± 2.4	14.6 ± 1.9	5.7 ± 1.2	5.0 ± 1.5
$t\bar{t}$	2272.7 ± 124.5	876.9 ± 49.2	365.9 ± 20.4	66.4 ± 4.0	26.9 ± 2.6
s-top	1137.1 ± 155.7	290.6 ± 38.7	84.9 ± 7.6	16.9 ± 1.4	10.1 ± 0.9
W+l	94.0 ± 18.5	26.7 ± 5.1	7.8 ± 1.5	2.1 ± 0.4	1.6 ± 0.3
W+cl	504.1 ± 40.4	139.4 ± 11.1	40.6 ± 3.4	9.8 ± 0.8	5.8 ± 0.5
W+hf	1081.2 ± 155.8	334.7 ± 45.8	123.9 ± 16.9	34.1 ± 4.6	32.8 ± 4.5
Z+l	7.4 ± 0.2	3.0 ± 0.1	0.6 ± 0.0	0.1 ± 0.0	0.0 ± 0.0
Z+cl	12.8 ± 0.3	4.8 ± 0.1	1.0 ± 0.0	0.2 ± 0.0	0.1 ± 0.0
Z+hf	112.0 ± 24.5	42.7 ± 9.5	9.0 ± 2.7	1.4 ± 0.4	0.5 ± 0.1
MJ_e	407.1 ± 57.8	133.8 ± 22.3	19.2 ± 4.7	3.7 ± 2.1	1.0 ± 0.4
MJ_μ	153.7 ± 54.7	13.3 ± 0.0	2.4 ± 1.1	0.2 ± 0.1	–
Total	5938.2 ± 67.1	1920.3 ± 27.3	687.5 ± 12.9	149.1 ± 3.8	93.9 ± 4.3
Data	5951	1914	712	163	93
$\frac{\mathrm{Sim-Data}}{\sigma}$	-0.13	0.12	-0.84	-1.08	0.09

Table 9.8: Table of post fit yields for 2-jet 2M-tag events. The uncertainties are the full postfit errors including all nusicance parameters with priors, floating normalizations, and the correlations deduced from the data. The difference in the data and the postfit simulation is compared to σ which is obtained from the sum in simulation as the sum in quadrature of the postfit and Poissonian error.

9.3.4. 2 jet, 2 TT b-Tag Signal Region

The final tagging category used for the global fit is the 'tight' (T) tagged region. The b-tagging efficiency used for tight jets is 50%. Post fit di-jet mass distributions are shown in Figure 9.5 for the five p_{T}^{V} bins in 2-jet events. Table 9.9 shows the yield tables for each p_{T}^{V} bin in the 2-jet tight tagged category.

The tight category is the most sensitive region with the signal having a 20% contribution in the highest p_{T}^{V} bin. At low p_{T}^{V} the major backgrounds are the $t\bar{t}$ and single-top which contribute $> 50\%$. At high p_{T}^{V}, the top backgrounds have decreased with the major background being W + hf with a 40% share of the total background. Similarly for the loose and medium regions, the QCD multijet background has a much greater contribution at low p_{T}^{V}than at high p_{T}^{V}. At low p_{T}^{V}, the contribution in the tight category is 5%, falling to a negligible amount at higher p_{T}^{V} bins.

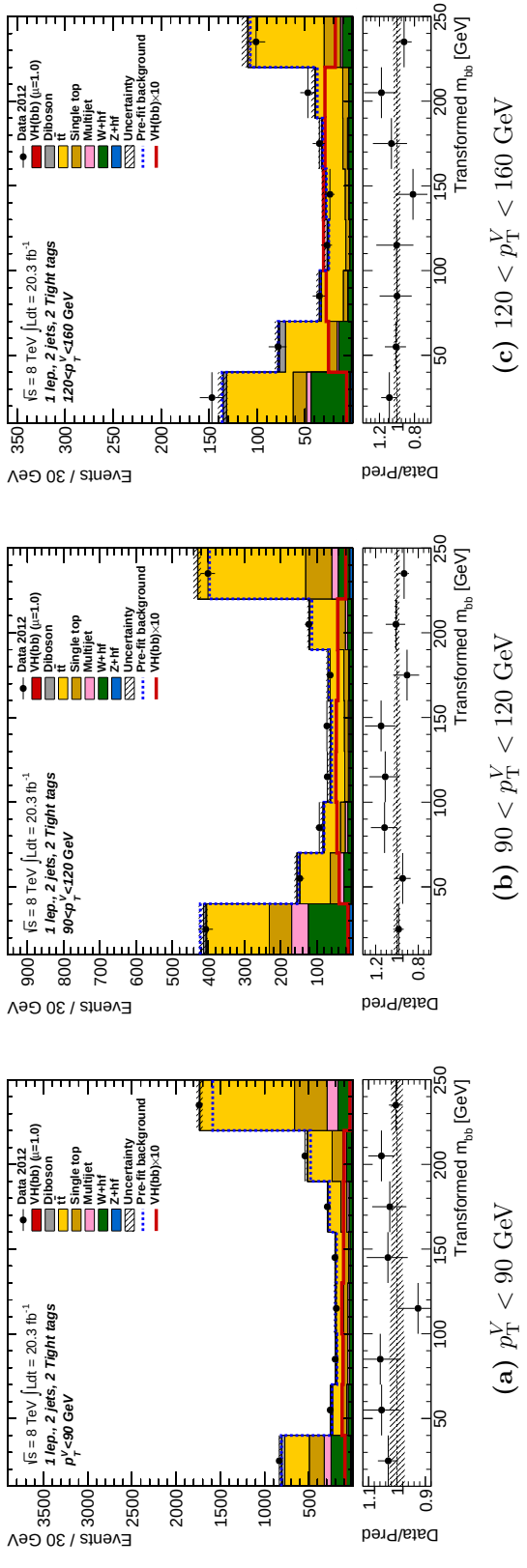

(b) $90 < p_{\mathrm{T}}^{V} < 120$ GeV

(c) $120 < p_{\mathrm{T}}^{V} < 160$ GeV

(a) $p_{\mathrm{T}}^{V} < 90$ GeV

(d) $160 < p_{\mathrm{T}}^{V} < 200$ GeV

(e) $p_{\mathrm{T}}^{V} > 200$ GeV

Figure 9.5: Dijet mass distributions in the 2 tight b-tag region after the application of the global fit for 2-jet events. The distributions shown are for the five p_{T}^{V} bins used for the global fit; (a) $p_{\mathrm{T}}^{V} < 90$ GeV, (b) $90 < p_{\mathrm{T}}^{V} < 120$ GeV, (c) $120 < p_{\mathrm{T}}^{V} < 160$ GeV, (d) $160 < p_{\mathrm{T}}^{V} < 200$ GeV and (e) $p_{\mathrm{T}}^{V} > 200$ GeV.

Sample	2T-tag				
	$p_{\mathrm{T}}^{V} < 90$ GeV	$90 < p_{\mathrm{T}}^{V} < 120$ GeV	$120 < p_{\mathrm{T}}^{V} < 160$ GeV	$160 < p_{\mathrm{T}}^{V} < 200$ GeV	$p_{\mathrm{T}}^{V} > 200$ GeV
VH	79.6 ± 26.9	29.3 ± 9.8	19.8 ± 6.6	10.6 ± 3.5	10.9 ± 3.6
VV	65.8 ± 5.2	22.7 ± 2.4	12.8 ± 1.9	5.1 ± 1.1	4.5 ± 1.4
$t\bar{t}$	2125.7 ± 115.6	799.3 ± 44.5	303.2 ± 16.7	35.5 ± 2.3	7.6 ± 0.8
s-top	929.0 ± 125.0	224.9 ± 30.2	64.0 ± 6.9	11.2 ± 1.1	4.1 ± 0.4
W+l	4.2 ± 0.1	1.0 ± 0.0	0.3 ± 0.0	0.1 ± 0.0	0.0 ± 0.0
W+cl	25.2 ± 4.6	7.6 ± 1.6	2.5 ± 0.4	0.4 ± 0.1	0.3 ± 0.1
W+hf	585.1 ± 89.6	203.7 ± 28.5	80.3 ± 11.3	24.7 ± 3.5	23.8 ± 3.4
Z+l	0.1 ± 0.0	0.1 ± 0.0	0.0 ± 0.0	0.0 ± 0.0	0.0 ± 0.0
Z+cl	0.5 ± 0.0	0.1 ± 0.0	0.0 ± 0.0	0.0 ± 0.0	0.0 ± 0.0
Z+hf	71.9 ± 21.1	29.2 ± 8.3	5.6 ± 1.7	1.1 ± 0.4	0.6 ± 0.2
MJ_e	253.7 ± 61.4	93.3 ± 20.9	10.9 ± 4.6	1.6 ± 1.3	1.6 ± 1.1
MJ_μ	86.6 ± 50.9	7.7 ± 4.7	0.6 ± 0.3	–	–
Total	4227.3 ± 56.0	1418.9 ± 25.3	500.1 ± 11.9	90.3 ± 3.4	53.5 ± 4.0
Data	4255	1376	494	86	51
$\frac{\mathrm{Sim-Data}}{\sigma}$	-0.32	0.95	0.24	0.42	0.3

Table 9.9: Table of post fit yields for 2-jet 2T-tag events. The uncertainties are the full postfit errors including all nusicance parameters with priors, floating normalizations, and the correlations deduced from the data. The difference in the data and the postfit simulation is compared to σ which is obtained from the sum in simulation as the sum in quadrature of the postfit and Poissonian error.

9.4. Limit Extraction

As described in Section 9.2, the limit is extracted from a maximum-likelihood fit to data using the distributions outlined in Table 9.4 and nuisance parameters either floating or constrained with priors. The nominal limit extraction is shown using the current jet calibrations in Section 9.4.1. An expected limit is extracted for the proposed jet calibrations from Sections 6.2 and 6.3, with comparisons made to the nominal analysis in Section 9.4.2.

9.4.1. Nominal Expected & Observed Limit

The nominal analysis is defined as using all the nominal jet calibrations (JES, GSC, muon-in-jet and jet p_{T} calibration). The MV1c and the dijet mass distributions scaled using parameters obtained using the global fit method are shown in Section 9.3 for the 1 b-tag and 2 b-tag respective regions. Both and observed and expected $\mathrm{CL_S}$ limit on the Higgs boson production cross-section times branching fraction for the $WH \to l\nu b\bar{b}$ process for a Higgs boson in the mass range $110 \leq m_{\mathrm{H}} \leq 140$ GeV have been calculated in 5 GeV bins with the results shown in Figure 9.6 of the expected and observed limit. The green and yellow bands represent the respective ± 1 and $\pm 2\sigma$ ranges of the expected limit in the absense of signal. The values for the expected and observed limit for each mass point are shown in Table 9.10. For $m_{\mathrm{H}} = 125$ GeV, the expected limit in the absense of signal is 1.51 times the Standard Model value, The observed limit is found to be 4.57 times the Standard Model.

The fitted signal strength parameter, μ for $m_{\mathrm{H}} = 125$ GeV in the nominal $WH \to l\nu b\bar{b}$ analysis is calculated as $\mu = 3.22^{+0.71}_{-0.69}(\mathrm{stat.})^{1.03}_{-0.87}(\mathrm{syst.})$. This result is compatible with that calculated for the dijet analysis in the 1-lepton channel in the most recent publication. The value obtained for the dijet analysis cross-check in the most recent publication for the search for the Higgs boson decaying to a pair of b-quarks, produced in association with a vector boson [48] was calculated to be $\mu = 1.23 \pm 0.44(\mathrm{stat.}) \pm 0.41(\mathrm{syst.})$. This result however is a combination of three channels, as opposed to the single channel analysed in this thesis.

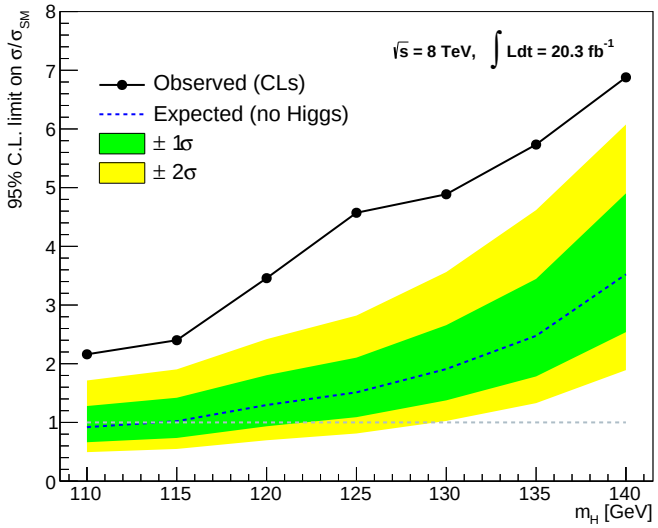

Figure 9.6: The expected (dashed) and observed (solid) upper limits on the total cross-section divided by the expected Standard Model Higgs boson cross-section times branching fraction, calculated using CL_S at 95% for both statisitcal and systematic uncertainties. The green and yellow bands centered on the expected line indicate the respective $\pm 1\sigma$ and $\pm 2\sigma$ ranges in which the statistical limit is expected to lie in the absense of a signal. The dashed grey line indicates the Standard Model expectation value of 1.

m_H (GeV)	Expected $(\sigma/\sigma_{\mathrm{SM}})$	Observed $(\sigma/\sigma_{\mathrm{SM}})$
$m_{\mathrm{H}} = 110$	0.92	2.16
$m_{\mathrm{H}} = 115$	1.02	2.40
$m_{\mathrm{H}} = 120$	1.30	3.46
$m_{\mathrm{H}} = 125$	1.51	4.57
$m_{\mathrm{H}} = 130$	1.91	4.89
$m_{\mathrm{H}} = 135$	2.48	5.73
$m_{\mathrm{H}} = 140$	3.52	6.88

Table 9.10: For each mass point used to calculate the CL_S at 95% for statistical and systematic uncertainties, the expected and observed upper limits on the total cross-section times branching fraction.

9.4.2. Additional Jet Calibration Expected Limit

Chapter 6 describes additional jet calibration methods for use as part of the analysis. in the form of a re-derivation of the jet p_{T} calibration ($p_{\mathrm{T}}^{\mathrm{Reco}}$) done separately for jets with a muon in the cone and for jets which do not contain a muon ($p_{\mathrm{T}}^{\mu,\mathrm{Reco}}$). An additional jet calibration in the form of a regression has also been investigated. This section compares the expected limits between the nominal analysis described in the previous section to the expected limits extracted by replacing the nominal $p_{\mathrm{T}}^{\mathrm{Reco}}$ with first the $p_{\mathrm{T}}^{\mu,\mathrm{Reco}}$ and finally the $p_{\mathrm{T}}^{\mu,\mathrm{Reco}}$ with a regression in addition. Only the expected limit is calculated as this is used as a measure of the power of the jet calibrations as part of the analysis.

The procedure for extracting the expected limit with the alternate jet calibration remains unchanged from the nominal analysis. A comparison between the nominal analysis, using $p_{\mathrm{T}}^{\mu,\mathrm{Reco}}$ and the regression expected limits are given for each mass point in Table 9.11. The mass range used is unchanged from the nominal; $110 \leq m_{\mathrm{H}} \leq 140$ GeV split into 5 GeV bins. At $m_{\mathrm{H}} = 125$ GeV, there is a $< 1\%$ improvement in the expected limit. The addition of the regression negates this improvement as the value decreases by 1.5% from the nominal analysis. These results are displayed in Figure 9.7.

m_H (GeV)	Nominal ($\sigma/\sigma_{\mathrm{SM}}$)	$p_{\mathrm{T}}^{\mu,\mathrm{Reco}}$($\sigma/\sigma_{\mathrm{SM}}$)	$p_{\mathrm{T}}^{\mu,\mathrm{Reco}}$ + Regression ($\sigma/\sigma_{\mathrm{SM}}$)
$m_{\mathrm{H}} = 110$	0.92	0.93	0.92
$m_{\mathrm{H}} = 115$	1.02	1.04	1.04
$m_{\mathrm{H}} = 120$	1.30	1.27	1.25
$m_{\mathrm{H}} = 125$	1.51	1.50	1.53
$m_{\mathrm{H}} = 130$	1.91	1.87	1.90
$m_{\mathrm{H}} = 135$	2.48	2.43	2.44
$m_{\mathrm{H}} = 140$	3.52	3.40	3.40

Table 9.11: Comparing the expected upper limits on the total Higgs boson cross-section times branching fraction of the $WH \to l\nu b\bar{b}$ process in the absense of signal between the nominal analysis, replacing the final jet p_{T} calibration with one derived separately for jets with muons and jets without muons ($p_{\mathrm{T}}^{\mu,\mathrm{Reco}}$) and using a regression in addition to $p_{\mathrm{T}}^{\mu,\mathrm{Reco}}$.

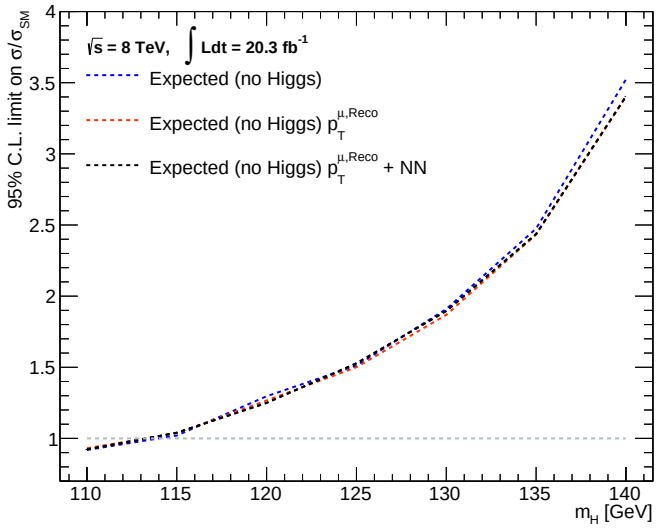

Figure 9.7: The expected upper limits on the total cross-section times branching fraction divided by the expected Standard Model Higgs boson cross-section times branching fraction calculated using CL_S at 95%. Comparing the nominal (Blue) to $p_T^{\mu,\text{Reco}}$(red) and a regression in addition to the $p_T^{\mu,\text{Reco}}$. The dashed grey line represents the Standard Model expectation value of 1.

The results obtained for the expected limit using alternate jet calibrations are in agreement with the trends which were obtained during the sensitivity calculations. The $p_T^{\mu,\text{Reco}}$ calibration offers some improvement whereas the regression offers very little improvement if any at all. For the regression, the input variables used do not offer enough for the training to learn from to improve the b-jet resolution which in turn can improve the limit extracted. By adding variables which could allow improved learning, a notable improvement can be earned. A description of adding a final neural network utilising additional variables can be found in Section 6.3.1.

A comparison between the nominal analysis and replacing the p_T^{Reco} with $p_T^{\mu,\text{Reco}}$and the new regression is shown in Table 9.12 for each mass point. At $m_H = 125$ GeV, a potential 2.5% improvement against the nominal analysis is achieved by utilising the secondary vertex variables in the regression training. The largest improvements are found to be at $m_H = 120$ GeV A comparison between the nominal, $p_T^{\mu,\text{Reco}}$and $p_T^{\mu,\text{Reco}}$with the new regression in addition is shown in Figure 9.8.

m_H (GeV)	Nominal ($\sigma/\sigma_{\mathrm{SM}}$)	$p_{\mathrm{T}}^{\mu,\mathrm{Reco}}$($\sigma/\sigma_{\mathrm{SM}}$)	$p_{\mathrm{T}}^{\mu,\mathrm{Reco}}$ + Regression ($\sigma/\sigma_{\mathrm{SM}}$)
$m_{\mathrm{H}} = 110$	0.92	0.93	0.91
$m_{\mathrm{H}} = 115$	1.02	1.04	1.03
$m_{\mathrm{H}} = 120$	1.30	1.27	1.18
$m_{\mathrm{H}} = 125$	1.51	1.50	1.47
$m_{\mathrm{H}} = 130$	1.91	1.87	1.89
$m_{\mathrm{H}} = 135$	2.48	2.43	2.49
$m_{\mathrm{H}} = 140$	3.52	3.40	3.40

Table 9.12: Comparisons between the nominal analysis, $p_{\mathrm{T}}^{\mu,\mathrm{Reco}}$and a different regression using poorly modelled variables of the expected upper limit on the total Higgs boson cross-section times branching fraction of the $WH \to l\nu b\bar{b}$ process in the absense of signal.

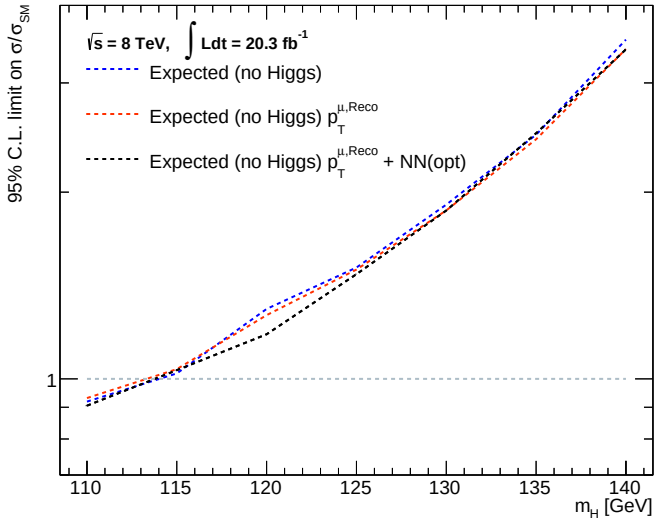

Figure 9.8: The expected upper limits on the total cross-section times branching fraction divided by the expected Standard Model Higgs boson cross-section times branching fraction calculated using $\mathrm{CL_S}$ at 95%. Comparing the nominal (Blue) to $p_{\mathrm{T}}^{\mu,\mathrm{Reco}}$(red) and a regression with additional secondary vertex variables in the training,in addition to the $p_{\mathrm{T}}^{\mu,\mathrm{Reco}}$. The dashed grey line represents the Standard Model expectation value of 1.

Chapter 10

Conclusions

The discovery of a new scalar boson in 2012 by the ATLAS and CMS experiements at the LHC completed the particle content of the Standard Model. The discovered particle has been studied during Run I, with the evidence collected so far suggesting the new boson is compatible with the Standard Model. The signal strength measured with respect to the Standard Model value by ATLAS and CMS is $1.18^{+0.10}_{-0.10}(\text{stat.})^{+0.11}_{-0.10}(\text{syst.})^{+0.08}_{-0.07}(\text{theo.})$ and $1.00 \pm 0.09(\text{stat.}) \pm 0.08(\text{syst.})^{+0.18}_{-0.17}(\text{theo.})$ respectively. The basis of this thesis has been the search for the Higgs boson decaying to a pair of b-quarks, produced in association with a vector boson. Both ATLAS and CMS have produced results in this decay mode. The dijet mass signal strength measured in a combination of three channels at ATLAS was $\mu = 1.23 \pm 0.44(\text{stat.}) \pm 0.41(\text{syst.})$ [48] and $\mu = 0.8 \pm 0.7$ at CMS [49].

This thesis independantly confirmed and built on the result for the cut-based $WH \to l\nu b\bar{b}$ analysis presented in [48], where a Higgs boson is produced in association with a W boson. The W boson decays leptonically to a electron-neutrino or muon-neutrino pair, and the Higgs boson decays to a pair of b-quarks.

The events selected as part of the analysis are categorised initially by the number of jets in the event, either two or three. By applying semi-continuous b-tagging to the categorised events allows the analysis sensitivity to improve. Four categories of b-tagging are used in total; split by the b-tagging efficiency. Further categorisation is applied by splitting each b-tagging category into two p_{T}^{V} bins for 1 b-tag events, and five p_{T}^{V} bins for each of the 2 b-tagging categories. Splitting by p_{T}^{V} allows a range of topological cuts to be applied, increasing the overall sensitivity of the analysis and suppressing the backgrounds.

The largest background contributions come from W + jets and $t\bar{t}$, with smaller contributions coming from single-top, diboson, QCD multijet and Z + jets. All the backgrounds with the exception of the QCD multijet are estimated using Monte Carlo

simulated events. The normalisations of the W/Z + jets heavy flavour is performed in the 1 b-tag control region. The remaining normalisations are constrained initially with comparisons to other Monte Carlo generators before being allowed to float within the uncertainties in the global fit.

Data collected from proton-proton collisions at the ATLAS detector at a centre-of-mass energy of $\sqrt{s} = 8$ TeV corresponding to an integrated luminosity of 20 fb^{-1} has been analysed. After the event selection is applied, a full log-likelihood fit has been performed. The background only upper limit has been calculated to be 1.51 times the Standard Model expectation. The measured signal strength parameter μ for a Higgs boson mass $m_H = 125$ GeV has been measured to be $\mu = 3.22^{+0.71}_{-0.69}(\text{stat.})^{+1.03}_{-0.87}(\text{syst.})$, which is compatible with the value obtained for the cut-based $WH \to l\nu b\bar{b}$ analysis in [48]. The signal strength for the cut-based analysis of a Higgs boson decaying to a pair of b-quarks, produced in association with a vector boson as measured on CMS as $\mu = 0.8 \pm 0.7$ [49].

Additional work has been performed in studying the current jet calibrations used as part of the Run I $WH \to l\nu b\bar{b}$ analysis. Two additional jet calibrations have been derived in order to increase the jet resolution and improve the analysis sensitivity. The first jet calibration is a jet p_{T} calibration applied using different calibrations depending upon whether the jet contains a muon or not. With the application of this calibration, the expected limit improved to 1.50 times the Standard Model expectation. The second additional jet calibration applied was a regression trained separately for 2- and 3-jet events. Well modelled variables were used as part of a training to improve the jet resolution. The application of the regression saw a negligible change in the jet resolution and expected limit in comparison to the additional jet p_{T} calibration.

As a test of the potential improvement to the expected limit by using a regression, a training was performed using all available variables irrespective of modelling. By applying this regression a 2.5% improvement was gained in the expected limit. With improved modelling of secondary vertex variables, a regression has the potential to add improvement to the $WH \to l\nu b\bar{b}$ analysis sensitivity.

2015 marks the beginning of Run II at the LHC with data currently being collected from collisions at a centre-of-mass energy $\sqrt{s} = 13$ TeV. The data collected during Run II will be used for continuing the search for the Higgs boson decaying to fermions, which as yet is undiscovered. By applying the newly derived jet calibrations to Run II analyses, the seach for $H \to b\bar{b}$ could come a step closer.

Bibliography

[1] G. Altarelli, *The Standard model of particle physics*, 2005, arXiv:hep-ph/0510281 [hep-ph].

[2] RAL, *Proceedings of the Summer School for Experimental Particle Physics Students*, 2011. http://www.stfc.ac.uk/PPD/resources/pdf/HEPSSproceedings2011v2.pdf.

[3] A. Bettini, *Introduction to Elementary Particle Physics*. Cambridge University Press, 2008.

[4] R. P. Feynman, *Mathematical Formulation of the Quantum Theory of Electromagnetic Interaction*, Phys. Rev. **80** (1950) 440–457. http://link.aps.org/doi/10.1103/PhysRev.80.440.

[5] J. Beringer et al. Phys. Rev. D **86** (2012) 010001.

[6] D. Griffiths, *Introduction to Elementary Particles*. Wiley, 2008.

[7] S. Weinberg, *A Model of Leptons*, Phys. Rev. Lett. **19** (1967) 1264–1266.

[8] A. Salam, *Weak and Electromagnetic Interactions*, Conf.Proc. **C680519** (1968) 367–377.

[9] Gargamelle Neutrino Collaboration, *Observation of neutrino-like interactions without muon or electron in the gargamelle neutrino experiment*, Physics Letters B **46** no. 1, (1973) 138 – 140.

[10] UA1 Collaboration, *Experimental observation of isolated large transverse energy electrons with associated missing energy at s=540*, Physics Letters B **122** no. 1, (1983) 103 – 116.

[11] UA1 Collaboration, *Experimental observation of lepton pairs of invariant mass around 95 GeV/c2 at the CERN SPS collider*, Physics Letters B **126** no. 5, (1983) 398 – 410.

[12] UA2 Collaboration, *Observation of single isolated electrons of high transverse momentum in events with missing transverse energy at the CERN pp collider*, Physics Letters B **122** no. 56, (1983) 476 – 485.

[13] UA2 Collaboration, *Evidence for Z0e+e at the CERN pp collider*, Physics Letters B **129** no. 12, (1983) 130 – 140.

[14] P. W. Higgs, *Broken Symmetries and the Masses of Gauge Bosons*, Phys. Rev. Lett. **13** (1964) 508–509.

[15] P. W. Higgs, *Broken Symmetries and the Masses of Gauge Bosons*, Phys. Rev. Lett. **13** (1964) 508–509.

[16] P. W. Higgs, *Spontaneous Symmetry Breakdown without Massless Bosons*, Phys. Rev. **145** (1966) 1156–1163.

[17] F. Englert and R. Brout, *Broken Symmetry and the Mass of Gauge Vector Mesons*, Phys. Rev. Lett. **13** (1964) 321–323.

[18] G. S. Guralnik, C. R. Hagen, and T. W. B. Kibble, *Global Conservation Laws and Massless Particles*, Phys. Rev. Lett. **13** (1964) 585–587.

[19] *The LEP Electroweak Working Group*, August, 2003. http://lepewwg.web.cern.ch/LEPEWWG/.

[20] ATLAS Collaboration, *Observation of a new particle in the search for the Standard Model Higgs boson with the ATLAS detector at the LHC*, Phys.Lett. **B716** (2012) 1–29, arXiv:1207.7214 [hep-ex].

[21] CMS Collaboration, *Observation of a new boson at a mass of 125 GeV with the CMS experiment at the LHC*, Phys.Lett. **B716** (2012) 30–61, arXiv:1207.7235 [hep-ex].

[22] J. M. Campbell, J. Huston, and W. Stirling, *Hard Interactions of Quarks and Gluons: A Primer for LHC Physics*, Rept.Prog.Phys. **70** (2007) 89, arXiv:hep-ph/0611148 [hep-ph].

[23] G. Altarelli and G. Parisi, *Asymptotic Freedom in Parton Language*, Nucl.Phys. **B126** (1977) 298.

[24] M. Dobbs, S. Frixione, E. Laenen, K. Tollefson, H. Baer, et al., *Les Houches guidebook to Monte Carlo generators for hadron collider physics*, 2004, arXiv:hep-ph/0403045 [hep-ph].

[25] T. Sjostrand, *Monte Carlo Generators*, 2006, arXiv:hep-ph/0611247 [hep-ph].

[26] T. Sjostrand, S. Mrenna, and P. Z. Skands, *A Brief Introduction to PYTHIA 8.1*, Comput.Phys.Commun. **178** (2008) 852–867, arXiv:0710.3820 [hep-ph].

[27] J. Pumplin, D. Stump, J. Huston, H. Lai, P. M. Nadolsky, et al., *New generation of parton distributions with uncertainties from global QCD analysis*, JHEP **0207** (2002) 012, arXiv:hep-ph/0201195 [hep-ph].

[28] T. Gleisberg, S. Hoeche, F. Krauss, M. Schonherr, S. Schumann, et al., *Event generation with SHERPA 1.1*, JHEP **0902** (2009) 007, arXiv:0811.4622 [hep-ph].

[29] H.-L. Lai, M. Guzzi, J. Huston, Z. Li, P. M. Nadolsky, et al., *New parton*

distributions for collider physics, Phys.Rev. **D82** (2010) 074024, arXiv:1007.2241 [hep-ph].

[30] C. Oleari, *The POWHEG-BOX*, Nucl.Phys.Proc.Suppl. **205-206** (2010) 36–41, arXiv:1007.3893 [hep-ph].

[31] B. P. Kersevan and E. Richter-Was, *The Monte Carlo event generator AcerMC versions 2.0 to 3.8 with interfaces to PYTHIA 6.4, HERWIG 6.5 and ARIADNE 4.1*, Comput.Phys.Commun. **184** (2013) 919–985, arXiv:hep-ph/0405247 [hep-ph].

[32] LHC Higgs Cross Section Working Group Collaboration, *Handbook of LHC Higgs Cross Sections: 1. Inclusive Observables*, 2011, arXiv:1101.0593 [hep-ph].

[33] H. M. Georgi, S. L. Glashow, M. E. Machacek, and D. V. Nanopoulos, *Higgs Bosons from Two-Gluon Annihilation in Proton-Proton Collisions*, Phys. Rev. Lett. **40** (1978) 692–694.

[34] S. Asai, G. Azuelos, C. Buttar, V. Cavasinni, D. Costanzo, et al., *Prospects for the search for a standard model Higgs boson in ATLAS using vector boson fusion*, Eur.Phys.J. **C32S2** (2004) 19–54, arXiv:hep-ph/0402254 [hep-ph].

[35] A. Stange, W. J. Marciano, and S. Willenbrock, *Associated production of Higgs and weak bosons, with $H \to b$ anti-b, at hadron colliders*, Phys.Rev. **D50** (1994) 4491–4498, arXiv:hep-ph/9404247 [hep-ph].

[36] J. Cammin and M. Schumacher, *The ATLAS discovery potential for the channel ttH, H to bb*, Jun, 2003. http://cds.cern.ch/record/685523.

[37] LHC Higgs Cross Section Working Group Collaboration, S. Heinemeyer et al., *Handbook of LHC Higgs Cross Sections: 3. Higgs Properties*, 2013, arXiv:1307.1347 [hep-ph].

[38] A. Djouadi, J. Kalinowski, and M. Spira, *HDECAY: A Program for Higgs boson decays in the standard model and its supersymmetric extension*, Comput.Phys.Commun. **108** (1998) 56–74, arXiv:hep-ph/9704448 [hep-ph].

[39] ALEPH Collaboration, *ALEPH: Technical Report 1983*, 1983. http://aleph.web.cern.ch/aleph/.

[40] DELPHI Collaboration, *DELPHI: Technical Proposal*, 1983. http://delphiwww.cern.ch/Welcome.html.

[41] OPAL Collaboration, *The Opal Detector Technical Proposal*, 1983. http://opal.web.cern.ch/Opal/.

[42] D0 Collaboration, *D0 Run IIB upgrade technical design report*, 2002. http://inspirehep.net/record/607594/files/pub-02-327-E.pdf.

[43] CDF Collaboration, *The CDF IIb detector Technical design report*, 2003.

http://inspirehep.net/record/613106/files/fermilab-tm-2198.PDF.

[44] R. Barate et al., *Search for the standard model Higgs boson at LEP*, Phys.Lett. **B565** (2003) 61–75, arXiv:hep-ex/0306033 [hep-ex].

[45] CDF, D0 Collaboration, *Higgs Boson Studies at the Tevatron*, Phys.Rev. **D88** no. 5, (2013) 052014, arXiv:1303.6346 [hep-ex].

[46] CMS Collaboration, *Precise determination of the mass of the Higgs boson and tests of compatibility of its couplings with the standard model predictions using proton collisions at 7 and 8 TeV*, Eur.Phys.J. **C75** no. 5, (2015) 212, arXiv:1412.8662 [hep-ex].

[47] ATLAS Collaboration, *Measurements of the Higgs boson production and decay rates and coupling strengths using pp collision data at s = 7 and 8 TeV in the ATLAS experiment*, Mar, 2015. http://cds.cern.ch/record/2002212.

[48] ATLAS Collaboration, *Search for the $b\bar{b}$ decay of the Standard Model Higgs boson in associated $(W/Z)H$ production with the ATLAS detector*, JHEP **1501** (2015) 069, arXiv:1409.6212 [hep-ex].

[49] CMS Collaboration, *Search for the standard model Higgs boson produced in association with a W or a Z boson and decaying to bottom quarks*, Phys.Rev. **D89** no. 1, (2014) 012003, arXiv:1310.3687 [hep-ex].

[50] O. S. Brüning, P. Collier, P. Lebrun, S. Myers, R. Ostojic, J. Poole, and P. Proudlock, *LHC Design Report*, CERN (2004). https://cdsweb.cern.ch/record/782076.

[51] K. Schindl, *The Injector Chain for the LHC; rev. version*, CERN (1999) 7 p. http://cds.cern.ch/record/384396/files/ps-99-018.pdf.

[52] "Schematic Diagram of the LHC Machines." http://maalpu.org/lhc/LHC.machines.png.

[53] TOTEM Collaboration, *Luminosity-Independent Measurement of the Proton-Proton Total Cross Section at $\sqrt{s}$ = 8 TeV*, Phys. Rev. Lett. **111** no. TOTEM-2012-005. CERN-PH-EP-2012-354, (2012).

[54] ATLAS Collaboration, *Improved luminosity determination in pp collisions at $\sqrt{s}$ = 7 TeV using the ATLAS detector at the LHC*, Eur.Phys.J. **C73** no. 8, (2013) 2518, 1302.4393 [hep-ex].

[55] "ATLAS Luminosity Public Results." https://twiki.cern.ch/twiki/bin/view/AtlasPublic/LuminosityPublicResults#Multiple_Year_Collision_Plots.

[56] D. Fournier, *Performance of the LHC, ATLAS and CMS in 2011*, EPJ Web of Conferences **28** (2012) 01003.

[57] ATLAS Collaboration, *The ATLAS Experiment at the CERN Large Hadron Collider*, Journal of Instrumentation **3** no. 08, (2008).

[58] J.-L. Caron, *ATLAS detector in A4 format with English captions*, 1998. https://cdsweb.cern.ch/record/841458/.

[59] J. Pequenao, *Computer Generated Image of the ATLAS Calorimeter*, 2008. http://cds.cern.ch/record/1095927.

[60] J. Pequenao, *Computer Generated Image of the ATLAS Muon Spectrometer*, 2008. http://cds.cern.ch/record/1095929.

[61] S. Agostinelli, J. Allison, K. Amako, et al., *GEANT4: A Simulation Toolkit*, Nuclear Instruments and Methods in Physics Research Section A: Accelerators, Spectrometers, Detectors and Associated Equipment **506** no. 3, (2003) 250 – 303.

[62] ATLAS Collaboration, *The ATLAS Simulation Infrastructure*, Eur. Phys. J. C **70** no. arXiv:1005.4568. CERN-PH-EP-2010-044, (2010) 823–874. 53 p.

[63] M. Villa, *The Luminosity Monitor of the ATLAS Experiment*, Nov, 2009. https://cds.cern.ch/record/1222513/.

[64] V. Cindro, D. Dobos, I. Dolenc, H. Frais-Kolbl, H. Frais-Koelbl, et al., *The ATLAS beam conditions monitor*, JINST **3** (2008) P02004.

[65] S. White, *Luminosity Scans at the LHC. Luminosity Scans at LHC*, 2011. https://cds.cern.ch/record/1357865.

[66] D. Belohrad, J.-J. Gras, L. K. Jensen, et al., *Commissioning and First Performance of the LHC Beam Current Measurement Systems*,. http://accelconf.web.cern.ch/AccelConf/IPAC10/papers/mope059.pdf.

[67] J. Pequenao and P. Schaffner, *A Computer Generated Image Representing How ATLAS Detects Particles*, 2013. https://cds.cern.ch/record/1505342.

[68] T. Cornelissen, M. Elsing, S. Fleischmann, W. Liebig, E. Moyse, and A. Salzburger, *Concepts, Design and Implementation of the ATLAS New Tracking (NEWT)*, Mar, 2007. http://cds.cern.ch/record/1020106.

[69] R. Frühwirth, *Application of Kalman Filtering to Track and Vertex Fitting*, Nuclear Instruments and Methods in Physics Research Section A: Accelerators, Spectrometers, Detectors and Associated Equipment **262** no. 23, (1987) 444 – 450.

[70] J. T. M. Baines, R. Bock, C. Hinkelbein, A. Kugel, et al., *Pattern Recognition in the TRT for the ATLAS B-Physics Trigger*, Jul, 1999. https://cdsweb.cern.ch/record/683897.

[71] W. Lampl, S. Laplace, D. Lelas, et al., *Calorimeter Clustering Algorithms: Description and Performance*, Apr, 2008. https://cdsweb.cern.ch/record/1099735.

[72] W. Waltenberger, R. Frühwirth, and P. Vanlaer, *Adaptive Vertex Fitting*, Journal of Physics G: Nuclear and Particle Physics no. 34, (2007).

[73] ATLAS Collaboration, *Performance of the ATLAS Inner Detector Track and Vertex Reconstruction in the High Pile-Up LHC Environment*, Mar, 2012. http://cds.cern.ch/record/1435196.

[74] ATLAS Collaboration, *Performance of the ATLAS Electron and Photon Trigger in p-p Collisions at sqrts = 7 TeV in 2011*, May, 2012. https://cds.cern.ch/record/1450089.

[75] ATLAS Collaboration, *Expected Electron Performance in the ATLAS Experiment*, Apr, 2011. https://cdsweb.cern.ch/record/1345327.

[76] ATLAS Collaboration, *Electron Performance Measurements With the ATLAS Detector Using the 2010 LHC Proton-Proton Collision Data*, The European Physical Journal C **72** no. 3, (2012).

[77] ATLAS Collaboration, *Electron Efficiency Measurements in Early 2012 Data,*. https://atlas.web.cern.ch/Atlas/GROUPS/PHYSICS/EGAMMA/PublicPlots/20120611/ElectronEfficiency2012/ATL-COM-PHYS-2011-783/index.html.

[78] ATLAS Collaboration, *Electron efficiency measurements with the ATLAS detector using the 2012 LHC proton-proton collision data*, Jun, 2014. http://cds.cern.ch/record/1706245.

[79] "TMVA." https://root.cern.ch/root/htmldoc/TMVA__MethodBDT.html.

[80] ATLAS Collaboration, *Performance of the ATLAS Trigger System in 2010*, Eur.Phys.J. **C72** no. CERN-PH-EP-2011-078, (2012) 1849, arXiv:1110.1530 [hep-ex].

[81] ATLAS Collaboration, *Performance of the ATLAS muon trigger in 2011*, Jul, 2012. http://cds.cern.ch/record/1462601.

[82] ATLAS Collaboration, *Measurement of the muon reconstruction performance of the ATLAS detector using 2011 and 2012 LHC proton-proton collision data*, Eur.Phys.J. **C74** no. 11, (2014) 3130, arXiv:1407.3935 [hep-ex].

[83] R. Nicolaidou, L. Chevalier, S. Hassani, et al., *Muon Identification Procedure for the ATLAS Detector at the LHC Using MuonBoy Reconstruction Package and Tests of its Performance Using Cosmic Rays and Single Beam Data*, Journal of Physics: Conference Series **219** no. 3, (2010).

[84] T. Lagouri, D. Adams, K. A. Assamagan, M. Biglietti, et al., *A Muon Identification and Combined Reconstruction Procedure for the ATLAS Detector at the LHC at CERN*, Oct, 2003. http://cds.cern.ch/record/681410?ln=en. revised version number 1 submitted on 2003-10-30 18:34:15.

[85] ATLAS Collaboration, *Jet Energy Measurement with the ATLAS Detector in*

Proton-Proton Collisions at $\sqrt{s} = 7$ *TeV*, Eur.Phys.J. **C73** no. 3, (2013) 2304, arXiv:1112.6426 [hep-ex].

[86] M. Cacciari, G. P. Salam, and G. Soyez, *The Anti-k(t) jet clustering algorithm*, JHEP **0804** no. LPTHE-07-03, (2008) 063, arXiv:0802.1189 [hep-ph].

[87] ATLAS Collaboration Collaboration, *Jet Energy Measurement and its Systematic Uncertainty in Proton-Proton Collisions at* $\sqrt{s} = 7$ *TeV with the ATLAS Detector*, Eur.Phys.J. **C75** no. 1, (2015) 17, arXiv:1406.0076 [hep-ex].

[88] ATLAS Collaboration, *Commissioning of the ATLAS high-performance b-tagging algorithms in the 7 TeV collision data*, Jul, 2011. https://cds.cern.ch/record/1369219.

[89] ATLAS Collaboration, *Calibration of b-tagging using dileptonic top pair events in a combinatorial likelihood approach with the ATLAS experiment*, Feb, 2014. https://cds.cern.ch/record/1664335.

[90] ATLAS Collaboration, *Calibration of the performance of b-tagging for c and light-flavour jets in the 2012 ATLAS data*, Jul, 2014. https://cds.cern.ch/record/1741020.

[91] ATLAS Collaboration, *Jet Energy Resolution in Proton-Proton Collisions at* $\sqrt{s} = 7$ *TeV Recorded in 2010 With the ATLAS Detector*, Eur.Phys.J. **C73** no. 3, (2013) 2306, arXiv:1210.6210 [hep-ex].

[92] ATLAS Collaboration, *Jet energy measurement and its systematic uncertainty in proton-proton collisions at* $\sqrt{s} = 7$ *TeV with the ATLAS detector*, Eur. Phys. J. **C75** (2015) 17, arXiv:1406.0076 [hep-ex].

[93] ATLAS Collaboration, *Jet global sequential calibration with the ATLAS detector in proton-proton collisions at sqrt(s) = 8 TeV*, Jan, 2015. https://cds.cern.ch/record/2001682.

[94] ATLAS Collaboration, *Performance of Missing Transverse Momentum Reconstruction in Proton-Proton Collisions at 7 TeV with ATLAS*, Eur.Phys.J. **C72** (2012) 1844, arXiv:1108.5602 [hep-ex].

[95] ATLAS Collaboration, *Performance of Missing Transverse Momentum Reconstruction in ATLAS studied in Proton-Proton Collisions recorded in 2012 at 8 TeV*, Aug, 2013. https://cds.cern.ch/record/1570993.

[96] P. Golonka and Z. Was, *PHOTOS Monte Carlo: A Precision tool for QED corrections in Z and W decays*, Eur.Phys.J. **C45** (2006) 97–107, arXiv:hep-ph/0506026 [hep-ph].

[97] Z. Was, *TAUOLA the library for tau lepton decay, and KKMC / KORALB / KORALZ /... status report*, Nucl.Phys.Proc.Suppl. **98** (2001) 96–102, arXiv:hep-ph/0011305 [hep-ph].

[98] LHC Higgs Cross Section Working Group Collaboration, *Handbook of LHC Higgs Cross Sections: 1. Inclusive Observables*, 2011, arXiv:1101.0593 [hep-ph].

[99] A. D. Bukin, *Fitting Function for Asymmetric Peaks*, November, 2007, arXiv:0711.4449 [physics.data-an].

[100] "TMultilayerPerceptron." https://root.cern.ch/root/html/TMultiLayerPerceptron.html.

[101] T. Aaltonen, A. Buzatu, B. Kilminster, Y. Nagai, and W. Yao, *Improved b-jet Energy Correction for $H \to b\bar{b}$ Searches at CDF*, 2011, arXiv:1107.3026 [hep-ex].

[102] C. G. Broyden, *The Convergence of a Class of Double-rank Minimization Algorithms 1. General Considerations*, IMA Journal of Applied Mathematics **6** no. 1, (1970) 76–90.

[103] "TMinuit Function Minimisation Package." https://root.cern.ch/root/html/TMinuit.html.

[104] I. W. Stewart and F. J. Tackmann, *Theory Uncertainties for Higgs and Other Searches Using Jet Bins*, Phys.Rev. **D85** (2012) 034011, arXiv:1107.2117 [hep-ph].

[105] A. Denner, S. Dittmaier, S. Kallweit, and A. Muck, *EW corrections to Higgs strahlung at the Tevatron and the LHC with HAWK*, PoS **EPS-HEP2011** (2011) 235, arXiv:1112.5258 [hep-ph].

[106] ATLAS Collaboration, *Improved luminosity determination in pp collisions at sqrt(s) = 7 TeV using the ATLAS detector at the LHC*, Eur.Phys.J. **C73** no. 8, (2013) 2518, arXiv:1302.4393 [hep-ex].

[107] ATLAS and CMS Collaboration, *Procedure for the LHC Higgs boson search combination in summer 2011*, Aug, 2011. https://cds.cern.ch/record/1375842.

[108] A. L. Read, *Presentation of search results: the CLs technique*, J.Phys no. G28, (2002) 2693–2704.

Chapter A

Additional Material for 3 Jet Events

A.1. Regression Training for 3 Jet Events

This section is an extension of the regression training outlined in Section 6.3 focussing on the regression training for 3-jet events. The extra jet in 3-jet events changes the background composition slightly compared to 2-jet events; There is a much higher $t\bar{t}$ background in all 3-jet categories and a decreased multijet background. For an accurate regression training used to calibrate the b-jets in the analysis, well modelled variables are required. With the change in background composition, different variables from those used in the 2-jet regression may now be viable. Figure A.1 shows the distributions for the jet kinematic variables: jet mass, jet p_{T}, jet E, whether or not the jet contains a muon and whether or not the jet contains a reconstructed secondary vertex. The jet calorimeter and track variables: EMF, FracEM3, FracTile0, JVF, NTrk, SumPtTrk, SumPtTrk / p_{T}, TrkWidth and jet width, are shown in Figure A.2 and Figure A.3 includes a selection of track and calorimeter variables along with a selection of secondary vertex varibles. The remaining secondary vertex variables are shown in Figure A.4.

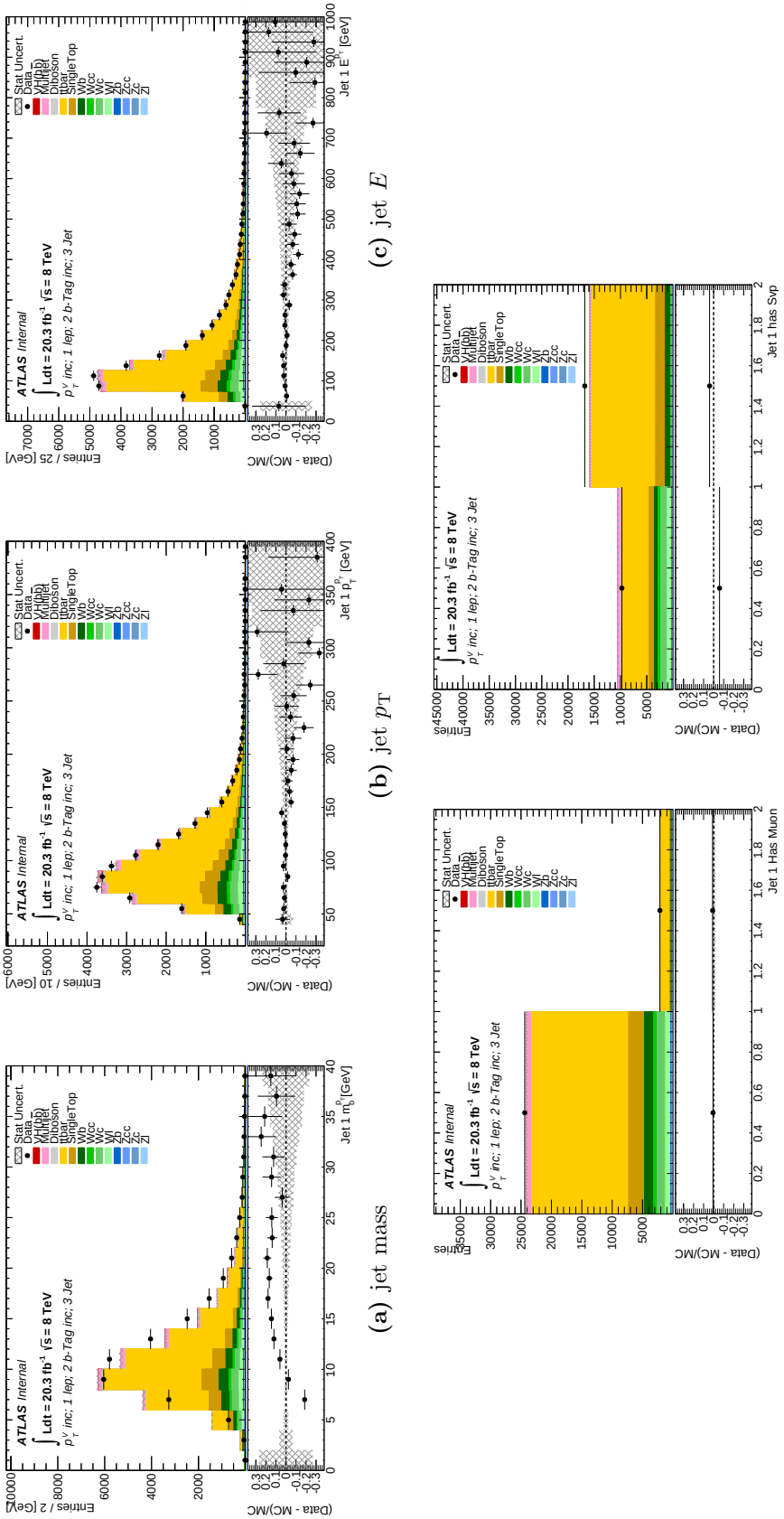

(a) jet mass

(b) jet p_{T}

(c) jet E

(d) jet has muon

(e) jet has secondary vertex

Figure A.1: Modelling of 3-jet, 2 b-tag, p_{T}^{V} inclusive, lepton inclusive jet kinematic and other jet variables to obtain a list of potential input variables into the regression training.

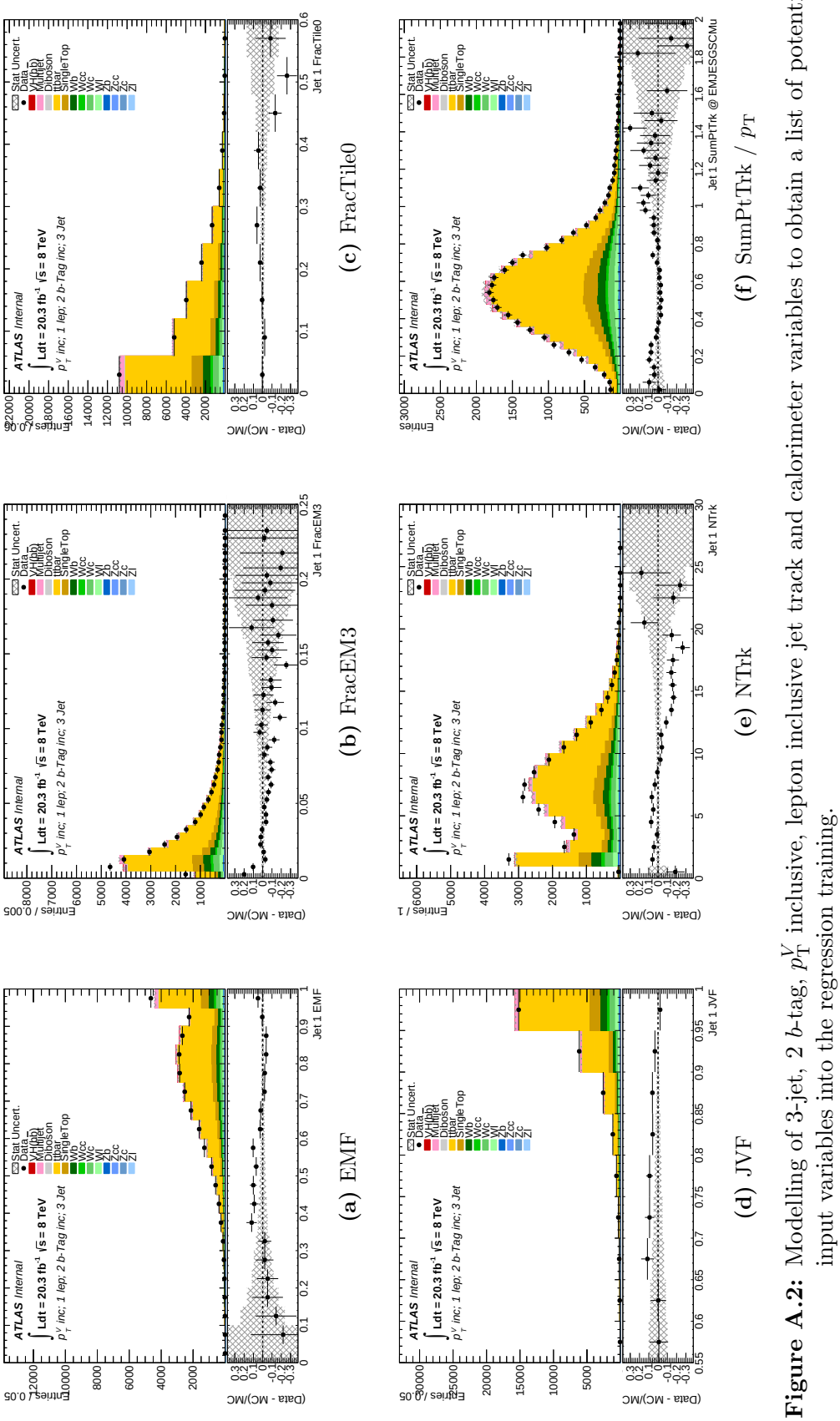

(a) EMF (b) FracEM3 (c) FracTile0

(d) JVF (e) NTrk (f) SumPtTrk / p_{T}

Figure A.2: Modelling of 3-jet, 2 b-tag, p_{T}^{V} inclusive, lepton inclusive jet track and calorimeter variables to obtain a list of potential input variables into the regression training.

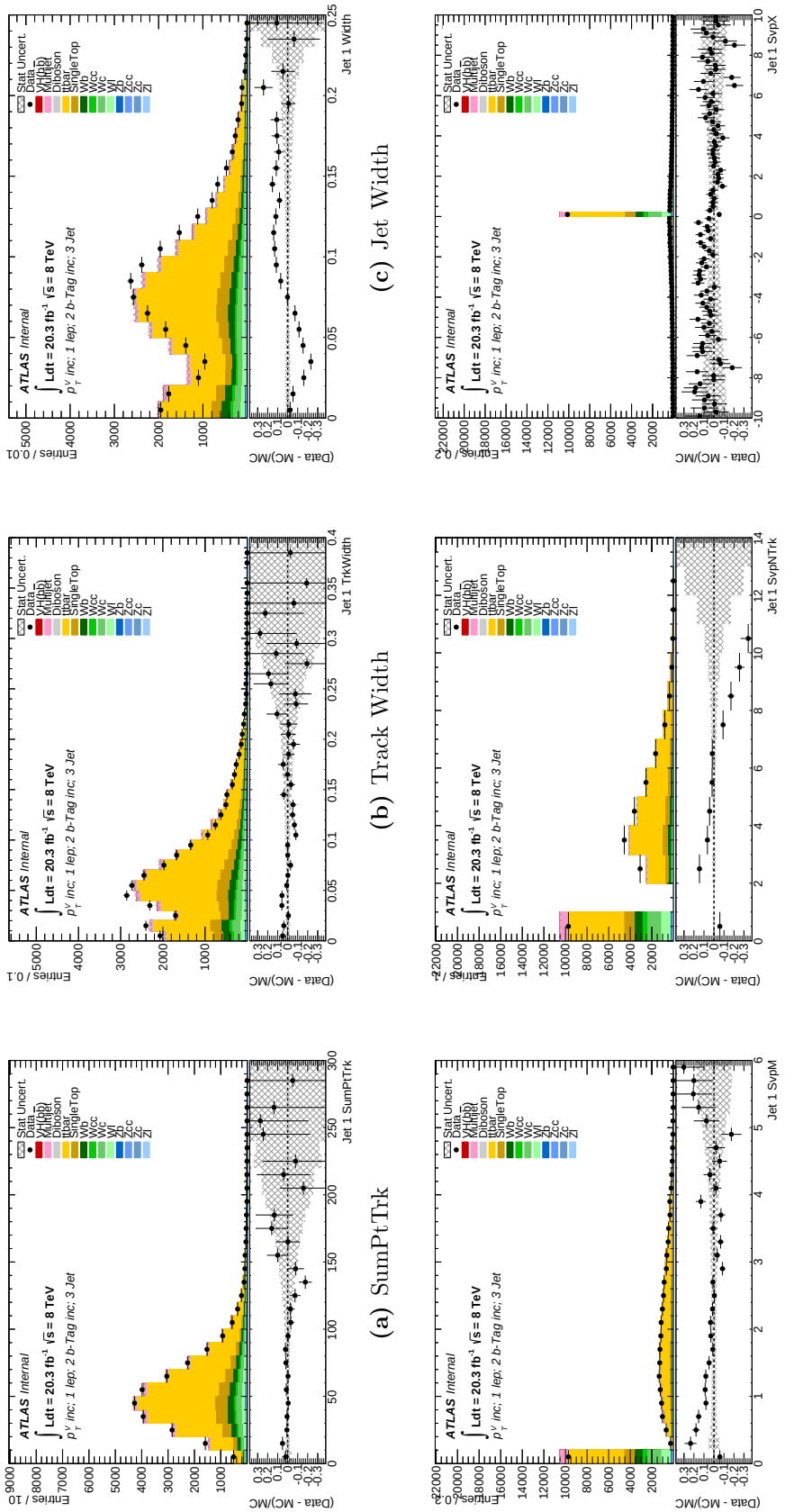

(a) SumPtTrk (b) Track Width (c) Jet Width

(d) SvpM (e) SvpNTrk (f) SvpX

Figure A.3: Modelling of 3-jet, 2 b-tag, p_{T}^{V} inclusive, lepton inclusive jet track, calorimeter and a selection of secondary vertex variables to obtain a list of potential input variables into the regression training.

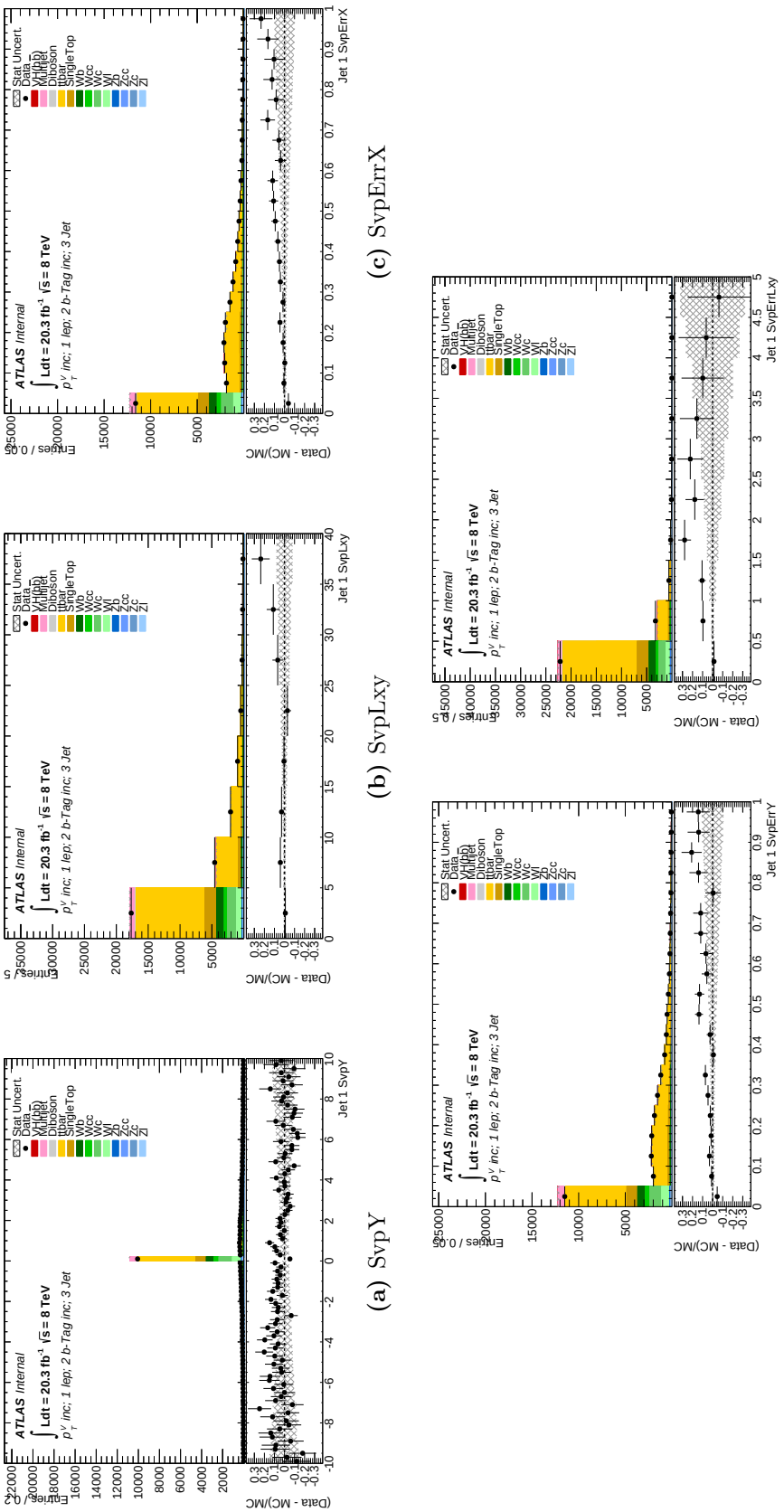

(a) SvpY (b) SvpLxy (c) SvpErrX

(d) SvpErrY (e) SvpErrLxy

Figure A.4: Modelling of 3-jet, 2 b-tag, p_{T}^{V} inclusive, lepton inclusive variables associated with a reconstructed secondary vertex to obtain a list of potential input variables into the regression training.

After studying the distributions for the potential input variables to train a regression to calibrate 3-jet events, the variables which are well modelled and will be used for the neural network (NN) training are the following: jet p_{T}, jet E, FracEM3, FracTile0, SumPtTrk / jet p_{T}, SumPtTrk, SvpLxy, SvpErrX, SvpErrY, SvpX, SvpY, TrkWidth and hasMuon. The technique used to train the 3-jet regression is the same as the 2-jet regression. The list of well modelled variables will be input input into the training to correct the jet p_{T}. After the initial training, the impact of each variable will be analysed with the weakest impacting variable removed in order to allow the strongest variables to have a greater impact. This process is repeated a second time, leading to a total of three regressions. The regression with the greatest improvement on the sensitivity will be chosen as the training to be taken forward to be used in the limit extraction. A summary of the NN training input parameters is shown in Table A.1.

Input Parameter	Value
Acivation Function	Sigmoid
Learning Method	BFGS
Epochs	100
InputVariables	E, p_{T}, EMF, FracTile0, FracEM3, NTrk, SumPtTrk / p_{T}, SumPtTrk, TrkWidth, SvpLxy, hasMuon, SvpErrX, SvpErrY, SvpX, SvpY
Output Variable	jet p_{T}

Table A.1: The input parameters used in the initial neural network training. After each training, one input variable will be removed before being re-trained. After three neural network trainings, the neural network with the greatest improvement in dijet width and mass reconstruction will be taken forward for a limit extraction.

After each training a test is performed for evidence of over training; as the number of epochs run over increases, the error on the NN decreases to a minimum value. Evidence for over training is associated with an increase in the NN error after it has reached a minimum. The over training test for the initial training is shown in Figure A.5, along with the variable impact distributions. There is no evidence for over training as the distribution reaches a minimum value and there is no increase.

For the second training, the track width variable is removed as it had the least impact

in the initial training. There is no evidence for over training in the second training as shown in Figure A.6a. For the final training the hasMuon variable has been removed as Figure A.6b shows it has the least impact on the training. The results for the final training are shown in Figure A.7; (a) shows there is no evidence for over training and (b) shows the impact of each input variable.

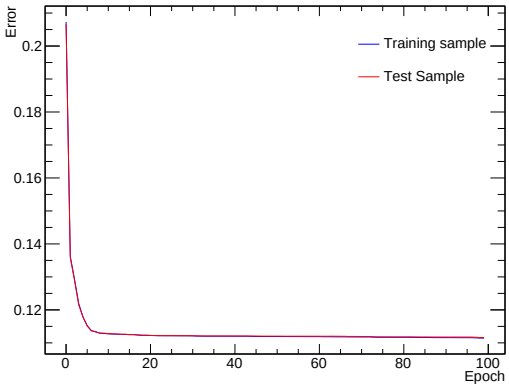

(a) Over-training test

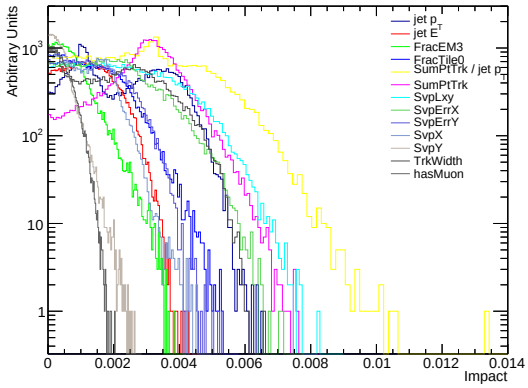

(b) Variable Impact

Figure A.5: The neural network error as a function of number of epochs as a test for over-training (a) and the impact each of the input variables has on the training of the initial neural network.

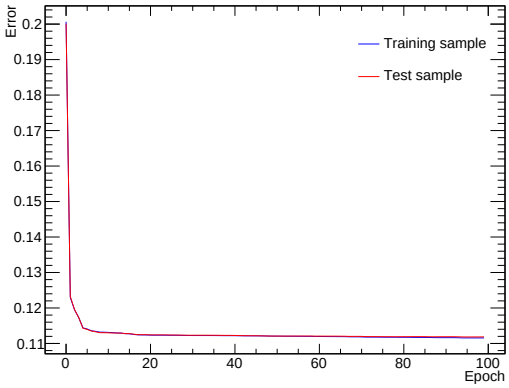

(a) Over-training test

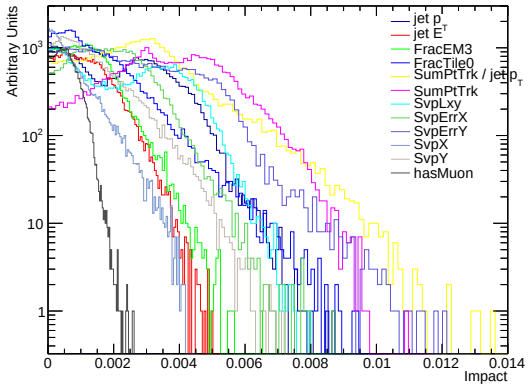

(b) Variable Impact

Figure A.6: The neural network error as a function of number of epochs as a test for over-training (a) and the impact each of the input variables has on the training of the second neural network.

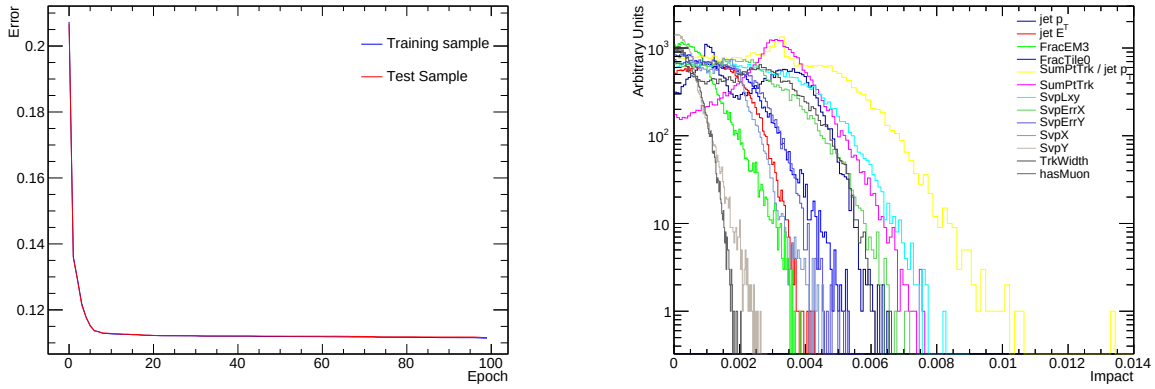

(a) Over-training test **(b)** Variable Impact

Figure A.7: The neural network error as a function of number of epochs as a test for over-training (a) and the impact each of the input variables has on the training of the final neural network.

As with the 2-jet neural network trainings, the effects of the 3-jet neural networks are studied by adding the regression calibration in addition to the $p_{\mathrm{T}}^{\mu,\mathrm{Reco}}$ calibration. The sensitivity calculations are performed with the neural networks applied to both signal and background processes. A comparison between the sensitivities of the 3-jet category with each 3-jet regression (NNJ1–3) applied is shown in Table A.2. The sensitivity values are split into bins of p_{T}^{V}, with the calculation performed using 50 bins in the range $0 < m_{b\bar{b}} < 500$ GeV. The nominal calibrations are represented as 'CC'. The improvement

Calibration	p_{T}^{V} Bin [GeV]				
	$p_{\mathrm{T}}^{V} < 90$	$90 < p_{\mathrm{T}}^{V} < 120$	$120 < p_{\mathrm{T}}^{V} < 160$	$160 < p_{\mathrm{T}}^{V} < 200$	$p_{\mathrm{T}}^{V} > 200$
CC+pT3	0.202	0.149	0.159	0.182	0.297
CC+pT3+NNJ1	0.202	0.149	0.159	0.181	0.295
CC+pT3+NNJ2	0.203	0.149	0.159	0.181	0.296
CC+pT3+NNJ3	0.202	0.149	0.159	0.181	0.295

Table A.2: Comparing the sensitivites between the 3-jet neural network trainings in order to choose the best performing calibration. The neural networks are applied in addition to the $p_{\mathrm{T}}^{\mu,\mathrm{Reco}}$calibration.

gained in the sensitivity is less apparent than for 2-jet events. At low p_{T}^{V}, the second neural network training offers a marginal improvement. For the remaining p_{T}^{V} categories, there is no observed improvement in the sensitivity. Since the only neural network

training to give any improvement to the analysis sensitivity is the second training; this will be studied further.

A comparison between the $p_{\mathrm{T}}^{\mu,\mathrm{Reco}}$ calibration, NNJ2, and the generator level is given in Table A.3 for the reconstructed dijet mass, width, resolution and the response. The mass reconstruction has decreased slightly, moving further away from the generator level value. There is a very slight improvement in the width of the dijet reconstruction, and a negligable change in the resolution from the $p_{\mathrm{T}}^{\mu,\mathrm{Reco}}$ calibration. There is a marginal increase in the response of 0.5% from the $p_{\mathrm{T}}^{\mu,\mathrm{Reco}}$ calibration, moving away from the generator level value. A visual representation of the changes in shape between the $p_{\mathrm{T}}^{\mu,\mathrm{Reco}}$ and NNJ2 calibrations are shown in Figure A.8, with the generator level used as a reference. The observed difference in shape between the $p_{\mathrm{T}}^{\mu,\mathrm{Reco}}$ calibration and NNJ2 is negligable whilst the difference between dijet mass reconstruction is marginal.

Calibration	Mean [GeV]	Width [GeV]	Resolution	Response
CC+Pt3	121.8 ± 3.5	13.0 ± 2.47	0.107 ± 0.021	1.02 ± 0.02
CC+Pt3+NNJ2	121.2 ± 3.5	12.9 ± 2.47	0.107 ± 0.021	1.02 ± 0.02
Generator Level	122.2 ± 3.2	5.30 ± 2.23	0.043 ± 0.018	1.00

Table A.3: Comparisons between the $p_{\mathrm{T}}^{\mu,\mathrm{Reco}}$calibration, the best performing regression (NNJ2) and the generator level. Comparing the dijet mass reconstruction, the width, resolution and the response.

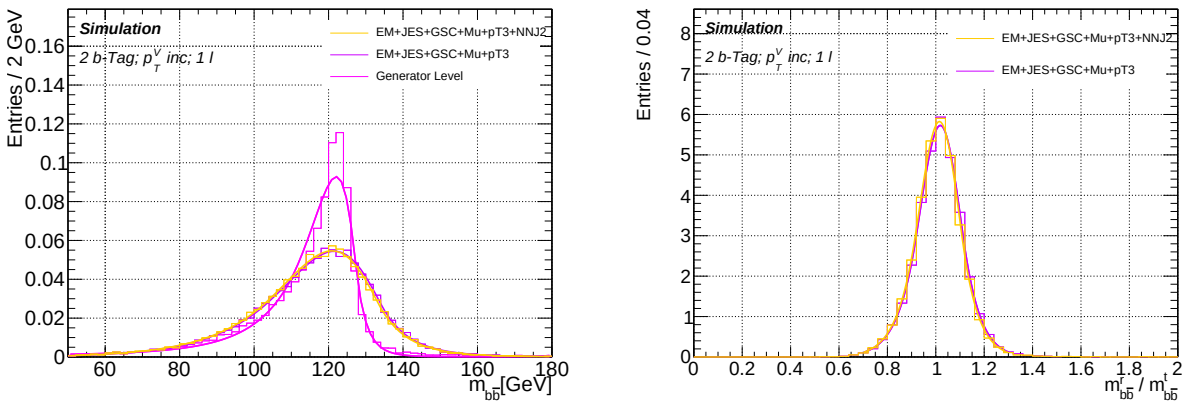

(a) dijet mass **(b)** dijet response

Figure A.8: Shape comparisons between the $p_{\mathrm{T}}^{\mu,\mathrm{Reco}}$ calibration, best performing regression and the generator level for the dijet mass and dijet response distributions using 3-jet 2 b-tag events.

A.2. Prefit Distributions & Yield Tables

This section is an extension of Chapter 8; showing the prefit distributions for 3-jet events. The main difference between 2- and 3-jet events is a larger contribution from $t\bar{t}$ production in the 3-jet category, due to the extra jet from a hadronically decaying W-boson another observed difference is the multijet background is reduced compared to 2-jet events. The same distributions are used as input to the global fit as highlighted in Table 9.4. The 1 b-tag region uses the MV1c distribution and the dijet mass distributions are used for each of the 2 b-tag categories. As well as the same distributions, the same p_{T}^{V} bins are used. For 1 b-tag; $p_{\mathrm{T}}^{V} < 120$ GeV and $p_{\mathrm{T}}^{V} > 120$ GeV and for each of the 2 b-tag categories: $p_{\mathrm{T}}^{V} < 90$ GeV, $90 < p_{\mathrm{T}}^{V} < 120$ GeV, $120 < p_{\mathrm{T}}^{V} < 160$, $160 < p_{\mathrm{T}}^{V} < 200$ GeV, and $p_{\mathrm{T}}^{V} > 200$ GeV.

Figure A.9 shows the prefit distributions for both p_{T}^{V} regions of the 1 b-tag category with the yield tables for each of the categories being shown in Table A.4. The distributions show good agreement between the data and sum of the signal and background within full prefit nuisance parameters.

The prefit distributions for the 2L b-tag category are shown in Figure A.10 for all p_{T}^{V} regions with the yield tables for each p_{T}^{V} category being shown in Table A.5. The distributions for the 2L category show good agreement between data and the total signal and background; within full prefit nuisance parameters.

The prefit distributions for the 2M b-tag category are shown in Figure A.11 for all p_{T}^{V} regions with the yield tables for each p_{T}^{V} category being shown in Table A.6. The 2M category distributions and yield tables show good agreement between data and total signal and background; well within the full prefit nuisance parameters.

The prefit distributions for the 2T b-tag category are shown in Figure A.12 for all p_{T}^{V} regions with the yield tables for each p_{T}^{V} category being shown in Table A.7. As with the previous categories, excellent agreement between data and the total signal and background is observed; within the full prefit nuisance parameters.

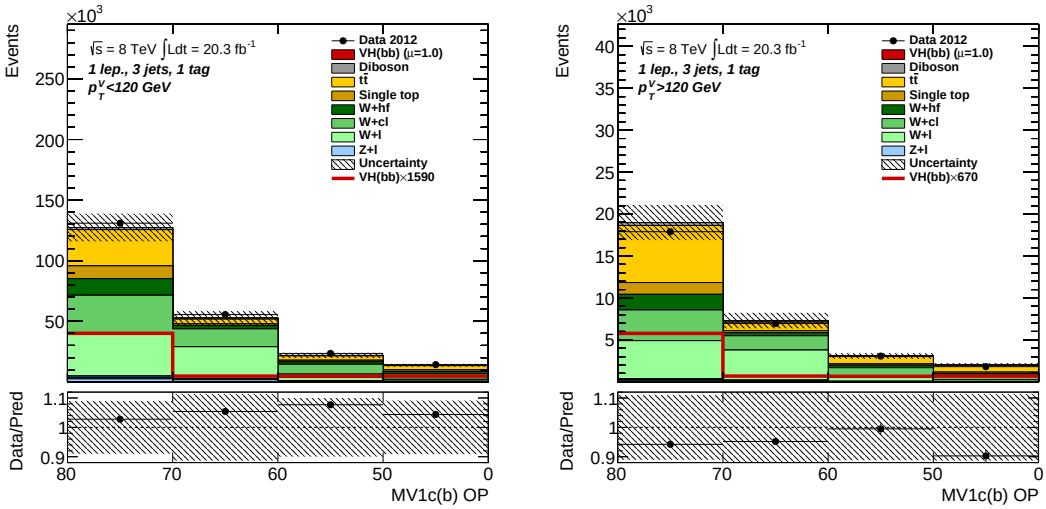

(a) $p_{\mathrm{T}}^{V} < 120$ GeV **(b)** $p_{\mathrm{T}}^{V} > 120$ GeV

Figure A.9: MV1c distributions in the 1 b-tag control region before the global fit for 3-jet events. The distributions are shown for the two p_{T}^{V} regions used as input to the global fit; (a) $p_{\mathrm{T}}^{V} < 120$ GeV and (b) $p_{\mathrm{T}}^{V} > 120$ GeV. Uncertainties are from full prefit nuisance parameters.

Sample	1-tag	
	$p_{\mathrm{T}}^{V} < 120$ GeV	$p_{\mathrm{T}}^{V} > 120$ GeV
VH	33.9 ± 5.8	11.6 ± 3.4
VV	3174.5 ± 56.3	645.6 ± 25.4
$t\bar{t}$	41052.0 ± 202.6	9489.0 ± 97.4
s-top	14542.9 ± 120.6	1976.6 ± 44.5
W+l	67781.7 ± 260.3	9021.4 ± 95.0
W+cl	59932.3 ± 244.8	6820.4 ± 82.6
W+hf	20173.0 ± 142.0	2770.0 ± 52.6
Z+l	4826.7 ± 69.5	363.9 ± 19.1
Z+cl	1982.3 ± 44.5	145.5 ± 12.1
Z+hf	1869.1 ± 43.2	125.3 ± 11.2
Total	215368.4 ± 464.1	31369.2 ± 177.1
Data	224026	29710

Table A.4: Table of prefit yields for 3-jet 1-tag events The uncertainties are from statistical sources only.

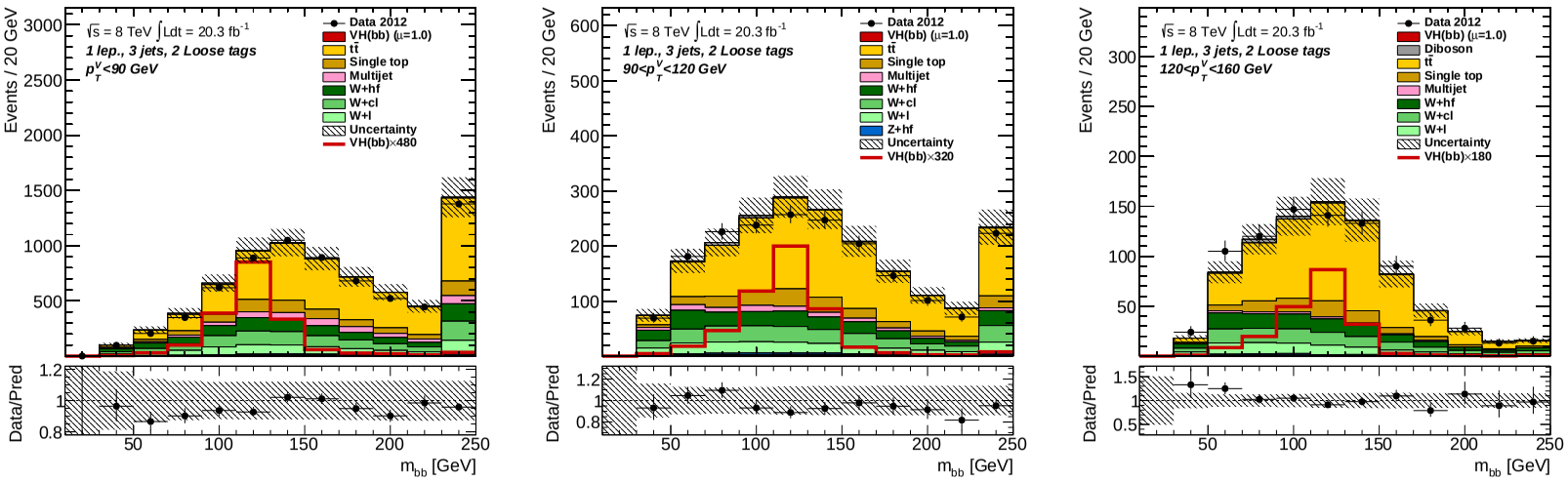

(a) $p_{\mathrm{T}}^{V} < 90$ GeV **(b)** $90 < p_{\mathrm{T}}^{V} < 120$ GeV **(c)** $120 < p_{\mathrm{T}}^{V} < 160$ GeV

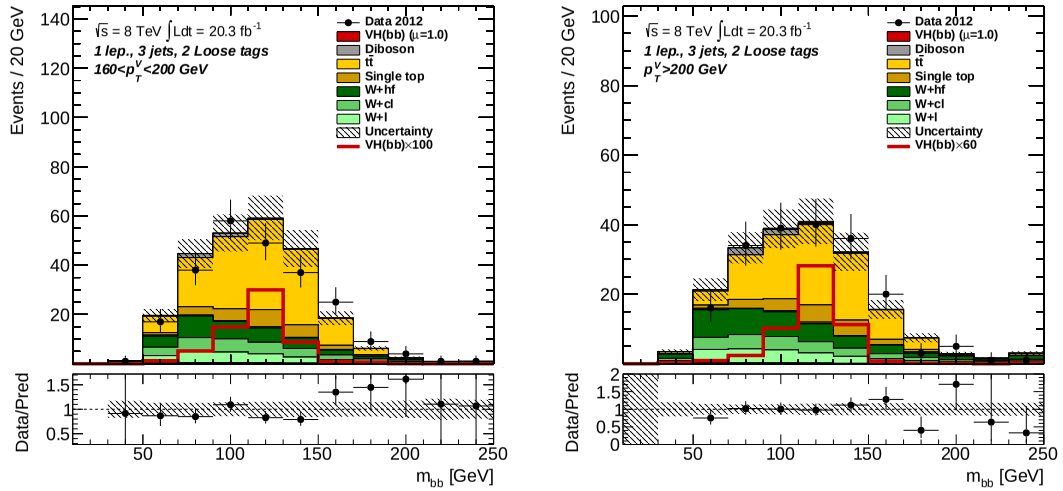

(d) $160 < p_{\mathrm{T}}^{V} < 200$ GeV **(e)** $p_{\mathrm{T}}^{V} > 200$ GeV

Figure A.10: Dijet mass distributions in the 2 L b-tag signal region before the global fit for 3-jet events. The distributions are shown for all five p_{T}^{V} regions used as input to the global fit; $p_{\mathrm{T}}^{V} < 90$ GeV, $90 < p_{\mathrm{T}}^{V} < 120$ GeV, $120 < p_{\mathrm{T}}^{V} < 160$ GeV, $160 < p_{\mathrm{T}}^{V} < 200$ GeV and $p_{\mathrm{T}}^{V} > 200$ GeV. Uncertainties are taken from full prefit nuisance parameters.

Sample	2L-tag				
	$p_{\mathrm{T}}^{V} < 90$ GeV	$90 < p_{\mathrm{T}}^{V} < 120$ GeV	$120 < p_{\mathrm{T}}^{V} < 160$ GeV	$160 < p_{\mathrm{T}}^{V} < 200$ GeV	$p_{\mathrm{T}}^{V} > 200$ GeV
VH	3.9 ± 2.0	1.6 ± 1.3	1.1 ± 1.1	0.6 ± 0.8	0.9 ± 1.0
VV	59.0 ± 7.7	19.9 ± 4.5	10.3 ± 3.2	4.2 ± 2.0	4.9 ± 2.2
$t\bar{t}$	3639.5 ± 60.3	1077.5 ± 32.8	465.5 ± 21.6	137.5 ± 11.7	90.6 ± 9.5
s-top	734.0 ± 27.1	192.5 ± 13.9	75.3 ± 8.7	24.1 ± 4.9	20.0 ± 4.5
W+l	626.7 ± 25.0	168.5 ± 13.0	67.2 ± 8.2	21.3 ± 4.6	21.0 ± 4.6
W+cl	919.9 ± 30.3	242.5 ± 15.6	91.0 ± 9.5	26.6 ± 5.2	21.8 ± 4.7
W+hf	874.5 ± 29.6	235.3 ± 15.3	96.8 ± 9.8	34.9 ± 5.9	39.0 ± 6.2
Z+l	45.1 ± 6.7	14.8 ± 3.8	3.4 ± 1.9	0.7 ± 0.8	0.4 ± 0.6
Z+cl	32.3 ± 5.7	9.7 ± 3.1	2.3 ± 1.5	0.5 ± 0.7	0.3 ± 0.5
Z+hf	70.4 ± 8.4	21.7 ± 4.7	6.8 ± 2.6	0.8 ± 0.9	0.5 ± 0.7
MJ_e	274.7 ± 16.6	59.6 ± 7.7	10.7 ± 3.3	1.7 ± 1.3	1.0 ± 1.0
MJ_μ	165.7 ± 12.9	16.0 ± 4.0	1.9 ± 1.4	0.6 ± 0.8	0.3 ± 0.6
Total	7445.6 ± 86.3	2059.4 ± 45.4	832.5 ± 28.9	253.6 ± 15.9	200.6 ± 14.2
Data	7129	1963	852	240	195

Table A.5: Table of prefit yields for 3-jet 2L-tag events The uncertainties are from statistical sources only.

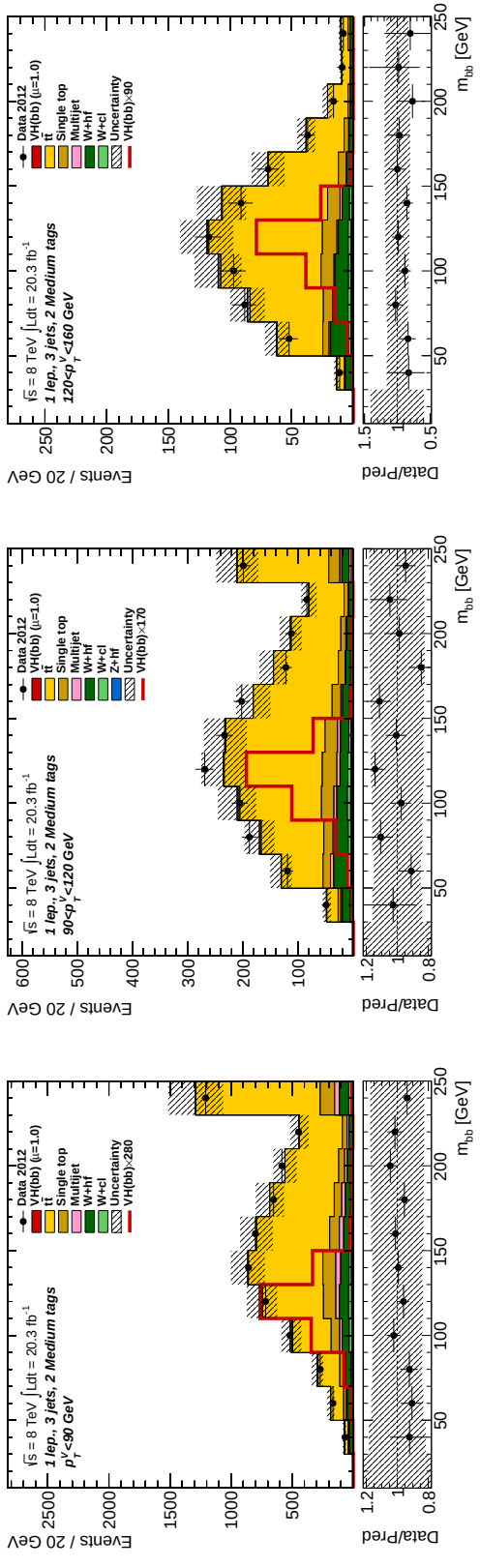

(a) $p_{\mathrm{T}}^{V} < 90$ GeV (b) $90 < p_{\mathrm{T}}^{V} < 120$ GeV (c) $120 < p_{\mathrm{T}}^{V} < 160$ GeV

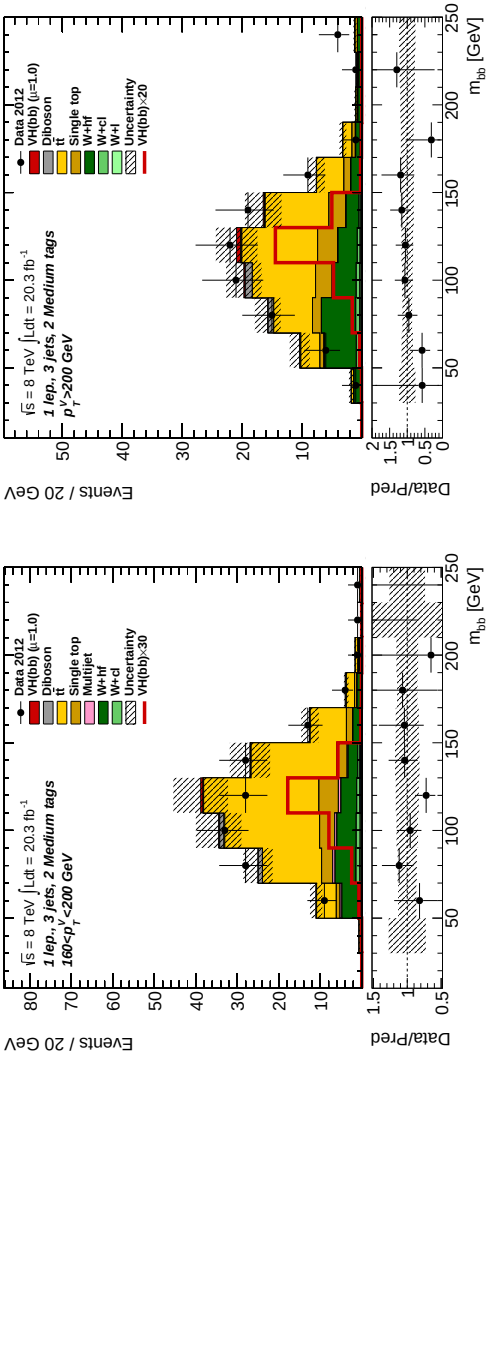

(d) $160 < p_{\mathrm{T}}^{V} < 200$ GeV (e) $p_{\mathrm{T}}^{V} > 200$ GeV

Figure A.11: Dijet mass distributions in the 2 M b-tag signal region before the global fit for 3-jet events. The distributions are shown for all five p_{T}^{V} regions used as input to the global fit; $p_{\mathrm{T}}^{V} < 90$ GeV, $90 < p_{\mathrm{T}}^{V} < 120$ GeV, $120 < p_{\mathrm{T}}^{V} < 160$ GeV, $160 < p_{\mathrm{T}}^{V} < 200$ GeV and $p_{\mathrm{T}}^{V} > 200$ GeV. Uncertainties are taken from full prefit nuisance parameters.

Sample	2M-tag				
	$p_{\mathrm{T}}^{V} < 90$ GeV	$90 < p_{\mathrm{T}}^{V} < 120$ GeV	$120 < p_{\mathrm{T}}^{V} < 160$ GeV	$160 < p_{\mathrm{T}}^{V} < 200$ GeV	$p_{\mathrm{T}}^{V} > 200$ GeV
VH	5.7 ± 2.4	2.5 ± 1.6	1.8 ± 1.4	1.2 ± 1.1	1.3 ± 1.1
VV	27.0 ± 5.2	9.7 ± 3.1	5.6 ± 2.4	2.5 ± 1.6	2.6 ± 1.6
$t\bar{t}$	4673.5 ± 68.4	1295.5 ± 36.0	478.5 ± 21.9	102.5 ± 10.1	50.3 ± 7.1
s-top	690.2 ± 26.3	170.6 ± 13.1	60.6 ± 7.8	16.8 ± 4.1	13.6 ± 3.7
W+l	43.8 ± 6.6	11.9 ± 3.5	4.6 ± 2.1	1.3 ± 1.1	1.2 ± 1.1
W+cl	154.9 ± 12.4	43.0 ± 6.6	14.2 ± 3.8	4.3 ± 2.1	3.1 ± 1.8
W+hf	526.5 ± 22.9	158.4 ± 12.6	65.8 ± 8.1	22.9 ± 4.8	25.4 ± 5.0
Z+l	3.2 ± 1.8	1.1 ± 1.0	0.2 ± 0.5	0.0 ± 0.2	0.0 ± 0.1
Z+cl	5.2 ± 2.3	1.9 ± 1.4	0.3 ± 0.5	0.1 ± 0.3	0.0 ± 0.1
Z+hf	49.1 ± 7.0	18.1 ± 4.3	5.1 ± 2.3	0.9 ± 0.9	0.5 ± 0.7
MJ_e	150.4 ± 12.3	31.2 ± 5.6	5.4 ± 2.3	2.0 ± 1.4	0.3 ± 0.6
MJ_μ	100.4 ± 10.0	11.3 ± 3.4	1.5 ± 1.2	0.8 ± 0.9	–
Total	6430.0 ± 80.2	1755.3 ± 41.9	643.8 ± 25.4	155.3 ± 12.5	98.5 ± 9.9
Data	6287	1782	595	146	99

Table A.6: Table of prefit yields for 3-jet 2M-tag events The uncertainties are from statistical sources only.

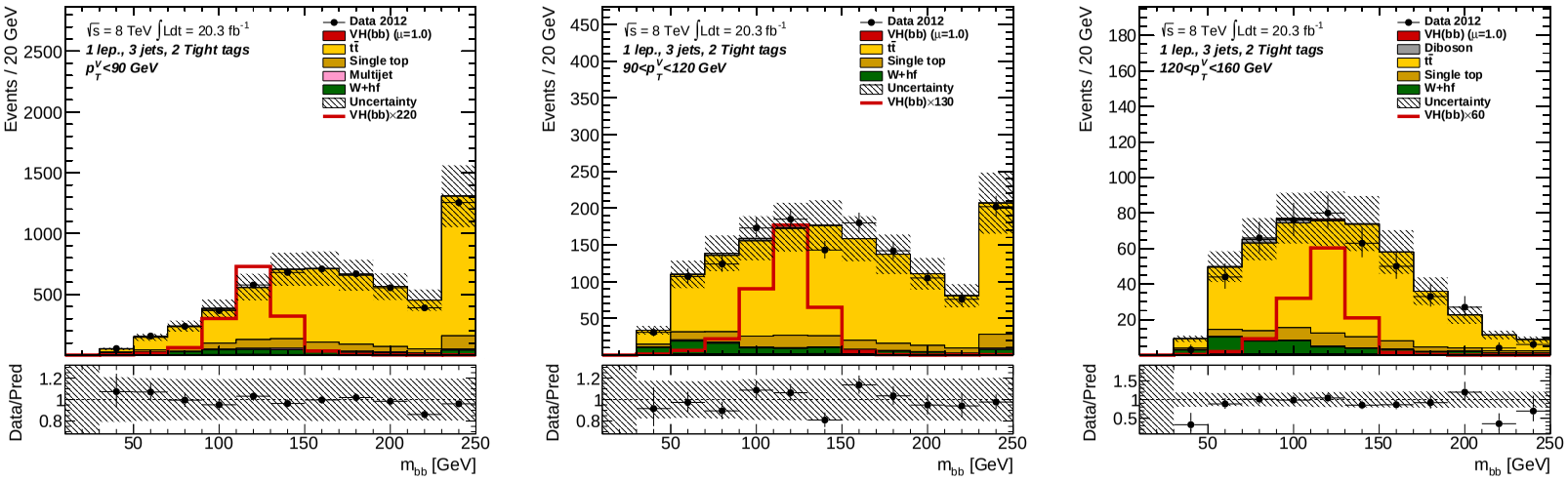

(a) $p_{\mathrm{T}}^{V} < 90$ GeV (b) $90 < p_{\mathrm{T}}^{V} < 120$ GeV (c) $120 < p_{\mathrm{T}}^{V} < 160$ GeV

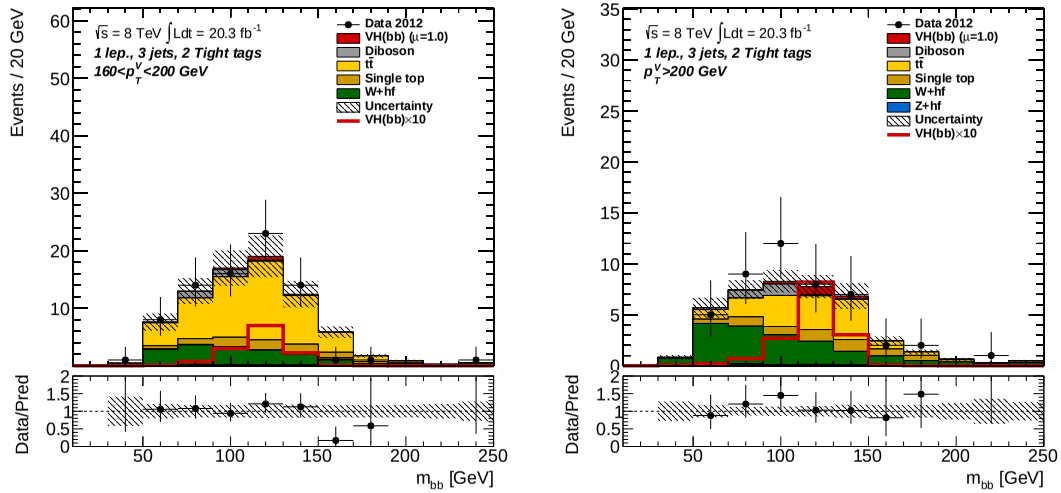

(d) $160 < p_{\mathrm{T}}^{V} < 200$ GeV (e) $p_{\mathrm{T}}^{V} > 200$ GeV

Figure A.12: Dijet mass distributions in the 2 T b-tag signal region before the global fit for 3-jet events. The distributions are shown for all five p_{T}^{V} regions used as input to the global fit; $p_{\mathrm{T}}^{V} < 90$ GeV, $90 < p_{\mathrm{T}}^{V} < 120$ GeV, $120 < p_{\mathrm{T}}^{V} < 160$ GeV, $160 < p_{\mathrm{T}}^{V} < 200$ GeV and $p_{\mathrm{T}}^{V} > 200$ GeV. Uncertainties are taken from full prefit nuisance parameters.

Sample	2T-tag				
	$p_{\mathrm{T}}^{V} < 90$ GeV	$90 < p_{\mathrm{T}}^{V} < 120$ GeV	$120 < p_{\mathrm{T}}^{V} < 160$ GeV	$160 < p_{\mathrm{T}}^{V} < 200$ GeV	$p_{\mathrm{T}}^{V} > 200$ GeV
VH	6.7 ± 2.6	2.8 ± 1.7	2.1 ± 1.5	1.3 ± 1.1	1.5 ± 1.2
VV	17.0 ± 4.1	7.4 ± 2.7	5.0 ± 2.2	2.7 ± 1.6	2.2 ± 1.5
$t\bar{t}$	4787.3 ± 69.2	1231.6 ± 35.1	390.3 ± 19.8	48.7 ± 7.0	14.3 ± 3.8
s-top	573.4 ± 23.9	132.3 ± 11.5	43.0 ± 6.6	8.5 ± 2.9	6.1 ± 2.5
W+l	1.3 ± 1.1	0.3 ± 0.5	0.1 ± 0.3	0.0 ± 0.1	0.0 ± 0.2
W+cl	7.1 ± 2.7	1.7 ± 1.3	0.7 ± 0.9	0.2 ± 0.4	0.1 ± 0.3
W+hf	283.8 ± 16.8	86.1 ± 9.3	42.2 ± 6.5	15.9 ± 4.0	17.3 ± 4.2
Z+l	0.1 ± 0.2	0.0 ± 0.1	0.0 ± 0.1	–	–
Z+cl	0.1 ± 0.4	0.1 ± 0.2	0.0 ± 0.2	0.0 ± 0.0	0.0 ± 0.1
Z+hf	32.5 ± 5.7	11.8 ± 3.4	3.3 ± 1.8	0.7 ± 0.8	0.5 ± 0.7
MJ_e	66.7 ± 8.2	12.0 ± 3.5	2.1 ± 1.4	0.6 ± 0.7	–
MJ_μ	0.0 ± 0.0	0.0 ± 0.0	0.0 ± 0.0	0.0 ± 0.0	–
Total	5775.9 ± 76.0	1486.1 ± 38.6	488.8 ± 22.1	78.6 ± 8.9	42.0 ± 6.5
Data	5647	1468	452	79	46

Table A.7: Table of prefit yields for 3-jet 2T-tag events The uncertainties are from statistical sources only.

A.3. Post-fit Distributions & Yield Tables

This section is an extension of Section 9.3; showing the distributions and yield tables after the global fit. Before the global fit, the distributions of the MV1c variable in the 1 b-tag distribution and the dijet mass in each of the 2 b-tag distributions have been transformed using the prescription described in Section 9.2 in order to improve the sensitivity. As with the prefit plots in the previous section, the main differences between the 2- and 3-jet events are the increase in $t\bar{t}$ background and decrease in multijet background.

The post-fit distributions for the 1 b-tag category for both p_{T}^{V} bins are shown in Figure A.13, and the yield tables are shown in Table A.8. Excellent agreement is observed between the data and the total signal and background.

Figure A.14 shows the dijet mass distributions for the 2L b-tag category after the application of the scale facts derived from the global fit. The yield tables are shown in Table A.9. Excellent agreement is observed between the data and the total signal and background.

The distributions after the application of the scale factors derived from the global fit are shown in Figure A.15 for the 2M b-tag category; with the yield tables being shown in Table A.10. Good agreement well within the full postfit statisitical and systematic uncertainties is observed between the data and the total signal and background.

Figure A.16 and Table A.11 show the respective distributions and yield tables for the 2T b-tag category after the application of scale factors derived in the global fit. As with the other categories, excellent agreement is observed between data and the total signal and background contributions.

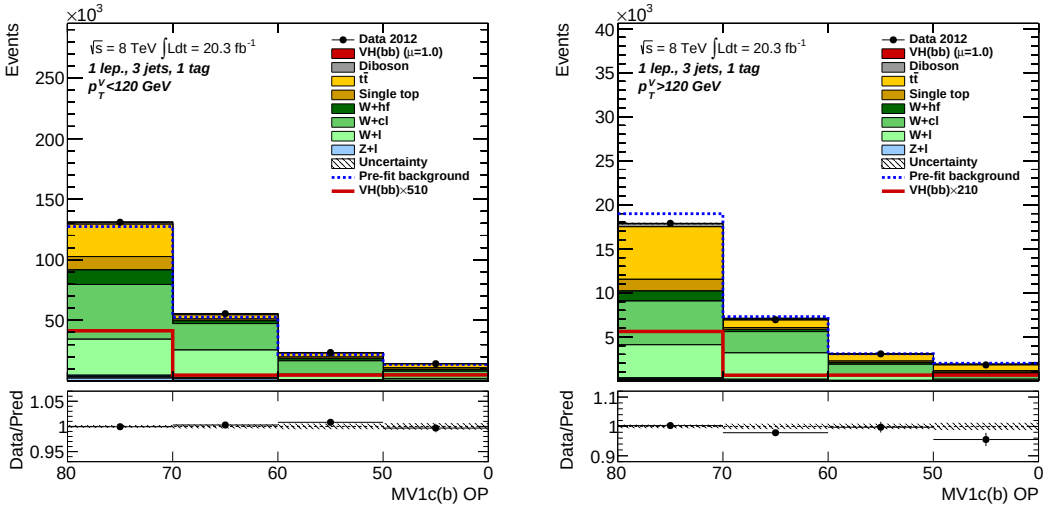

(a) $p_{\mathrm{T}}^{V} < 120$ GeV **(b)** $p_{\mathrm{T}}^{V} > 120$ GeV

Figure A.13: MV1c distributions in the 1 b-tag control region after the application after the global fit for 3-jet events. The distributions shown are for the two p_{T}^{V} regions used as input to the fit; (a) $p_{\mathrm{T}}^{V} < 120$ GeV (b) $p_{\mathrm{T}}^{V} > 120$ GeV.

Sample	1-tag	
	$p_{\mathrm{T}}^{V} < 120$ GeV	$p_{\mathrm{T}}^{V} > 120$ GeV
VH	109.4 ± 39.9	36.0 ± 13.1
VV	3048.3 ± 305.7	622.0 ± 76.7
$t\bar{t}$	36641.0 ± 1421.9	8304.2 ± 403.1
s-top	15111.5 ± 993.6	1857.1 ± 224.8
W+l	58706.6 ± 5336.2	7459.0 ± 646.2
W+cl	84332.6 ± 6179.2	9322.3 ± 689.0
W+hf	17627.1 ± 2563.2	1729.2 ± 366.5
Z+l	4452.0 ± 556.7	327.5 ± 56.7
Z+cl	1983.9 ± 53.7	145.6 ± 3.9
Z+hf	1870.6 ± 50.7	125.4 ± 3.4
Total	223883.1 ± 494.5	29928.4 ± 163.8
Data	224026	29710
$\frac{\mathrm{Sim}-\mathrm{Data}}{\sigma}$	-0.21	0.92

Table A.8: Table of post unconditional fit yields for 3-jet 1-tag events. The uncertainties are the full postfit errors including all nusicance parameters with priors, floating normalizations, and the correlations deduced from the data. The difference in the data and the postfit simulation is compared to σ which is obtained from the sum in simulation as the sum in quadrature of the postfit and Poissonian error.

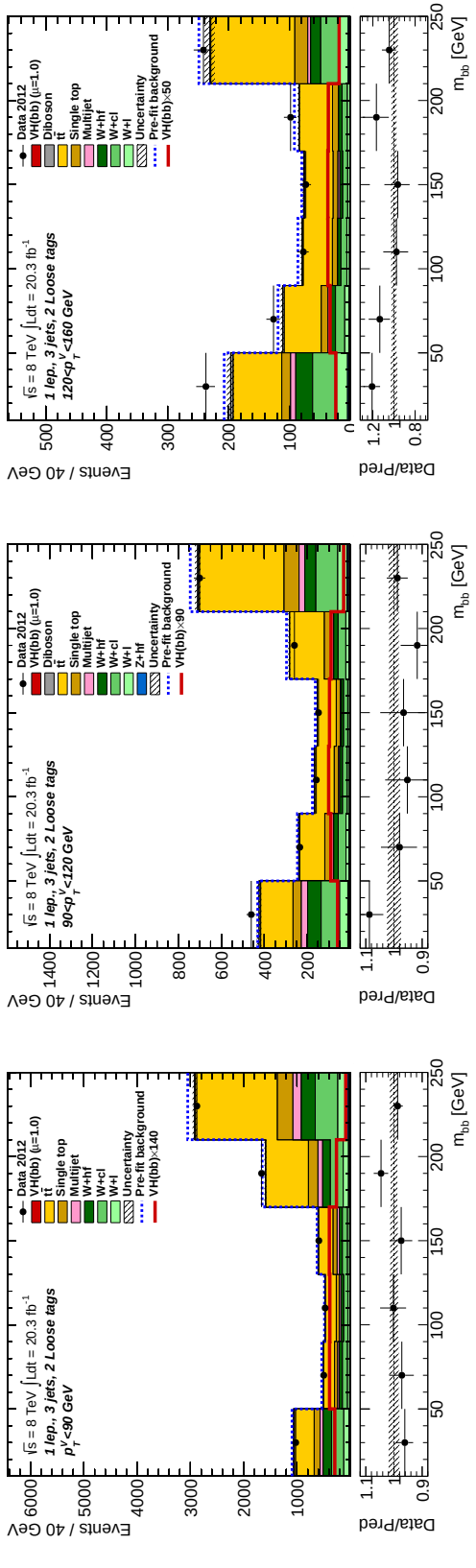

(a) $p_{\mathrm{T}}^{V} < 90$ GeV (b) $90 < p_{\mathrm{T}}^{V} < 120$ GeV (c) $120 < p_{\mathrm{T}}^{V} < 160$

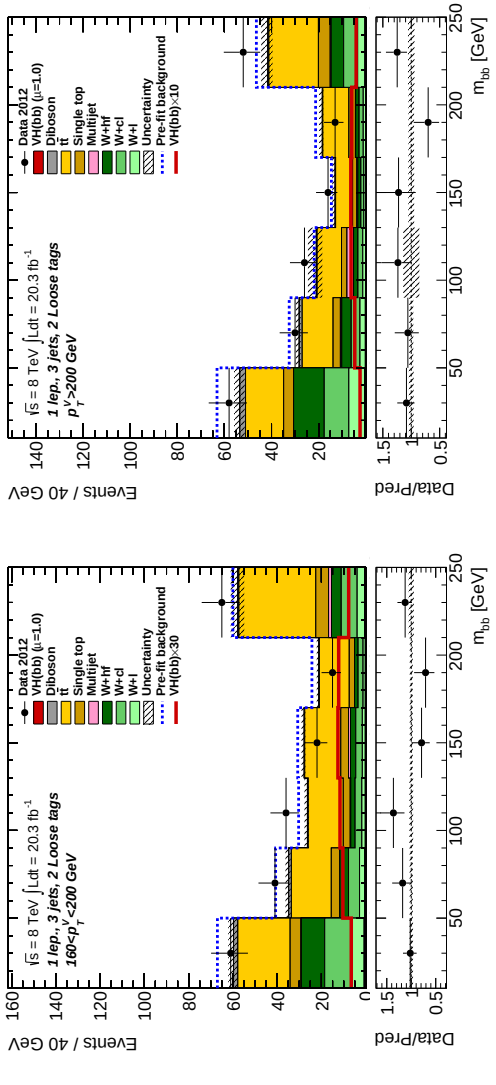

(d) $160 < p_{\mathrm{T}}^{V} < 200$ GeV (e) $p_{\mathrm{T}}^{V} > 200$ GeV

Figure A.14: Dijet mass distributions in the 2 loose b-tag region after the application of the global fit for 3-jet events. The distributions shown are for the five p_{T}^{V} bins used for the global fit; (a) $p_{\mathrm{T}}^{V} < 90$ GeV, (b) $90 < p_{\mathrm{T}}^{V} < 120$ GeV, (c) $120 < p_{\mathrm{T}}^{V} < 160$ GeV, (d) $160 < p_{\mathrm{T}}^{V} < 200$ GeV and (e) $p_{\mathrm{T}}^{V} > 200$ GeV.

Sample	2L-tag				
	$p_{\mathrm{T}}^{V} < 90$ GeV	$90 < p_{\mathrm{T}}^{V} < 120$ GeV	$120 < p_{\mathrm{T}}^{V} < 160$ GeV	$160 < p_{\mathrm{T}}^{V} < 200$ GeV	$p_{\mathrm{T}}^{V} > 200$ GeV
VH	12.9 ± 4.6	5.2 ± 1.9	3.7 ± 1.3	2.0 ± 0.7	3.0 ± 1.0
VV	59.0 ± 1.6	19.9 ± 0.5	10.3 ± 0.3	4.2 ± 0.1	4.6 ± 0.8
$t\bar{t}$	3393.3 ± 90.6	1002.0 ± 30.3	427.9 ± 16.7	122.1 ± 6.3	79.0 ± 7.2
s-top	775.7 ± 48.8	203.6 ± 13.9	72.8 ± 8.3	23.5 ± 3.2	19.1 ± 2.7
W+l	480.8 ± 62.3	126.2 ± 16.0	49.8 ± 6.3	15.6 ± 2.0	14.9 ± 2.0
W+cl	1166.2 ± 78.0	301.8 ± 20.6	112.9 ± 7.8	32.3 ± 2.3	25.2 ± 2.0
W+hf	733.9 ± 100.7	180.1 ± 31.3	68.9 ± 11.9	24.9 ± 4.3	27.0 ± 4.6
Z+l	45.1 ± 1.2	14.8 ± 0.4	3.4 ± 0.1	0.7 ± 0.0	0.4 ± 0.0
Z+cl	32.3 ± 0.9	9.7 ± 0.3	2.3 ± 0.1	0.5 ± 0.0	0.3 ± 0.0
Z+hf	70.4 ± 1.9	21.7 ± 0.6	6.8 ± 0.2	0.8 ± 0.0	0.5 ± 0.0
MJ_e	239.8 ± 25.6	78.5 ± 14.0	18.4 ± 7.2	2.0 ± 0.4	4.0 ± 4.2
MJ_μ	163.0 ± 37.2	16.0	1.9 ± 0.0	0.6 ± 0.0	0.3 ± 0.0
Total	7172.5 ± 65.6	1979.5 ± 25.8	779.2 ± 13.3	229.2 ± 4.9	178.2 ± 6.6
Data	7129	1963	852	240	195
$\frac{\mathrm{Sim-Data}}{\sigma}$	0.41	0.32	-2.35	-0.68	-1.13

Table A.9: Table of post unconditional fit yields for 3-jet 2L-tag events. The uncertainties are the full postfit errors including all nusicance parameters with priors, floating normalizations, and the correlations deduced from the data. The difference in the data and the postfit simulation is compared to σ which is obtained from the sum in simulation as the sum in quadrature of the postfit and Poissonian error.

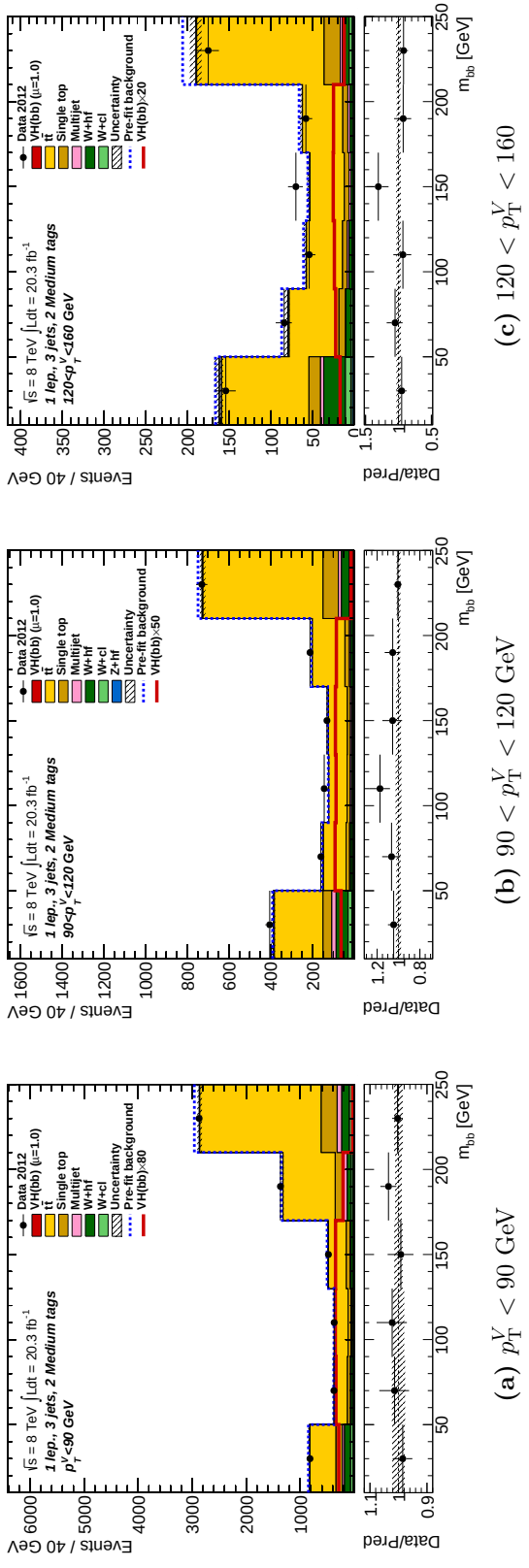

(a) $p_{\mathrm{T}}^{V} < 90$ GeV (b) $90 < p_{\mathrm{T}}^{V} < 120$ GeV (c) $120 < p_{\mathrm{T}}^{V} < 160$

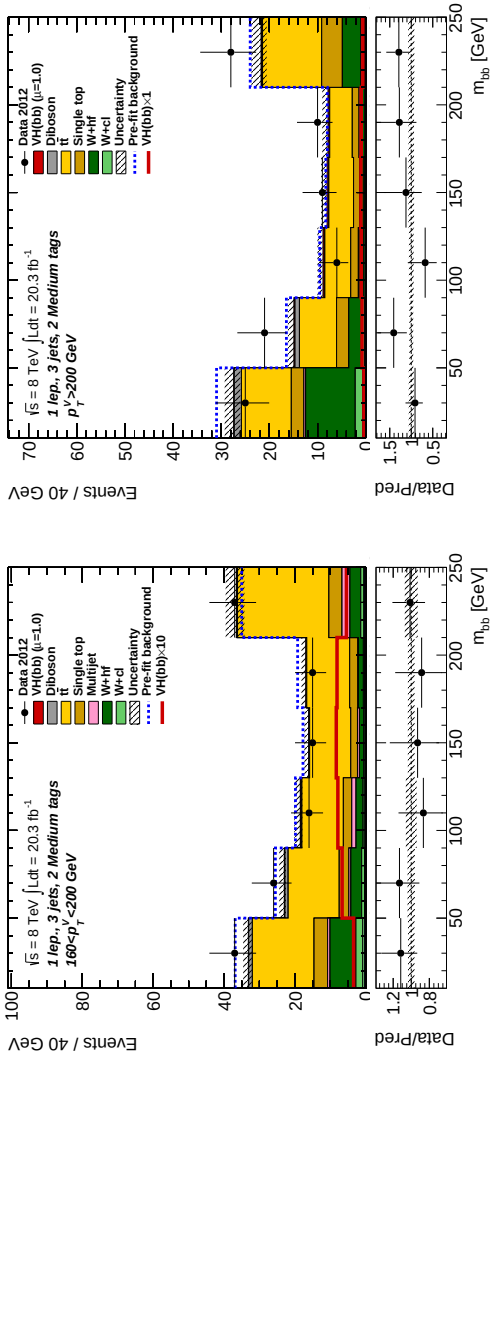

(d) $160 < p_{\mathrm{T}}^{V} < 200$ GeV (e) $p_{\mathrm{T}}^{V} > 200$ GeV

Figure A.15: Dijet mass distributions in the 2 medium b-tag region after the application of the global fit for 3-jet events. The distributions shown are for the five p_{T}^{V} bins used for the global fit; (a) $p_{\mathrm{T}}^{V} < 90$ GeV, (b) $90 < p_{\mathrm{T}}^{V} < 120$ GeV, (c) $120 < p_{\mathrm{T}}^{V} < 160$ GeV, (d) $160 < p_{\mathrm{T}}^{V} < 200$ GeV and (e) $p_{\mathrm{T}}^{V} > 200$ GeV.

Sample	2M-tag				
	$p_{\mathrm{T}}^{V} < 90$ GeV	$90 < p_{\mathrm{T}}^{V} < 120$ GeV	$120 < p_{\mathrm{T}}^{V} < 160$ GeV	$160 < p_{\mathrm{T}}^{V} < 200$ GeV	$p_{\mathrm{T}}^{V} > 200$ GeV
VH	19.5 ± 6.9	8.7 ± 3.1	6.3 ± 2.2	4.0 ± 1.4	4.6 ± 1.6
VV	27.0 ± 0.7	9.7 ± 0.3	5.6 ± 0.2	2.4 ± 0.3	2.8 ± 0.4
$t\bar{t}$	4513.8 ± 80.4	1248.9 ± 28.8	449.7 ± 15.6	93.1 ± 4.4	45.5 ± 4.2
s-top	754.6 ± 50.5	184.2 ± 12.8	58.4 ± 6.2	16.9 ± 2.3	13.7 ± 1.9
W+l	43.9 ± 1.2	11.9 ± 0.3	4.6 ± 0.1	1.3 ± 0.0	0.8 ± 0.2
W+cl	178.0 ± 14.8	48.5 ± 4.1	15.9 ± 1.3	4.9 ± 0.4	3.4 ± 0.3
W+hf	422.4 ± 60.4	126.8 ± 19.9	50.0 ± 7.8	18.0 ± 2.8	19.8 ± 3.2
Z+l	3.2 ± 0.1	1.1 ± 0.0	0.2 ± 0.0	0.0 ± 0.0	0.0 ± 0.0
Z+cl	5.2 ± 0.1	1.9 ± 0.1	0.3 ± 0.0	0.1 ± 0.0	0.0 ± 0.0
Z+hf	49.1 ± 1.3	18.1 ± 0.5	5.2 ± 0.1	0.9 ± 0.0	0.5 ± 0.2
MJ_e	127.1 ± 15.8	46.5 ± 11.8	11.9 ± 6.7	4.6 ± 2.6	0.7 ± 0.2
MJ_μ	104.3 ± 21.1	11.3	1.5 ± 0.0	0.8 ± 0.0	–
Total	6248.0 ± 54.0	1717.6 ± 22.0	609.6 ± 12.9	147.0 ± 4.0	91.9 ± 3.8
Data	6287	1782	595	146	99
$\frac{\mathrm{Sim-Data}}{\sigma}$	-0.41	-1.37	0.53	0.08	-0.68

Table A.10: Table of post unconditional fit yields for 3-jet 2M-tag events. The uncertainties are the full postfit errors including all nusicance parameters with priors, floating normalizations, and the correlations deduced from the data. The difference in the data and the postfit simulation is compared to σ which is obtained from the sum in simulation as the sum in quadrature of the postfit and Poissonian error.

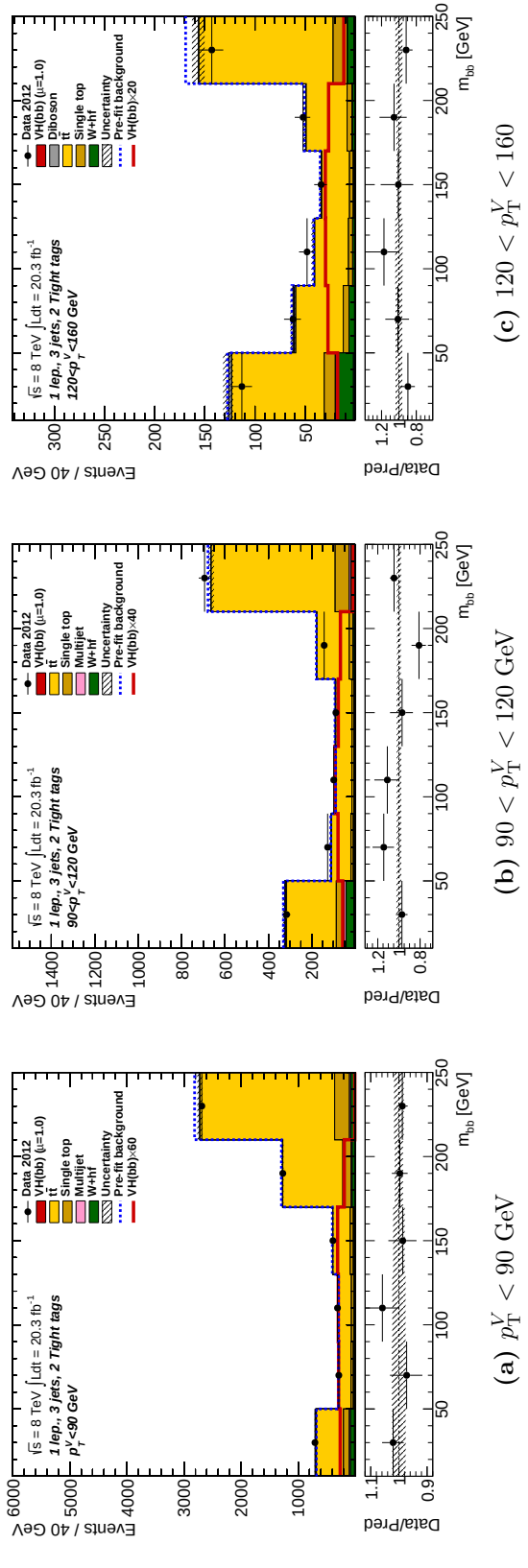

(a) $p_{\mathrm{T}}^{V} < 90$ GeV (b) $90 < p_{\mathrm{T}}^{V} < 120$ GeV (c) $120 < p_{\mathrm{T}}^{V} < 160$

(d) $160 < p_{\mathrm{T}}^{V} < 200$ GeV (e) $p_{\mathrm{T}}^{V} > 200$ GeV

Figure A.16: Dijet mass distributions in the 2 medium b-tag region after the application of the global fit for 3-jet events. The distributions shown are for the five p_{T}^{V} bins used for the global fit; (a) $p_{\mathrm{T}}^{V} < 90$ GeV, (b) $90 < p_{\mathrm{T}}^{V} < 120$ GeV, (c) $120 < p_{\mathrm{T}}^{V} < 160$ GeV, (d) $160 < p_{\mathrm{T}}^{V} < 200$ GeV and (e) $p_{\mathrm{T}}^{V} > 200$ GeV.

Sample	2T-tag				
	$p_{\mathrm{T}}^{V} < 90$ GeV	$90 < p_{\mathrm{T}}^{V} < 120$ GeV	$120 < p_{\mathrm{T}}^{V} < 160$ GeV	$160 < p_{\mathrm{T}}^{V} < 200$ GeV	$p_{\mathrm{T}}^{V} > 200$ GeV
VH	22.6 ± 7.9	9.6 ± 3.3	7.1 ± 2.4	4.4 ± 1.5	5.2 ± 1.7
VV	17.0 ± 0.5	7.4 ± 0.2	5.0 ± 0.1	2.7 ± 0.4	2.3 ± 0.4
$t\bar{t}$	4637.8 ± 78.1	1190.9 ± 27.0	375.3 ± 13.2	45.4 ± 2.4	12.5 ± 1.4
s-top	640.4 ± 44.9	149.0 ± 10.9	43.2 ± 4.9	8.6 ± 1.1	6.2 ± 0.9
W+l	1.3 ± 0.0	0.3 ± 0.0	0.1 ± 0.0	0.0 ± 0.0	0.0 ± 0.0
W+cl	9.3 ± 0.8	2.2 ± 0.2	1.0 ± 0.1	0.2 ± 0.0	0.1 ± 0.0
W+hf	234.4 ± 36.9	71.4 ± 11.8	35.0 ± 5.6	13.6 ± 2.2	14.7 ± 2.4
Z+l	0.1 ± 0.0	0.0 ± 0.0	0.0 ± 0.0	–	–
Z+cl	0.1 ± 0.0	0.1 ± 0.0	0.0 ± 0.0	0.0 ± 0.0	0.0 ± 0.0
Z+hf	32.5 ± 0.9	11.8 ± 0.3	3.3 ± 0.1	0.7 ± 0.3	0.5 ± 0.2
MJ_e	86.7 ± 14.8	21.4 ± 7.8	2.4 ± 0.3	0.6	–
MJ_μ	0.0	0.0	0.0	0.0	–
Total	5682.2 ± 57.6	1464.0 ± 22.4	472.3 ± 11.3	76.2 ± 2.9	41.5 ± 2.7
Data	5647	1468	452	79	46
$\frac{\mathrm{Sim-Data}}{\sigma}$	0.37	-0.09	0.83	-0.3	-0.65

Table A.11: Table of post unconditional fit yields for 3-jet 2T-tag events. The uncertainties are the full postfit errors including all nusicance parameters with priors, floating normalizations, and the correlations deduced from the data. The difference in the data and the postfit simulation is compared to σ which is obtained from the sum in simulation as the sum in quadrature of the postfit and Poissonian error.